Irradiation Damage in $REBa_2Cu_3O_{7-x}$ Superconductors



Yatir Linden

Mansfield College, University of Oxford

A thesis submitted for the degree of Doctor of Philosophy

Supervised by: Prof. C. R. M. Grovenor & Prof. Susannah Speller

Hilary Term 2023

Abstract

Future designs of fusion power reactors will require superconducting magnet windings that, in service, will be subjected to high fluxes of particles, in particular 14 MeV neutrons generated in the fusion reaction. It is an engineering priority and challenge to generate the highest magnetic fields possible to reduce the size of the reactor and increase its power output, which can be achieved by the use of high temperature superconducting tapes. Despite efforts to understand the irradiation effects associated with the impact of energetic particles on the complex structure of high temperature superconductors, little is known about the microstructural evolution under irradiation. Understanding the mechanism of irradiation damage is thus of great importance for the development of fusion reactors.

The characterisation work used Transmission Electron Microscopy as the primary tool together with imaging processing techniques and analytical tools to assess subtle changes of the structural parameters following irradiation. An in-reactor sample of superconducting tape was irradiated by neutrons to a fluence of 3.3×10^{18} cm^{-2}, and to validate the findings, results were compared with a pristine reference sample without neutron irradiation. In order to further study the mechanisms of radiation damage on the REBCO matrix, extensive in-situ ion irradiation experiments in a TEM were taken place using different energies, temperatures, and incident ions at the MIAMI2 facility at the University of Huddersfield.

The first section of the experimental results presented in this thesis is a qualitative evaluation of selected irradiated samples. The impact of both ion and neutron irradiation is illustrated, and HRTEM images compared at the pre- and post-irradiation stages. Both neutron and proxy ion irradiation using heavy ions (Kr, Xe) also show small (2-10 nm) damage cascades. Lighter ion

irradiation using He presents clear evidence for homogenous lattice degradation. The effects of temperature, irradiation energy, and incident particle mass are also discussed.

The second results section uses HAADF/STEM atomic-resolution images as an input in order to fit the lattice atomic locations. These locations are then used to extract the structural parameters of the Ba_1-RE-Ba_2 sublattice, that are then discussed as in terms of the associated damage mechanisms. Using the precise locations of the atomic columns, I was able to extract a wide-array of structural parameters from every unit cell and pool these together to a meaningful statistical results, insights that could not be replicated using traditional approaches such as XRD.

In the last results section, I report for the first time on image processing technique that allows a precise quantification of the irradiation damage compared relative to reference states of unirradiated and amorphous material. The performance of these entropy measurements in the frequency domain were proved robust and accurate by analysing more than 1000 HRTEM images irradiated under different conditions. I illustrate the direct, linear-like, correlation of the expected lattice damage, as experimentally observed in the first section, to the entropy values extracted. I also elaborate on the underlying reasons why the observed correlation exists.

By using a combination of a large dataset and new analytical tools, this thesis sheds light on the irradiation mechanisms in high temperature superconductors. The data analysis conducted is also relevant for application in the study of other irradiated materials.

Acknowledgements

This thesis would not have come to fruition without the support of my direct supervisors, Prof. Chris Grovenor and Prof. Susie Speller. Their continual guidance and endless support, along with their technical and professional knowledge, got me through times of frustration and self-doubt on this challenging journey.

A big thanks to Dr. Will Iliffe who was my closest colleague from the first until the last day of this project. I would also like to thank Dr. Junliang Liu and Dr. Guanze He who were always willing to offer their precious time, sharing their broad technical experience and actively brainstorming ideas to tackle complex questions. A noteworthy part of the dataset that presented in this thesis are thanks to them: for the sample preparation side from Dr. Liu and for TEM/STEM characterisation from Dr. He. Thanks also to Prof. Sergio Lozano-Perez who was always there to help with any intricate topic related to Electron Microscopy.

A special thanks to the staff of the David Cockayne Centre for Electron Microscopy (DCCEM) who provided immediate support. I especially extend my gratitude to Dr. Neil Young for supporting every detail on the TEMs, Dr. Gareth Hughes for his dedication to keep the FIB machines up and running, and also Dr. Ian Griffiths, Mrs Jennifer Holter and Mr Graham Wyatt.

Also, huge appreciation for the invaluable help of Dr. Graeme Greaves at the University of Huddersfield who dedicated dozens of hours to collect a hefty amount of data at the MIAMI2 in-situ irradiation facility. Thanks also to the staff at the MRF Culham Centre, especially to Dr. Andrew London who trained me on the hot FIB facility and provided technical and professional help, and also to Mrs Kate Breach who coordinated my visits.

I would like to thank Dr. Mohsen Danaie at the electron Physical Science Imaging Centre, Diamond Light Source, who is not only directly responsible for a large portion of the fantastic atomic-resolution results presented in this work but was also willing to share with me his knowledge in data processing, which resulted in very useful professional discussions. A distinctive thanks for Dr. Samuel Murphy at the University of Lancaster who provided the missing piece in the jigsaw through his excellent theoretical work of irradiation damage.

Thanks also to my other friends in the Department of Materials who provided a fertile ground for friendly yet inspirational discussions, including Dr. Guillaume Matthews, Dr. Jack C. Haley, Mr Xiaonan Luo, and Mr Kevin Treder, to name but a few.

Finally, I wish to express my gratitude to my dear family. My parents (Binyamin and Malka Lindzen) and my wife's parents (Yorai and Orly Winograd), who have given me the opportunity to live my wildest dreams. Without their support, this journey could not have been embarked upon. And most importantly, to my dear wife and best friend, Nitzan, who has been the most incredible partner on this journey and accompanied me emotionally and mentally these last few years. And lastly, to our little daughter, Arielle, who was born in the midst of my thesis; her little smiles that turned into sounds and words have kept me sane and encouraged me to continue, despite all the hurdles, pursing my DPhil degree.

This doctoral thesis is dedicated to my wife, daughter and parents.

Preface / Declaration

The work reported in this thesis was carried out by the author in the Department of Materials at the University of Oxford between October 2017 and May 2022, under the supervision of Prof. C.R.M Grovenor and Prof. S.C. Speller. All the work shown is original and has not been submitted for any other degree at the University of Oxford or elsewhere. The work of others included in this thesis has been referenced and acknowledged.

Publications

Linden, Y., et al. "Analysing neutron radiation damage in $YBa_2Cu_3O_{7-x}$ high-temperature superconductor tapes." Journal of Microscopy 286.1 (2022): 3-12. Selected for the *Paper of the Quarter* for important contribution to the Journal.

Conferences

European Conference of Applied Superconductivity. Glasgow, UK. September 2019. Poster – "Radiation damage mechanisms in coated conductors".

Microscopy of Radiation Damage conference. Oxford, UK. March 2018. Poster – Radiation Damage in Superconducting Materials.

Acronyms

A

American Superconductor Corporation
(AMSC), 77
annular dark-field
(ADF), 89
artificial neural networks
(ANN), 71
artificial pinning centres
(APCs), 21

B

Bardeen-Cooper-Schrieffer
(BSC), 10
binary collision approximation
(BCA), 30
blind IQA
(BIQA), 62
bright field
(BF), 27

C

chemical solution deposition
(CSD), 16
coated conductor
(CC), 19
coefficient of variation
(CV), 231
contrast transfer function
(CTF), 89
convolutional neural network
(CNN), 75
Culham Centre for Fusion Energy
(CCFE), 88

D

dark field
(DF), 43
density functional theory
(DFT), 177
deuterium-tritium
(DT), 2
difference mean opinion score
(DMOS), 63
difference of Gaussian
(DoG), 65
direct current
(DC), 68
discrete cosine transformation
(DCT), 66
displacements per atom
(dpa), 34
distortion-aware
(DA), 63
distortion-unaware
(DU), 63

E

Electron energy loss spectroscopy
(EELS), 48
electron Physical Science Imaging Centre
(ePSIC), 88
energy dispersive spectroscopy
(EDS), 45
Environmental TEM
(E-TEM), 75

F

face centered cubic
(FFC), 110
fast Fourier transform
(FFT), 53
field emission gun
(FEG), 88
focused ion beam
(FIB), 80
Fourier transform
(FT), 66
Frenkel pairs
(FPs), 32
full width half maximum
(FWHM), 153
full-reference IQA
(FR-IQA), 62

G

geometric phase analysis
(GPA), 74
grain boundaries

(GBs), 19
gray level co-occurrence matrix approach
(GLCM), 64
grazing incidence XRD
(GIXRD), 142
grey level run-length matrix
(GLRLM), 64

H

high resolution transmission electron microscope
(HRTEM), 7
high temperature superconductors
(HTS), 4
high-angle annular dark-field
(HAADF), 90

I

image quality assessment
(IQA), 62
International Atomic Energy Agency
(IAEA), 78
interquartile range
(IQR), 274
inverse DCT
(IDCT), 208
inverse FFT
(IFFT), 75
ion beam assisted deposition
(IBAD), 20

J

Joint European Torus
(JET), 3

L

Laplacian of Gaussian
(LoG), 65
local binary pattern
(LBP), 64
low temperature superconductors
(LTS), 3
low-angle annular dark-field
(LAADF), 90

M

magnetization-magnetic field curve
(M-H), 23
Materials Research Facility
(MRF), 87
medium-angle annular dark-field
(MAADF), 90
metal organic chemical vapor deposition
(MOCVD), 20
Molecular Dynamics
(MD), 30
Monte Carlo N-particle
(MCNP), 30

N

neural networks
(NN), 71
no-reference IQA
(NR-IQA), 62
normal-superconductor
(N-S), 19

O

oxygen reordering
(ORO), 46

P

physical vapor deposition
(PVD), 20
positron annihilation lifetime spectroscopy
(PALS), 125
pressurized water reactor
(PWR), 41
primary knock-on atom
(PKA), 30
principal component analysis
(PCA), 281
probability distribution function
(PDF), 74
pseudo-Wigner distribution
(PWD), 73
pulsed laser deposition
(PLD), 20

R

rare earth barium copper oxide compounds
(REBCO), 3
reduced-reference IQA
(RR-IQA), 62
region of interest
(ROI), 79
rolling-assisted biaxially textured substrate
(RABiTS), 20

S

Scanning electron microscope
(SEM), 83
scanning transmission electron microscopy
(STEM), 5
secondary electrons
(SE), 43
selected area electron diffraction
(SAED), 91
short-time Fourier transform
(STFT), 70
spatial-spectral entropy-based quality
(SSEQ), 73

T

thermal diffuse scattering
(TDS), 127
threshold displacement energies
(TDE), 130
Transmission Electron Microscopy
(TEM), 10
twin boundaries
(TB), 20
two-beam
(TB), 49

X

x-ray absorption spectra
(XANES), 183
X-ray diffraction
(XRD), 144

Z

zone axis
(ZA), 97

Table of Contents

Abstract ---- ii

Acknowledgements ---- iv

Preface / Declaration ---- vi

Acronyms ---- vii

List of Tables ---- xiii

List of Figures ---- xv

1. Introduction ---- 1

1.1. The Future of Fossil Fuels ---- 1

1.2. Nuclear Fusion Power ---- 2

1.3. Problems for superconducting magnets in fusion reactors ---- 4

1.4. Objectives ---- 5

2. Literature Review ---- 7

2.1. Superconducting materials ---- 7

2.1.1. Theory of superconductivity ---- 8

2.1.2. High temperature superconducting oxides (HTS) ---- 10

2.2. Irradiation Damage in HTS ---- 29

2.2.1. Radiation damage mechanisms ---- 30

2.2.2. YBCO post-irradiation structure and superconducting properties ---- 39

2.2.3. Summary ---- 61

2.3. Introduction to Image Processing Techniques ---- 62

2.3.1. Image Quality Assessment (IQA) ---- 62

2.3.2. Image processing classes ---- 63

2.3.3. Image processing in Transmission Electron Microscopy ---- 74

3. Materials and Experimental Methods ---- 77

3.1. Materials ---- 77

3.1.1. $REBa_2Cu_3O_{7-x}$ (REBCO, RE = Rare Earth) tapes ---- 77

3.1.2. Neutron-irradiated samples ---- 78

3.2. Sample preparation ---- 79

3.2.1. Etching REBCO protective layers ---- 79

3.2.2. TEM lamellae preparation by Focused Ion Beam milling ---- 80
3.3. TEM imaging ---- 88
3.4. In-situ TEM irradiation ---- 91
3.4.1. The importance of in-situ TEM for the current study ---- 92
3.4.2. Design of the first in-situ experiments ---- 93
3.4.3. Design of second in-situ experiment ---- 94
3.4.4. Real fluence in MIAMI2 experiments ---- 95
3.5. Data Analysis ---- 96
3.5.1. Analysis of STEM/HAADF images ---- 97
3.5.2. HRTEM Quality assessment ---- 116
4. Irradiation damage mechanisms ---- 121
4.1. Neutron-irradiation damage ---- 121
4.2. Ion-irradiation damage ---- 128
4.2.1. The effect of ion mass ---- 129
4.2.2. The effect of sample temperature during irradiation ---- 139
4.2.3. Summary ---- 142
5. STEM/HAADF image analysis ---- 144
5.1. Introduction ---- 144
5.2. Neutron and ion irradiation mechanisms ---- 147
5.2.1. Analysing image sets ---- 147
5.2.2. Analysing individual images ---- 156
5.2.3. Analysing local variations within images ---- 160
5.3. Effect of projectile on light ion irradiation damage ---- 164
5.4. Effect of temperature on Heavy ion irradiation ---- 168
5.5. Discussion ---- 177
5.5.1. Ba_1-Ba_2 separations ---- 177
5.5.2. Neutron and ion-irradiation ---- 183
5.5.3. Light ion irradiation ---- 187
5.5.4. Effect of irradiation temperature ---- 188
5.5.5. Experimental errors ---- 191
5.5.6. Statistical significance analysis ---- 194
6. HRTEM images analysis ---- 196
6.1. Introduction ---- 196

6.2. Why image quality assessment is not likely to succeed in the spatial domain ---------- 196
6.3. Entropy changes in the frequency domain ---------- 200
6.3.1. Amorphous HRTEM images ---------- 203
6.3.2. Why does FFT entropy increase? ---------- 205
6.3.3. Why does DCT entropy increase? ---------- 208
6.3.4. Summary ---------- 220
6.4. Quantitative analysis of entropy changes in HRTEM images ---------- 220
6.4.1. Neutron-irradiation damage ---------- 220
6.4.2. Ion irradiation ---------- 222
6.4.3. Effect of irradiation temperature ---------- 226
6.4.4. Comparison of all samples ---------- 227
6.5. DCT and FFT comparison ---------- 230
7. Conclusions and Future Work ---------- 232
7.1. Conclusions ---------- 232
7.2. Suggestions for Future Work ---------- 235
References ---------- 237
Appendix A Chapter 4 Supplementary Information ---------- 268
Appendix B Chapter 5 Supplementary Information ---------- 271
Appendix C Chapter 6 Supplementary Information ---------- 278

List of Tables

Table 2.1: Physical properties of YBCO and GdBCO type II superconductors. ---------- 22
Table 3.1: Irradiation parameters used in the first in-situ TEM experiments at the MIAMI2 facility.---------- 94
Table 3.2: Specifications of the second in-situ TEM irradiation experiments at the MIAMI2 facility. In each group of samples there are three irradiation parameters that are fixed and one parameter that varies.---------- 95
Table 3.3: Summary of the samples used for STEM/HAADF images analysis. ---------- 97
Table 3.4: MATLAB program control variables for fitting REBCO sublattices. ----------102
Table 3.5: Summary of the image acquisition spesifications for each type of microsccpe broken down into one-frame and stack images acquisition methods. The first row displays the total number of images analysed taken from pristine samples. ----------108
Table 3.6: Number of Au nanoparticle STEM images taken from ARM300CF and ARM200f microscopes in different image acquisition modes. ----------110
Table 3.7: Irradiation conditions for the samples used for HRTEM analysis.----------118
Table 4.1: Average dpa values estimated using SRIM for 100 nm thick YBCO for five types of ions irradiated at 350 keV.----------131
Table 5.1: REBCO structural parameters as were extracted from STEM images (one-frame images taken on the ARM300CF microscope) for un-irradiated (pristine) and three irradiated samples; neutron-irradiated, Xe-ion at 298 K and He-ions. The first two rows show the average REBCO lattice parameters (a/b- and c-axis). The third and forth rows present a comparison of unit cell volume and c/a axes lattice parameter ratio (assuming a/b-axes lattice parameters are equal). For the sake of comparison, the c/a ratios taken from the literature are 3.028 and 3.026 for YBCO and GdBCO, respectively. The presented shift from the theoretical values of the a/b-axis compared to c-axis is explained in section 3.5.1.4.1. The last three rows quote the a-, b-, and c-axis lattice parameters extracted from X-ray diffraction (XRD) measurements [419]. ---150

Table 5.2: Inter- and intra-cell Ba_1-Ba_2 distances as a fraction of average c-axis lattice parameter for pristine, neutron-irradiated, He-irradiated, and Xe-ion irradiation at 298 K. The numbers are the average of one-frame & stacks images taken on the ARM300CF microscope. ----------152
Table 5.3: Average REBCO lattice parameters (a/b- and c-axis) and inter- and intra-cell Ba_1-Ba_2 fractions for un-irradiated (pristine) and three irradiated samples; Ne-ions, Ar-ions and He-ions as was measured from STEM images extracted from one-frame images (lattice parameters) and one-frame & stack images (inter- and intra-cell fractions) taken on the ARM200f and ARM300CF microscopes, shown on the left and right side of the table, respectively.----------167
Table 5.4: Average REBCO lattice parameters and inter- and intra-cell fractions of Xe-ions irradiated samples at 100 and 298 K benchmarked against un-irradiated (pristine) values. Lattice parameters values were extracted from one-frame and inter- and intra-cell fraction were extracted from both one-frame and stacks images, both taken on the ARM300CF microscope. ----------172
Table 5.5: ARM200f microscope typical aberration coefficients in the corrected state at 200 kV. Kindly provided by Dr. Ian Griffiths.----------192
Table 6.1: Entropy values of 'almost-amorphous' samples used for this study compared to fully-amorphous images taken from the sample edge. To make this comparison, the entropy values were calculated from 512X512 pixel blocks from HRTEM images. ----------204
Table 6.2: the effect of the choice of inner and outer radii of the medium frequency band on the entropy values calculated from images of pristine and amorphous samples. The entropy values change also due to the change in the number of pixels on which the entropy values were calculated, but the difference in percentage terms is essentially unchanged. The entropy values are averages measured from 410 and 44 HRTEM images of pristine and amorphous material, respectively.----------206
Table 6.3: Percentage of damage for the samples presented in this study derived from the assumption of 0% damage for pristine samples and 100% for amorphous samples. ----------230

List of Figures

Figure 1.1: Global energy resource allocation (updated to 2012) [10]. ---------- 1
Figure 1.2: Examples of fusion reactor vessel on the relatively large JET (a) and the smaller ST25 (b).---------- 4
Figure 2.1: Transition temperatures evolution of superconductors [51].---------- 8
Figure 2.2: Schematic illustration of Meissner effect in the normal, shown at the left side, and superconducting state on the right side. The lines represent the magnetic fields lines [54]. ------ 9
Figure 2.3: (a) Pictorial representation of Abrikosov lattice. The magnetic field B applied parallel to vortex lines and induced currents perpendicular the surface [62]. (b) Direct observation using Transmission Electron Microscopy (TEM) of triangular array of Abrikosov lattice in Pb-4 at.% In superconductor [57].---------- 10
Figure 2.4: Comparison of the critical current as a function of applied field of several types of low and high temperature superconductors (data taken from several sources; courtesy of (https://nationalmaglab.org/magnet-development/applied-superconductivity-center/plots). 11
Figure 2.5: YBCO orthorhombic crystal structure [66].---------- 12
Figure 2.6: Sandwich structure of $CuO2$ and insulating layers [71]. In high temperature superconductors, the structure along c-axis can be presented as alternating layers of CuO_2 separated by different layers of insulating layers, represented here as X, Y, Z, where X and Z are the BaO_2 planes and Y are the rare-earth, Oxygen-free planes. ---------- 13
Figure 2.7: Properties of REBCO films with different lanthanide elements. (a) Critical temperature (T_c), and critical current (J_c) for different RE elements measured at 77 K. (b) J_c measured at 77 K in different magnetic fields [74]. ---------- 14
Figure 2.8: Critical temperature as a function of oxygen content in YBCO [87]. ---------- 14
Figure 2.9: High resolution TEM (HRTEM) images, strain maps and illustrations of intergrowth unit cells. (a-b) STEM/HAADF images taken along [010] zone axis show the bending of the YBCO's layered structure perpendicular to the c-axis. (c-e) Lattice strain maps, $\varepsilon xx, \varepsilon yy, \varepsilon xy$, respectively, calculated from the rectangular region shown in (b). (f) Schematic illustrations of the Y123, Y124, Y125, phases [88], [89]. ---------- 15

Figure 2.10: The angular dependence of J_c in YBCO at 64 K and 3 T for unirradiated (black squares) and after neutron irradiation at 4×10^{21} n/m^2 (red circles), 1×10^{22} n/m^2 (green triangles) [95]. ---------- 16
Figure 2.11: Typical phase diagram for superconductors [99]. ---------- 18
Figure 2.12: Different vortex states and phase transformations [105]. ---------- 18
Figure 2.13: The correlation between critical current (J_c), applied magnetic field (H), and temperature (T) creates a critical surface that separates the normal and superconductor (N-S) states [107]. ---------- 19
Figure 2.14: Temperature dependent transition behaviour when in applied fields H=0, 10, 25, 50, 100, 250, 500, 1000, 1400, 1900 Oe, from bottom to top [114]. ---------- 19
Figure 2.15: Layered-structure of SuperPower's REBCO CC layered-structure [126]. ---------- 20
Figure 2.16: STEM/HAADF image of REBCO containing $BaZrO_3$ (BZO) nanorods. The green and brown colours represent the local orientation of the lattice, [010] and [100], respectively, caused by the TB domains separated by dashed white lines. The arrows indicate partial dislocations and the inset shows an enlarged region with Y125 intergrowth [128]. ---------- 21
Figure 2.17: Critical current (J_c) (left figure) and pinning force (F_p) (right figure) measured in various magnetic fields, H||c, at 65 K on different YBCO films. YBCO stands for pure film; whereas the other samples contained different wt.% of $BaSnO_3$ (BSO) nanorods aligned along the c-axis and Y_2O_3 (YO) nano-spheres with concentration of 2.2 (YOA) and 3.0 wt.% (YOB) [145]. ---------- 23
Figure 2.18: A schematic view of the effectiveness of APCs in different temperature (y-axis) and magnetic field (x-axis) regimes that can be tailored for specific applications. They are divided into 3 regions from high temperatures and low fields at the top and down to low temperatures and low fields at the bottom. The angular J_c dependency is also shown for each region to illustrate the anisotropy characteristics where θ=0 defined as the field parallel to the c-axis [153]. ---------- 25
Figure 2.19: TEM bright field (BF) images taken along [100]/[010] ZA from (Gd,Y)BCO with 15 mol.% Zr added and different (Ba + Zr)/Cu ratios, low-0.72(a), medium-0.76(b), and high-0.85(c), corresponding to Ba molar concentrations of 1.8, 1.97 and 2.35, respectively. RE_2O_3

phase is marked by white arrows (a) and alternating width of BZO rods is emphasised by red dashed lines (b) [170]. ---------- 27
Figure 2.20: Critical current (J_c) at 4.2 K in different magnetic fields of (Gd,Y)BCO-BZO as a function of Ba content from 1.8 to 2.35 (equivalent to (Ba + Zr)/Cu 0.72 to 0.85) with a constant 15 mol.% Zr addition [170].---------- 28
Figure 2.21: Schematic representation of the behaviour of pinning centres in an oblique magnetic field. (a) Vortices exhibit 'jumps' from pinning site to another, until the loss of ability to provide strong pinning force. (b) 3D-APC sustain the pinning force independent on the field direction [145]. ---------- 29
Figure 2.22: Flux density for the TRIGA MARK-II reactor at a power of 250 kW. The solid line is the input spectrum as provided by the reactor manufacturer and the broken line is a measured data obtain by Weber et.al. [192]. ---------- 32
Figure 2.23: Pictorial image of the damage morphologies created by different irradiation particles; T is the typical energy for PKA, and ε is the damage efficiency [191]. The shaded areas are collision cascades where any crystalline material normally becomes amorphous. ---------- 33
Figure 2.24: Electronic and Nuclear stopping power of iron ions moving into an iron target depicted as the energy loss as a function of energy [199].---------- 35
Figure 2.25: Schematic illustration of the initial stage of the collision cascade [225]. ---------- 36
Figure 2.26: Number of subcascades produced as a function of PKA energy in targets of different atomic mass computed using the binary collision approximation (BCA) model [229]. 37
Figure 2.27: Schematic illustration of the amorphisation fraction (y-axis) as a function of irradiation fluence (x-axis) according to models proposed in the literature (adopted from [236]). ---------- 39
Figure 2.28: Neutron flux as a function energy for pressurized water reactor (PWR) fission reactor and DEMO fusion reactor [251]. ---------- 41
Figure 2.29: Representative HRTEM images of amorphous tracks in YBCO irradiated with 5.3 GeV Pb ions to a dose of $6 \times 1011\ ions/cm2$ (a) cross-section view and (b) plan-view [249]. 42
Figure 2.30: TEM bright field (BF) (a-b) and dark field (DF) (c) images tilted 15° from c-axis showing damage after ion-irradiation of YBCO single crystals. (a) 1.3 GeV U-ions. (b) 2.29 GeV

Xe-ions. (c) DF (the authors have not mentioned the corresponding g-vector) after 2.25 GeV Au-ions [255]. ---------- 43
Figure 2.31: YBCO resistance as a function of critical temperature (T_c) presented for different irradiation fluences [cm^{-2}] of 3.5 GeV Xe-ions [258]. ---------- 44
Figure 2.32: Filtered (a) and experimental and modeled (b) HRTEM images of damage cascade in YBCO following 107 MeV ^{84}Kr-ions irradiation. (a) filtered HRTEM of the damaged region (inset D) and the non-damaged regions in its vicinity (5-20 nm) presented in insets P1-P6. (b) experimental HRTEM image with a modeled HRTEM image including 3 nm void (c) [260]. ------ 46
Figure 2.33: TEM/HRTEM images of YBCO, taken after 1.3 GeV U-ion irradiation. (a) HRTEM image taken along [001] direction showing bow-tie contrast, aligned along the b-axis around a latent track. (b) TEM BF image showing a network of bow-ties fusing together. (c) pictorial representation of the interweaved bow-ties [255], [264]. ---------- 47
Figure 2.34: TEM image of shows a cellular structure in YBCO doped with LiF following 1×10^{22} m^{-2} neutron-irradiation [266]. ---------- 47
Figure 2.35: STEM/HAADF images taken along [100]/[010] ZA of Dy-doped YBCO CC irradiated with 18 MeV Au^{+5} ions to a fluence of 3×10^{11} cm^{-2}, (a) before annealing, (b) after annealing in oxygen atmosphere at 170 ℃ for 60 min [267]. ---------- 49
Figure 2.36: Two-beam (TB) TEM images of unirradiated and post-neutron irradiation to 2×10^{21} m^{-2}. Left image taken from pre-irradiated sample with g=[200], post-irradiation central image using g=[200], and right post-irradiation image with g=[006]. Both TEM/TB images of the post-irradiated samples show black/white features a few nanometers in diameter [253]. ---------- 50
Figure 2.37: HRTEM images taken along [100] before (left) and after (right) neutron-irradiation to a fluence of 2×10^{21} m^{-2}. The irradiated sample show signs of intercalation and increasing c-axis lattice parameter [269]. ---------- 51
Figure 2.38: HRTEM direct observation of amorphous-like region, marked by dotted line circle, following 500 keV Si-ion irradiation to a fluence of 2×10^{10} cm^{-2} [273]. ---------- 52
Figure 2.39: HRTEM images taken along [031] zone axis from proton irradiated YBCO films at fluence of to 1×10^{15} cm^{-2}. The irradiation defects are shown in red dashed circles and the insets show FFT extracted from the areas marked by yellow dashed squares [274]. ---------- 53

Figure 2.40: TEM/TB g=[200] (bottom row) and g=[002] (lower row) images taken from pristine (a,c) and proton irradiated to 2×10^{16} cm^{-2} (b,d) YBCO superconductor tape. The irradiated images show small defects in higher-contrast that do not show in the unirradiated images. The larger particles are a second phase of Dy_2O_3 [275]. ---------- 54
Figure 2.41: (a) Critical temperature (T_c) dependence on neutron irradiation fluence [37], and (b) the broadening of superconducting transition temperature after 74 MeV Ag-ions irradiation to fluences of $10^{11} – 10^{13}$ cm^{-2} [277].---------- 56
Figure 2.42: REBCO CC before and after neutron irradiation at $2.3 \times 1022\ n/m2$ measured with magnetic fields applied (a) parallel to the ab-plane and (b) c-axis [279].---------- 57
Figure 2.43: irreversibility line before and after irradiation in two types of REBCO CC measured for (a) H||ab and (b) H||c [279].---------- 58
Figure 2.44: (a) J_c dependence on dose for five different REBCO CC measured at 30 K and applied fields of 15 T parallel to the c-axis. The two of them denoted as SCS4050-AP contain APCs. (b) Schematic comparison of J_c as a function of defect density in CC with (upper sketch) and without (bottom sketch) pre-existing APCs [37]. ---------- 59
Figure 2.45: Critical current enhancement as a function of 3.5 MeV oxygen ion irradiation and pre- and post-irradiation TEM images. (a) Critical current as a function of irradiation dose at performed at 5, 27, and 45 K, shown by closed and open circles, and triangles, respectively. Pre-(b) and post-(c) irradiation TEM images using (002) BF/TB imaging condition following 1×10^{13} cm^{-2}, 3.5 MeV oxygen-ion irradiation [285].---------- 60
Figure 2.46: (a-c) TEM plan-view images (with ~15° tilt from the c-axis) of YBCO single crystals irradiated with 3.9 GeV Au-ions (a) As-irradiated. (b) After 20 minutes at 420 ℃. (c) After one hour anneal in each stage at 400, 450, 500, 550, 575, 600 ℃. At this stage, the width variations disappeared [261].---------- 61
Figure 2.47: Partial list of areas in which image processing is implemented [288]. ---------- 62
Figure 2.48: An example of gray level co-occurrence matrix approach (GLCM). (a) A 4X4 pixels input image, where each pixel represents intensity. (b) GLCM matrix corresponds to shift vector d=(1,0). The values in the co-occurrence matrix are the number of pixels having gray levels i and j and separated by d, mathematically defined as $n_{ij} = P_d[i,j]$. For example, the co-occurrence

matrix in position (2,5) and d=(1,1) counts the number of occurrences where the first gray-tone in a location of (i,j) ((2,5) in this example) has the value of 2 and the second gray-tone in the location of (i+1,j+1) has a value of 5. The non-light brown colours correlate to the number of repetitions of intensity i in (0,0) location and intensity j in (1,0) location in the input image (a). (c) normalisation of GLCM matrix (b) by the total size of the matrix [308]. ---------- 65
Figure 2.49: An example of gradients and relative gradients maps performed on an undistorted image (a). (b) gradient magnitude, (c) relative gradient orientation, (d) relative gradient magnitude [314]. Distortions affect the statistics of the three maps in a different manner, and in order to capture these differences the authors calculated the variance of every map in 2 scales (6 features in total) and show a promising correlation to DMOS results. ---------- 66
Figure 2.50: Radial Binary masks for preserving the low (left) medium (middle) or high (right) frequency components. Black pixels represent the value '1' and white '0' [320].---------- 68
Figure 2.51: Discrete Cosine Transformation basis signals of size 8×8 [324].---------- 69
Figure 2.52: An illustration of short-time Fourier transform (STFT) and wavelets characteristics when applied to 1D signal that changes over time and type of mother wavelets. (a) STFT analysis shows a constant window size both in frequency and time, (b) Wavelet windows sizes show an inverse proportionality of time and frequency [336]. (c) Examples of six types of wavelets families [337]. ---------- 70
Figure 2.53: Different types of entropies on a logarithm time scale. The colours presented represent the sections in which these entropies are discussed in the original publication [361]. ---------- 72
Figure 2.54: Histogram of spatial (a) and spectral (b) entropies derived from 8×8 pixel blocks taken from reference images (ori), Gaussian blur (blur), white noise (noise), JP2K compression (JP2K), JPEG compression (jpeg), and fast Rayleigh fading (ff) [316].---------- 74
Figure 2.55: number of publications per year that include the keywords "machine learning" and "microscopy" in the title/abstract/keywords, as collected from Scopus.---------- 76
Figure 3.1: Layered-structure of SuperPower's REBCO Coated Conductor [126].---------- 78
Figure 3.2 REBCO tape etching process. (a) cross sectional optical images of SuperPower CC layers before (top) and after (bottom) etching process. The etching removes Cu and Ag from

both sides of the tapes and leaves the ~ 1 μm thick superconducting layer (black) on top of the substrate. (b) A piece of REBCO tape before and after etching. 1: un-etched Cu layer; 2: REBCO layer after exposure to $FeCl_3$; 3: By-products appearance after etching for insufficient time with $FeCl_3$ and H_2O_2:NH_4OH solutions; 4: exposed REBCO layer after allowing enough time to be etched with H_2O_2:NH_4OH. The image in (b) was kindly provided by Dr. Will Illife. ---------- 80
Figure 3.3: Scanning electron microscope (SEM) images showing the TEM lamella lift-out process. (a-b) Lamella ready for liftout including undercut viewed at 54° and 0° tilt, respectively. The Ga^+ current is gradually decreased when getting closer to the desired thickness of the future lamella, 13 nA, 3 nA, and 1.5 nA, at the distances of >5 μm, >3 μm, and <1 μm, respectively. (c) Needle is attached to the lamella at the stage where it is detached from the bulk sample. (d) Lamella is attached to the Omniprobe grid pole. (e) Deposition of Pt welds the lamella to the grid and the needle separated, and from this stage the lamella will undergo several thinning steps to reach to about 100 nm thickness using decreasing currents down to 80 pA before the last step of low energy surface cleaning. ---------- 83
Figure 3.4: HRTEM images taken along [100]/[010] zone axis and at magnifications of (a) 600K and (b,c) 1.2M from pristine samples to illustrate the problems of FIB-induced damage. The corresponding local FFTs taken from the crystalline regions are shown in insets. (a) and (b) show less well defined atomic columns compared to a non-damaged sample (c), and the FFT images show fewer spots at high-frequencies (a) and a faint amorphous halo (b). ---------- 85
Figure 3.5: SEM image of TEM lamella after surface cleaning showing thin regions that are transparent at 5 kV. The approximate top of the original superconducting layer before thinning is marked with red dotted line, and the FIB-damaged regions (like those shown in Figure 3.4 are marked by the black arrows to emphasis the vulnerability to FIB damage. Delamination of the superconducting layer from the substrate resulting in curvature of the layer is also shown in the image. ---------- 86
Figure 3.6: TEM lamella attached to the V-shaped pin. ---------- 87
Figure 3.7: (a) The potential energy, V(r), in a periodic crystal structure. The gray background represents electrons that are free to move around the crystal and the black circles are the ions.

(b) The potential energy of the incoming electrons becomes more negative the closer they get to the positive potential near the ions [389]. ---------- 89
Figure 3.8: a schematic representation of (a) phase-contrast HRTEM and (b) Z-contrast STEM/HAADF image modes [393]. (c)The location of ADF detectors in STEM mode [394].------ 90
Figure 3.9: (a) Photograph of the MIAMI2 system showing the Hitachi TEM and the attached ion beamline. (b) A schematic configuration of the electron and ion beams on the TEM sample [239]. ---------- 92
Figure 3.10: Direct HRTEM image comparison between pristine sample (a) and the same sample He-irradiated at 300 kV and a fluence of 10^{16} cm^{-2} (b). Both images were taken from exactly the same region and under the same microscope imaging conditions, i.e. 800 K magnification, [100]/[010] zone axis (ZA), and 200 kV accelerating voltage. ---------- 93
Figure 3.11: (a) STEM/HAADF stack image taken along [100]/[010] ZA from an unirradiated (pristine) SuperPower sample, with the white arrow indicating the growth direction of the REBCO layer. (b) StatSTEM fitting coordinates represented by a grayscale map. ---------- 99
Figure 3.12: initial user inputs and lattice directions. (a) 3 input coordinates of the RE and Ba sublattice chosen from one unit cell. Two Gd/Y atomic column locations along a/b- and c-axis directions are also selected as shown in the figure. (b) Lattice directions determined according the atomic columns input in (a). ----------100
Figure 3.13: RE and Ba sublattice fitting. (a) Fitting algorithm process. Step 1 scans along the a/b-axis until it reaches the end and continues to Step 2 where the adjacent atomic column along c-axis direction is situated. Step 3 runs the same as step 1. (b) The result of the Ba_1, Gd/Y, Ba_2 atomic columns fitting procedure marked by white arrows and represented by red, blue, and green coloured circles, respectively.----------102
Figure 3.14: Model validation of unit cell alignment. Validation along (a) the c direction and (b) the a/b- direction, where each colour represents adjacent unit cells along the a/b or c-direction. (c) Validation along the a/b direction that shows misalignment emphasised by the enlarged sub image captured from the region noted with red rectangle. ----------103
Figure 3.15: Cu sublattice fitting. Cu_1, Cu_2, and Cu_3 are represented by yellow, cyan, and magenta colours, respectively. (a) An example of the vectors from the reference RE or Ba

sublattice atoms to the forecasted locations of the Cu atoms. The inset shows the Cu vectors at higher magnification. (b) Fitting of the experimental data to atomic column types, including the Cu sublattice. Red, blue, and green represent the Ba_1, RE, and Ba_2, respectively. ----------104
Figure 3.16: A flow chart with the main steps undertaken in the MATLAB program for the STEM/HAADF image analysis.----------105
Figure 3.17: Unit cell and lattice constant definition. The growth direction (c-axis) goes from the bottom to the upper part. The conventional unit cell is defined as a 2D cell that contains Ba_1, RE, Ba_2, Cu_1, Cu_2 and Cu_3 columns as shown with red arrows. For convenience, the notification was done on separate unit cells. Lattice constants are measured, in this example, with respect to the Gd/Y atom as shown by the white arrows.----------107
Figure 3.18: Average lattice parameters from pristine samples images calculated as a pair-wise unit cell distances using StatSTEM software and custom algorithm without introducing correction factors. (a) a/b-axis lattice parameters and (b) c-axis lattice parameters. ----------109
Figure 3.19: Gaussian fitting to find the location of the {111} and {200} rings as was performed using HyperSpy module in Python. X-axis represents the number of pixels from the FFT image centre and the y-axis is the normalized intensity measured radially. The red dots are the measured signal (after subtracting the background intensity), the blue line is the fitting to the measured signal, and the green and blue lines are two Gaussians fitted the measured signal.111
Figure 3.20: Magnification average percentage differences between the digital readout and Au-calibration for the two microscopes, and stack and one-frame image acquisition.----------112
Figure 3.21: Calibrated lattice parameters from the pristine samples after taking into account the difference between the digital readout and the Au-calibrated magnifications. ----------113
Figure 3.22: REBCO STEM/HAADF image showing the minimum scanning areas for pair-wise lattice parameter measurements of the a/b- and c-axes. The red and blue rectangles show the area of the image that has be scanned in order for the a/b- and c-axes lattice parameters to be calculated, respectively. The two green rectangles contain two neighboring rows of Ba_2 atomic columns. ----------114
Figure 3.23: Schematic of YBCO two unit-cells with an indication of the Ba_1-Ba_2 inter- and intra-cell distances as defined in this thesis. Reproduced from [400]. ----------115

Figure 3.24: Scatter plots presenting the inter- and intra-cell Ba_1-Ba_2 distances as a fraction of average c-axis lattice parameter per image for pristine samples. The scatter on the left (a) does not include images with intergrowths whereas the figure on the right (b) contains all unit-cells in every image that was analysed. The data includes one-frame & stack images taken on the ARM300CF microscope. ----------116
Figure 3.25: HRTEM image taken along [100]/[101] ZA from an unirradiated sample. (a) ROI consists of 512X512 pixels taken from the amorphous edge. (b) 2048X2048 pixel ROI sub-image taken from REBCO crystalline region, avoiding a $BaZrO_3$ rod. ----------117
Figure 3.26: A schematic overview of the entropy calculation framework. ----------120
Figure 4.1: A cross-sectional HRTEM image of typical amorphous cascades formed in the neutron-irradiated samples and Fast Fourier Transforms (FFT) from selected regions. (a) A HRTEM image taken at [100]/[010] orientation shows three different phases: the GdBCO matrix identified by the periodic layered structure of the ab-planes (1), crystalline BZO rods (2), and amorphous cascades (3) (arrowed) identified by the loss of the periodic plane structure. (b-d) Fourier Transforms for each phase, (b) for the GdBCO matrix, (c) BZO rod, (d) amorphous cascade, taken from regions 1, 2, and 3, respectively. ----------123
Figure 4.2: Typical HRTEM images taken along [100]/[010] and the corresponding FFT images (shown in insets) from (a) an as-manufactured and (b) neutron-irradiated SuperPower sample, showing no obvious intercalation defects in either material. ----------126
Figure 4.3: BF/HADDF STEM images taken from neutron-irradiated samples along [100]/[010] ZA. (a-b) images at a magnification of 5 Mx showing (a) HADDF and (b) BF signals; (c-d) images taken at magnification of 4 Mx, (c) HADDF and (d) BF. ----------128
Figure 4.4: Displacement per atom (dpa) as a function of depth in YBCO calculated using threshold displacement energies (TDE) of 40 [207], 45 [207], 33 [208], and 8 [207], [209] eV for Y, Ba, Cu, and O, respectively. The vertical dotted line marks the approximate thickness of the TEM foil.----------130
Figure 4.5: Direct HRTEM image comparison, taken along [100]/[010], of (a, c) pre- and (b, d) post-He-irradiation at room temperature, accelerating voltage of 300 kV, and to a fluence of 10^{16} cm^{-2}. The two pairs of images were taken from exactly the same region under the same

microscope imaging conditions, i.e. 800 K magnification, [100]/[010] ZA, and 200 kV accelerating voltage.----------132
Figure 4.6: High magnification HRTEM images, taken along [100]/[010], of He-irradiated samples show no obvious signs of local cascades or intercalation damage.----------133
Figure 4.7: Typical HRTEM images taken along [100]/[010] from (a) pristine and (b) Ne-irradiated samples. Note that these images, were not taken from the same sample. ----------134
Figure 4.8: HRTEM images of Ar-irradiated samples taken along [100]/[010]. The irradiation took place at room temperature, 350 kV accelerating voltage, and a fluence of 10^{13} cm^{-2}. The white arrow in (a) points to a local amorphous/highly distorted damage cascade, similarly to the circles in (b) that show potentially buried cascades. ----------135
Figure 4.9: Direct HRTEM image comparison, taken along [100]/[010], from (a) pre- and (b) post- Kr-irradiation to a fluence of 10^{13} cm^{-2}. The arrows point to partially-crystalline BZO rod at the fully-amorphous sample edge. The images were taken from exactly the same region under the same microscope imaging conditions, i.e. 800 K magnification, ZA, and 200 kV accelerating voltage.----------137
Figure 4.10: Displacement per atom (dpa) as a function of depth. The dpa calculation was performed according to SRIM output with Xe-ion incident into YBCO. The vertical dotted line marks the approximate thickness of the TEM foil.----------138
Figure 4.11: HRTEM images taken along [100]/[010] of Xe-ion irradiated samples. The fluence and temperature were kept constant, 10^{13} cm^{-2} and 298 K, whereas the energy was 30, 95, 160, and 225 keV for a, b, c, and d, respectively. ----------139
Figure 4.12: Direct HRTEM image comparison, taken along [100]/[010], from pre- (a,c) and post- (b,d) Xe-irradiation experiments conducted at room temperature (298 K) (b) and at 100 K (d). The images were taken from exactly the same regions under the same microscope imaging conditions, i.e. 800 K magnification, [100]/[010] ZA, 300 kV accelerating voltage, and a fluence of 7×10^{12} cm^{-2}. ----------141
Figure 5.1: Analysis of local variations in lattice parameters extracted from a STEM/HAADF image of an unirradiated REBCO sample. (a) STEM/HAADF 10-frame stack image taken along [100]/[010] ZA. (b) Fitting of Ba-(GdY) sublattices, red, blue, and green colours represent Ba_1,

Gd/Y, and Ba_2 atom columns, respectively. (c-d) local colour maps of (c) the a/b and (d) the c lattice parameters calculated from the Ba_1 atom locations.----------146
Figure 5.2: Bar charts comparing a/b (blue bars) and c-axis (red figure) lattice parameters of neutron-irradiated to a fluence of 3.3×10^{18} cm^{-2},He-irradiated to 1×10^{16} cm^{-2}, and Xe ion irradiation conducted at room temperature to a fluence of 7×10^{12} cm^{-2}. The data is shown as percentage change compared to pristine sample. The errorbars stand for the standard deviation. The values were extracted from one-frame images taken on the ARM300CF microscope, by the analysis of 62, 14, and 18 images of neutron-irradiated, Xe-irradiated at 298 K and He-irradiated samples, respectively. ----------149
Figure 5.3: Comparison of the inter- (red bars) and intra-cell (blue bars) Ba_1-Ba_2 distances as a fraction of average c-axis lattice parameter in neutron-irradiated, He-irradiated, and Xe-ion (T=298 K) presented as a percentage change compared to pristine sample. The errorbars stand for the standard deviation. The analysis includes one-frame & stacks images taken on the ARM300CF microscope. ----------152
Figure 5.4: Normalised distribution of a/b-axis lattice parameters from pristine (blue bars), neutron-irradiated to a fluence of 3.3×10^{18} cm^{-2} (red bars), and He-irradiated to a fluence of 1×10^{16} cm^{-2} (yellow bars) samples. Data was taken from one-frame images taken on the ARM300CF microscope. 1% of extreme outliers were removed from every image to avoid distortion of the overall distributions. ----------154
Figure 5.5: Normalised distribution of c-axis lattice parameters from pristine (blue bars), neutron-irradiated (red bars), and He-irradiated (yellow bars) samples. Data was taken from one-frame images taken on the ARM300CF microscope. 1% of extreme outliers were removed from every image to avoid distortion of the overall distributions. ----------155
Figure 5.6: Lattice parameters of pristine samples shown as averages on a scatter plot (a) and a pair-wise a/b lattice parameters plotted as a histogram (b). Data was taken from stacks images taken on the ARM300CF microscope.----------156
Figure 5.7: Scatter plot presenting the average lattice parameters per image for pristine (blue circles), neutron-irradiated (red circles), and He-irradiated (yellow circles) samples. The blue and yellow ellipses represent the clusters of pristine, and He-irradiated, respectively. The cross

markers show the average lattice parameters of every sample type. The data includes one-frame images taken on the ARM300CF microscope. ----------157
Figure 5.8: Scatter plot of standard deviations of a/b- and c-axes lattice parameters of pristine (blue circles), neutron-irradiated (red circles), and He-irradiated (yellow circles) samples. Data is taken from one-frame images taken on the ARM300CF microscope. ----------158
Figure 5.9: correlation between a/b-axis lattice parameters and their corresponding standard deviations in neutron-irradiated samples. The data was taken from one-frame images taken on the ARM300CF microscope. ----------159
Figure 5.10: Scatter plots presenting the inter- (y-axis) and intra-cell (x-axis) Ba_1-Ba_2 distances as a fraction of average c-axis lattice parameter. (a) for pristine (blue), neutron-irradiated (red) and He-irradiated (yellow) samples showing no distinguishable clustering; (b) for pristine and Xe-irradiated (room temperature) samples presenting two separate clusters, shown in blue and red, respectively. The data includes one-frame & stack images taken on the ARM300CF microscope and unit cells that contain intergrowth were removed from the analysis as elaborated in section 3.5.1.5. ----------160
Figure 5.11: STEM images of neutron-irradiated sample and local analysis of lattice parameters. HAADF (a) and ABF (b) images taken along [100]/[010] ZA. a/b-axis (d) and c-axis (e) lattice parameter distributions presented using blue and red colour bars as extracted from inside and outside the Region of Interest (ROI) as shown in the fitted Ba-GdY sublattice image in (c). ----162
Figure 5.12: Shift in average lattice parameters measured in undamaged (blue circles) vs 'damaged' (red circles) regions in neutron-irradiated samples as identified by dark contrast in STEM/ABF images. ----------164
Figure 5.13: Bar chart comparing average percentage change a/b- (blue bars) and c-axes (red bars) lattice parameters of He, Ne and Ar ion irradiated samples compared to pristine samples. The data was extracted from one-frame images taken on the ARM200f microscope on the left and ARM300CF microscope on the right. The errorbars stand for the standard deviation. -----165
Figure 5.14: Comparison of the inter- (red bars) and intra-cell (blue bars) Ba_1-Ba_2 distances along the c-axis as a fraction of average c-axis lattice parameter for Ne and Ar ion irradiation shown as percentage change compared to pristine sample. The errorbars stand for the standard

deviation. Data was extracted from images taken on the ARM200f microscope (left dotted box) and He-irradiated sample taken on the ARM300CF microscope (right dotted box).----------166
Figure 5.15: STEM/HAADF image and atomic location analysis using StatSTEM of a He-irradiated sample. (a) STEM/HAADF taken along [100]/[010] ZA and the corresponding StatSTEM fitting (b). (c) Fitting of Ba-GdY sublattice, where red, blue, and green colours represent Ba_1, Gd/Y, and Ba_2 atoms, respectively. (d) Ba-GdY sublattice atoms in their perfect lattice sites shown in white and stacking faults/interstitial atoms in orange. Potential extra layers, namely, stacking faults, are shown by red ellipses in a-c. ----------168
Figure 5.16: STEM/HAADF image and atomic location analysis using StatSTEM of sample Xe-irradiated at 100 K. (a) STEM/HAADF taken along [100]/[010] ZA and the corresponding StatSTEM model with Ba-GdY sublattice, where red, blue, and green colours represent Ba_1, Gd/Y, and Ba_2 atoms, respectively (b). (c) Ba-GdY sublattice atoms in their perfect lattice sites shown in white and incomplete displaced atomic columns atoms in orange.----------170
Figure 5.17: Comparison of lattice parameters (a) and inter- and intra-cell Ba_1-Ba_2 fractions (b) of Xe-ion samples irradiated at 298 K and 100 K presented as a percentage change compared to pristine sample. The errorbars in both figures stand for the standard deviation. The one-frame images (a) and one-frame & stacks images (b) used for this analysis taken on the ARM300CF microscope. ----------172
Figure 5.18: Scatter plot presenting the inter- and intra-cell Ba_1-Ba_2 distances as a fraction of average c-axis lattice parameter for pristine and Xe-irradiated at room temperature and 100 K samples. The data includes one-frame & stacks images taken on the ARM300CF microscope.173
Figure 5.19: Normalised distribution of a/b-axis lattice parameters from a sample Xe-irradiated at 100 K (blue bars) and at room temperature (red bars). 1% of extreme outliers were removed from every image. ----------174
Figure 5.20: Normalised distribution of c-axis lattice parameters from a sample Xe-irradiated at 100 K (blue bars) and at room temperature (red bars). 1% of extreme outliers were removed from every image. ----------175
Figure 5.21: Shift from average lattice parameters (b) and inter- and intra-cell fractions (c) as measured in damage cascade regions (The areas in the vicinity to the ROIs shown in (a)) and the

surrounding matrix (Three regions of interest (ROIs) shown in (a)) in a sample Xe-ions irradiated at 100 K.----------177
Figure 5.22: Graphical representation of YBCO unit cell. The numbers 1-7 stand for the defects' site locations and the oxygen, copper, barium, and yttrium ions are represented by red, blue, green, and yellow spheres, respectively [421]. ----------178
Figure 5.23: DFT theoretical predictions of the percentage change in Ba_1-Ba_2 inter- and intra-cell distances in the presence of Cu/O vacancies and interstitials. The graphs show different defects positions in the REBCO unit cell; CuO chain (sites 1-2), O(4) plane (sites 3-4), CuO_2 planes for O(2) and O(3), and RE-plane (sites 5-7), respectively. Interstitials are marked with hexagrams and vacancies with circles.----------179
Figure 5.24: Combined scatter plot including DFT theoretical predictions and experimental results of the percentage change in Ba_1-Ba_2 inter- and intra-cell fractions. The DFT theoretical results are shown with hexagrams for interstitials and squares for vacancies as calculated by Murphy [421], and pentagrams for defects with interstitials and diamonds for vacancies as analysed by Nicholls et.al. [419]. The experimental results are marked with circles and do not include the results of Xe-irradiated samples. ----------181
Figure 6.1: Entropy values in the spatial domain extracted from 1024X1024 pixel blocks for all the sample types in the dataset, ordered by increasing values from left to right. Standard deviation values are shown by error bars. The total number of HRTEM images used for this analysis amounts to about 1000. The colour-coding for the bars was chosen according to the observed damage in HRTEM image, no-damage (pristine in green), light-medium damage (He-irradiation in yellow), severe-damage (Kr-irradiation and Xe-ion irradiation undertaken at 100 K) in maroon, and amorphous in red. Black bars belong to samples that were not categorised according to their damage severity.----------198
Figure 6.2: examples of (a) pristine and (b) 'almost amorphous' HRTEM images taken along [100]/[010] ZA. The TEM foil in (b) was irradiated in-situ with 350 keV Xe-ions at 100 K to a fluence of 1×10^{13} $cm^{-.2}$ ----------199

Figure 6.3: Normalised histograms of pixel intensities of 44 HRTEM images of pristine and amorphous samples. (a) Gray-scale (b) gray scales values after shifting the mean values to zero. ----------200
Figure 6.4: Spectral entropy values as measured from a random series of numbers from 1 to 1000 and a signal length from 6000 to 150M with 25000 data points where entropy was calculated. ----------202
Figure 6.5: A scatter plot of entropy values in the mid-frequency FFT on the x-axis and DCT domain on the y-axis of pristine (blue hexagrams), amorphous edge (black circles) and amorphous (green squares) as extracted from 512X512 pixel image blocks.----------203
Figure 6.6: Examples of HRTEM images of almost-amorphous REBCO samples. The corresponding FFT images are shown in insets. ----------204
Figure 6.7: Typical examples of FFT patterns taken from [100]/010] ZA HRTEM images. (a) pristine REBCO. (b) almost-amorphous REBCO sample. ----------206
Figure 6.8: Histograms of medium-frequency (2.4 – 4.5 [1/nm]) FFT and power coefficients collected from 44 pristine and amorphous images. (a) probability distribution of the FFT coefficients, (b) power spectral density of the FFT power coefficients.----------207
Figure 6.9: Enlarged HRTEM images of pristine (a) and amorphous (e) samples taken along [100]/[010] ZA and the corresponding inverse DCT (IDCT) images. The DCT coefficients from which the IDCT images were built include the lowest frequency components as shown in the red square in (i) and include a square of side with a length equal to about 2.5% (b,f), 5.0% (c,g), and 7.5% (d,h) of the size of the total DCT matrix. ----------209
Figure 6.10: Enlarged HRTEM images from pristine (a) and amorphous (c) samples taken along [100]/[010] ZA and the corresponding inverse DCT (IDCT) images (b,d). The IDCT images were extracted from DCT coefficients that are larger than a threshold of 0.65, which accounts to about 0.06% (pristine), and 0.53% (amorphous) of the total number of DCT coefficients.------210
Figure 6.11: Histogram plot showing 150X150 low frequency DCT coefficients extracted from 44 pristine (blue bars) and amorphous (red bars) images. Both histograms are normalised and plotted with equal bin width. ----------211

Figure 6.12: Raw HRTEM images from (a) pristine and (c) amorphous materials taken along [100]/[010] ZA and the corresponding representation of the DCT domain, (b) and (d), respectively. DCT contour plots were extracted using a threshold value of 0.65 for high-weighted DCT coefficients and present the 250X250 pixels low-frequency coefficients. ----------213
Figure 6.13: Comparison of DCT coefficients from HRTEM images taken along [100]/[010] ZA pre- (a) and post- (c) Kr-ion irradiation. The corresponding DCT coefficients are presented using 250X250 pixel contour plots from high-weighted DCT coefficients defined as above a threshold value of 0.65 for pre-irradiation (b) and post-irradiation (d) conditions. ----------215
Figure 6.14: An illustration of DCT pattern creation from an FFT using an image of a pristine REBCO sample. (a) FFT pattern with the zero frequency point (DC) situated in the centre and a model of the pattern in (b). The FFT pattern is rotated along the vertical direction (b) and along the horizontal direction (c) to get an example of a DCT pattern with the DC point situated at the upper left corner of the image. The dotted red lines in (d) show the observed zig-zag pattern of the DCT image. ----------217
Figure 6.15: DCT patterns from a pristine REBCO sample, and IDCT & IFFT images taken after applying a mask around specific planes. (a) 250X250 low frequency pixels taken from a 2048X2048 pixel DCT image presenting the high coefficients with a lower threshold of 0.65. The 3 digits numbers are Miller indices in the original image (Figure 6.13a). (b-d) IDCT images taken from the clusters of high coefficients marked by red circles in (a). (e-g) the equivalent IFFT images taken after applying a mask on the FFT pattern shown in the inset. The FFT inset also specifies the centre in the red circle, plane indices in red, and the red arrow points to the equivalent spot in the DCT pattern in (a). ----------219
Figure 6.16: A scatter plot showing entropy values calculated from 1024X1024 pixel blocks in HRTEM images both in the mid-frequency band FFT, and DCT domains for pristine (blue hexagrams), neutron-irradiated (red diamonds) and amorphous (green squares). ----------222
Figure 6.17: Entropy values in the FFT (mid-frequency, x-axis) and DCT (y-axis) domains for pristine and for samples irradiated with He, Ne, Ar and Kr ions shown as a scatter plot. Pristine samples are marked with blue hexagrams, and data for the four different ions marked with circles with different colours as shown in the legend. ----------223

Figure 6.18: A 2D chart presenting the entropy values in the FFT and DCT domains in pristine, He-irradiated, Ne-irradiated, Ar-irradiated, and Kr-irradiated samples. Standard deviations for each domain, FFT on x-axis and DCT on y-axis, are presented by error bars. ----------224
Figure 6.19: Damage percentages calculated from different irradiated samples in the DCT and FFT domains. The percentages were calculated relative to average entropy values in the un-irradiated sample (0% damage) and amorphous samples (100% damage). ----------225
Figure 6.20: Scatter plot of the entropy in the DCT and FFT domains for samples irradiated with Xe ions at 298 K (orange triangles) and 100 K (black triangles), and amorphous samples (green squares). ----------226
Figure 6.21: Scatter plot of k-mean clustering of Xe-irradiated samples irradiated at 100 K and 298 K, and amorphous samples. The green circles show the misclassified data points. ----------227
Figure 6.22: scatter plot of the entropy calculated from the DCT and FFT (mid-frequency) domains for all the samples in the dataset.----------228
Figure 6.23: A pseudo-scatter plot with the average entropy in the FFT and DCT domains represented by one symbol. The ellipse size is determined by two radii, the half standard deviation of the FFT domain as a radius along the x-axis and the half standard deviation in the DCT domain along the y-axis. ----------229
Figure 6.24: Bar chart of the percentage damage in the DCT and FFT domains for all the samples studied here. The calculation is based on the assumption that the entropy increasing linearly from the un-damaged pristine samples with a value of 0% up to the amorphous state with an entropy of 100%.----------230
Figure 6.25: Histograms showing the spectral entropy value distribution of 348 HRTEM images (each 512X512 pixels) of the amorphous edge of TEM samples in the mid-frequency FFT (a) and DCT (b) domains.----------232

1. Introduction

1.1. The Future of Fossil Fuels

Continuous energy supply is vital for the sustainability of modern civilization, which generates ever increasing energy demands. However questions have been raised about whether the current energy sources will keep pace with the exponentially growing energy demands start from the second half of the 20th century [1]. To address this continuously-growing necessity, fossil fuels, namely coal, oil and natural gas, are the main sources that supply around 68% of global energy generation (Figure 1.1). Nonetheless, two main problems are associated with this massive fossil-based energy production; diluted natural resources and adverse environmental effects. Firstly, predictions point out that fossil fuel extraction will soon reach a maximum [2]–[4], and secondly that fossil fuel combustion results in *greenhouse gas* emissions, particularly carbon dioxide (CO_2), that have been growing exponentially since early in the 19th century [5]. Many scientists speculate that this phenomenon intensifies global warming [6]–[9]. Therefore, immediate steps are imperative to reduce greenhouse gas emissions.

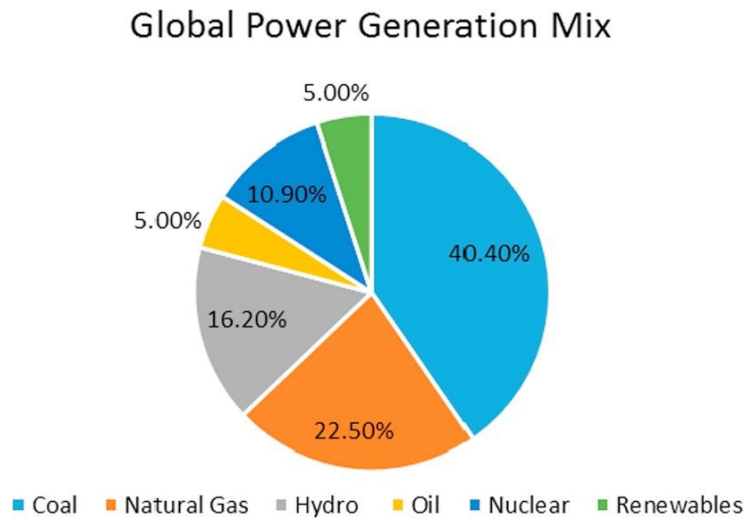


Figure 1.1: Global energy resource allocation (updated to 2012) [10].

1.2. Nuclear Fusion Power

Since the 1950s [11], attempts have been made to harness the enormous amount of energy stored in atomic nuclei for energy production by using two techniques. The first, achieved by the bombardment of heavier nuclei (usually ^{235}U) with uncharged particles, e.g. neutrons, to split them to lighter ones, is a process called *fission*. Secondly, *fusion* reactions occur when two light elements, usually the hydrogen isotopes deuterium (^{2}H) and tritium (^{3}H), fuse together to form helium and an energetic neutron according to the following reaction [12]

Equation 1.1: $^{2}H + {}^{3}H \longrightarrow {}^{3}He\ (3.5\ MeV) + n\ (14.1\ MeV)$

The physical quantity governing the amount of energy released in both fission and fusion is named the *mass defect*. The observed atomic mass of the product nuclei is slightly smaller than the sum of the parent particles masses, which results in a release of stored energy.

Fission has been utilised for energy production for 50 years, and contributes a substantial amount to energy supply for many countries [13]. Despite that, there are deep-rooted problems, e.g. nuclear waste disposal, weapons proliferation and terrorism, safety and fuel reserves, which have not yet been completely resolved [14]; Hence, fusion energy seems the best option for the long-term future.

In future magnetic confinement fusion reactors, the *deuterium-tritium* (DT) plasma must be kept at temperatures of over a hundred million kelvin to facilitate the fusion reaction [15]. Tokamaks, which have been studied over the last 50 years [16], are a promising reactor design based on a sophisticated configuration of strong toroidal magnetic fields that confine the plasma. Based on these concepts, there have been several successful attempts to test the concept of fusion energy.

The *Joint European Torus* (JET) [17], which was one of the first fusion reactors projects and currently the largest tokomak, started to operate in 1983 and uses cooled copper wires to create magnetic fields. On the 9th of February 2022, JET latest experiment achieved the highest energy pulse sustained for 5 seconds, smashes the 25 year records [18].

The choice of the windings for magnets of fusion reactors, although affected by other properties, is a strong function of their ability to carry large current (and proportional to the magnetic fields produced shown by Biot-Savart law), as the fusion power produced scales as B^4 [19]. Using conductors with higher current density can dramatically decrease the large capital costs associated with tokamak construction, i.e. the same power can be achieved in a much smaller scale. Mainly due to this reason, designs such as the American ARC [20], the British ST135 designed by Tokamak Energy [21], the Japanese FFHR [22], the Chinese CFETR [23], all intend to use *rare earth barium copper oxide compounds* (REBCO) high temperature superconductor to generate the magnetic field. On the other hand, ITER megaproject aims to test the feasibility of fusion energy production [24] by using low temperature Nb_3Sn superconducting magnets [25]. The next generation, DEMO [26], is the first fusion reactor planned to produce electricity continuously on a large scale and to overcome scientific and engineering issues of ITER, and is planned to start operating in 2050 according to the European road map for future energy [27]. Demo, will certainly benefit from REBCO superconductors [28], [29], though it can also operate using *low temperature superconductors* (LTS) [30]. Figure 1.2 shows two designs of tokomaks, (a) is the relatively large JET vessel [31] and (b) the smaller ST25 reactor [32] with an arrow pointing to the vessel. The magnets in smaller tokamaks are centimetres away from the plasma.

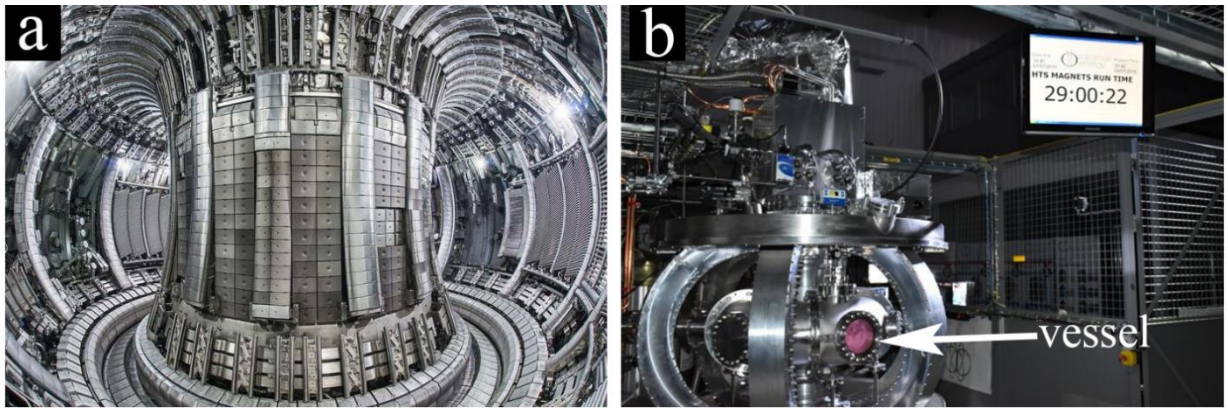


Figure 1.2: Examples of fusion reactor vessel on the relatively large JET (a) and the smaller ST25 (b).

1.3. Problems for superconducting magnets in fusion reactors

The materials that will make up the future fusion reactors will be exposed to a flux of 14.1 MeV neutrons, and we might expect this to be especially damaging for the superconducting materials in the magnets due to generation of point defect and collision cascades [33]. Some consideration has been given to possible degradation of properties of both low temperature superconductors (LTS) [34], [35], such as Nb_3Sn, and the *high temperature superconductors* (HTS) [36], [37] discussed in section 2.1.2, and their response to irradiation follows a similar behaviour. The general trend for the evolution of its critical current density (J_c), except in very low magnetic fields, is an initial increase at low dose followed by rapid decrease after a critical dose which depends on the type of conductor, measurement temperature and type of projectile. The initial improvement in J_c has been associated with the introduction of additional flux pinning centres, and the subsequent rapid degradation occurs due to the increased rate of flux creep rate (caused by the reduced separation of flux pinning centres decreasing the activation barrier) [38] and eventually loss of superconducting cross-sectional area [39]. The ability of REBCO windings to carry current without degrading in service is a critical part of the success of future fusion

reactors, and better understating of the irradiation effects on their properties is crucial for designing a fusion reactor for long term energy generation.

1.4. Objectives

In fusion reactors, the magnetic field produced by the superconducting magnet windings is vital to shrink the reactor size, as the ability of the superconducting tapes to carry electrical current gets higher, the magnetic field increases, which results in the same power output from a small system. HTS show promising transport characteristics, and thus are the chosen material for all small fusion reactor designs. Among many challenges to utilise HTS in this application, high-energy neutrons ejected from the plasma reaction are considered to be a major one; therefore this project concentrates on understanding the microstructural evolution in one type of HTS tape under irradiation by neutrons and proxy ions.

The literature review in Chapter 2 includes a wide array of studies on the consequences of irradiation on both transport properties and lattice damage. Most of the studies of radiation damage in HTS focus on changes in transport properties, with less attention given to the microstructural degradation. Studies that did focus on microstructural evolution lack the specificity of the sometimes subtle irradiation damage effects on the HTS matrix. Therefore, my project aims to contribute to the understanding of irradiation mechanisms in HTS.

The direct effects of both neutrons and in-situ light and heavy ion irradiation are shown in Chapter 4. This helps build a better understanding of the lattice degradation before they are assessed quantitatively in Chapters 5 & 6. In Chapter 5, the structural parameters changes are discussed. Using a large set of *scanning transmission electron microscopy* (STEM) images, I was able to extract statistically-significant small changes in the HTS unit cell configurations

under wide range of irradiation conditions. In Chapter 6, the observed lattice degradation is tested against image features extracted from 1000+ HRTEM images.

It is anticipated that results and methods presented in this thesis will continue to be collected and developed, and will make a valuable contribution to the development of our understanding of irradiation damage at the nanometre-scale.

2. Literature Review

This literature review is divided into three sections. The first discusses the theoretical concepts of HTS materials and then probes the structure and properties of the REBCO compounds in more detail. Section 2.2 analyses the theory of irradiation damage, and then separately dissects the post-irradiation transport properties and microstructure of REBCO, with relevant examples. The last section gives a brief overview of image processing techniques in order to shed light on the available mathematical tools to quantitatively assess irradiation damage in *high resolution transmission electron microscope* (HRTEM) images.

2.1. Superconducting materials

One of the fundamental laws of electric conductivity, shown in normal metals, is the presence of resistance to electron motion, described by Ohm's law. This paradigm was broken in 1911 [40] when mercury, cooled down to 4.19 K, exhibited zero electrical resistance, and the term *superconductivity* was coined. For the following 77 years, superconductivity was considered to be a low temperature phenomenon, i.e. upper limit of about 40 K.

In 1986 Bednorz and Muller [41] discovered a new Ba-La-Cu-O copper oxide-based system with a critical temperature of 30 K. Shortly after, Wu et.al [42] presented the Y-Ba-Cu-O compound, and the era of *high temperature superconductors* (HTS) had officially begun (Figure 2.1). Hitherto, the highest known transition temperature of oxide-based superconductors in ambient environment is 135 K [43] (and 250-294 K under pressure [44]–[46]), while other classes such as iron pnictides [47], [48] and fullerenes [49], [50] remain far behind in terms of their transition temperature.

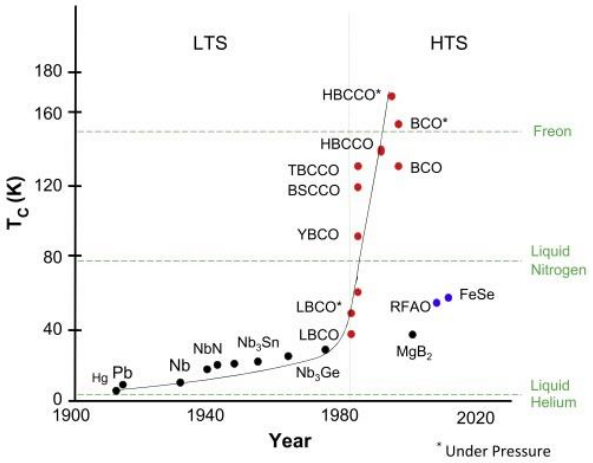


Figure 2.1: Transition temperatures evolution of superconductors [51].

The performance of a given superconductor is embodied in its *critical* parameters, namely, *temperature* (T_c), *current density* (J_c), and *magnetic field* (H_{c2}). Above these critical values the resistance-free current density is lost. For each superconducting material these three critical parameters are interdependent, as will be discussed below.

2.1.1. Theory of superconductivity

In 1933, it was shown that a superconductor cooled below T_c exhibited a unique magnetic response, known as the *Meissner effect* [52] (Figure 2.2), in which magnetic field is expelled completely from its interior. Shortly after, F. and H. London [53] hypothesised that the magnetic field penetrating the superconductor's surface decays exponentially, with a characteristic distance called the *London penetration depth* (λ).

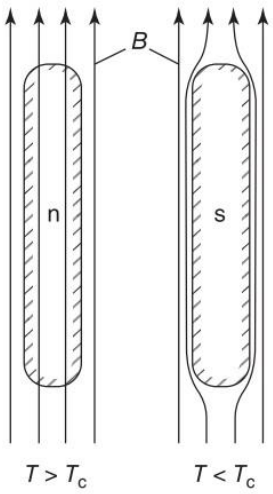


Figure 2.2: Schematic illustration of Meissner effect in the normal, shown at the left side, and superconducting state on the right side. The lines represent the magnetic fields lines [54].

Later on, the model was refined by Ginzburg & Landau [55] by introducing the *coherence length*, ξ(T), which expresses the distance of mutual interactions between electron pairs. Type II superconductors are defined when the *Ginzburg-Landau parameter*, $\kappa = \frac{\lambda}{\xi}$, is greater than $\frac{1}{\sqrt{2}}$.

Unlike type I superconductors which never contain quantised magnetic flux lines, type II superconductors exhibit a *mixed state*, i.e. partial magnetic field penetration governed by the balance of surface energy between the normal and superconducting states [55].

The penetration of magnetic flux was described by Abrikosov (1957) [56] as flux lines or *vortices* with core radius of about ξ through which a single *flux quantum* (Φ_0) passes, encompassed by a circulating supercurrent. The *Abrikosov vortex lattice* is a state in which vortex lines arrange themselves in specific long-range symmetry, governed by minimisation of energy and mutual repulsion between the magnetic flux lines (Figure 2.3a). Abrikosov's square lattice configuration has proved wrong [57], [58] and triangular arrangements are normally observed (Figure 2.3b).

Abrikosov's theory was contemporary with the *Bardeen-Cooper-Schrieffer* (BSC) theory that formulates the microscopic mechanism for superconductivity [59]. Frohlich [60] and Bardeen [61] postulated that phonons, under certain conditions, facilitate the bonding of pairs of electrons through mutual attractive forces. These *Cooper pairs* (after Leon N. Cooper) constitute electrons (usually) opposite in their spins and momentum manifested in electron pairs that travel with no loss within the material. When either the temperature or magnetic field reaches the critical value, the energy is sufficient to break the electron pairs, and the material returns to its normal state.

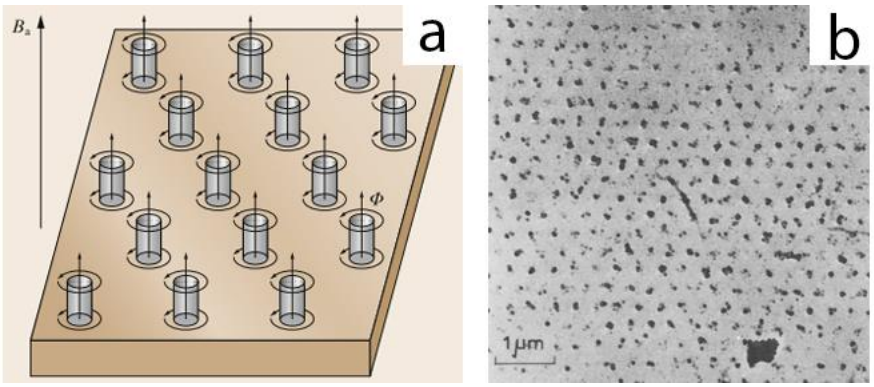


Figure 2.3: (a) Pictorial representation of Abrikosov lattice. The magnetic field B applied parallel to vortex lines and induced currents perpendicular the surface [62]. (b) Direct observation using Transmission Electron Microscopy (TEM) of triangular array of Abrikosov lattice in Pb-4 at.% In superconductor [57].

2.1.2. High temperature superconducting oxides (HTS)

YBCO and the more general REBCO (RE=Rare Earth) compounds are among the most widely investigated superconductors due to their ability to carry very high currents in high magnetic fields (Figure 2.4). The following section covers some of the basic properties of REBCO HTS.

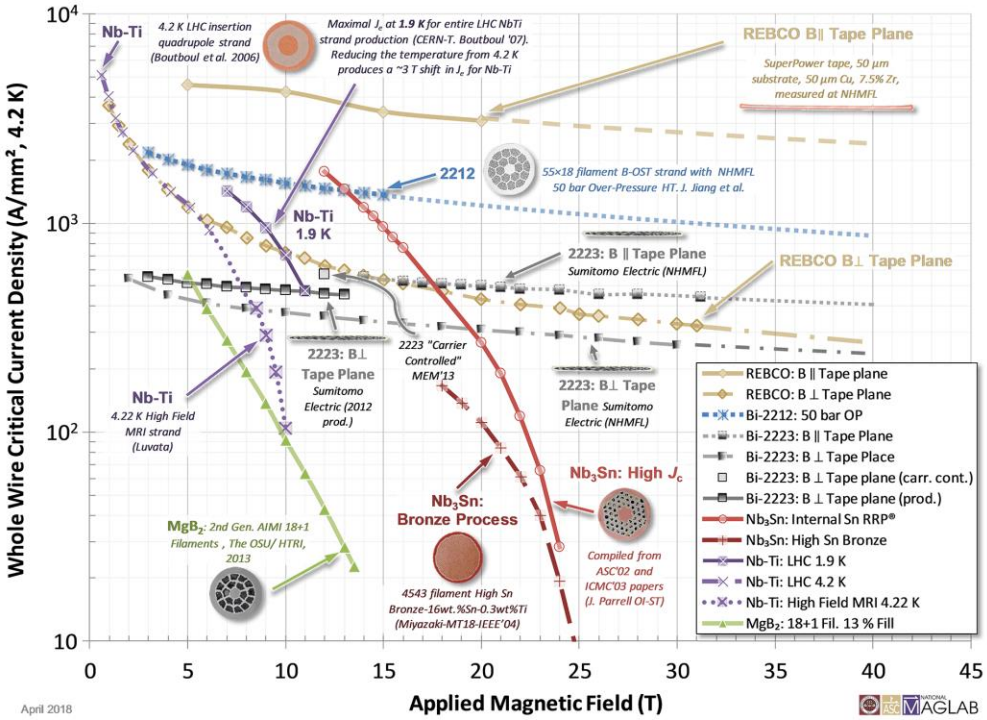


Figure 2.4: Comparison of the critical current as a function of applied field of several types of low and high temperature superconductors (data taken from several sources; courtesy of (https://nationalmaglab.org/magnet-development/applied-superconductivity-center/plots).

2.1.2.1. Crystal structure

$YBa_2Cu_3O_x$ (usually $6 \leq x \leq 7$), hereafter called *YBCO* or *Y123*, possesses two crystal structures, i.e. orthorhombic and tetragonal, as a function of cooling rate and atmosphere pressure and composition [63], [64]. The desirable superconducting orthorhombic phase shown in Figure 2.5, has *Pmmm* symmetry and lattice parameters a= 0.3822 nm, b=0.3891 nm and c=1.1677 nm [65].

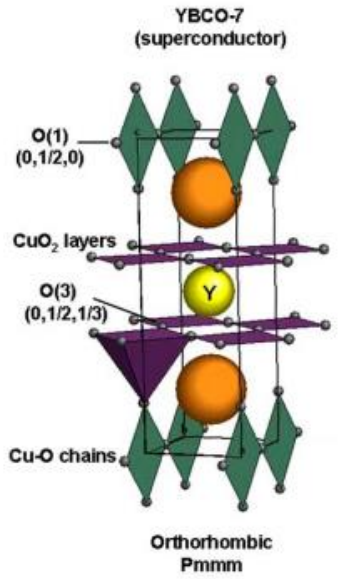


Figure 2.5: YBCO orthorhombic crystal structure [66].

HTS-oxide properties are associated with three main variables; structure, doping, and oxygen stoichiometry.

The unique feature in all HTS-oxides, commonly referred to as the *cuprate* structure, is a stack of CuO_2 conducting layers separated by insulating, charge reservoir layers along the c-axis [65] (Figure 2.6). YBCO's distinct feature is one-dimensional (1D) *Cu-O chains* that lie on the *basal plane* (z=0) and run along the b-axis [67]–[69]. Superconductivity occurs only if CuO_2 two-dimensional (2D) layers are doped by the charge reservoirs in order to form free holes, which move almost exclusively in the CuO_2 planes. The layered structure results in an inherent large *anisotropy* in coherence lengths in a/b and c directions ($\gamma = \frac{\xi_{\parallel c}}{\xi_{\perp c}}$), which is between seven and eight in YBCO [70], and also anisotropy in mechanical properties, with fracture of the brittle ceramic preferentially in the c-plane.

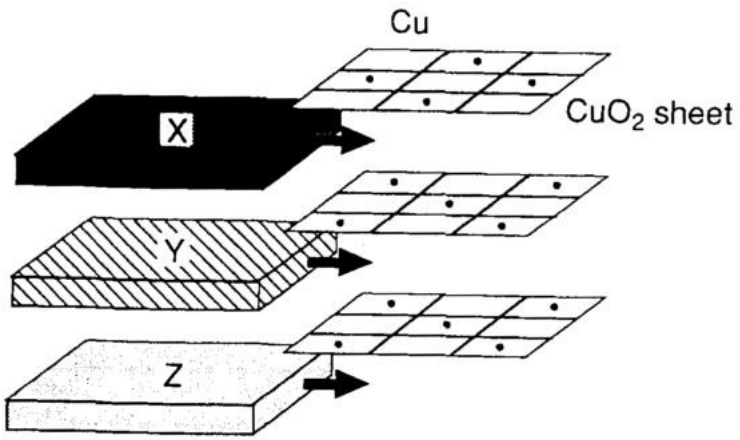


Figure 2.6: Sandwich structure of CuO_2 and insulating layers [71]. In high temperature superconductors, the structure along c-axis can be presented as alternating layers of CuO_2 separated by different layers of insulating layers, represented here as X, Y, Z, where X and Z are the BaO_2 planes and Y are the rare-earth, Oxygen-free planes.

Doping is associated with adding substitutional atoms on the yttrium, barium (e.g. [72]) and copper (e.g. [73]) sites, which controls the superconducting properties while retaining the crystal structure [74]. The motivation behind the introduction of substitutional atoms is to improve the superconductor's transport properties. Studies have shown that T_c generally increases by 1 to 6 °C with most lanthanides atoms [74], [75], but the effect of RE-substitution on J_c is more complicated, and generally YBCO is not inferior compared to other REBCO compounds over a range of temperatures and fields [76]. An example of the effect of several substitutional atoms and the associated T_c and J_c properties is shown in Figure 2.7. On the other hand, copper substitution by Fe, Co, Ni, Zn, Ga, and Al are accompanied mostly with adverse effects [67], that vary according to the orthorhombic-tetragonal transformation and occupancy of Cu1 (chain) and Cu2 (plane) sites [77]–[79].

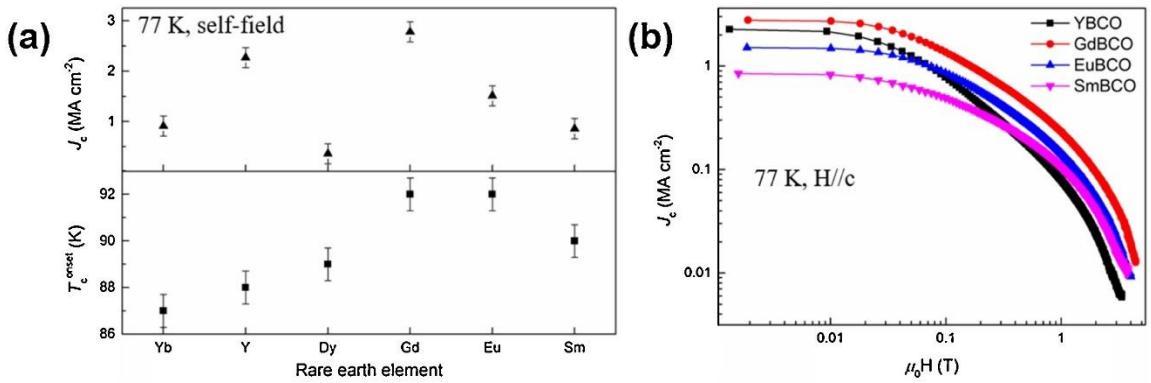


Figure 2.7: Properties of REBCO films with different lanthanide elements. (a) Critical temperature (T_c), and critical current (J_c) for different RE elements measured at 77 K. (b) J_c measured at 77 K in different magnetic fields [74].

The oxygen content is a consequence of annealing environment [80]. Many research groups [81]–[83] showed that T_c undergoes rapid decline with a loss of oxygen, and exhibits two plateaux around x = 6.9 and x = 6.6 (Figure 2.8). The decrease in T_c is associated with the orthorhombic to tetragonal phase transformation, accompanying the loss of oxygen from the Cu-O chains [63], [80]. Formation of oxygen vacancies provokes an order-disorder transformation, as shown by TEM [68], [83]–[85]. These empirical results underpin the importance of Cu-O chains in the superconducting mechanism [63], [86].

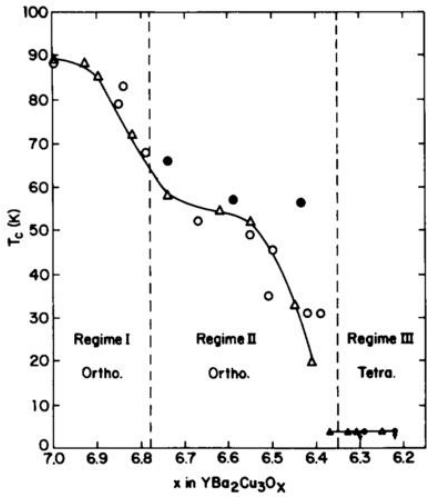


Figure 2.8: Critical temperature as a function of oxygen content in YBCO [87].

2.1.2.2. Inherent 2D defects

The most common defects in the REBCO lattice are *intergrowths*, along the [001] direction, and can be considered as stacking faults [88]. Intergrowths are individual or ordered arrays of plane stacking sequences along the c-direction like $Y_2Ba_4Cu_8O_{16}$ (Y248) [89], [90], $YBa_2Cu_4O_8$ (Y124) [91], [92] or $YBa_2Cu_5O_9$ (Y125) [88]. The pinning from these defects emanates from (001) plane bending around the intergrowths that induces large anisotropic strains (Figure 2.9) mainly along the c-direction and over a range of about 5 unit cells [93]. Regardless of the fabrication method [94], these ab-plane pinning centres (in addition to REBCO layered structure itself [94]) lead to anisotropic J_c values manifested in a sharp peak when the applied field is parallel to the ab-plane ($H \parallel ab$), see Figure 2.10.

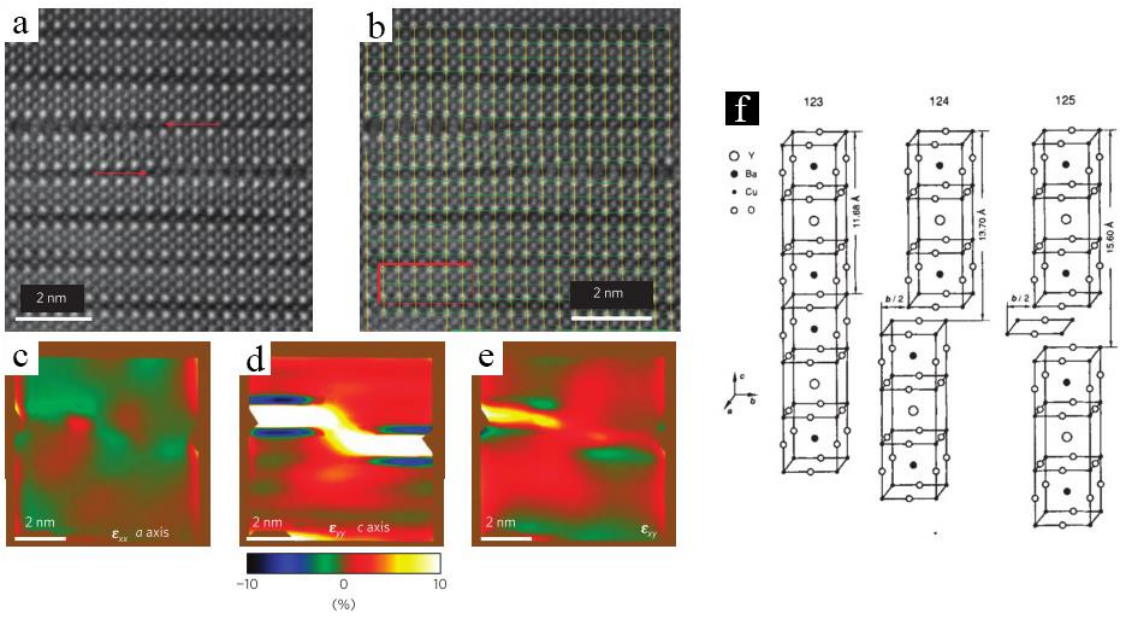


Figure 2.9: High resolution TEM (HRTEM) images, strain maps and illustrations of intergrowth unit cells. (a-b) STEM/HAADF images taken along [010] zone axis show the bending of the YBCO's layered structure perpendicular to the c-axis. (c-e) Lattice strain maps, $\varepsilon_{xx}, \varepsilon_{yy}, \varepsilon_{xy}$, respectively, calculated from the rectangular region shown in (b). (f) Schematic illustrations of the Y123, Y124, Y125, phases [88], [89].

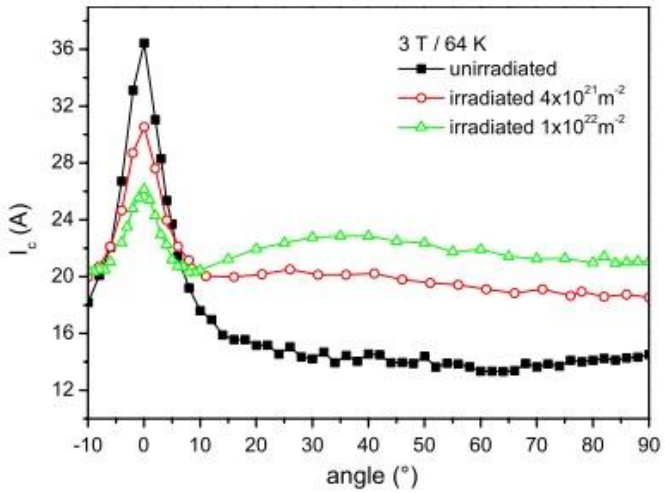


Figure 2.10: The angular dependence of J_c in YBCO at 64 K and 3 T for unirradiated (black squares) and after neutron irradiation at 4×10^{21} n/m^2 (red circles), 1×10^{22} n/m^2 (green triangles) [95].

Y124 intergrowths are commonly present in REBCO, and were heavily studied almost from the very first publications on HTS materials [96]. Y124 shows as an extra CuO chain inserted adjacent to the basal plane (z=0) along the [010] direction to form double CuO chains with a displacement vector of [0 , b/2, c/6] [97] and surrounded by a partial (stacking fault) dislocation. Li et.al. [98] investigated the effect of Y124 intergrowths on the transport properties of YBCO tapes with a thickness ranging from 5 to 250 nm produced by *chemical solution deposition* (CSD) on (100) $LaAlO_3$ (LAO) substrates. Since the bulk Y124 phase displays non-superconducting behaviour, the effective superconducting volume decreases with film thickness to a threshold of about 10 nm, where J_c is effectively zero. However, as will be explained in the next section, the behaviour of Y124 is more complex and consists of nano-strained 'cocktail effect' of oxygen vacancies and modified electronic structure that suppresses Cooper pair formation [89].

2.1.2.3. Vortex state

One of the most important properties measured in superconductors is their ability to carry current without loss of energy when operated below T_c, and this relies on the immobility of the vortices when an electric current is applied and exerts a Lorentz force on them. Using the concept of the vortex lattice, one can depict the typical *H-T phase diagram*, Figure 2.11, for superconductors that contain pinning centres.

The Meissner phase exists in a narrow region below the *lower critical magnetic field*, H_{c1}, and is characterized by no penetration of vortices (see Figure 2.11). Above H_{c1}, in the *vortex glass* state, the vortices are pinned to randomly ordered lattice sites and defects [99], [100]; The vortices are then static and exhibit no dissipation of energy when a current is passed through the material. If there are no pinning sites, the vortices arrange themselves with *vortex lattice* symmetry, as has already been discussed. Increasing the temperature at zero applied magnetic field enhances the thermal fluctuations, and the solid long-range order or short-range order glass structure melts [101] approaching T_c [102]. The melting process is a transformation to a *vortex liquid* [103] accompanied by collective movement of vortex bundles [104].

The vortex liquid region, bordered by the *melting temperature*, T_g, and the *upper critical magnetic field*, H_{c2}, is characterized by freely moving vortices that give rise to resistivity, and brings J_c to zero. When passing beyond the H_{c2} curve, the vortices are effectively overlap and the magnetic field fully penetrates the materials, and it returns to the normal state.

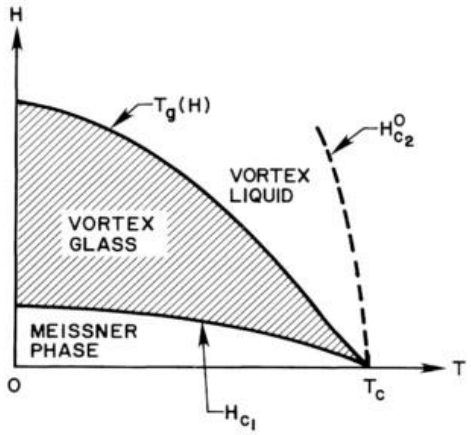


Figure 2.11: Typical phase diagram for superconductors [99].

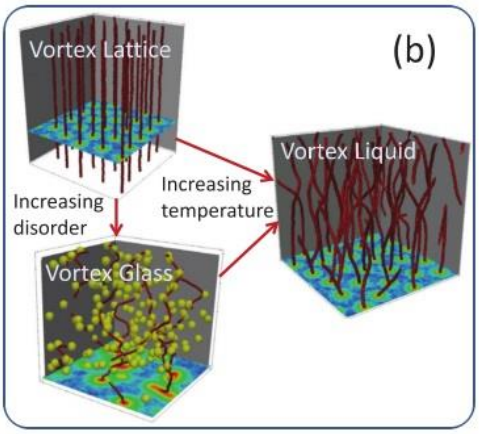


Figure 2.12: Different vortex states and phase transformations [105].

2.1.2.4. Critical current density

The most important characteristic of a superconductor is its ability to carry a large current density. J_c, as opposed to T_c, is not an intrinsic property, but a function of microstructure, temperature, external applied field and its direction, $J_c(T,H,\theta)$ [106]. Usually, J_c plotted against T and B forms the critical surface [107] (Figure 2.13). The temperature-dependence of J_c can be modelled by the following equation [108].

Equation 2.1: $J_c(T) = J_c(0)(1 - \frac{T}{T_c})^n$

Here $J_c(0)$ is the critical temperature at 0 K and n is a constant usually ranging between 0.4 to 1. In YBCO, n=0.5 at 77 K [109].

The applied magnetic field changes J_c in a complex way [110], in part due to the effect of magnetic field direction: when field is applied in parallel to c-axis J_c is several times smaller (this number depends on temperature and field strength [111], [112]) compared to applied field perpendicular to c-axis. This is caused due to the high anisotropy of the properties of the cuprates

[105]. The *Lorentz forces* described in section 2.1.2.3 act on the vortices, and, unless the pinning force is very large, this results in broadening of the *normal-superconductor* (N-S) transition temperature (Figure 2.14) when H increases. The same forces generate the *irreversibility line* [99], [113], which separates the vortex-liquid state and pinned vortex-glass state (Figure 2.11).

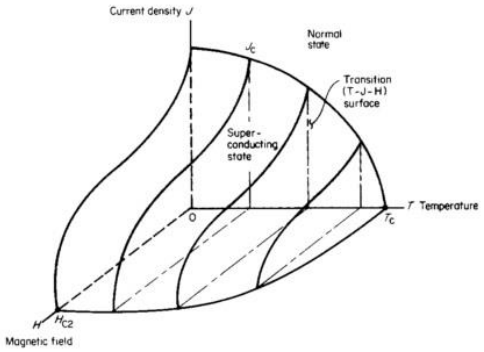


Figure 2.13: The correlation between critical current (J_c), applied magnetic field (H), and temperature (T) creates a critical surface that separates the normal and superconductor (N-S) states [107].

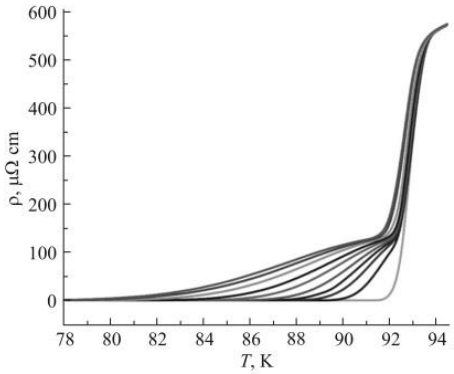


Figure 2.14: Temperature dependent transition behaviour when in applied fields H=0, 10, 25, 50, 100, 250, 500, 1000, 1400, 1900 Oe, from bottom to top [114].

The existence of *grain boundaries* (GBs) in polycrystalline samples form regions where the superconducting properties are degraded, generating *weak links* because of the need for tunneling through boundaries which act as *Josephson junctions*, which can be thought of a thin insulating layer [115]. Low-angle grain boundaries, i.e. less than 5°, have negligible effect on J_c [116], but at grain boundaries with misorientations of 20°, J_c is reduced by several orders of magnitude [117].

The GB problem has been addressed using *coated conductor* (CC) technology, which aims to maximise both the superconducting properties and mechanical stability. Growing REBCO films

containing only low angle GBs on a strong, flexible metallic substrate is crucial to enable manufacturers to produce tapes hundreds of meters long. The crystallographic texture can be achieved in the REBCO layer using two techniques [118]: *ion beam assisted deposition* (IBAD) [119] and *rolling-assisted biaxially textured substrate* (RABiTS) [120]. IBAD deposits textured thin films on a randomly-oriented metal substrate by *physical vapor deposition* (PVD) [121], *metal organic chemical vapor deposition* (MOCVD) [122], *pulsed laser deposition* (PLD) [123] and *reactive co-evaporation* [124]. In contrast, the RABiTS approach relies on textured metal substrates achieved by rolling and annealing [120]. The 0.8-3.8 µm thick REBCO layer is only a minor section of the approximately 100 µm thick CC [125] (Figure 2.15). The other layers in the CC function, inter alia, as diffusion barriers to keep reactive metals away from the superconducting cuprate and reducing the lattice mismatch to encourage epitaxial growth of REBCO on a perovskite layer like $LaMoO_3$ (LMO) or $SrTiO_3$ (STO).

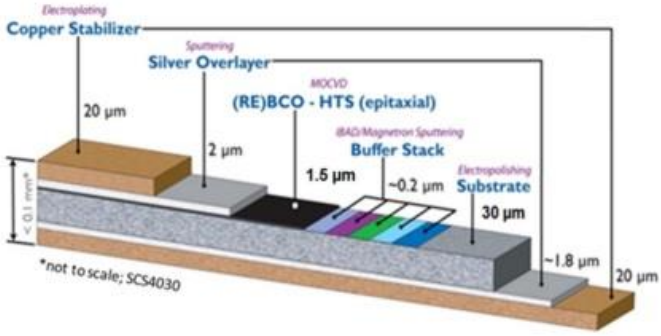


Figure 2.15: Layered-structure of SuperPower's REBCO CC layered-structure [126].

CC fabrication process gives rise to the presence of *twin boundaries* (TB). The REBCO layers, although biaxially textured to form effectively single crystal thin films, are also twinned on a length scale of a few 10s of nm along [100]/[010] axes, typically aligned along the rolling direction of the tape [127]. Twin boundaries also contribute to the aggregate vortex pinning, and, according to one study, provide to 21% of the total pinning force when 1D *artificial pinning*

centres (APCs, discussed in section 2.1.2.5) exist, and up to 84% in the absence of APCs, measured at 65 K [128]. Although TB are inevitably present in REBCO tapes, their formation might be interrupted by local stresses emanating from the partial dislocations associated with the presence of intergrowths, as shown in Figure 2.16. Incoherent $BaZrO_3$ (BZO) nanorods also give rise to local stresses and thus promote the formation of intergrowths. The aggregate effect of BZO nanorods is thus promotion of intergrowths, which behave as nucleation sites for TB that are irregular in shape and shorter in length [128].

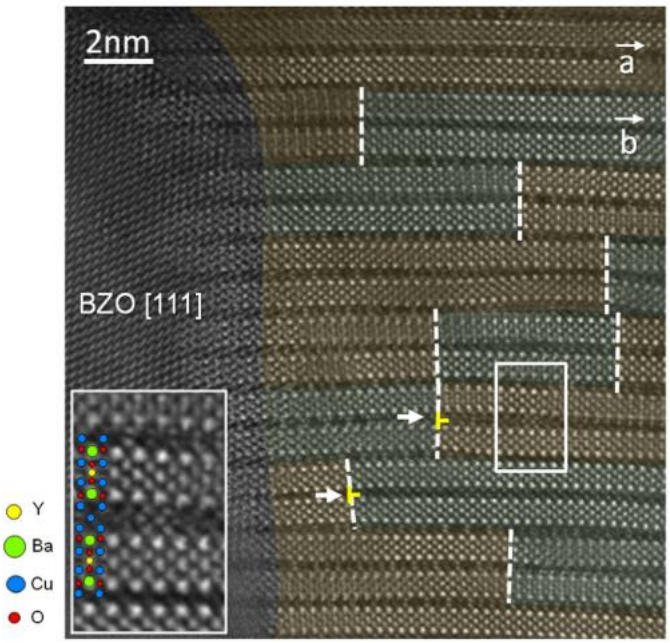


Figure 2.16: STEM/HAADF image of REBCO containing $BaZrO_3$ (BZO) nanorods. The green and brown colours represent the local orientation of the lattice, [010] and [100], respectively, caused by the TB domains separated by dashed white lines. The arrows indicate partial dislocations and the inset shows an enlarged region with Y125 intergrowth [128].

A summary of YBCO properties is presented in Table 2.1, including the available data on GdBCO which has been studied in this thesis.

Table 2.1: Physical properties of YBCO and GdBCO type II superconductors.

	YBCO		GdBCO	
Parameter	**Value**	**Reference**	**Value**	**Reference**
T_c	92.5 K	[129]	94-95 K	[75]
Symmetry	Pmmm	[130]	Pmmm	[131]
Lattice parameters	a= 0.3822 nm b=0.3891 nm c=1.1677 nm	[129]	a= 0.3839 nm b=0.3899 nm c=1.1706 nm	[132]
$\xi_{\parallel c}$ $(\mathbf{T = 0})$	0.30 nm	[133]	0.22 nm	[134]
$\xi_{\perp c}$ $(\mathbf{T = 0})$	1.64 nm	[133]	---	
$\lambda_{\parallel c}(\mathbf{T = 4.5\ K})$	26 nm	[135]	---	
$\lambda_{\perp c}$ $(\mathbf{T = 4.5\ K})$	125 nm	[135]	---	
κ $(\mathbf{T = 0})$	7.6	[135]	---	
γ $(\mathbf{T = 80\ K})$	7.7	[70]	5.0	[136]
$J_{c\parallel c}(\mathbf{0\ T, 4.5\ K})$	$3.2 * 10^6\ A * cm^{-2}$	[135]	$3.2 * 10^6\ A * cm^{-2}$ $(\mathbf{0\ T, 77\ K})$	[137]
$J_{c\perp c}(\mathbf{0\ T, 4.5\ K})$	$1.6 * 10^5\ \frac{A}{cm^2}$	[135]	---	
$H_{c1\parallel c}(\boldsymbol{T = 0\ K})$	0.085 T	[138]	---	
$H_{c1\perp c}(\boldsymbol{T = 0\ K})$	0.025 T	[138]	---	
$H_{c2\parallel c}(\boldsymbol{T = 0\ K})$	29 T	[135]	80-90 T	[139]
$H_{c1\perp c}(\boldsymbol{T = 0\ K})$	140 T	[135]	---	

2.1.2.5. Flux pinning

Flux pinning is one of the most important ways of increasing J_c. As mentioned for type I superconductor, when the vortices move, a resistivity is measured [140], [141]; therefore it is

imperative that the vortices are fixed in place. To impede movement of vortices, the pinning force, which relates to the pinning site characteristics [142], [143], must exceed the Lorentz force in the presence of magnetic fields, electric current and thermal fluctuations. The pinning force strength can be deduced from the *magnetization-magnetic field curve* (M-H) [144]. An example of pinning force (F_p) and J_c measured at 65 K is shown in Figure 2.17 on different YBCO films containing $BaSnO_3$ (BSO) nanorods and a third phase of Y_2O_3 (YO) at different concentrations. One can observe that pure YBCO films have the lowest F_p (and hence the lowest J_c values), and incorporating both nanorods and YO nano-spheres pushes the maximum pinning force to higher magnetic fields as the nano-spheres act as additional pinning centres in between the nanorods [145].

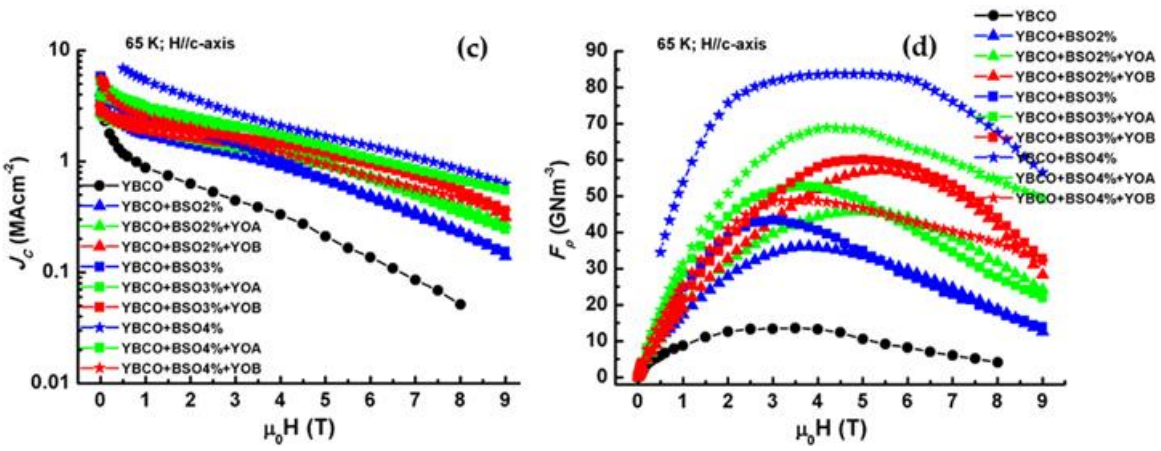


Figure 2.17: Critical current (J_c) (left figure) and pinning force (F_p) (right figure) measured in various magnetic fields, H||c, at 65 K on different YBCO films. YBCO stands for pure film; whereas the other samples contained different wt.% of $BaSnO_3$ (BSO) nanorods aligned along the c-axis and Y_2O_3 (YO) nano-spheres with concentration of 2.2 (YOA) and 3.0 wt.% (YOB) [145].

Pinning centres include inherent lattice defects such as oxygen vacancies, twin boundaries and the REBCO layered structure itself, called *intrinsic pinning* [146], [147]. However, pinning sites can also be added by including additional normal phases with the size of about the coherence

length (ξ) value (Table 2.1) [109], [143], [148], called artificial pinning centres (APCs), and have large effect on J_c enhancement by providing an energy barrier for the motion of vortices. APCs include adding second phases in shape of rods (1D) or particles (3D), subtracting matter to produce nano-voids, and amorphous regions caused by irradiation [149], and can be designed using experimental or computer-assisted [150], [151] methods. It is worth noting that CC structures are designed to operate in specific environment of temperature and field (see Figure 2.18) [125], [152], and so the APC landscape needs to be optimised for specific applications.

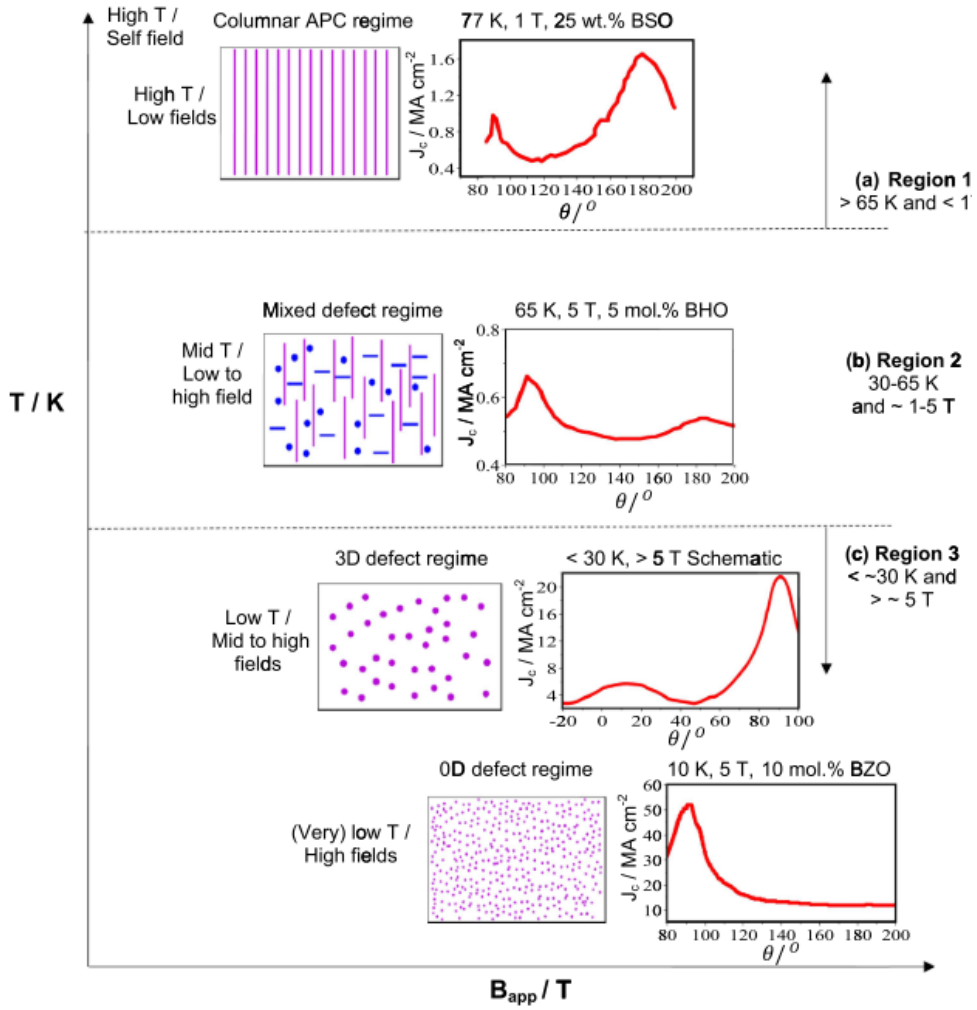


Figure 2.18: A schematic view of the effectiveness of APCs in different temperature (y-axis) and magnetic field (x-axis) regimes that can be tailored for specific applications. They are divided into 3 regions from high temperatures and low fields at the top and down to low temperatures and low fields at the bottom. The angular J_c dependency is also shown for each region to illustrate the anisotropy characteristics where ϑ=0 defined as the field parallel to the c-axis [153].

Aye et.al. [154] found that incorporating $BaHfO_3$ (BHO)/$BaZrO_3$ (BZO) or $BaSnO_3$ (BSO) nanorods into YBCO films tripled J_c at 10 K / 1 T. In the high temperature regime (77 K, 1 T), Selvamanickam and co-workers [155] showed a 70% increase in J_c in (Gd,Y)$Ba_2Cu_3O_{7-x}$ by incorporating BZO nanorods. Miura et.al. [156] supported these findings of enhanced J_c in all

conditions studied, i.e. 5 – 75 K and 0 T up to 60 T. Effective pinning in REBCO occurs when the core size of the defect corresponds to the superconductor's coherence length (ξ), which is only a few nanometres when T is close to zero K [157] (refer to the values for REBCO in Table 2.1). The coherence length increases with temperature, and thus the efficacy of the pinning is controlled by matching ξ and defect size. Thus as a general guideline, small defects are preferable at low temperatures while larger precipitates and nano-rods are better at elevated temperatures [153].

One-dimensional (1D) columnar defects are known to increase J_c for fields applied along this direction, are more effective at higher temperatures [156], and their effectiveness is a function of diameter [158], spacing [159] and length [160]. Although nano-rods can be composed of several different phases with different morphologies such as $BaHfO_3$ (BHO) [161], $BaSnO_3$ (BSO) [162], Ba_2YNbO_6 (BYNO) [163], Ba_2YTaO_6 (BYTO) [164], $Ba_2Y(Nb,Ta)O_6$ (BYNTO) [165], RE_2O_3 [166], $RE_2Cu_2O_5$ [156], and RE_2BaCuO_5 [167], they usually made of $BaZrO_3$ (BZO) due to the limited solubility of Zr in YBCO, which promotes formation of smaller rods. BZO tends to form along the c-axis [168] due to the crystalline mismatch [89], although at high BZO contents they can also inhabit the ab-plane [169] or change to a particle morphology [155], and thus incrementally eliminate the J_c anisotropy when $H \parallel c$ [169]. Galstyan et.al. [170] analysed the effect of Zr addition, 0, 5, and 15 mol.%, and Ba molar ratio ranging from 1.8 to 2.35 in (Gd,Y)BCO. TEM analysis shows that at 15% Zr, increasing the Ba content from 1.8 to 2.35 (and thus the (Ba + Zr) / Cu ratio from 0.72 to 0.85) prevents the formation of RE_2O_3 (REO) nano-particles that lie in the ab-plane due to the excess RE content, and also results in more continuous BZO nanorods (Figure 2.19c). As a consequence of the different microstructures, the peak of J_c at 4.2 K shifts to higher (Ba+Zr)/Cu ratios as a function of applied field (see Figure

2.20) as a result of a larger contribution of weaker pinning sites such as oxygen vacancies at high magnetic fields (Figure 2.18) that exist due to local stresses.

Although the addition of BZO is very useful for improving the transport properties, there is a compromise in performance between the stronger pinning and degradation of T_c due to the inhomogeneities in the REBCO layer, e.g. intergrowths [98]. T_c degradation becomes dominant with increasing rod density [149], [171] and is hypothesised to be due to local stresses that cause charge rearrangements in the CuO_2 planes [172].

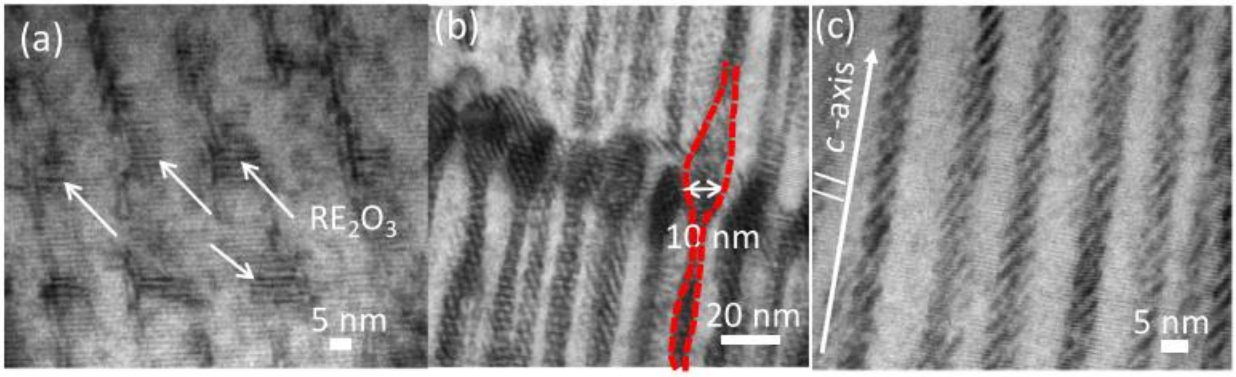


Figure 2.19: TEM bright field (BF) images taken along [100]/[010] ZA from (Gd,Y)BCO with 15 mol.% Zr added and different (Ba + Zr)/Cu ratios, low-0.72(a), medium-0.76(b), and high-0.85(c), corresponding to Ba molar concentrations of 1.8, 1.97 and 2.35, respectively. RE_2O_3 phase is marked by white arrows (a) and alternating width of BZO rods is emphasised by red dashed lines (b) [170].

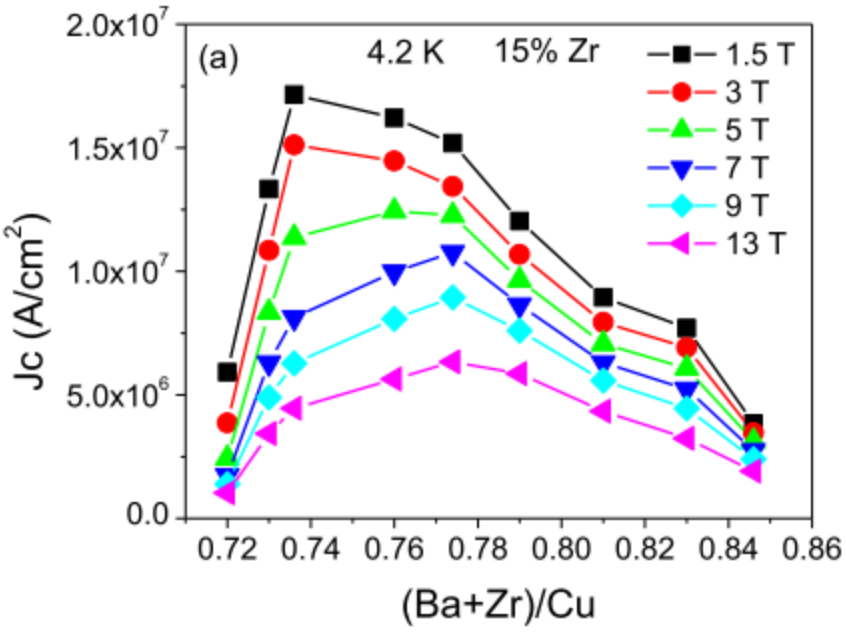


Figure 2.20: Critical current (J_c) at 4.2 K in different magnetic fields of (Gd,Y)BCO-BZO as a function of Ba content from 1.8 to 2.35 (equivalent to (Ba + Zr)/Cu 0.72 to 0.85) with a constant 15 mol.% Zr addition [170].

CCs in magnets are wound at a variety of directions with respect to the generated field [173] and therefore the J_c/B anisotropy can be a drawback. Three-dimensional (3D) nanoparticles can diminish the effects of applied field direction on the transport properties, and thus give more uniform J_c when tilting the applied or working field [174]. Introducing Y_2O_3 nanoparticles can increase J_c at a wide range of temperatures and fields, but especially at low temperatures [175]. Nanoparticles also show reduced adverse effects on T_c with comparison to 1D-APC [90], [176], [177].

Since 1D and 3D APCs can both contribute to REBCO tape performance, it is feasible to utilize the advantages of both to maximize the performance and to control the J_c dependence on field orientation (Figure 2.21). The *hybrid structure* is more efficient at high fields [162], [178], [179] and temperatures [180]. The advantages of the hybrid structure are two-fold; first improvement

of the J_c at intermediate angles between ab-plane and c-axis, and second to serve as auxiliary pinning points at higher fields for 1D-APCs in the vicinity of the c-axis [162].

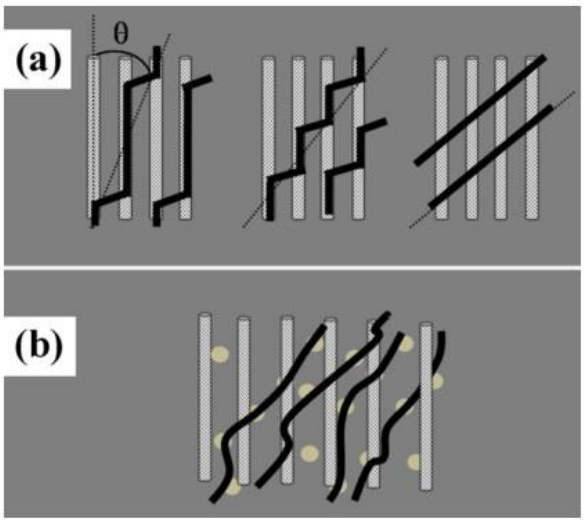


Figure 2.21: Schematic representation of the behaviour of pinning centres in an oblique magnetic field. (a) Vortices exhibit 'jumps' from pinning site to another, until the loss of ability to provide strong pinning force. (b) 3D-APC sustain the pinning force independent on the field direction [145].

2.2. Irradiation Damage in HTS

Irradiation damage in superconductors has been studied in the last few decades, and research was also dedicated to low temperature superconductors (LTS) (The interested reader is referred to [34], [35], [181] and the references within). YBCO and the more general REBCO (RE=Rare Earth) are being considered for the magnet windings in small fusion machines as discussed in section 1.2 due to their ability to carry very high currents in high magnetic fields (Figure 2.4). Although the breeder blanket and radiation shielding layers in a fusion reactor absorb most of the neutron flux, a small fraction may penetrate and collide with the superconductor wires in the magnet confining the fusion plasma. This is especially true in compact reactor designs where the plasma and central magnet components may only be separated by a few cm [182].

To calculate the neutron flux and energy from a given neutron source, the *Monte Carlo N-particle* (MCNP) code [183] is commonly used, and it has shown that radiation shield attenuates the neutron flux by a half every 0.053 m and halving its energy every 0.43 m [182]; however, an increased thickness of the neutron shielding between the superconductors wires and the fusion plasma dramatically increases the cost of building the reactor [184]. In a fusion reactor such as ITER the neutron flux produced by the fusion reaction is in the order of 5×10^{20} m^{-2} [185], and the shield thickness is designed to be around 0.25 m [186], which lowers the effective flux on the superconducting tapes by about one order of magnitude. Thus, the effect of high energy neutron damage on REBCO need to be understood. This section covers the general theory of irradiation damage, and the implications for microstructural evolution and superconducting properties in REBCO materials. Section 2.2.1 presents the evolution of collision cascades and discusses amorphisation models, and section 2.2.2 details previous work on irradiation-induced microstructural and superconducting properties evolution in REBCO tapes.

2.2.1. Radiation damage mechanisms

Although differing from one material to another [187], [188], radiation damage has some well-defined general characteristics. A colliding particle transfers its energy to target atoms and creates a displaced *primary knock-on atom* (PKA) [189], [190], which if it has sufficient energy can create many additional local displacements to generate a *collision cascade*. The cascade's *timeline of events* can be divided into four stages; *displacement*, *thermal spike*, *quenching*, and *annealing*, and computer simulations such as *Molecular Dynamics* (MD) and *binary collision approximation* (BCA) are useful for understanding the atomic displacement events. Additionally,

experimental and theoretical studies attempt to shed light on larger scale amorphisation processes.

2.2.1.1. The collision cascade

2.2.1.1.1. Recoil spectrum and particle type

The incident particle type and energy define the recoil spectrum, which is the range of damage energies with respect to the PKA energy. The recoil spectrum is an important tool to analyze the type, number and distribution of post-irradiation defects. Neutrons tend to generate large, separate and homogenous cascades in the irradiated material [191]. However, experiments with neutrons have several problems such as lack of sources of energetic neutrons, transmutation products, activating reactions and long radiation dwell times, which makes it hard and expensive to study the real effects of neutron damage. These drawbacks make other energetic particles attractive for emulating the effects of irradiation by neutrons.

It is also worth noting that in the case of neutron irradiation, the energy cannot be stated as a single value as for ion-irradiation, but rather displays a distribution of flux density as a function of energy [192]. As can be seen in Figure 2.22, the emitted neutrons in the TRIGA reactor in Vienna have a range of energies ranging from thermal neutrons where $E < 0.55$ eV up to about 14 MeV.

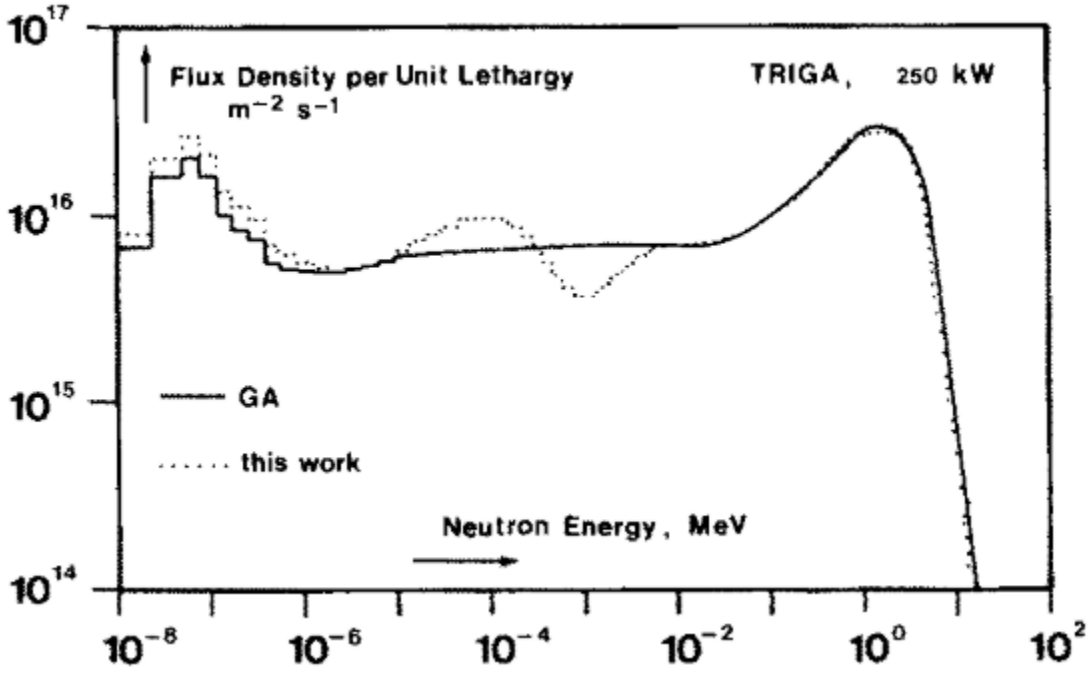


Figure 2.22: Flux density for the TRIGA MARK-II reactor at a power of 250 kW. The solid line is the input spectrum as provided by the reactor manufacturer and the broken line is a measured data obtain by Weber et.al. [192].

The available particles for irradiation experiments are electrons, protons and light/heavy ions as well as neutrons. Electrons are unable to produce cascades and generate mostly vacancy and interstitial pairs known as *Frenkel pairs* (FPs) [193]. Protons produce dispersed FPs and exhibit a smooth damage profile with a peak damage region at a significant penetration depth [194], [195], and are widely used for emulating neutron damage [196]. Ion radiation damage is mass dependent; the damage characteristic of light ions is comparable with protons and electrons [197], whereas heavy ions generate many more local FPs [198], which tend to condense to form fewer [199] and denser [200] cascades. Thus, heavy ions are also commonly used as a proxy for neutrons [201]. Self-ion irradiation avoids chemical changes to the target material which may add additional alterations to the sample properties [202], [203]. The figure below illustrates the damage morphologies provoked by different particles.

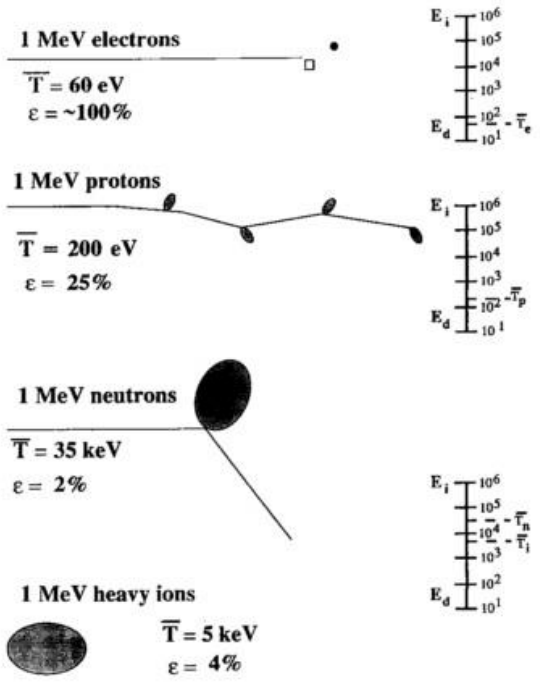


Figure 2.23: Pictorial image of the damage morphologies created by different irradiation particles; $\bar{T}$ is the typical energy for PKA, and ε is the damage efficiency [191]*. The shaded areas are collision cascades where any crystalline material normally becomes amorphous.*

2.2.1.1.2. Displacement phase

To produce a displacement, a minimum *displacement threshold energy*, E_d, must be transferred from the incident particle to an atom in its lattice site. This energy is 40 eV in iron [204] and also depends on the crystallographic direction [205] and temperature [206]. In YBCO, the Y, Ba, Cu and O atoms have E_d (in eV) of 40 [207], 45 [207], 15-33 [208], [209], and 7-10 [207], [209], respectively. Oxygen E_d values vary according to its location and there is lack of consensus in the literature. The standard method [204], [210] to quantify the number of atoms displaced per PKA (N_{NRT}) is the *NRT model* [211], which uses the energy of the PKA atom, E_{PKA}.

Equation 2.2: $N_{NRT} = \frac{0.8 * E_{PKA}}{2E_d}$

to calculate N_{NRT} which can be converted to *displacements per atom* [212], dpa, which represents the number of displacements for every atom in the target material. Dpa values are calculated as follows:

Equation 2.3: $dpa(x) = 10^8 \frac{\upsilon(x)}{n_T} \Phi$

where $\upsilon(x)$ is the number of vacancies per angstrom per ion, n_T is the target material density in [atoms/cm^3] and Φ is the fluence in [ions/cm^2] [213]. These displaced atoms initially leave a vacancy at the lattice site and occupy an interstitial site. Their aggregate number, N_F, are then affect the *displacement efficiency*, η (sometimes shown as ε), which quantifies the fraction of 'freely migrating' defects.

Equation 2.4: $\eta = \frac{N_F}{N_{NRT}}$

The efficiency curve with respect to E_{PKA} fits a decreasing polynomial function that corresponds to N_F [214], [215]. A combination of electron and nuclear interactions govern the slowing-down process of displaced atoms [199], [216]. At low energies, nuclear interactions dominate the stopping power, whereas at high energies electronic losses associated with the screening Coulomb potential exerted on charged particles are dramatically increased [217] (see Figure 2.24). The *nuclear stopping power* (S_n) contributes to lattice damage whereas the *electronic stopping power* (S_e) goes into heating and even local melting [218]. The dominance of S_e and an increasing number of point defect recombination events [219] leads to a saturation in damage efficiency at high energies [220].

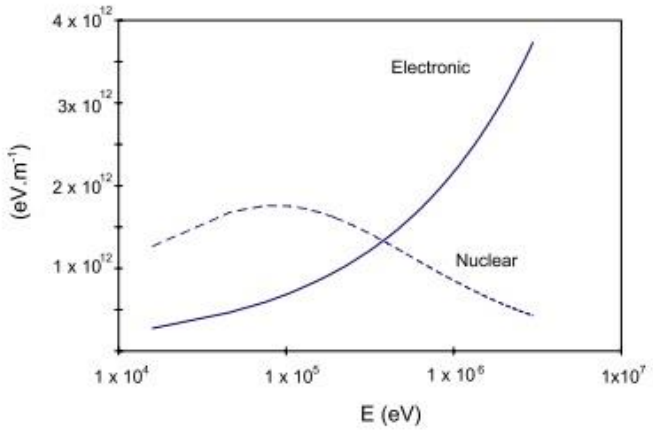


Figure 2.24: Electronic and Nuclear stopping power of iron ions moving into an iron target depicted as the energy loss as a function of energy [199].

2.2.1.1.3. Thermal spikes

Invariably in any irradiation experiment the energy of the PKA is much greater than E_d, so the PKA continues to collide with many atoms before it loses its energy. The displaced atoms have sufficient energy to stimulate a chain reaction of secondary and tertiary knock-on atoms [199] accompanied with violent hyper/super-sonic shock waves [221], [222] and even local melting. The thermal spike [223] defines at the stage where the number of displaced atoms reaches a maximum [224], leading to a collision cascade as shown in Figure 2.25.

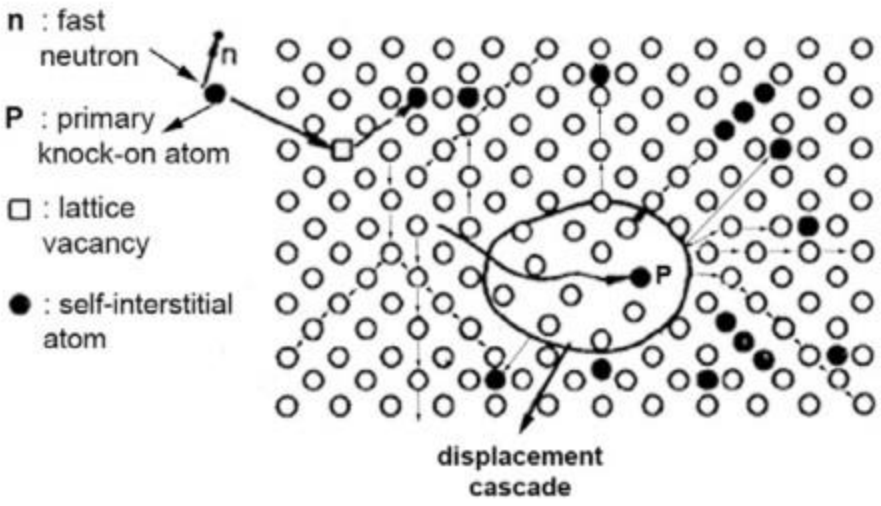


Figure 2.25: Schematic illustration of the initial stage of the collision cascade [225].

2.2.1.1.4. Quenching

During relaxation of the thermal spike, rapid cooling at the order of 10^{15} K/s [226] occurs in the melting zone. The *characteristic cooling time*, τ, usually ranges from 1-10 ps [227] and is governed by electron-phonon coupling [228]. During this time, the cascade is likely to change to *subcascades* when the energy is sufficiently high [224]. The fragmentation of the molten area to subcascades favors the creation of small clusters which are mainly populated by small defect clusters and Frenkel pairs. This universal linear log-log branching as a function of PKA energy is demonstrated quantitatively in Figure 2.26.

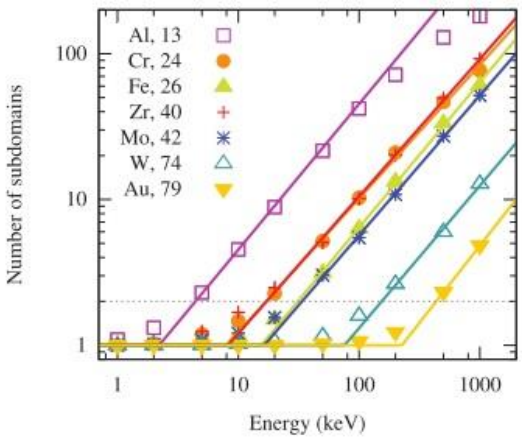


Figure 2.26: Number of subcascades produced as a function of PKA energy in targets of different atomic mass computed using the binary collision approximation (BCA) model [229].

Cascades and subcascades comprise mostly of assemblies of FPs generated by atomic displacements in the thermal spike. Their distribution is inhomogeneous; vacancy clusters push toward the centre of the cascade [187], [223], [226], whereas interstitial clusters form in the periphery [230]. In REBCO, and more broadly in oxide materials, this mechanism might be more complex and anisotropic, but evidence for amorphous tracks in YBCO supports the lower density at the cascade core [231]. As the thermal spike cools down, some of the point defects exist in the cascade region can be eliminated by mutual recombination of point defects and can also be lost to *sinks*, i.e. imperfections in the lattice like GBs and surfaces.

2.2.1.1.5. Amorphisation models

The amorphisation process under ion irradiation is not yet well-understood, and several models have been suggested in order to describe this behavior. Early models discussed the amorphisation of Si due to on the use of ion beam implantation in the semiconductor industry, and since then these models have been applied to other kinds of materials such as intermetallics [232] and ceramics [233]. Morehead et.al. [234] first proposed a heterogeneous model where

amorphisation occurs when isolated amorphous islands overlap as the fluence increases up to the point of complete amorphisation. This model is most appropriate for the case of neutron or heavy-ion irradiation, but cannot describe light-ion irradiation that does not produce damage cascades. In order to account for this, Gibbons [235] proposed a homogenous model that occurs by introducing irradiation damage, mainly Frenkel pairs and perhaps a small concentration of divacancies, that keeps accumulating until a point where the amorphous phase is thermodynamically stable [232]. This homogenous model predicts that the transformation from crystalline to amorphous will occur over a narrow range of irradiation fluence when the crystalline material becomes unstable.

Figure 2.27 shows schematic amorphisation curves for the heterogeneous and homogenous models. The heterogeneous model is characterized by the accumulation of amorphous cascades manifested by a rapid amorphisation process, but if an increasing number of overlapping damage events are necessary to trigger complete amorphisation, the process becomes slower and is pushed to higher fluence [236].

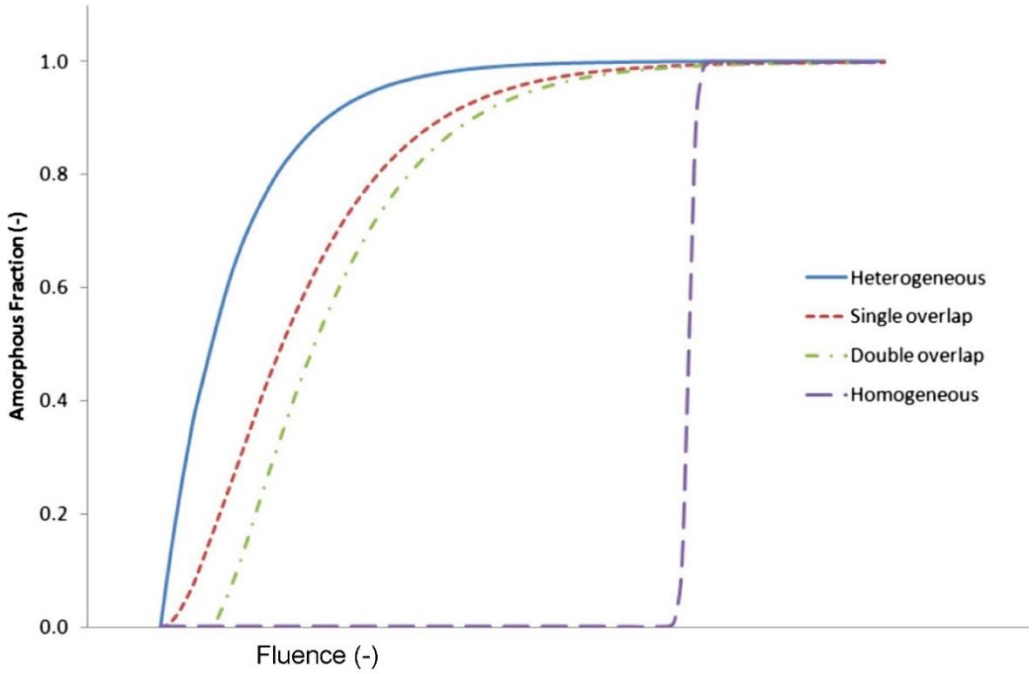


Figure 2.27: Schematic illustration of the amorphisation fraction (y-axis) as a function of irradiation fluence (x-axis) according to models proposed in the literature (adopted from [236]*).*

2.2.2. YBCO post-irradiation structure and superconducting properties

The properties of superconductors exposed to various incident particles over a wide range of energies have been investigated in the literature, but not many groups have analysed the microstructural evolution. In addition to emulating the real conditions in fusion reactors, irradiation defects have been suggested as an alternative way to generate APCs as a way to increase superconductor performance, but the effect of point defects on properties is also important. The following section covers the implications of irradiation on the microstructure and superconducting properties of REBCO materials. Many variables characterising the irradiating particles and the target material have been identified as influential factors on the microstructural

evolution. The irradiation process can be tuned by particle energy, type and dose. The materials variables can be the crystallographic orientation, oxygen vacancy concentration and existing crystal imperfections [237].

2.2.2.1. Post-irradiation microstructure

Usually, irradiation takes place on bulk materials either in a reactor in the case of neutrons [192] or in ion accelerators facilities [238], [239] , then, the sample properties are investigated. TEM studies require the preparation of a thin lamella sample. This destructive procedure eliminates the option to do a 'pre- and post' comparison from the same region. Thus, neither induced damage during sample preparation [240] nor random variations in the initial microstructure (stacking faults are a case in point in the case of REBCO) can be evaluated. There are very few cases that have studied the exact same sample volume before and after irradiation of REBCO, and they are discussed below.

Fast neutrons and heavy ions can generate in REBCO materials collision cascades or, if sufficiently energetic, amorphous columns a few nanometres in diameter [241]. In contrast, electrons produce point defects which are mostly invisible in the TEM [242], and protons produce defect clusters a few nanometres across without creating amorphous regions [243]. When using ions, it is critical to understand the incident energy and electronic stopping power, S_e [244], since the nature of the defects may vary from amorphous tracks near the surface to point defects deeper into the material [245]. It is intriguing to observe that although dislocation loops are a common product of irradiation damage in both metallic [246] and ionic [233], [247] materials, they are rarely seen in YBCO. Clark et.al. [248] postulate that the absence of

dislocation loops could be explained either by point defects not forming clusters and collapsing to loops, or that loop nucleation is inhibited by a thermodynamic barrier.

2.2.2.1.1. Columnar damage and damage cascades

The larger defects produced by irradiation with highly energetic heavy ions fall into two regimes. Provided that the criteria S_e > 12-18 keV/nm [249] for generating amorphous volumes is satisfied, cylindrical damaged regions start to form, which transform to continuous tracks when the S_e threshold of 28-35 keV/nm is exceeded [244], [250]. This criterion holds true for different types of oxides including YBCO. Lower energy irradiation generates point defects, e.g. FP, which are less effective as pinning sites, but can alter the properties of the superconducting matrix. The reader should note than the range of energies discussed in this section is generally higher than the highest energy found in fusion reactor (Figure 2.28) but nevertheless can enrich one's knowledge on HTS response to irradiation.

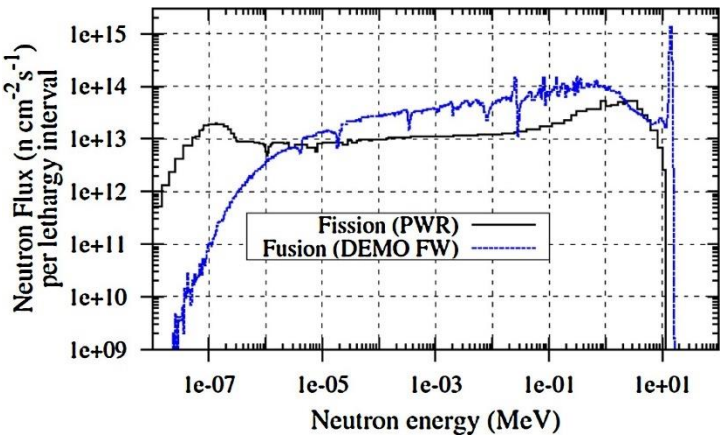


Figure 2.28: Neutron flux as a function energy for pressurized water reactor (PWR) fission reactor and DEMO fusion reactor [251].

Although columnar defects are produced by the same mechanism of electronic stopping, they can exhibit different morphologies, and consequently affect the pinning force differently. Their

typical size is several nanometres and the structure varies from completely amorphous (Figure 2.29) to distorted crystalline [252]. The strain fields associated with these defects extend to about twice their core size [253]. Figure 2.30a-c shows columnar irradiation damage with 1.3 GeV U, 2.29 GeV Xe and 2.25 GeV Au ions, which exhibit tracks that are uniform and continuous, discontinuous and slightly slanted from the c-axis, respectively. Civale et.al. [254] reported that the oblique track trajectory, pertinent to Figure 2.30c, emanates from Rutherford scattering, which is more pronounced in lighter ion irradiation.

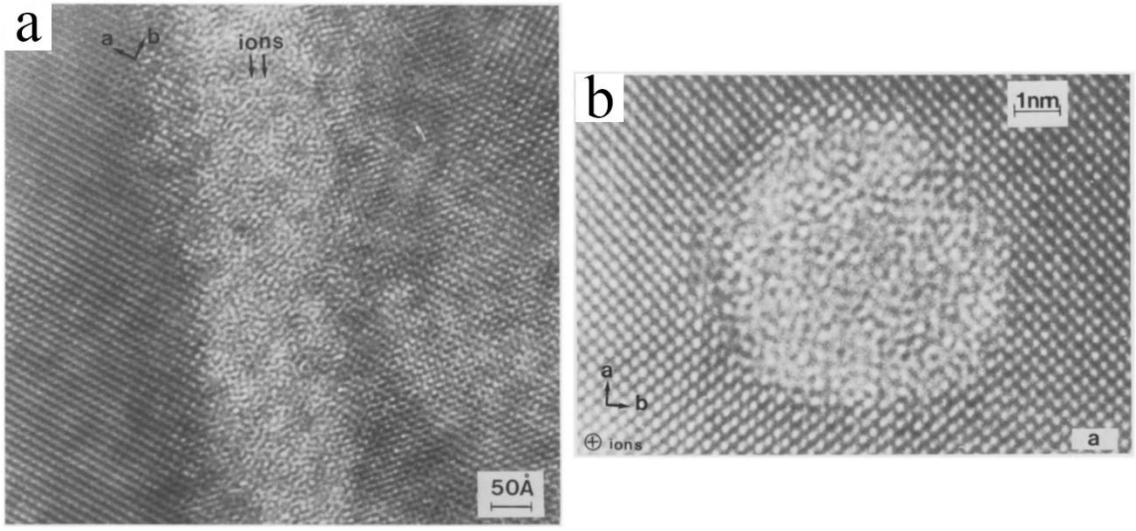


Figure 2.29: Representative HRTEM images of amorphous tracks in YBCO irradiated with 5.3 GeV Pb ions to a dose of $6 \times 10^{11}\ ions/cm^2$ *(a) cross-section view and (b) plan-view* [249].

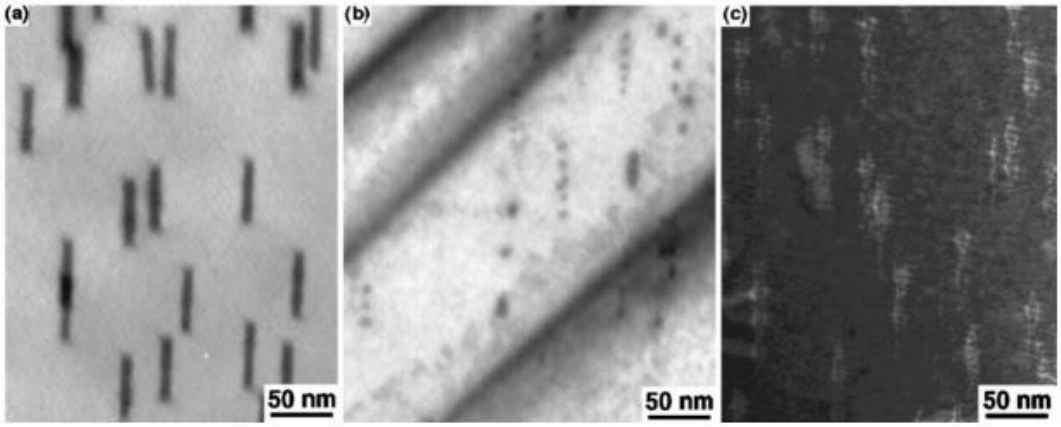


Figure 2.30: TEM bright field (BF) (a-b) and dark field (DF) (c) images tilted 15° from c-axis showing damage after ion-irradiation of YBCO single crystals. (a) 1.3 GeV U-ions. (b) 2.29 GeV Xe-ions. (c) DF (the authors have not mentioned the corresponding g-vector) after 2.25 GeV Au-ions [255].

Other studies have shown an unexpectedly severe T_c decrease even when the tracks occupy a very small volume fraction [256], [257]. This is surprising because T_c will be defined by the properties of the matrix between the tracks where there is little evidence of lattice damage. Electronic stopping interactions can produce *secondary electrons* (SE) that have sufficient energy to escape beyond the track boundaries and damage the pristine crystal in its vicinity. The maximum energy of the SEs is given by:

Equation 2.5: $\varepsilon_0^{max} = 4m(\frac{E}{M})$

where E is the energy of the colliding particle, m is the electron mass and M is the mass of the primary particle. For example, the maximum energy of the SE for 250 MeV Ag ions is about 5 keV with a mean free path of ~160 nm in YBCO, and can provoke local disorder in the Cu(1)-O chains [256]. T_c degradation as a result of the local disorder around the tracks [258] varies with fluence, at low fluence regime there is a minimal impact where there only a few cascades [256],

while high fluence regime results in complete elimination of superconductivity. Figure 2.31 shows an example of this manifestation.

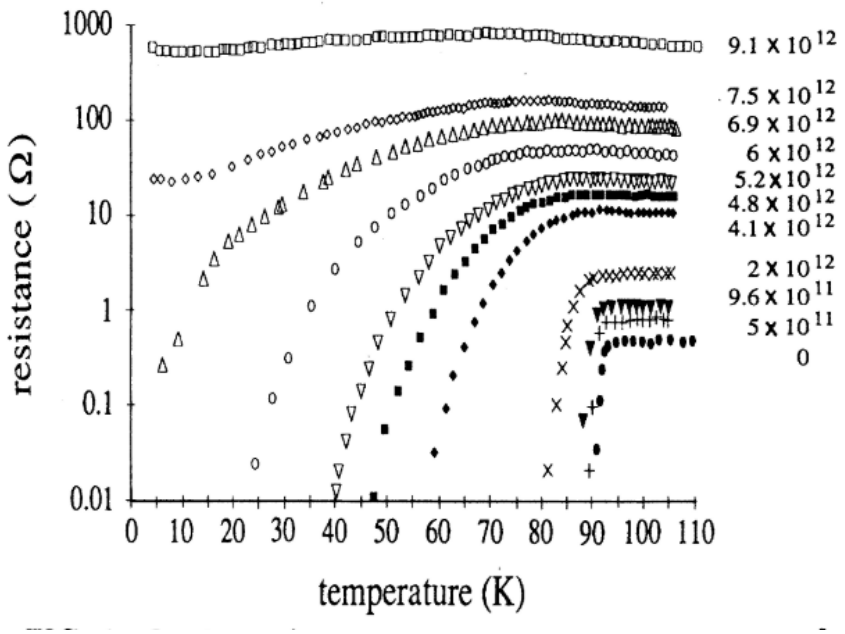


Figure 2.31: YBCO resistance as a function of critical temperature (T_c) presented for different irradiation fluences [cm^{-2}] of 3.5 GeV Xe-ions [258].

Zhu et.al. [237] conducted a TEM study on bulk YBCO with four different incident ions, 300 GeV Au, 276 GeV Ag, 236 GeV Cu, 182 GeV Si, and found different defect types and densities. For lighter ions, Si and Cu, a high density of dislocations loops with diameter from 10 to 20 nm formed rather than cascades or tracks. With Cu, in addition to dislocation loops, occasional amorphous tracks were seen. For heavier ions, Au and Ag, the measured columnar defect density in Au was very similar to the dose value, while Ag has a lower probability of forming amorphous tracks. The track size increases from 2.4, 5.9, and 10.6 nm for Cu, Ag, and Au, respectively. The shape, and especially the length of the damaged regions depends heavily on projectile energy and that is important because flux lines in superconductors are linear features so interact differently with defects of different shape.

The track density under certain ion-irradiation conditions is equal to the dose, which means that every ion generates a detectable cascade [237], [252], [259]. Suvorova et.al. [231] conducted irradiation experiment on SuperPower YBCO CC using 167, 77, and 46 MeV Xe ions to fluences of 1×10^{11} cm^{-2} (for 167 MeV) and 5×10^{11} cm^{-2} for the latter two. It was observed that the track morphology was continuous for the highest energy and discontinuous for the lower energies. A study of the nature of the amorphous tracks using *energy dispersive spectroscopy* (EDS) line scans reveals lower counts of every atom type at the core of the track, with a total density of 3.6 gr/cm^3 compared to 6.3 gr/cm^3 in the matrix and a slight enrichment of Ba atoms at the track shell. Despite the calculated 2% – 3.3% overall damaged volume, J_c increased for every ion energy and T_c was decreased slightly to 88-89 K. Suvorova et.al. [260] used *high-resolution TEM* (HRTEM), simulations, and EDS to study the latent tracks, namely, the radiation damage along the ion path, and interpreted them as spherical voids approximately 3 nm in diameter (Figure 2.32).

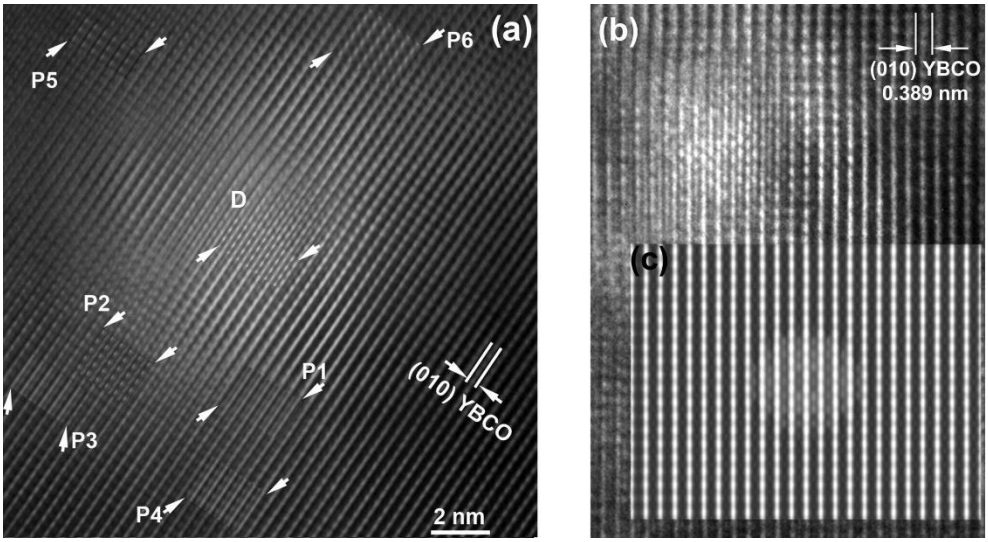


Figure 2.32: Filtered (a) and experimental and modeled (b) HRTEM images of damage cascade in YBCO following 107 MeV ^{84}Kr-ions irradiation. (a) filtered HRTEM of the damaged region (inset D) and the non-damaged regions in its vicinity (5-20 nm) presented in insets P1-P6. (b) experimental HRTEM image with a modeled HRTEM image including 3 nm void (c) [260].

Another interesting phenomenon introduced by several authors [237], [261] showed that the tracks exhibit a *bow-tie* shape. Yan et.al. [255], [262] observed bow-tie-like contrast along the b-axis in the vicinity of amorphous latent tracks (Figure 2.33a), and a nanotwin-like microstructure when they overlap (Figure 2.33b-c). According to their model, the bow-tie contrast emanates from a stress relaxation mechanism of the compression stress fields [263] generated by the amorphous tracks. The fixed alignment along the b-axis occurs by enhanced *local oxygen reordering* (ORO) along Cu-O chains [264].

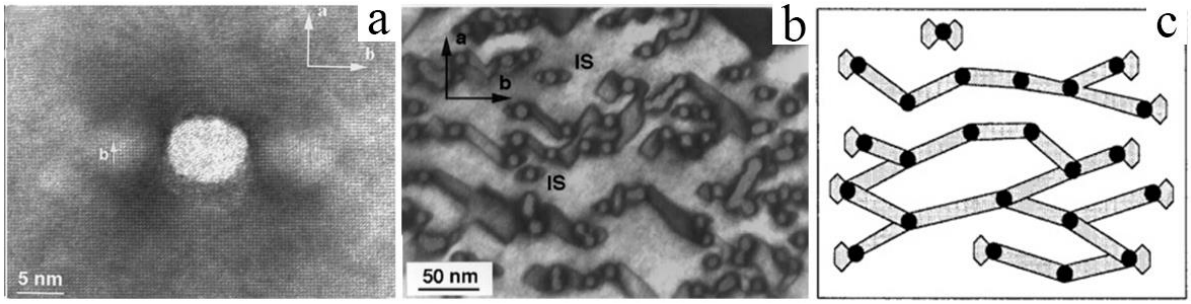


Figure 2.33: TEM/HRTEM images of YBCO, taken after 1.3 GeV U-ion irradiation. (a) HRTEM image taken along [001] direction showing bow-tie contrast, aligned along the b-axis around a latent track. (b) TEM BF image showing a network of bow-ties fusing together. (c) pictorial representation of the interweaved bow-ties [255], [264].

As for neutron-irradiation, an interesting amorphisation mechanism for irradiated YBCO has been proposed by Kirk et.al. [265]. Kirk reported that neutron irradiation leads to the formation of 20-40 nm micro-domains, that they described as a cellular structure, where the cells are almost undamaged and situated between the highly-damaged borders. When the fluence increases, the damaged boundaries expand at the expense of the undamaged cells. Vasiliu et.al. [266] also reported formation of a cellular structure in bulk YBCO doped with LiF following neutron-irradiation to a fluence of 1×10^{22} m^{-2} as can be seen in Figure 2.34. Frischherz et.al. [253] also reported a cellular structure after relatively high fluence of neutron-irradiation.

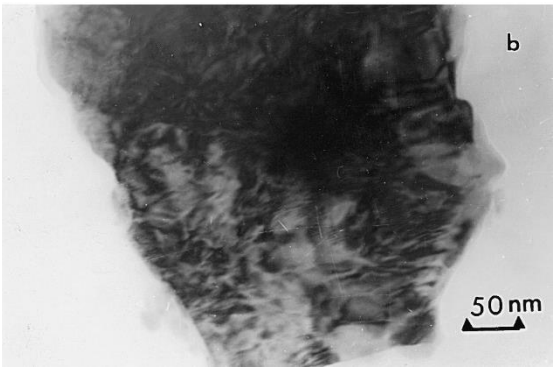


Figure 2.34: TEM image of shows a cellular structure in YBCO doped with LiF following 1×10^{22} m^{-2} neutron-irradiation [266].

2.2.2.1.2. Localised lattice damage

In contrast to tracks created by heavy ions with accelerating voltage of hundreds of MeV to GeV, the use of lower energies and/or lighter ions generates more localised irradiation damage ranging from amorphous cascades to smaller defects such as vacancies/interstitials, Frenkel Pairs, and clusters of point defects.

Zhang et.al. [267] investigated the post-annealing behaviour of irradiated Dy-doped YBCO CC with 18 MeV Au^{5+} ions to a fluence of 3×10^{11} cm^{-2} along the c-axis using STEM and *Electron energy loss spectroscopy* (EELS). As expected, isolated 2-5 nm amorphous cascades appeared surrounded by highly-distorted lattice structure formed as a relaxation mechanism, and after annealing the lattice distortion of the YBCO planes in the vicinity of the amorphous cascades relaxes, Figure 2.35. Similar observations of planar defects in the vicinity of amorphous cascades have also been shown in [268]. In order to further study the chemical changes occurring during the annealing process, EELS analysis was first performed on the as irradiated samples and found that both the amorphous defects and several unit cells in the vicinity display oxygen deficiency due to diffusion out of the damaged region. Annealing restores the oxygen concentrations, mainly in the planes, as was revealed from EELS results.

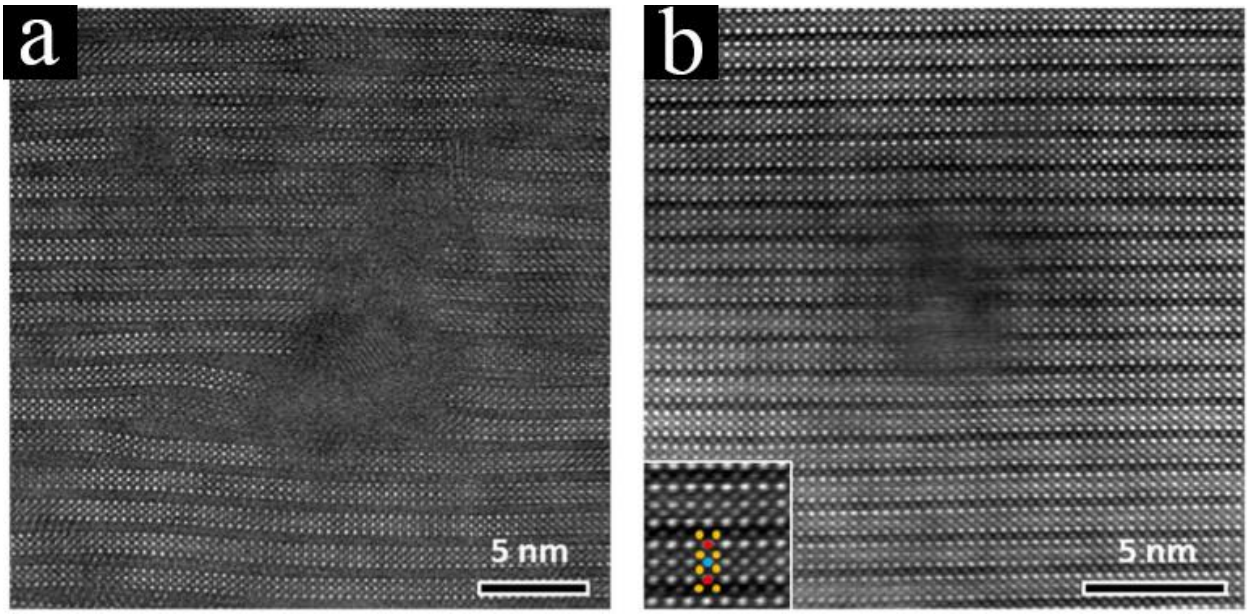


Figure 2.35: STEM/HAADF images taken along [100]/[010] ZA of Dy-doped YBCO CC irradiated with 18 MeV Au^{+5} ions to a fluence of 3×10^{11} cm^{-2}, (a) before annealing, (b) after annealing in oxygen atmosphere at 170 ℃ for 60 min [267].

Frischherz et.al. [253] looked at YBCO single crystals before and after neutron-irradiation to a fluence of 2×10^{21} m^{-2}, at the point where J_c was maximised; higher fluences were also examined but less extensively. Frischherz used *two-beam* (TB) imaging conditions from g = [200], [020] and [006] to maximise diffraction contrast from damage cascades, Figure 2.36. Their estimate of the density of amorphous or highly distorted regions was $1.0(\pm0.3)\times10^{22}$ m^{-3}, with a mean diameter of about 2.5 nm. Strain fields around these damaged regions extended about 6 nm in diameter (measured perpendicular to the defect interface). Annealing at room temperature for 3 weeks, and 3 months, reveals only minor changes in the estimated defect density and suggests that annealing of these rather large defects is very slow at room temperature. Higher annealing temperatures of up to 8 hours 300 ℃ shows only a minor decrease in the defect density and arguably a slight decrease in size, which can be due to stress relief at the matrix-defect interface.

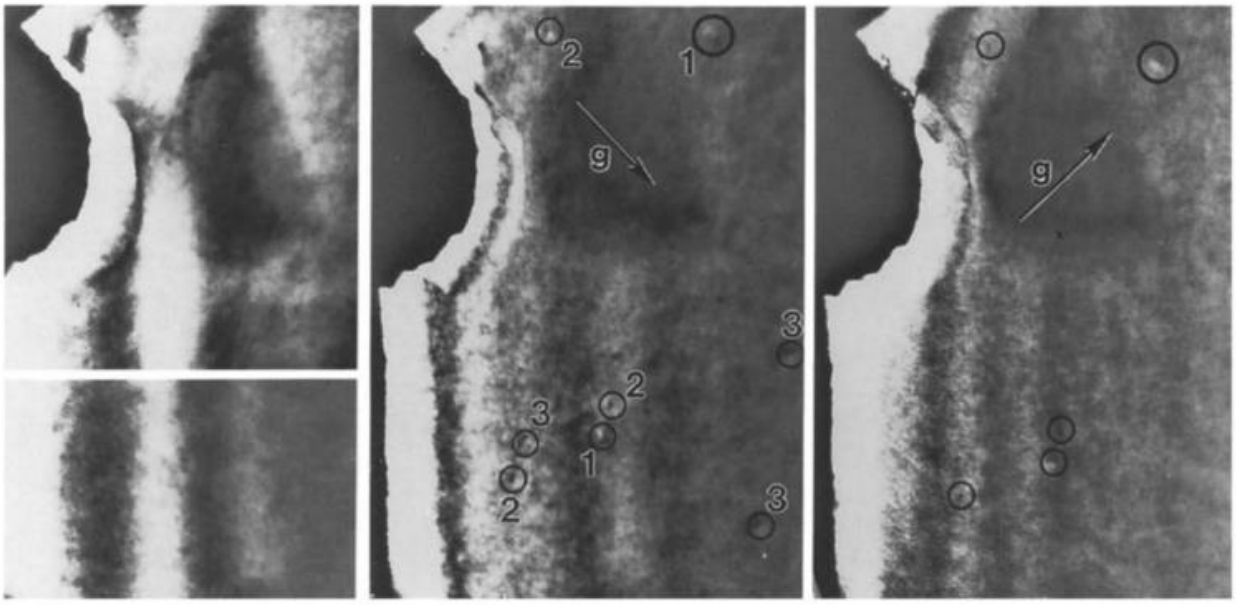


Figure 2.36: Two-beam (TB) TEM images of unirradiated and post-neutron irradiation to 2×10^{21} m^{-2}. Left image taken from pre-irradiated sample with g=[200], post-irradiation central image using g=[200], and right post-irradiation image with g=[006]. Both TEM/TB images of the post-irradiated samples show black/white features a few nanometers in diameter [253].

Using the same imaging conditions, i.e. TEM/TB g=[200], [020], and [006], Frischherz [241] et.al. used 50 keV Kr^{+} (1.3×10^{11} cm^{-2}) and 85 keV Xe^{+} ions as a proxy for neutron-irradiation, and found similar defects with dispersed black/white lobes. The nature of the defects, i.e. size and contrast, was similar to those seen in the neutron-irradiated samples as well as their stability to annealing. HRTEM images also reveal nanometer-scale amorphous cascades that they argued might recrystallize either coherently or incoherently with the matrix. Small cascades tend to start the recrystallization from the edge inward and achieve coherence with the matrix; larger cascades on the other hand crystallizes first in the interior without retaining the orientation of the matrix.

Zandbergen et.al [269] used HRTEM on crushed particles of large-grained $YBa_2Cu_3O_7$ to show damage as a result of neutron irradiation up to a fluence of 2×10^{21} m^{-2}. No amorphous regions

were found, but rather a general lattice disorder, which manifests as darker contrast and changes in the interplanar spacing along the c-axis (as can be seen in Figure 2.37). There is some question whether this disorder arose from a rapid reaction of a thin REBCO sample when exposed to humid air [270] or was generated by the collision of neutrons with the lattice. In reference [271] Janan et.al. argued that the local larger c-axis lattice parameter of about 13.6 Å viewed using HRTEM is a consequence of neutron-irradiation damage to a fluence of 1×10^{20} m^{-2}. This finding is arguable given the fact that the 'defect stripes' are very similar to Y124 defects that could be present as intrinsic defects before irradiation both on how they appear in the HRTEM images and the c-axis enlargement, which is precisely 1/6 of a unit cell along the c-direction.

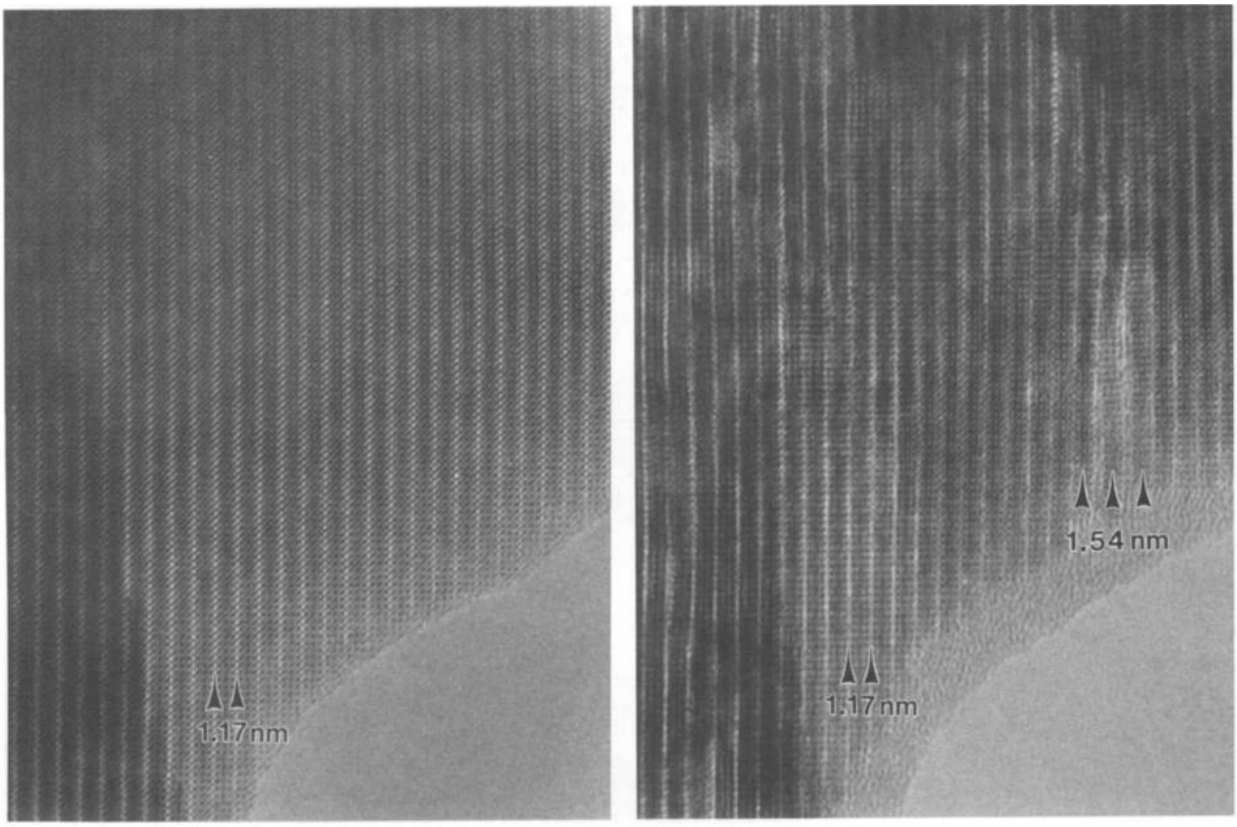


Figure 2.37: HRTEM images taken along [100] before (left) and after (right) neutron-irradiation to a fluence of 2×10^{21} m^{-2}. The irradiated sample show signs of intercalation and increasing c-axis lattice parameter [269].

Van Tendeloo [272] used TEM to investigate crushed $GdBa_2Cu_3O_{7-x}$ single crystals irradiated by 300 keV Ne ions (up to 2.5×10^{14} cm^{-2}) and 100 keV Xe (up to 1×10^{12} cm^{-2}) ions. DF g=[200] images show spherical defect clusters as black/white contrast with a diameter ranging from 2.5 to 15 nm. HRTEM images present clear amorphous/highly-distorted regions manifested by brighter contrast that presumably cannot be observed directly since the damage is buried in the sample thickness. It has also been argued that ion irradiation produces mobile dislocation loops, studied using different DF conditions, that disappear after a period of annealing. In contrast, the amorphous regions are stable and do not change with aging. Similar HRTEM damage cascade direct observations of YBCO irradiated with 200-750 keV Si ions and 200 keV B ions were reported by Matsui et.al. [273] (Figure 2.38).

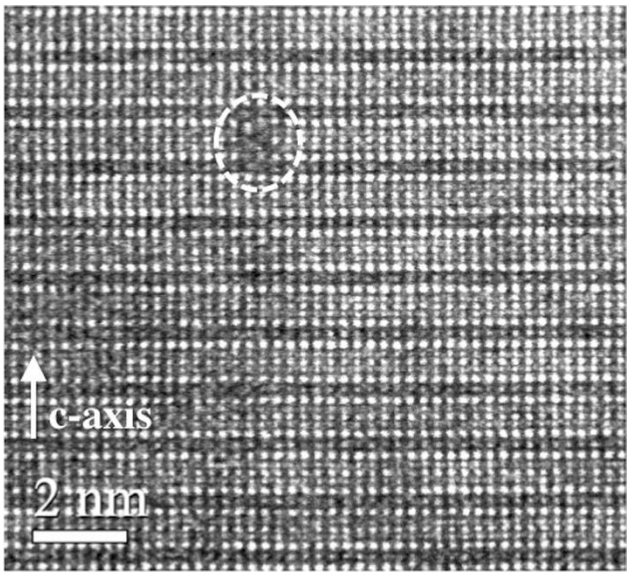


Figure 2.38: HRTEM direct observation of amorphous-like region, marked by dotted line circle, following 500 keV Si-ion irradiation to a fluence of 2×10^{10} cm^{-2} [273].

Several studies were conducted using protons to irradiate YBCO CC. Huang et.al. [274] used low energy, 60 keV proton irradiation of $BaTiO_3$-doped YBCO films. HRTEM observation shows small defects (2-4 nm in diameter) manifested by darker contrast and with a faint

amorphous halo in the *fast Fourier transform* (FFT) (Figure 2.39). Jia et.al. used 4 MeV proton irradiation to a fluence of 2×10^{16} cm^{-2} and found 2-5 nm defects showed under TB conditions from g=[200] and g=[002] that showed as black spots (Figure 2.40) [275]. The same observation was also reported in [276] in samples irradiated by 3.4 MeV protons to a fluence of 1×10^{16} cm^{-2} using TEM/BF conditions. 200 MeV proton irradiation to 2×10^{16} cm^{-2} conducted by Kramer et.al. [243] revealed 2-7 nm higher-contrast clusters in BF and TB images using g=200. It was also hypothesised that point defects created by protons had clustered into these nano-sized defects. These observations are interesting due to the similarity of the images even when the irradiation energies change by 3 orders of magnitude.

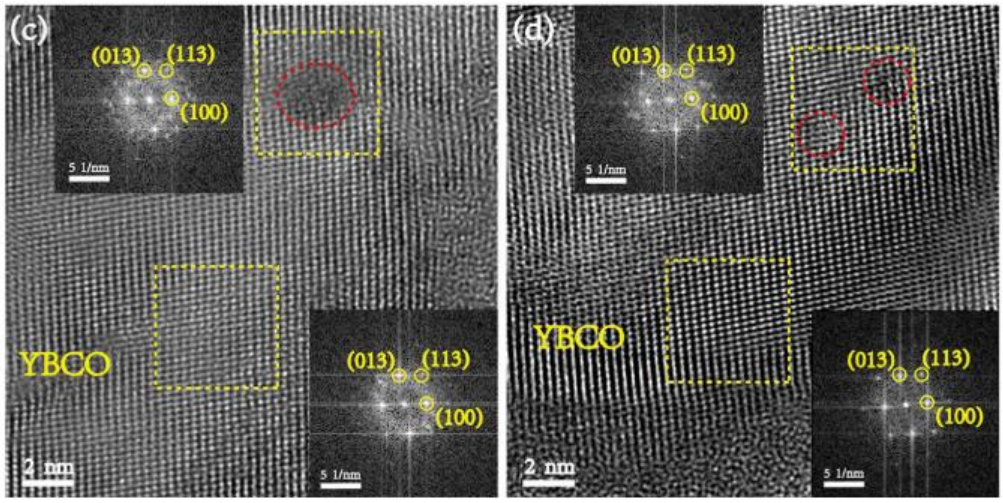


Figure 2.39: HRTEM images taken along [0$\bar{3}$1] zone axis from proton irradiated YBCO films at fluence of to 1×10^{15} cm^{-2}. The irradiation defects are shown in red dashed circles and the insets show FFT extracted from the areas marked by yellow dashed squares [274].

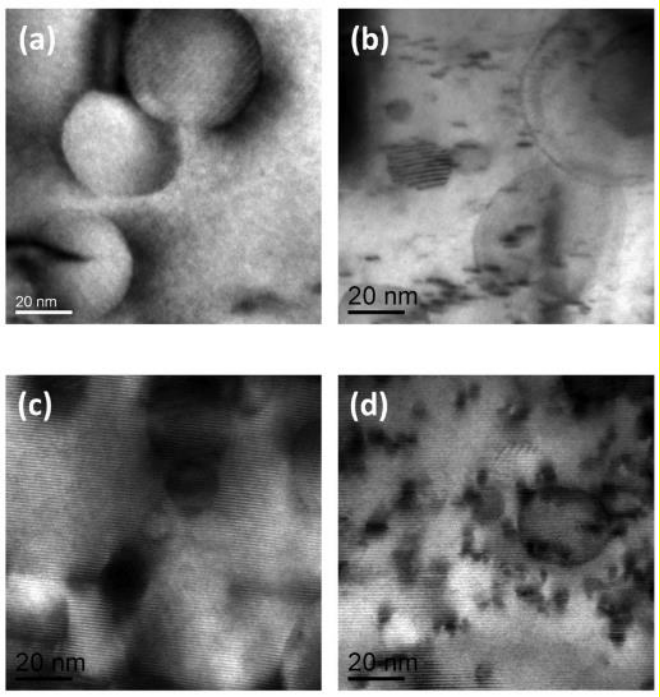


Figure 2.40: TEM/TB g=[200] (bottom row) and g=[002] (lower row) images taken from pristine (a,c) and proton irradiated to 2×10^{16} cm^{-2} (b,d) YBCO superconductor tape. The irradiated images show small defects in higher-contrast that do not show in the unirradiated images. The larger particles are a second phase of Dy_2O_3 [275].

2.2.2.2. Superconducting properties

Irradiation-induced defects have proved to be an effective mechanism for increasing J_c up to a threshold of defect density when J_c begins to deteriorate again, and the superconducting properties can be lost altogether [277]. In order to optimise the superconducting properties it is imperative to understand [253]:

1. The kind of defects, density and distribution.
2. The threshold defect density resulting in maximum J_c.
3. The stability of defects at the operational temperature (and any excursions to higher temperatures during maintenance).

4. Defects formation mechanisms.

The post-irradiation behaviour can be modified by controlling the pre-irradiation defect structure, the irradiation temperature and fluence that controls the density and morphology of the new defects introduced, and the applied field and its direction during the measurement of superconducting properties [95].

2.2.2.2.1. Critical temperature

The immediate consequence of irradiation is a decrease in T_c caused by an increase in point defect density [278], but the precise behaviour is different under proxy ions and neutrons. For neutrons, a linear reduction in T_c with a slope of approximately 3% per 1×10^{22} n/m^2 fluence is reported [37], [95], [279], [280] (Figure 2.41a), but the width of the superconductor/normal transition temperature is unchanged [95]. In contrast, ion-irradiation broadens the transition temperature and the decrease in T_c can be more significant (Figure 2.41b) [252], [277]. Although neutrons and ions fluences cannot be easily compared directly, the reader should appreciate the different T_c behaviour.

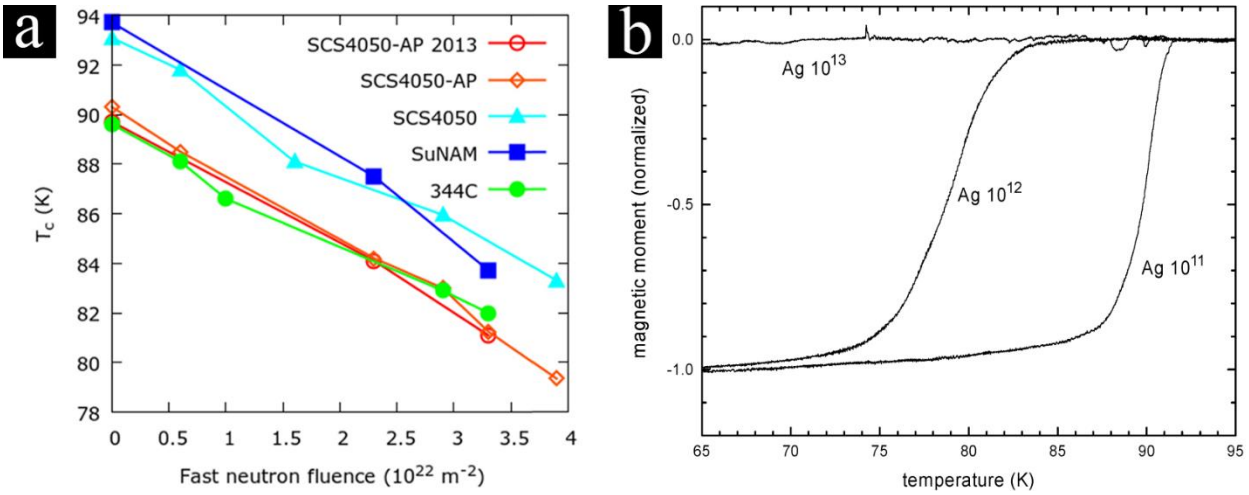


Figure 2.41: (a) Critical temperature (T_c) dependence on neutron irradiation fluence [37], and (b) the broadening of superconducting transition temperature after 74 MeV Ag-ions irradiation to fluences of 10^{11} – 10^{13} cm^{-2} [277].

2.2.2.2.2. Critical current and irreversibility line

Some authors (e.g. [278], [281], [282]) claim that neutron-irradiation introduces, in addition to collision cascades, small defects that are more homogenously distributed. An example of neutron-irradiation is given in Figure 2.42, showing J_c as a function of magnetic field, H, parallel (Figure 2.42a) or perpendicular (Figure 2.42b) to the c-axis. Two effects can be seen. First, J_c decreases slightly after irradiation when $H \parallel ab$ [95] since the irradiation weakens the intrinsic pinning sites (such as stacking faults) of the layered structure. Secondly, J_c generally increases following irradiation but its behaviour varies with operating temperature and applied field, but is more pronounced at lower temperatures due to more effective pinning of small defects [153].

Another aspect is the angular dependence of J_c. Some kinds of irradiation can reduce the anisotropy of the superconducting properties. Neutron irradiation, which is generally non-directional flattens the natural peak of J_c when $H \parallel ab$, and increases J_c across wide range of angles [283]. Strickland et.al. [277], [284] point out that directional ion irradiation shows a small

effect on the J_c peak when $H \parallel ab$, whereas the $H \parallel c$ peak increases in width and magnitude. So it is important when considering irradiation to introduce flux pinning centres to select the pin shape and distribution to match the field shape under which the conductor will be operating.

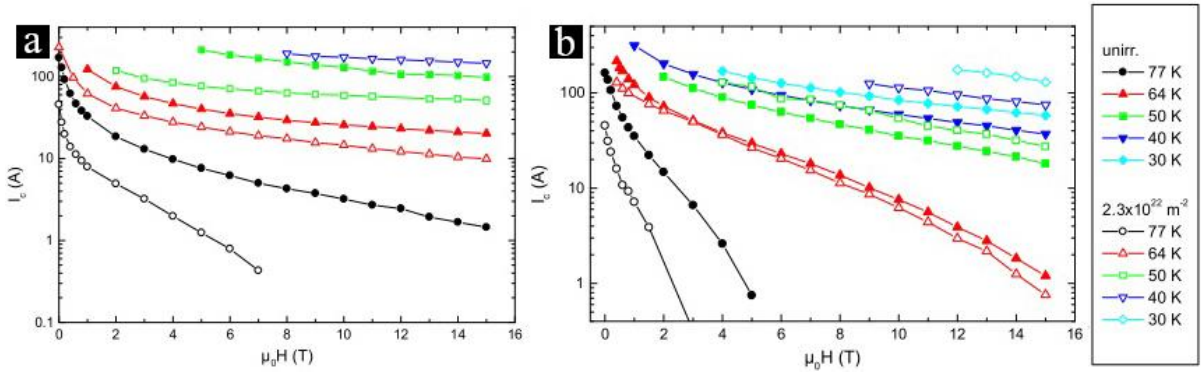


Figure 2.42: REBCO CC before and after neutron irradiation at $2.3 \times 10^{22}\ n/m^2$ *measured with magnetic fields applied (a) parallel to the ab-plane and (b) c-axis* [279].

The irreversibility field (H_{irr}), is another important parameter in assessing superconductor performance, and tends to decline after irradiation mainly due to T_c reduction. Nonetheless, H_{irr} exhibits slightly different slopes compared to the unirradiated superconductor in both field directions. When the field is applied parallel to the c-axis, the slope becomes steeper at low fluence, i.e. H_{irr} improves, and flattens at higher fluence [279], whereas when $H \parallel ab$, H_{irr} deteriorates at all fields and temperatures (Figure 2.43).

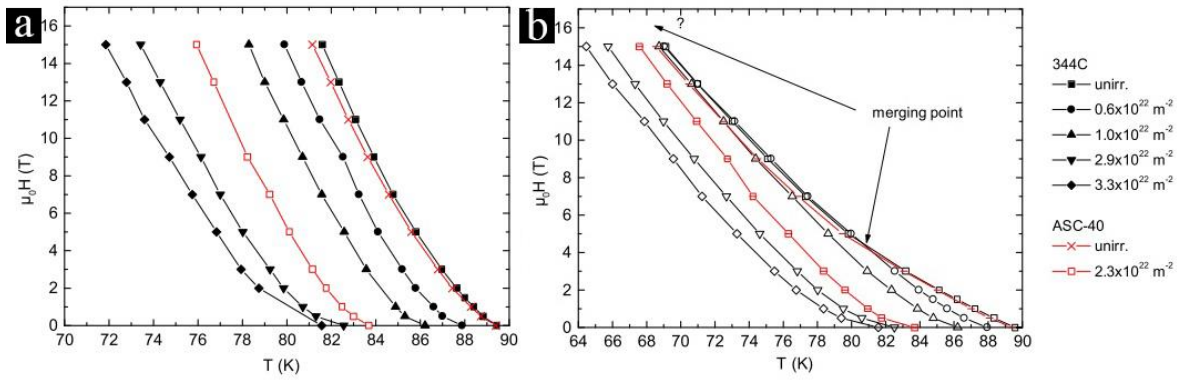


Figure 2.43: irreversibility line before and after irradiation in two types of REBCO CC measured for (a) H||ab and (b) H||c [279].

2.2.2.2.3. The effect of irradiation dose on the critical current

The origin of the initial decrease in J_c is associated with the introduction of new pinning sites, whereas the threshold is seen when a rapid degradation of the superconducting properties occurs due to loss of superconducting cross section as defects overlap [39]. The *optimal dose* is field and temperature dependent [285].

Fischer et.al. [37] identified a striking negative correlation between coated conductor samples containing pre-existing APCs and the optimal dose (Figure 2.44). Under irradiation, the peak in the J_c performance lies at a higher dose in tapes without APCs than in samples already containing APC. Chudy et.al. [278] underpin Fischer's correlation by demonstrating a linear increase of J_c with respect to the total defect concentration, regardless of their origin. This linear increase of J_c as a function of total defect concentration changes in slope when adjusting the

measurement temperature or field due to the different pinning efficiencies of a given landscape of sites under different conditions.

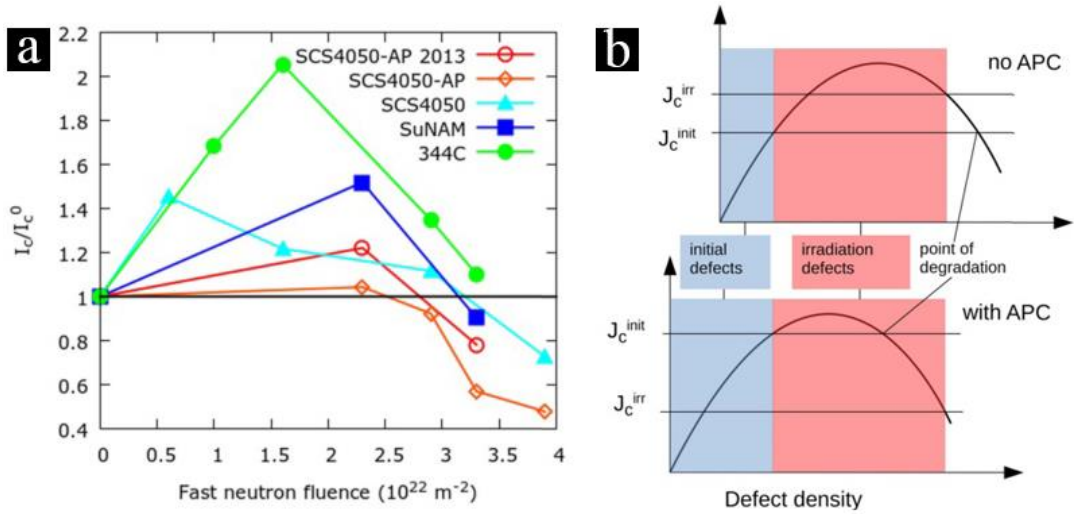


Figure 2.44: (a) J_c dependence on dose for five different REBCO CC measured at 30 K and applied fields of 15 T parallel to the c-axis. The two of them denoted as SCS4050-AP contain APCs. (b) Schematic comparison of J_c as a function of defect density in CC with (upper sketch) and without (bottom sketch) pre-existing APCs [37].

The optimal dose, i.e. when J_c is maximised as a function of fluence, also depends on both the magnetic field and measurement temperature. Leroux et.al. [285] used Dy-doped YBCO tapes and 3.5 MeV oxygen ion irradiation to investigate the effect of dose and temperature on J_c as shown in Figure 2.45a, and reveals increasing pinning efficiency at low temperatures and high fields due to the defects estimated to be ~5 nm in diameter. Figure 2.45c present TEM BF/TB images of the irradiation defects in the REBCO matrix that were not found in the unirradiated sample (Figure 2.45b). Using proton irradiation with similar energy (4 MeV), Jia et.al. [275] showed a steady increase of J_c measured at 27 K as a function of applied field up to twice its initial value at 6 T.

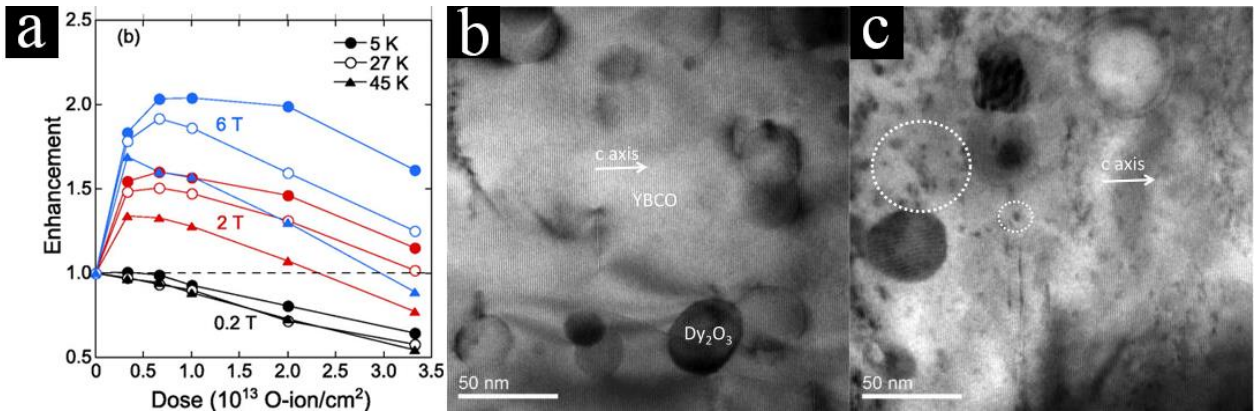


Figure 2.45: Critical current enhancement as a function of 3.5 MeV oxygen ion irradiation and pre- and post-irradiation TEM images. (a) Critical current as a function of irradiation dose at performed at 5, 27, and 45 K, shown by closed and open circles, and triangles, respectively. Pre-(b) and post-(c) irradiation TEM images using (002) BF/TB imaging condition following 1×10^{13} cm^{-2}, 3.5 MeV oxygen-ion irradiation [285].

2.2.2.2.4. Annealing

Annealing irradiated CC with degraded performance is not a panacea that reverses the irradiation damage, but it achieves a partial removal of point defects [278] without recrystallizing the amorphous regions [253], [284], [286]. Petrean et.al. [261] depict the effects of annealing on J_c and the corresponding changes in the structure after heavy ion irradiation. Figure 2.46a-c shows TEM images demonstrating that although the morphology and defect size change after irradiation, namely, "string-of-pearls" morphology (Figure 2.46a) to homogenous cylinder shape with reduced diameter, they do not disappear altogether. The critical current measurements at 10, 45, 77 K show different behaviours. At 10 K, J_c decreases systematically, whereas at the higher temperatures J_c reaches a peak after annealing at 450 ℃ for one hour. Beyond 450 ℃, J_c decreases rapidly. It is also worth mentioning that room temperature annealing has been reported following 2 MeV He-ions irradiation at 40 K of GdBCO CC to be affective in partially reversing

superconducting properties [213]. With regards to neutron-irradiation, a recent paper [287] reports on both T_c and J_c improvement in REBCO CC at annealing temperatures of up to 400 °C.

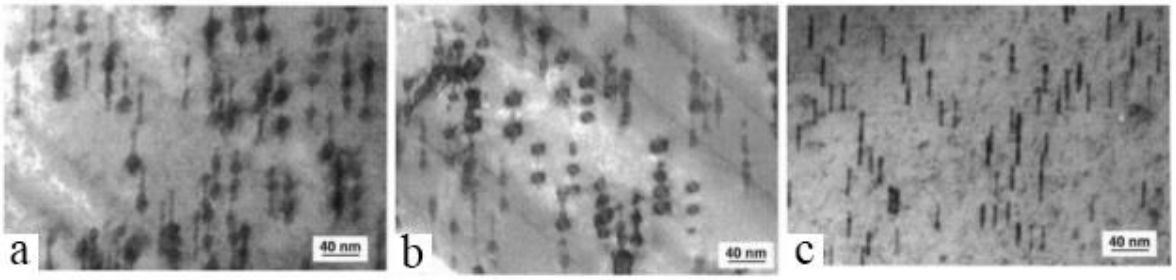


Figure 2.46: (a-c) TEM plan-view images (with ~15° tilt from the c-axis) of YBCO single crystals irradiated with 3.9 GeV Au-ions (a) As-irradiated. (b) After 20 minutes at 420 ℃. (c) After one hour anneal in each stage at 400, 450, 500, 550, 575, 600 ℃. At this stage, the width variations disappeared [261].

2.2.3. Summary

In summary, not many electron microscopy studies have been conducted on neutron-irradiation damage, and the few that have use mainly BF/TB imaging conditions which do not reveal the nature of the nanometer-scale defects. Ion irradiation experiments are more abundant and performed using a wide range of energies and ion-mass. High-energy, heavy ion irradiation produced amorphous tracks a few nanometres in diameter; whereas low-energy, low mass ions generate subtle damage that can be observed using BF/TB conditions. Point defects and small clusters are effectively invisible under TEM. There is still a major gap in our understanding of the lattice damage in between the visible cascades/distorted regions, and a challenge studying them using TEM techniques.

2.3. Introduction to Image Processing Techniques

This section introduces the field of digital image processing. Image processing is used in almost every field of science as can be seen in Figure 2.47, from very basic image manipulation up to the most sophisticated algorithms. The techniques that will be presented in this section aim to illustrate the different approaches exist and do not serve as a comprehensive review, and as needed, the reader will be referred to external references for further reading. The more relevant techniques for the current work will be explained in more detail.

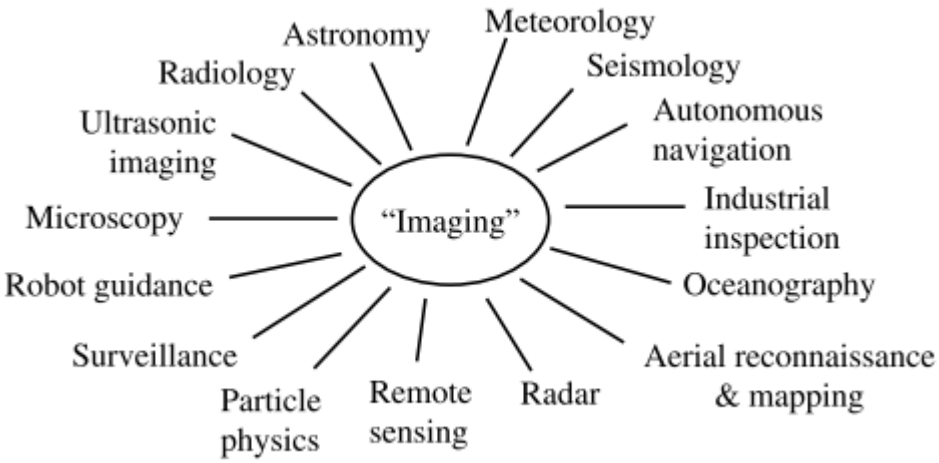


Figure 2.47: Partial list of areas in which image processing is implemented [288].

2.3.1. Image Quality Assessment (IQA)

In a wide range of applications such as image watermarking [289], face recognition [290], image de-noising [291], fingerprint recognition [292] and image compression [293], *image quality assessment* (IQA) is an important and challenging task [294] in an era generating a plethora of visual media content.

IQA can be classified into three main categories; *full-reference IQA* (FR-IQA), *reduced-reference IQA* (RR-IQA), and *no-reference IQA* (NR-IQA) / *blind IQA* (BIQA). The former two

require complete or partial image as a reference in order to evaluate quality, the latter requires no reference image and thus makes it highly desirable since an undistorted reference is usually absent in real-life applications. NR-IQA can then be further broken down into *'distortion-aware'* (DA) and *'distortion-unaware'* (DU) methods. The former requires a prior knowledge on the type of distortion, and is programmed to handle a specific type of distortion, e.g. blur [295]. DU methods on the other hand are more general and allow completely blind image quality assessment.

NR-IQA typically performed on what are called *Natural Scene* images. Natural scene images, in contrast to, for example, artificial images, have certain statistical fingerprints that distinguish them from distorted images. IQAs rely on large databases, such as Live IQA [296], that contain pristine and distorted images with a specific type of distortion. For most image databases, each image is given a *difference mean opinion score* (DMOS) score, which represents the subjective evaluation of image quality. Usually, IQA methods are built to extract certain statistical features that represent the difference between distorted and un-distorted images. The model is then trained to predict the quality score vs the DMOS score. One of the challenges is to capture much more complex real-life distortions referred to as *authentically distorted* [297], and much more can be done in this area with the target of improving the current algorithms.

2.3.2. Image processing classes

In this section, I will focus on image processing main categories used to extract information on the image texture. Image texture is defined as the spatial arrangement of intensities in an image, and represented by texture primitives referred to as texels, which are continuous set of pixels. Texture can be described by two properties, structure and tone, the former represents the mutual

relationship between texels and can be thought of as a spatial distribution, whereas the latter characterises the pixel intensity characteristics of the texel [298]. For example, where texels are large, the resulting texture will be coarse [299]. Tone and texture are always present in any image, although their relative importance varies.

Generally, IQA can be broken into six main categories [300]:

2.3.2.1. Statistical approaches

This basic but widely used and diverse image processing class utilises statistics implemented on the intensity levels in the spatial domain of an image. They represent the texture indirectly by a set of statistical measures based on the relationships between the grey levels in an image. The statistical order of a given method is determined by the number of pixels defining a local feature, classified into first-order, second-order, and higher-order statistics. First-order statistics considers one pixel without investigating its relationship to adjacent pixels, second-order statistics use only nearest neighbour pixels with respect to a given pixel, and lastly, high-order statistics have more than one adjacent pixel. A partial list of methods includes gray level co-occurrence matrix approach (GLCM) [298] (see Figure 2.48 as an example), grey level run-length matrix (GLRLM) [301], local binary pattern (LBP) [302], autocorrelation [303], local energy pattern [304], variogram [305], shape index histograms [306], and deterministic walk [307].

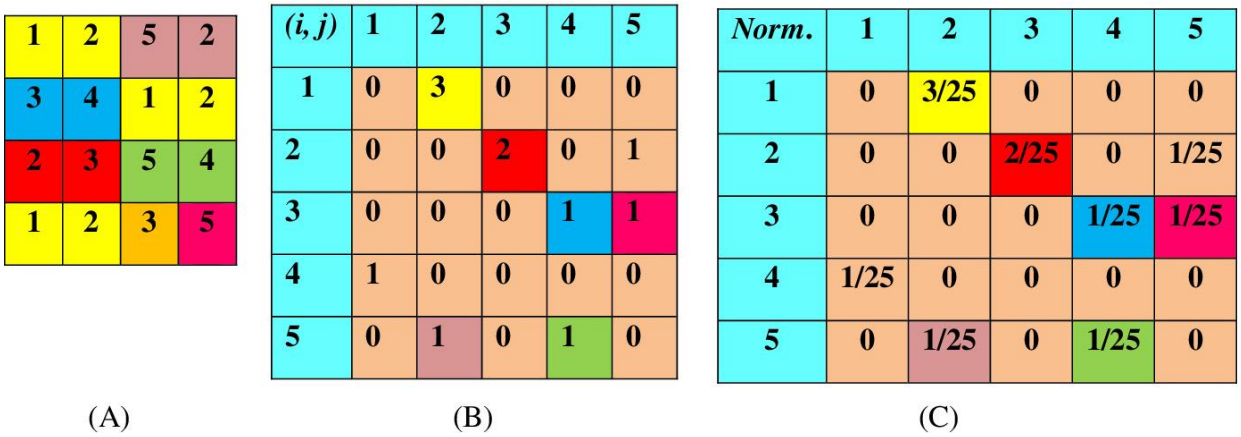


Figure 2.48: An example of gray level co-occurrence matrix approach (GLCM). (a) A 4X4 pixels input image, where each pixel represents intensity. (b) GLCM matrix corresponds to shift vector d=(1,0). The values in the co-occurrence matrix are the number of pixels having gray levels i and j and separated by d, mathematically defined as $n_{ij} = P_d[i,j]$. For example, the co-occurrence matrix in position (2,5) and d=(1,1) counts the number of occurrences where the first gray-tone in a location of (i,j) ((2,5) in this example) has the value of 2 and the second gray-tone in the location of (i+1,j+1) has a value of 5. The non-light brown colours correlate to the number of repetitions of intensity i in (0,0) location and intensity j in (1,0) location in the input image (a). (c) normalisation of GLCM matrix (b) by the total size of the matrix [308].

2.3.2.2. Structural approaches

As mentioned, primitives are represented by structure and tone. To describe a texture, one must first define the texture primitives and placement rules. The choice of primitives depends on the image and task in hand, and some examples could be gray level peaks, line segments, etc. To identify the primitives, different algorithms can be applied, for example, boundary detection methods are analysed via *difference of Gaussian* (DoG) [309], *Laplacian of Gaussian* (LoG) [310], and phase congruency [311]. The placement rule is in simple words the repetition of a primitive that can be either periodic (like in fabric) [312] or random [313]. The structural approaches give a symbolic representation and can be further analysed by probabilities and distributions as explained in the statistical approaches (section 2.3.2.1), for example, variance of primitive distributions [314]. An example of one implementation can be seen in Figure 2.49 which is based on image gradients [314].

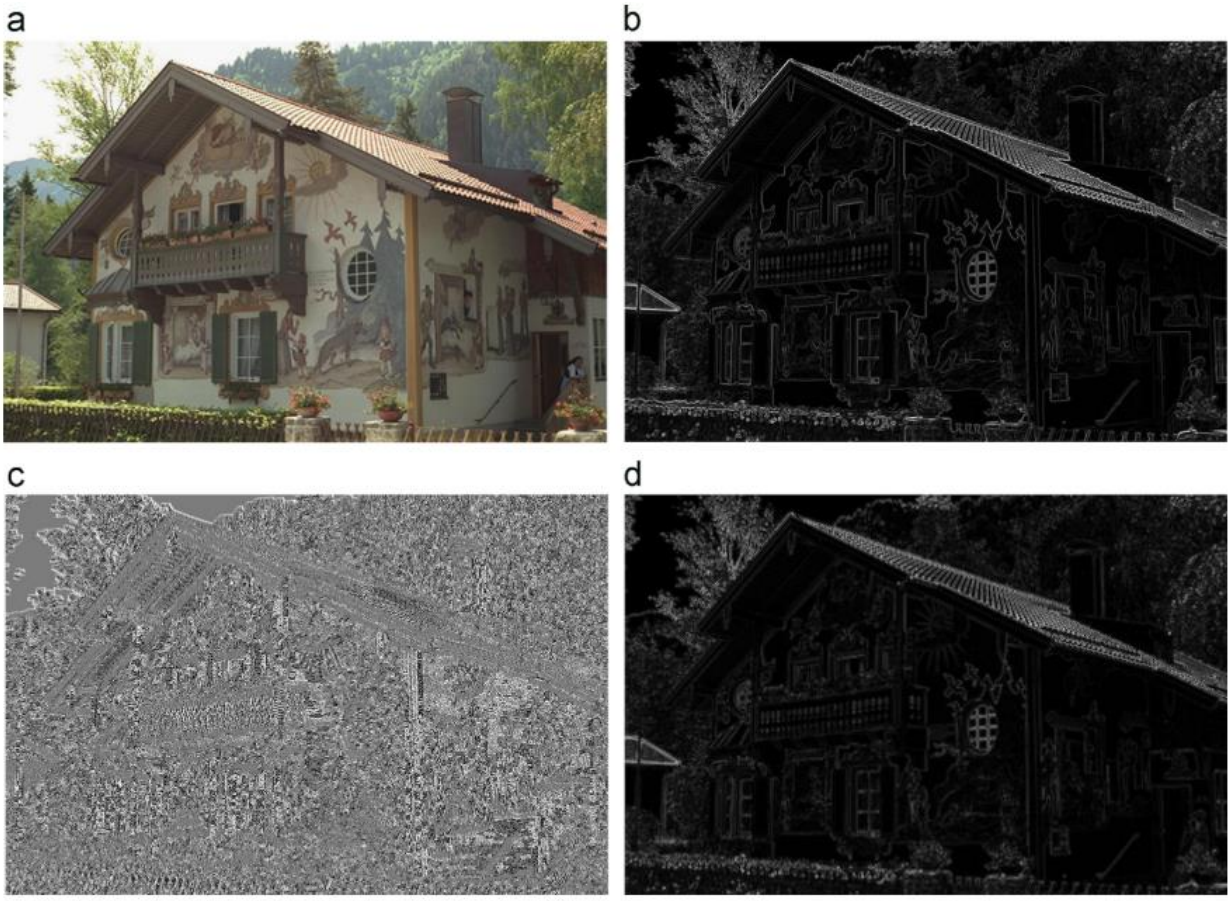


Figure 2.49: An example of gradients and relative gradients maps performed on an undistorted image (a). (b) gradient magnitude, (c) relative gradient orientation, (d) relative gradient magnitude [314]*. Distortions affect the statistics of the three maps in a different manner, and in order to capture these differences the authors calculated the variance of every map in 2 scales (6 features in total) and show a promising correlation to DMOS results.*

2.3.2.3. Transform-based approaches

Image transformation is a mathematical operation carried out on an image. Similar to the previous approaches described, transform-based approaches also use the statistical signature of an image to analyse the texture such as energy [315], entropy [316] or histogram [317]. The most abundant and useful transformations are *Fourier transform* (FT), *discrete cosine transformation* (DCT), and wavelet decomposition.

2.3.2.3.1. Fourier transform (FT)

The *Fourier transform* (FT) translates a function from the time/space domain to a function in the frequency domain [318] and is represented by complex exponential wave functions. The faster algorithm, the *fast Fourier transform* (FFT), was introduced in 1965 [319] and is much more computationally effective. The 2D FT function is characterised by two frequencies (measured by cycles/pixel), which represent the oscillation along orthogonal directions, which can then be used for image texture analysis in terms of radial frequencies and orientation [320]. Frequency is inverse to the space domain and thus a smooth image is characterised by low frequency components that manifest larger intensities near the zero frequency origin (usually the centre of the image), whereas high frequency parts are represented by intensities far away from the FT origin. Analysing texture using FT is especially powerful when applied to periodic texture classifications [321] and for determining the anisotropy of surfaces [322].

Another useful application of FT is to deliberately remove radial or orientation image frequencies using the inverse Fourier transform after multiplying the FT coefficients matrix with a binary mask that preserves the desired frequencies, as can be seen schematically in Figure 2.50.



Figure 2.50: Radial Binary masks for preserving the low (left) medium (middle) or high (right) frequency components. Black pixels represent the value '1' and white '0' [320].

2.3.2.3.2. Discrete cosine transformation (DCT)

The *discrete cosine transformation* (DCT) was first introduced in 1974 [323]. The underlying idea of DCT is that every signal can be represented by a sum of cosine functions, where the number of cosine functions is equal to the length of the signal. For example, 8×8 2D signal is represented by a sum of 64 cosine functions (known as coefficients). Figure 2.51 shows an example of DCT basis signals on a 8×8 matrix, it can be seen that these cosine functions oscillate with increasing frequencies from (0,0), which is situated in the upper left side, in horizontal and vertical directions. The (0,0) coefficient is called the *direct current* (DC) coefficient and does not represent the texture of an image since it is essentially flat and thus determines the overall intensity of the whole image. The other DCT coefficients in the matrix are a product of the respective horizontal (row 1) and vertical (column 1) basis functions, similar to the multiplication matrix. To represent any 8×8 image (as for this example), each of the DCT coefficients (namely, the matrix cells), is weighted according to its relative contribution to the overall image. So in practice, one get a summation of cosine functions with different frequencies and directions, where each is multiplied by its relative weight.

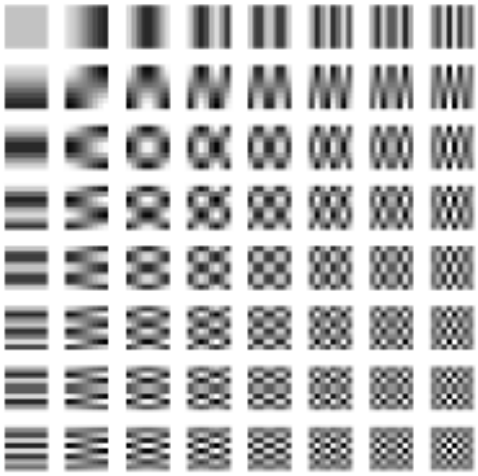


Figure 2.51: Discrete Cosine Transformation basis signals of size 8×8 [324].

2.3.2.3.3. Wavelet Decomposition

The idea of wavelets, which based on Fourier transformation of analysing signals in the frequency domain, was first introduced by A.Haar [325] in 1910 but it was not until the 1980's that they were used for signal processing [326] and has wide-array of applications such as fingerprint data storage [327], image compression [328], edge detection [329], noise reduction [330], and fusion of images [331]. Signal transformations are represented by their basis functions: FT uses sines and cosines and DCT uses cosines. A wavelet, on the other hand, has infinite number of wavelets choices, i.e. basis functions, that can be used for specific applications [332], [333]. These were called Mother Wavelets [332] (see Figure 2.52c), and one can notice that they exist locally and thus allow a local analysis of signals, which is shown for 1D signal in Figure 2.52a-b. Further details on this transformation is beyond the scope of this thesis and the reader is referred to other sources [334]–[336].

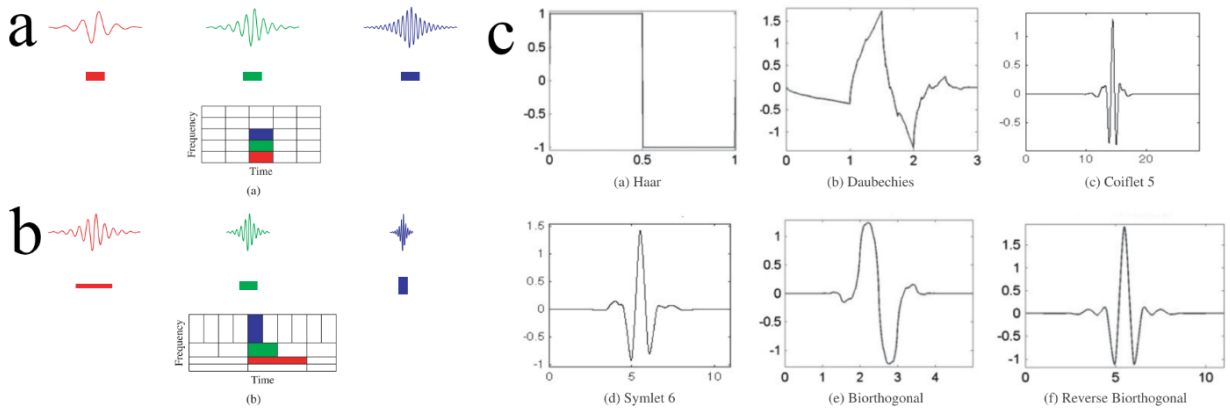


Figure 2.52: An illustration of short-time Fourier transform (STFT) and wavelets characteristics when applied to 1D signal that changes over time and type of mother wavelets. (a) STFT analysis shows a constant window size both in frequency and time, (b) Wavelet windows sizes show an inverse proportionality of time and frequency [336]*. (c) Examples of six types of wavelets families* [337]*.*

2.3.2.3.4. Other transforms

Other image transformations exist and are also being developed but are outside the scope of the current work. Some examples include Laplacian pyramid [338], contourlet transform [339] Laws texture energy measures [340], Gabor filters [341], shearlet transform [342], and curvelet transform [343].

2.3.2.4. Model-based approaches

Model-based approaches for texture classification are based on mathematical models that try to pre-define the texture using parameters. A detailed explanation of these approaches is beyond the scope of the work in this thesis and further details on several approaches such as 'fractional dimensions' [344] Autoregressive [345], [346], gravitational [347], complex network [348], Wold decomposition [349], and mosaic models [350], can be found in the accompanied references.

2.3.2.5. Learning-based approaches

Deep learning methods for image classification and texture classification has been heavily researched in recent years. They are based on the idea of *neural networks* (NN) of the human brain (or more generally in biological systems) where each neuron is connected to other neurons to form a complex hierarchical groups of neurons with similar functionally to process information in several steps [351]. Similarly, a*rtificial neural networks* (ANN) each 'neuron' represents a mathematical function as part of architecture that consists of several layers of information processing [352]. This multilevel nonlinear information processing was proven to be robust compared to traditional feature descriptors extraction. ANN methods are commonly used for image classification but were recently also adapted to texture recognition [353]–[355] and has a great potential in the years to come.

2.3.2.6. Entropy-based approaches

Shannon entropy was first proposed in 1948 [356] and is a key measure in a sub-branch of mathematics called *Information Theory*, which studies communication and digital information. Entropy is a common measure of uncertainty, or equivalently the amount of information present in a signal/image. Consider a signal S consisting of n individual components s_i {i=1,2,3,…,n}, the entropy H is measured as follows:

Equation 2.6: $H(S) = -\sum_s P(s_i) * log_2(P(s_i))$

where $P(s_i)$ is the probability of the component s_i and $\sum_i P_i = 1$. In other words, entropy measures the ability to predict the value of each one of the s_i components. If the ability (=probability) to correctly predict the s_i value is low, i.e. there is more uncertainty in the signal,

the entropy rises and one concludes that the signal contains more information. For example, an image that contains a background such as blue sky with minimum detail has a narrow probability distribution (since the range of colours is limited) and thus carries less information. On the other hand, an image with many details and different colours (e.g. a city scape) has a broader probability distribution and higher entropy. Entropy is a robust method that can be used to spot irregularities in periodic structures [357], [358], or for the purpose of texture classification [359], [360].

Although Shannon entropy was a milestone in information theory it is not the first entropy measure proposed. The term entropy was first coined in the 19th century and was applied to thermodynamics. Since then, a wide range of entropy types (see Figure 2.53) have been defined and have been used in various applications. The different types of entropies show high degree of similarity to one another and their aim is to quantify the uncertainty in a system [361].

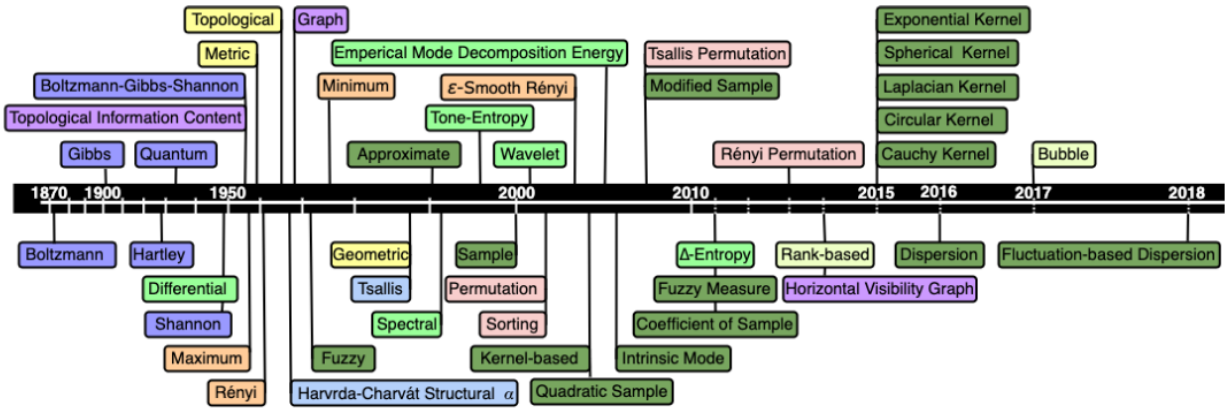


Figure 2.53: Different types of entropies on a logarithm time scale. The colours presented represent the sections in which these entropies are discussed in the original publication [361].

In a frequency domain, it is common to analyse signals using a power spectrum (also known as power spectral density), which represents the power of a signal computed as the amplitude squared as a function of frequency. An entropy measurement derived from Shannon entropy was

first proposed by Kapur et.al in 1992 [362] and named *Spectral Entropy*, which aims to quantify the spectral complexity of a system. The mathematical representation is identical to Shannon entropy but computed on the power spectrum instead of probability density distribution. As a consequence, high spectral entropy is characterised by a broad distribution of the power spectrum, whereas low spectral entropy has narrower distribution and thus more predictable signal [363].

As showed by Liu et.al. [316], different types of distortions not only change the entropy of an image but also change it in a predictable way that allows categorisation of the type of distortion. The authors developed a methods called the spatial-spectral entropy-based quality (SSEQ) index that divides the image into 8×8 blocks of pixels taken from 29 reference images and 799 distorted images by 5 types of distortions [296], and extracted the Shannon entropy from the spatial domain and spectral entropy from the DCT domain. As shown in Figure 2.54, entropies from both domains carry unique statistical characteristics, which is an indication for the type of distortion. After calculating the entropy values from the 8×8 blocks, 60% percentile pooling from the centre (i.e. excluding the 20% from both extremes) was used. Percentile pooling is a known method that ensures that poor quality regions will not disproportionately affect the subjective quality measure [364]. Lastly, a 3×4 feature matrix was extracted and included the mean and skewness values of the spatial and spectral entropies in 3 subsampling steps and underwent two-stage framework [365] to extract a quality score. Cui [366] presented the same approach for spatial-spectral entropy calculations on 8×8 pixel blocks in three scales.

Other methods were explored by Gabarda and Cristóbal [367] based on the argument that noise cannot be distinguished from information and renders entropy features a poor indicator for image quality. Instead, they used the normalised *pseudo-Wigner distribution* (PWD) [368], which is an

approximate form of the *probability distribution function* (PDF) but computed along 1D only, to represent the anisotropy in an image as a better proxy for image quality. Rényi entropy [369] was then calculated at the pixel-level. In [370] Gu et.al. hypothesised that high contrast images convey more information and thus have higher quality. They combined autoregressive model to estimate and remove the predictable parts in the image and then performed entropy calculations on the unpredictable parts as an evaluation of image quality.

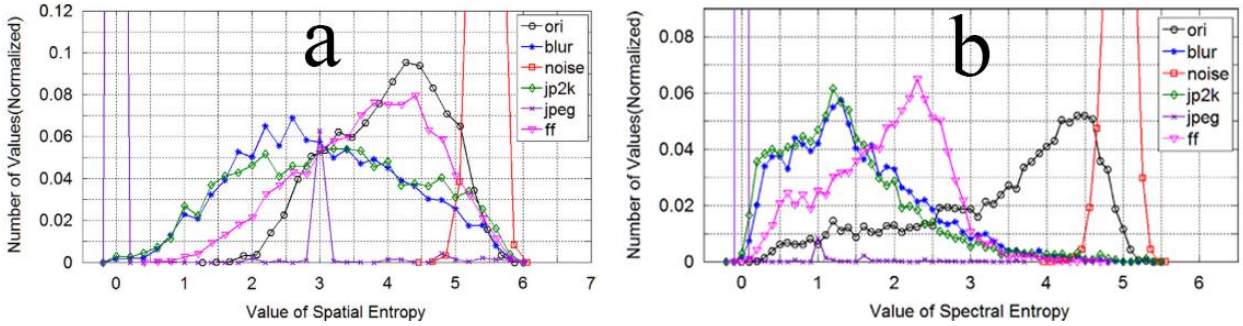


Figure 2.54: Histogram of spatial (a) and spectral (b) entropies derived from 8×8 pixel blocks taken from reference images (ori), Gaussian blur (blur), white noise (noise), JP2K compression (JP2K), JPEG compression (jpeg), and fast Rayleigh fading (ff) [316].

2.3.3. Image processing in Transmission Electron Microscopy

To the best of my knowledge, no attempts have been made to quantify irradiation damage, or more generally, HRTEM image quality, using one or more of the image processing classes described above. However, like in many fields, image processing is crucial in materials science in general and electron microscopy in particular. In this short summary, I will present selected examples of image processing applications.

The transformation-based FFT method is one of the most utilised tool in HRTEM/STEM applications. In a highly-cited article, Hÿtch et.al. [371] presents the *geometric phase analysis* (GPA) to quantitatively measure strain fields in a given region compared to a reference region.

Although the mathematical description of this method is beyond to scope of this work, the fundamental idea is simple. First, the reciprocal displacement vector is determined as the difference between the reference and target region, then, it translates to the displacement in the real space, and lastly the strain fields are calculated by taking the derivative of the displacement fields [372]. The *inverse FFT* (IFFT) function is used to isolate specific frequencies after applying a mask on the FFT images. The isolation of frequencies can help detecting stacking faults and dislocation loops [373], [374]. Additionally, FFT is a good tool to get an information on the local degree of crystallinity and detecting amorphous regions that manifested in the presence of amorphous halo [375].

Manipulation of images in the real space can be performed using several methods. Nikishin et.al. [376] used the learning-based (see section 2.3.2.5) approach of neural network on TEM images for automatic detection of the cup-shaped, extracellular vesicles with a diameter of at least several dozens nanometres. Other learning-based classification methods have been applied to identify crystalline regions on an amorphous background from HRTEM micrograph using a combination of *convolutional neural network* (CNN) [377], quantifying nano-particles location, densities, and sizes from the highly noisy *Environmental TEM* (E-TEM) images using machine learning [378], and automatic detection of He-bubbles of irradiated Ni-based X-750 alloy from TEM images using CNN [379], among others.

In conclusion, although this section does not aim to be an exhaustive list, it gives a taste of the possible usage of image processing in electron microscopy. As can be schematically seen in Figure 2.55, machine learning methods are on the rise in recent years and this trend is likely to continue as models improve and develop.

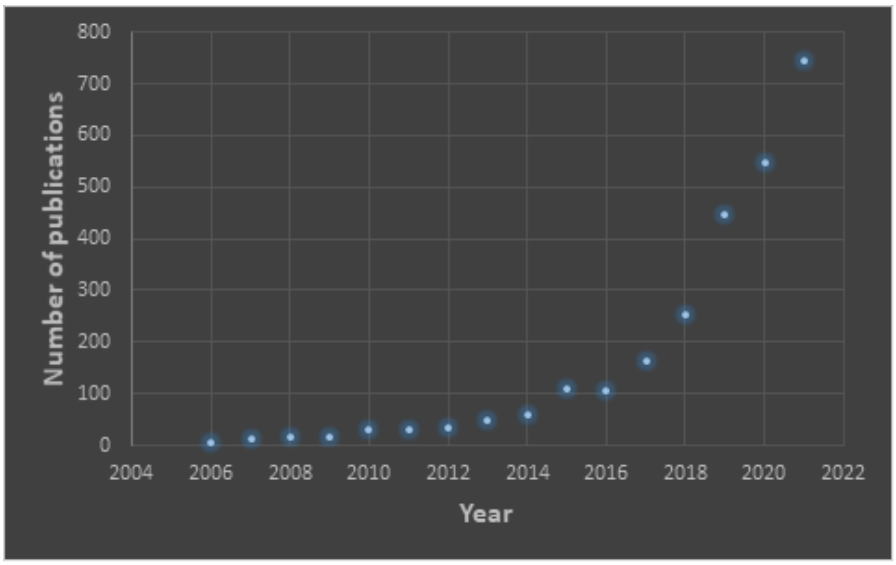


Figure 2.55: number of publications per year that include the keywords "machine learning" and "microscopy" in the title/abstract/keywords, as collected from Scopus.

3. Materials and Experimental Methods

This chapter gives an overview of the materials, instruments, experiments and data analysis used in the current study. The first and second sections present the materials and the preparation techniques carried out to make samples suitable for TEM analysis, which was the primary characterisation tool used throughout the thesis. The third section discusses TEM imaging techniques and the associated characterisation methods. Section four describes the design of in-situ TEM experiments carried out at the University of Huddersfield. Lastly, section five details the data analysis techniques developed to extract quantitative data from TEM images.

3.1. Materials

3.1.1. $REBa_2Cu_3O_{7-x}$ (REBCO, RE = Rare Earth) tapes

REBCO superconductors tapes are commercially produced by several companies, including American Superconductor Corporation (AMSC), Bruker Corporation, Furukawa Electric, and Fujikura Ltd. Although the general structure described in Section 2.1.2.1 of a stack of CuO_2 conducting layers separated by insulating, charged reservoir layers along the c-axis is virtually the same in all these materials, they differ in their choice of rare earth element(s), tape architecture and the nature of the artificial pinning centres (APCs) that they contain. Hereafter, all the samples described are produced by SuperPower Inc, unless stated otherwise. The architecture of the SuperPower tapes is shown in Figure 3.1. The rare earth (RE) site in the specific SuperPower REBCO tape analysed throughout the thesis contains 50 at.% Y and 50 at.% Gd, except for the neutron-irradiated tapes that contain 100% Gd.

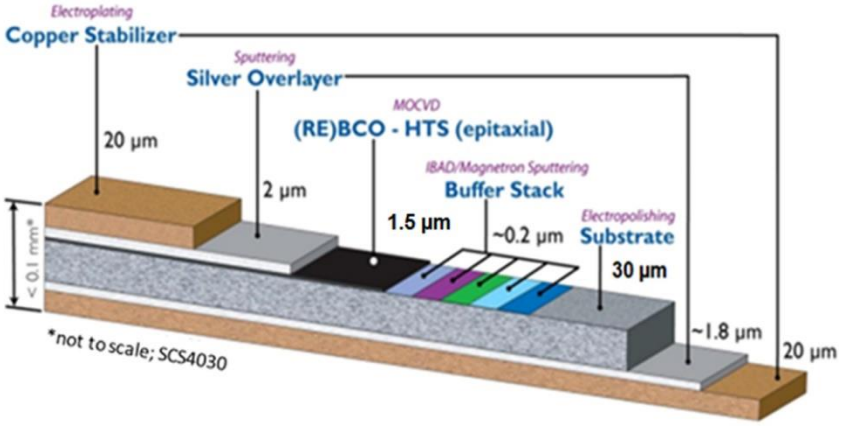


Figure 3.1: Layered-structure of SuperPower's REBCO Coated Conductor [126].

3.1.2. Neutron-irradiated samples

The samples used for this study were shielded with cadmium foil to absorb the thermal neutrons (E_{kin} < 0.55 eV) and irradiated in the TRIGA MARK II reactor at the Atominstitut, Vienna, to a cumulative fluence of 3.3×10^{18} cm^{-2} [37]. The neutrons have a range of energies from fractions of eV up to 15 MeV [192], where fast neutrons (E_{kin} > 0.1 MeV) comprise 36% of the neutron energy spectrum. After irradiation to this fluence, the J_c value is reduced by about 30% from its initial value, namely, from 89.5 A down to 62.7 A, see Figure 2.44a (section 2.2.2.2.3) [37]. As a reference, I was also given un-irradiated samples from the same manufacturing batch. The sample that was chosen underwent the highest cumulative fluence and was allowed enough time to reduce its activity levels to below the useable threshold according to *International Atomic Energy Agency* (IAEA) transport regulations, which classifies the threshold as 4 Bq × cm^{-2} beta and gamma radiation and a dose rate of 0.005 mSv/h. Using the most damaged sample with 30% degradation in J_c ensures that damage is present, which is what I aim to study.

3.2. Sample preparation

This section details the preparation of TEM samples from the initial ~100 µm thick superconducting tapes by undertaking two main steps; exposing the superconducting layer and TEM lamellae preparation.

3.2.1. Etching REBCO protective layers

As seen from Figure 3.1, the ~100 µm thick REBCO tapes contains a ~1 µm thick ceramic superconducting layer which carries the electrical current. The superconducting *region of interest* (ROI) layer is 20 µm below the tape surface, underneath protective coatings of Ag (~2 µm) and Cu (~18 µm). To make the TEM sample preparation easier I etched away these protective layers using chemical solutions.

The wet etching process was performed in two steps as described in [380]. The first step was to remove the copper layer by using $FeCl_3$ solution (60 g $FeCl_3$, 100 g Deionized H_2O), which formed a porous AgCl layer that was removed, with any remaining metallic Ag, in a 1:1 solution of 30% aqueous solutions of H_2O_2 and NH_4OH. Figure 3.2 demonstrates (a) the removal of Cu and Ag envelopes after etching and (b) the REBCO tapes in different stages of etching after it was submerged sequentially in $FeCl_3$ and H_2O_2:NH_4OH solutions. Once exposed, the REBCO tape was kept in a dry air environment [270].

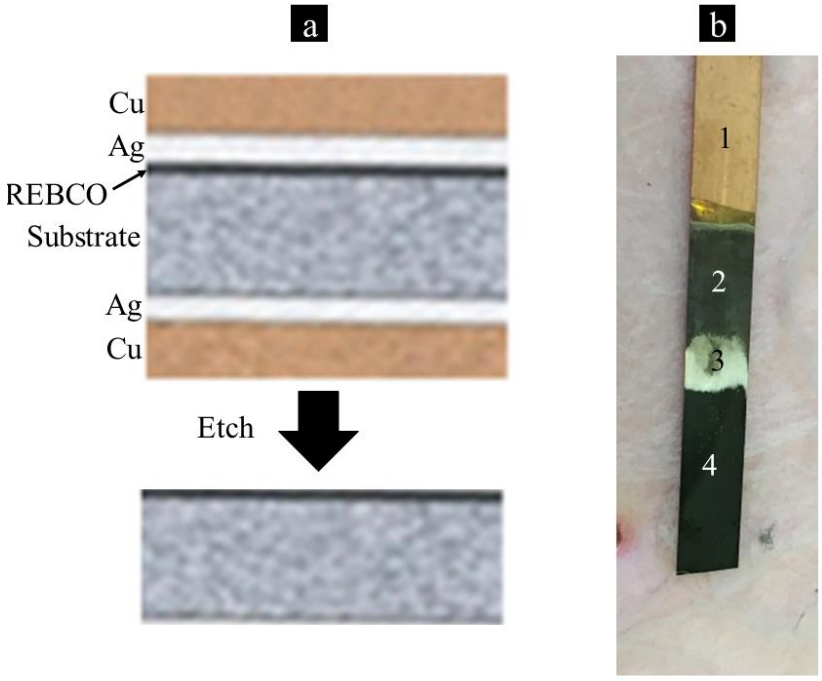


Figure 3.2 REBCO tape etching process. (a) cross sectional optical images of SuperPower CC layers before (top) and after (bottom) etching process. The etching removes Cu and Ag from both sides of the tapes and leaves the ~ 1 µm thick superconducting layer (black) on top of the substrate. (b) A piece of REBCO tape before and after etching. 1: un-etched Cu layer; 2: REBCO layer after exposure to $FeCl_3$; 3: By-products appearance after etching for insufficient time with $FeCl_3$ and H_2O_2:NH_4OH solutions; 4: exposed REBCO layer after allowing enough time to be etched with H_2O_2:NH_4OH. The image in (b) was kindly provided by Dr. Will Illife.

3.2.2. TEM lamellae preparation by Focused Ion Beam milling

TEM sample preparation from a bulk sample is a destructive technique that entails removing material to make selected regions transparent to electrons. Transparency varies between different materials but as a rule of thumb can only be achieved when the sample thickness is less than a few hundred nanometres. There are a wide range of TEM sample preparation techniques [381]–[383], but over the past 20 years it has been shown that *focused ion beam* (FIB) techniques have many advantages such as site selection, the ability to image while the milling is carried out and

precise control of the lamella thickness [384]. In the current project, the TEM samples were all prepared using FIB.

For the TEM lamella lift-out, I followed the standard procedure of a cross-section TEM sample preparation presented in [385]. The lift-out process steps for a sample with Cu and Ag protection layers can be seen in Figure 3.3. The main differences in preparation steps for an exposed sample compared to an Ag/Cu coated sample are the pre-deposition of protective Pt layer with a typical volume of 20×2×1 μm^3 in order to protect the TEM lamella from FIB damage, and shallower trenches, ~20 µm in depth since the superconducting layer is not buried within the volume of the tape. The accelerating voltage throughout the sample preparation was kept constant at 30 kV and was only reduced at the surface cleaning stage. The surface cleaning is undertaken from a lamella thickness of about 100 nm until the desired thickness is achieved using a current of 80 pA and low-energy 2 kV in order to remove FIB damage from previous stages while introducing as little new damage as possible.

After the Pt deposition (for exposed REBCO), two 25×20 μm^2 trenches from both sides of the ROI are milled. Then, milling of the side and bottom part ('undercut') of the lamella uses a current of 3 nA (see arrows in Figure 3.3a). Figure 3.3c shows the stage where the micro-manipulator is attached and welded with Pt to the corner of the lamella; then the other side of the lamella was milled away. At this stage, the lamella is detached form the bulk sample and ready for lift-out. In Figure 3.3d the lamella is positioned to the side of the Omniprobe grid middle pole and then welded using Pt. Lastly, the needle was separated using a current of 1.5 nA, as can be seen in Figure 3.3e.

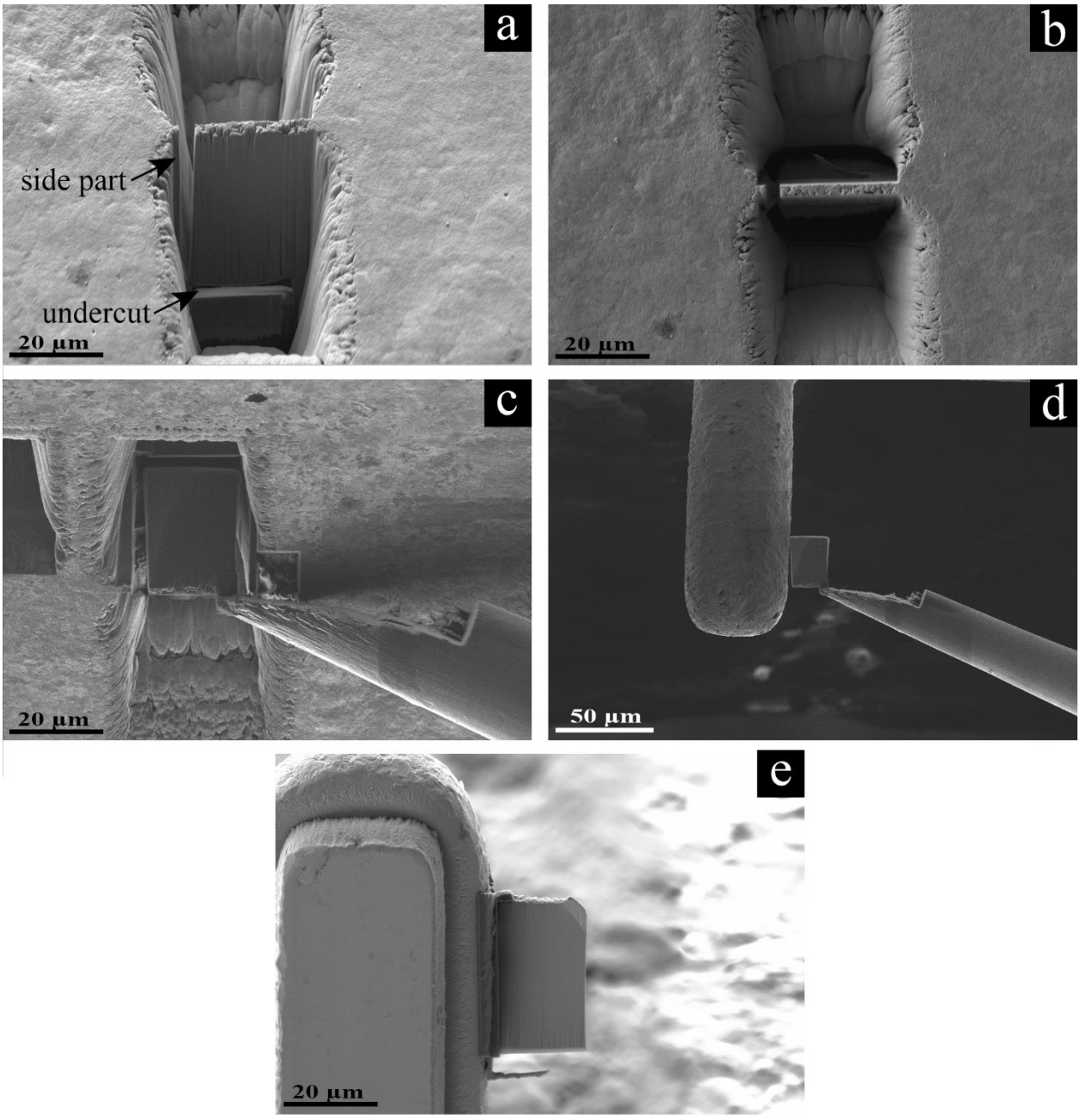

a
side part
undercut
20 µm
b
20 µm
c
20 µm
d
50 µm
e
20 µm

Figure 3.3: Scanning electron microscope (SEM) images showing the TEM lamella lift-out process. (a-b) Lamella ready for liftout including undercut viewed at 54° and 0° tilt, respectively. The Ga^+ current is gradually decreased when getting closer to the desired thickness of the future lamella, 13 nA, 3 nA, and 1.5 nA, at the distances of >5 µm, >3 µm, and <1 µm, respectively. (c) Needle is attached to the lamella at the stage where it is detached from the bulk sample. (d) Lamella is attached to the Omniprobe grid pole. (e) Deposition of Pt welds the lamella to the grid and the needle separated, and from this stage the lamella will undergo several thinning steps to reach to about 100 nm thickness using decreasing currents down to 80 pA before the last step of low energy surface cleaning.

Generally, this lift-out process of cross-sectional TEM foils does not vary much from sample to sample, however the final thinning and low energy surface cleaning steps, i.e. the steps where thickness is reduced to about 40-100 nm, was adapted according to the nature of the characterisation work that is planned, as well as the sample material reaction to Ga^+ ion bombardment that can introduce extensive lattice damage [386], [387]. In the current study, the main characterisation modes were HRTEM and STEM, and both require as-thin-as-possible samples. According to my experience in this project however, REBCO materials are susceptible to FIB damage created by the Ga^+ ions, even at low energies, and thus limits the option for a long surface cleaning to achieve the desired thickness throughout the superconducting layer. I chose low energy surface cleaning using 2 kV 250 pA Ga^+ ions for about 2-3 minutes from each side, which is enough to remove surface damage created prior to this step with introducing only a few nanometers of new damage from both sides of the lamella.

HRTEM images of a pristine, unirradiated sample and the corresponding FFTs can be seen in Figure 3.4. As a reference, Figure 3.4c shows what I consider as a pristine sample and FFT with

little sign of FIB damage. The samples were prepared following identical procedure. Both Figure 3.4a-b images show a weaker contrast compared to a non-damaged sample, best recognised by the contrast of the individual atomic columns, but this is a very subjective observation. The corresponding FFTs, taken from selected areas of the crystalline regions, avoiding the $BaZrO_3$ APCs that show strong Moire fringes in these images, are shown in the insets and have more clearly defined differences. Image (a) shows many fewer diffraction spots, and there is a clear amorphous halo in (b); whereas in (c) the FFT contains a large number of diffraction spots to higher order planes (what will be defined below as the high-frequency components) and only a very weak amorphous halo.

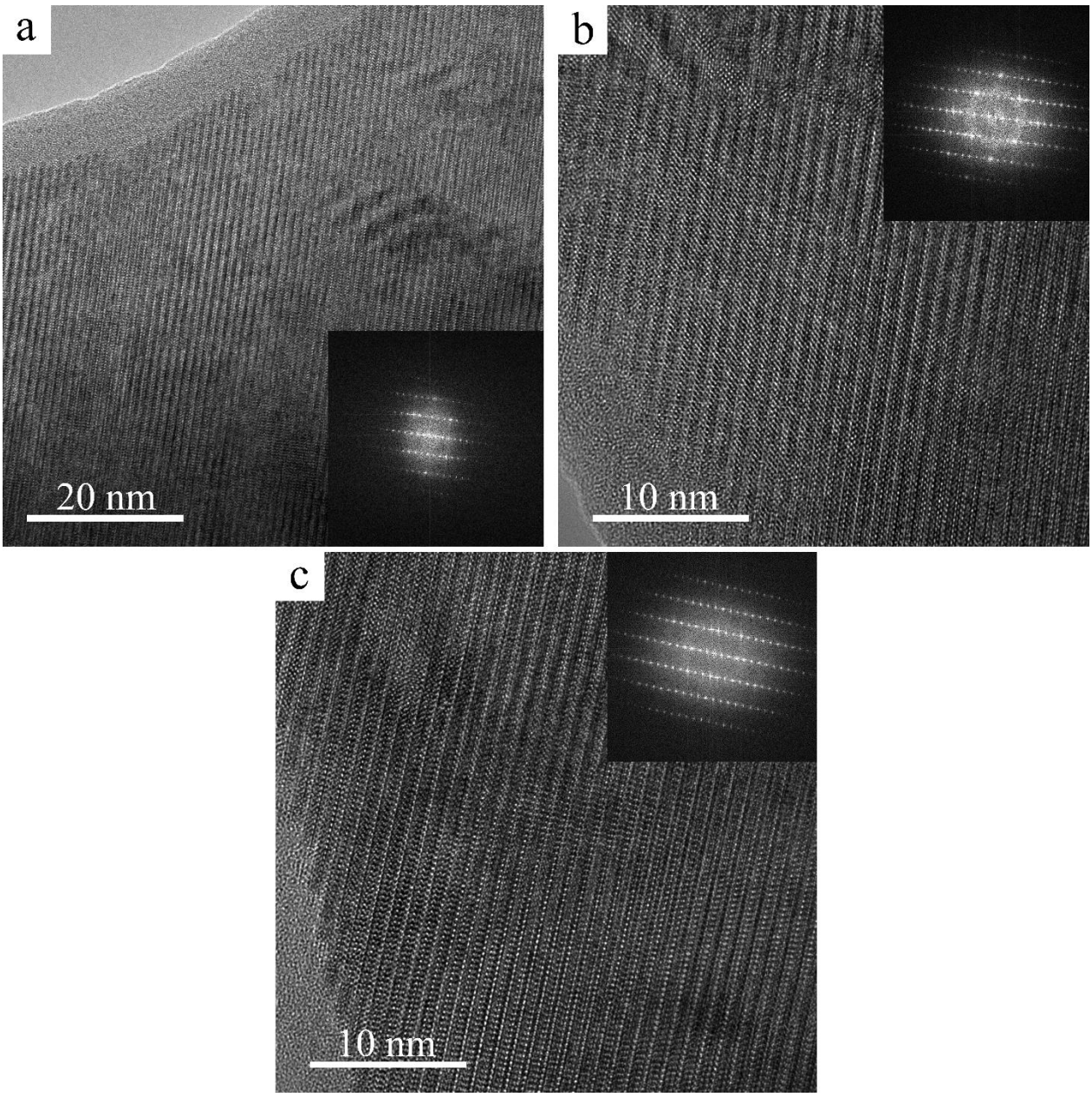


Figure 3.4: HRTEM images taken along [100]/[010] zone axis and at magnifications of (a) 600K and (b,c) 1.2M from pristine samples to illustrate the problems of FIB-induced damage. The corresponding local FFTs taken from the crystalline regions are shown in insets. (a) and (b) show less well defined atomic columns compared to a non-damaged sample (c), and the FFT images show fewer spots at high-frequencies (a) and a faint amorphous halo (b).

In order to allow the preparation of wide TEM lamella like that shown in Figure 3.5, a much thicker part is deliberately left in the middle of the lamella for mechanical support. This allows the successful lift-out of lamellae around 20-25 µm in width (compared to a standard width of 15 µm). Then a thinning process was carried out independently on the two regions on either side of this support, which increases the chance of getting a region of thin and un-damaged TEM sample.

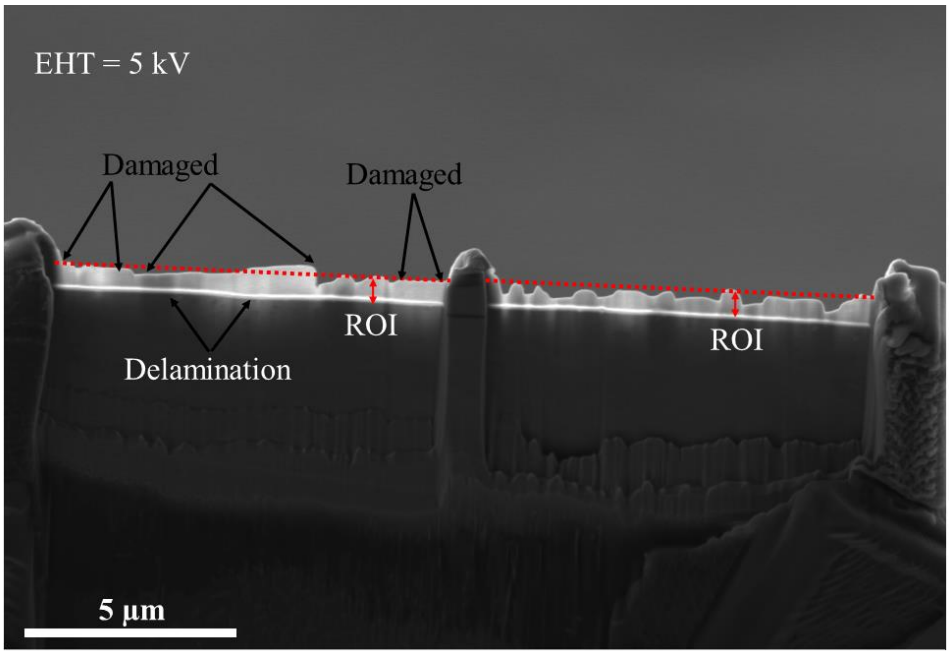


Figure 3.5: SEM image of TEM lamella after surface cleaning showing thin regions that are transparent at 5 kV. The approximate top of the original superconducting layer before thinning is marked with red dotted line, and the FIB-damaged regions (like those shown in Figure 3.4 are marked by the black arrows to emphasis the vulnerability to FIB damage. Delamination of the superconducting layer from the substrate resulting in curvature of the layer is also shown in the image.

While most of the steps described above apply also to the preparation of samples for the in-situ irradiation experiments described below, the major difference is that exposure of the TEM foil to

a flux of energetic ions leads to irradiation-induced bending [388]. This phenomenon necessitates an alternative method to weld the lamellae to the grid. The OmniProbe 3 mm half grids commonly used for TEM foil lift-outs usually contain 3 posts, one is a vertical-edged post and the other two have a valley on a 'V' shaped pin. The first is used as a standard position for TEM lamellae and benefits from a simpler 'lamella parking' procedure (Figure 3.3e), but the latter can be valuable where extra mechanical reinforcement is needed as the lamella is welded on both sides (see Figure 3.6). This method was used for the TEM samples for all the in-situ ion irradiation experiments.

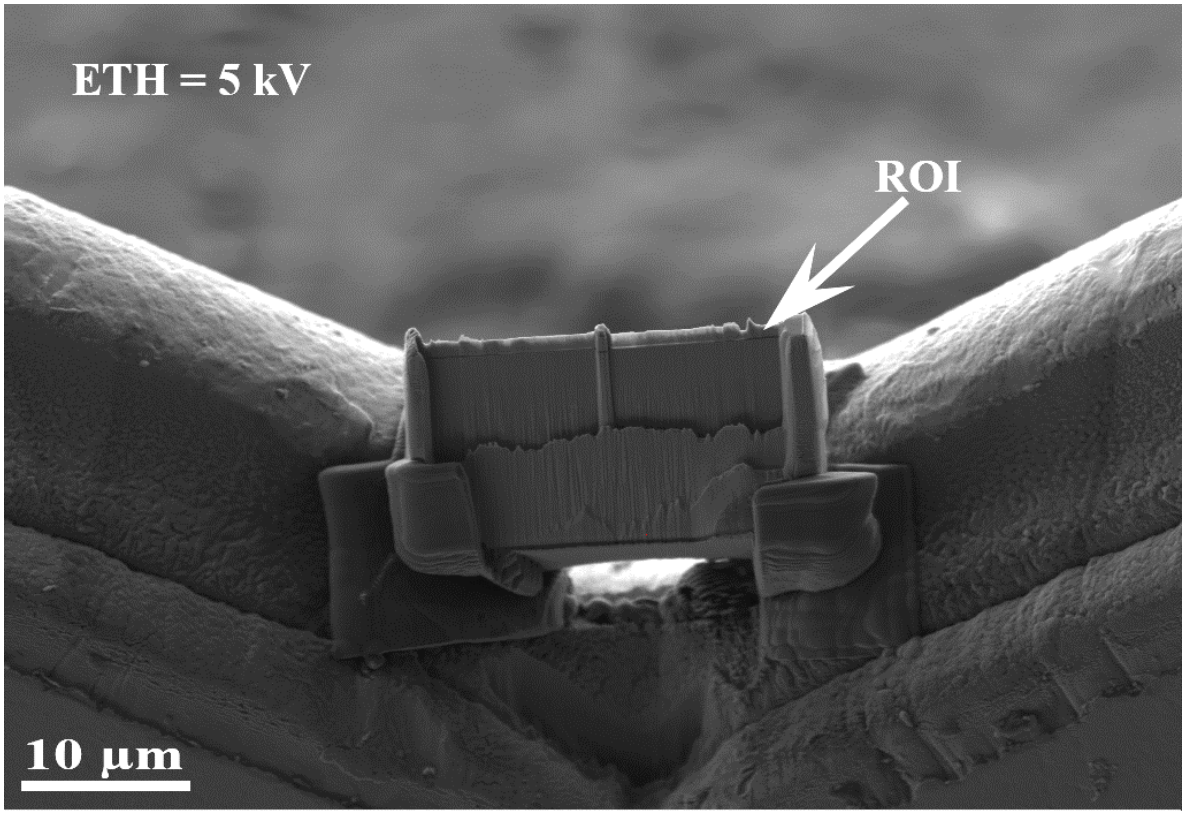


Figure 3.6: TEM lamella attached to the V-shaped pin.

TEM samples from all the un-irradiated samples used in this study were prepared using a ZEISS NVision 40 FIB-SEM. Due to their radioactive nature, TEM samples from all the neutron irradiated materials were prepared in the *Materials Research Facility* (MRF) at the *Culham*

Centre for Fusion Energy (CCFE) using a FEI Helios Nanolab 600i FIB dedicated to handling radioactive materials.

3.3. TEM imaging

Transmission electron microscopy (TEM) offers a powerful combination of imaging, structural, and spectroscopy capabilities from the micron scale down to the angstrom-level. The majority of the work reported in this thesis was carried out using a JEOL JEM-3000F *field emission gun* (FEG) TEM operating at 200-300 kV accelerating voltage. Scanning transmission electron microscopy (STEM) work was conducted on the double aberration-corrected JEOL ARM300CF equipped with cold FEG at 300 kV located at the electron Physical Science Imaging Centre (ePSIC) on the Harwell Campus, and a JEOL ARM200F with cold FEG source operating at 200 kV.

There are several imaging modes that can be used in TEM. Here, the focus is on two high resolution modes; using a parallel beam to form high-resolution transmission electron microscopy (HRTEM) images, and a convergent beam for STEM. For more details on TEM imaging modes and theory, the interested reader is referred to [389], [390].

HRTEM uses a highly spread beam to form a plane wave. The contrast arises from interactions of the incident electrons with the sample, or more specifically, interactions with the atomic potential of the crystal, V(x,y,z), as depicted in Figure 3.7. It can be seen that the lattice has a positive potential from the positive ion/atom cores. As a result, some of the electrons are diffracted, which leads to an exit-wave that consists of a plane wave and multiple diffracted waves at different scattering angles. The phase change as a consequence of interference between the direct and diffracted waves (collected with an appropriate aperture in the diffraction plane) is a maximum at the atomic column positions, and thus the phase image created has a contrast that

represents the inner potential of the lattice but carries little chemical information. Thus HRTEM images are generated by phase-contrast and are not a direct representation of the crystallographic structure. The resulting phase shift of the exit wave can be viewed as contrast, as can be mathematically represented using the *contrast transfer function* (CTF) that is dependent on microscope parameters such as aperture selection and focus [389].

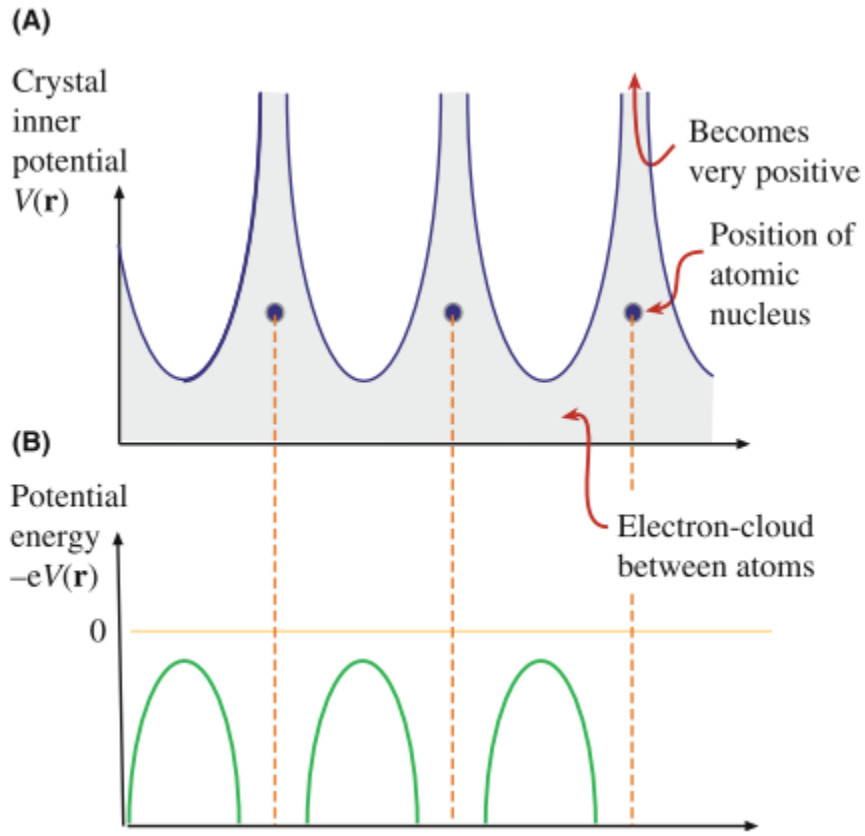


Figure 3.7: (a) The potential energy, V(r), in a periodic crystal structure. The gray background represents electrons that are free to move around the crystal and the black circles are the ions. (b) The potential energy of the incoming electrons becomes more negative the closer they get to the positive potential near the ions [389].

STEM, on the other hand, uses the condenser lenses to converge the electron beam to a narrow probe that is scanned across the sample by the scanning coils, and thus allow a combination of a scanning probe and TEM. Doughnut-shaped *annular dark-field* (ADF) detectors are positioned

below the sample to collect the exiting diffracted wave signal [391]. There are three main imaging mode conditions in STEM: *low-angle annular dark-field* (LAADF), *medium-angle annular dark-field* (MAADF), and *high-angle annular dark-field* (HAADF), as Figure 3.8c shows. The first two are reminiscent of BF/DF modes in conventional TEM since the scattering angles are small and dominated by diffraction, whereas HAADF imaging collects electrons where Rutherford scattering dominates, and the intensity is proportional to the square of the average atomic mass [389]. As a consequence, the images can be thought of as atomic number (Z) contrast images. Thus, STEM/HAADF images are a very good proxy for the positions of the lattice atomic columns, and the local contrast can be easily interpreted as an elemental (atomic mass) map [392]. A pictorial representation of HRTEM and STEM imaging modes as well as the locations of the STEM detectors can be seen in Figure 3.8.

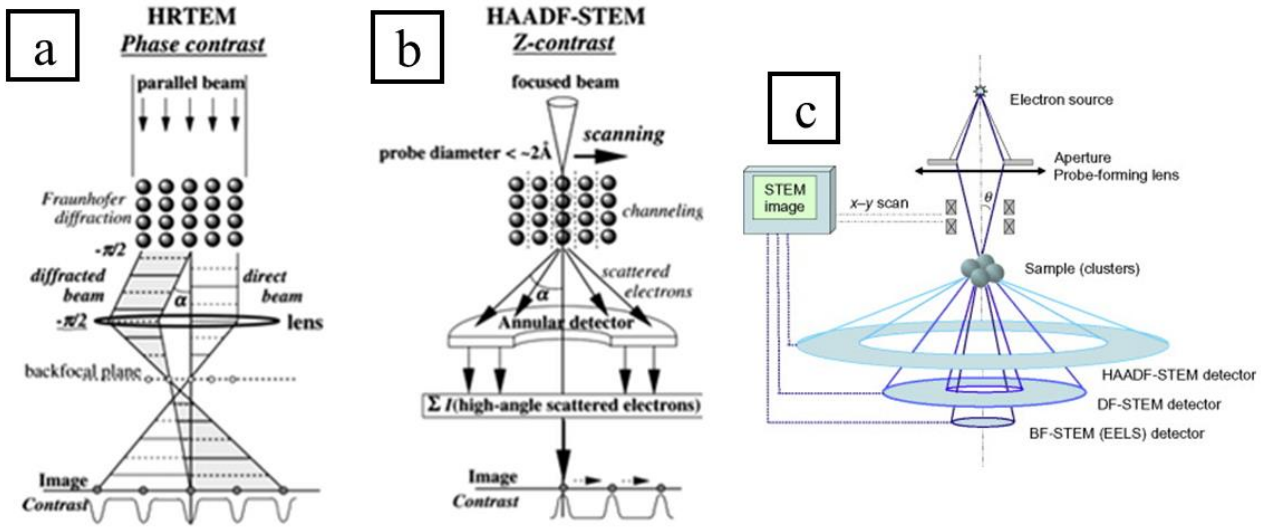


Figure 3.8: a schematic representation of (a) phase-contrast HRTEM and (b) Z-contrast STEM/HAADF image modes [393]. *(c)The location of ADF detectors in STEM mode* [394].

In the current study, the HRTEM images were used to quantify the amount of damage induced, and STEM/HAADF images to calculate the change in lattice parameters, both as a result of

irradiation. Typical images can be seen in Figure 3.10a (HRTEM) and Figure 3.11a (STEM/HAADF).

3.4. In-situ TEM irradiation

In-situ TEM irradiation refers to the use of a conventional TEM equipped with an additional ion beamline attached to the TEM column and allows a real-time observation of structural evolution under ion irradiation. In-situ TEM experiments were carried out at the MIAMI2 facility based at the University of Huddersfield, UK [239], where a Hitachi-9000 microscope operated at 300 kV with a LaB_6 electron source and two ion beamlines (see Figure 3.9). All the TEM lamellae for the experiments were extracted from SuperPower CC tapes (except one sample in the first experiment that was manufactured by SuNAM) using FIB. Every sample was mapped with the aid of *scanning electron microscope* (SEM) images of the TEM foil to select appropriate locations from which pre-irradiation HRTEM images were taken. During the irradiation, a video was recorded at relatively high magnification to get a live-view observation on the damage being generated. The experiment was also accompanied by *selected area electron diffraction* (SAED) of pre- and post-irradiation conditions. Lastly, ex-situ post-mortem HRTEM characterisation was carried out in Oxford.

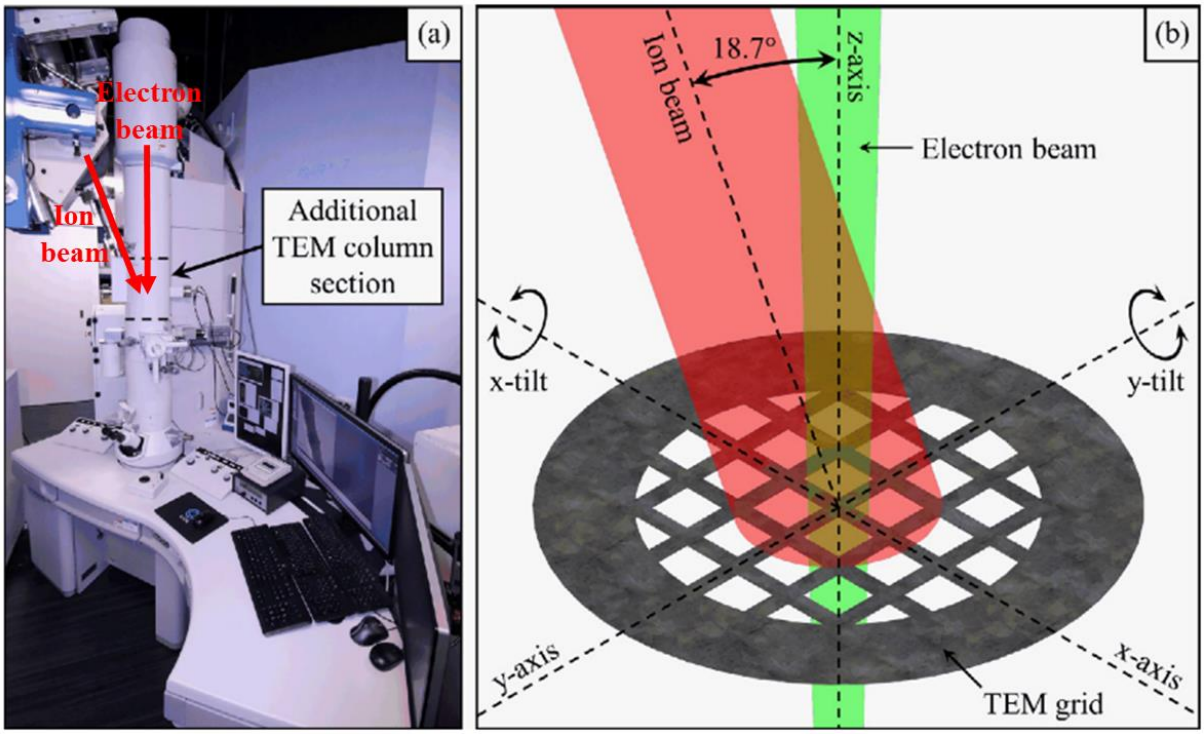


Figure 3.9: (a) Photograph of the MIAMI2 system showing the Hitachi TEM and the attached ion beamline. (b) A schematic configuration of the electron and ion beams on the TEM sample [239].

3.4.1. The importance of in-situ TEM for the current study

In contrast to irradiation of bulk samples, the main advantage of in-situ TEM is the ability to irradiate a TEM lamella and to investigate exactly the same regions before and after lattice damage. Figure 3.10 shows two HRTEM images of the same sample (a) pre- and (b) post-irradiation with 300 kV He-ions at a fluence of 10^{16} cm^{-2}. Interpreting images of irradiated samples could be misleading if there are defects in the perfect lattice structure created during the growth of the original material and damage introduced during FIB milling, and both of these could be erroneously considered a result of irradiation. The availability of an image of the pristine TEM lamella as a control for comparison with the irradiated state is especially important when subtle damage is introduced homogenously across the sample.

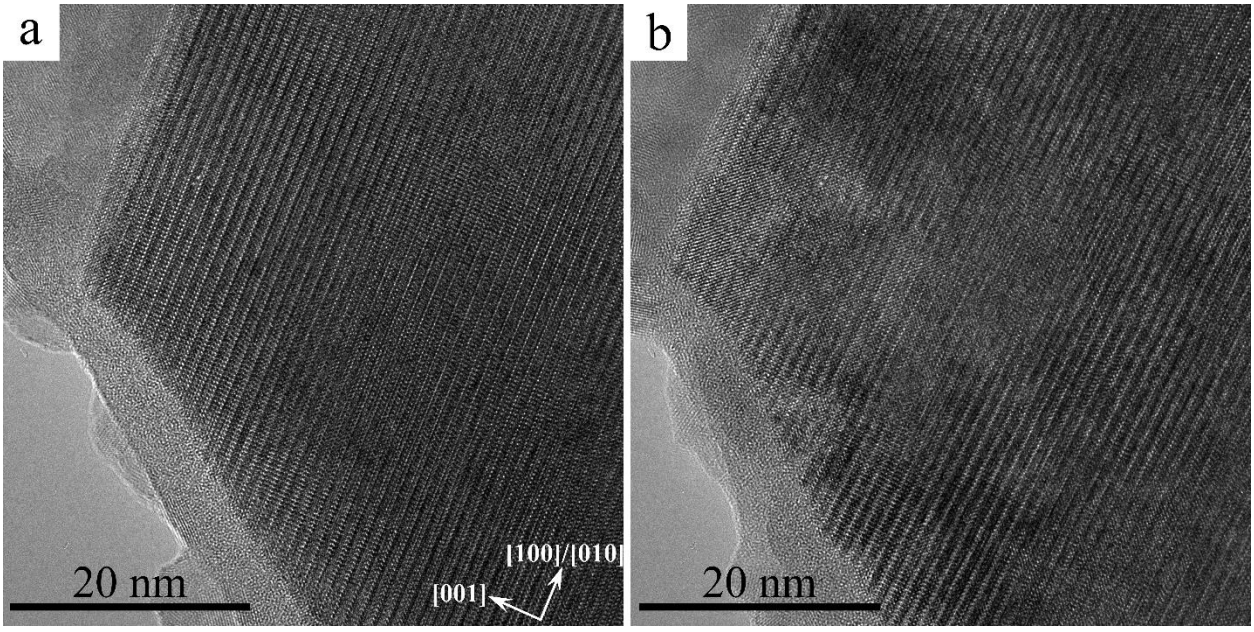


Figure 3.10: Direct HRTEM image comparison between pristine sample (a) and the same sample He-irradiated at 300 kV and a fluence of 10^{16} cm^{-2} (b). Both images were taken from exactly the same region and under the same microscope imaging conditions, i.e. 800 K magnification, [100]/[010] zone axis (ZA), and 200 kV accelerating voltage.

3.4.2. Design of the first in-situ experiments

Although the expected damage can be modelled for a chosen combination of projectile mass and energy by a programme like SRIM [395], I selected the dose for this series of experiments based on Van Tendeloo et.al. [272] who observed "distorted regions" under 300 keV Ne-ion and 100 keV Xe-ion irradiation, both following a fluence of the order of 10^{12} cm^2. However, I chose to irradiate the samples with heavy ions (Xe-ions) to explore the creation of amorphous cascades, at two fluences: 10^{12} and 10^{13} cm^{-2}. Another important choice is the irradiation temperature because the superconducting windings in a magnet for a fusion reactor will be held at cryogenic temperatures. As a result, two irradiation temperatures were selected, 298 K and 100 K. The latter is the lowest temperature that can be achieved using a cold stage TEM holder at MIAMI2

facility. Lastly, as a comparison, Ar-ion irradiation at room temperature to a fluence of 10^{12} cm^{-2} was also chosen to compare the nature and extent of lattice damage to that created by the heavier Xe-ions. The table Table 3.1 shows a summary of the irradiation parameters for this first set of experiments.

Table 3.1: Irradiation parameters used in the first in-situ TEM experiments at the MIAMI2 facility.

Sample name	**SP11-5**	**SP11-1**	**SP11-3**	**SP11-7**	**SP11-4**	**SuNAM-G-03**
Ion type	Xe	Xe	Xe	Xe	Ar	Ar
Energy [keV]	350	350	350	350	350	350
Irradiation temperature [K]	298	100	298	100	298	298
Reported fluence [cm^{-2}] *	1×10^{12}	1×10^{13}	1×10^{12}	1×10^{13}	1×10^{13}	1×10^{13}
Manufacturer	SuperPower	SuperPower	SuperPower	SuperPower	SuperPower	Sunam

*The reported fluence is different than the real fluence due to a false reading, further details in section 3.4.4.

3.4.3. Design of second in-situ experiment

The aims of the second set of in-situ experiments were to evaluate the effect of temperature, energy and ion type on the type and extent of damage. The samples used for this experiment were again manufactured by SuperPower, and the flux, 5×10^{10} cm^{-2} s^{-1}, was kept constant. I divided the samples into three groups, where in each only one irradiation parameter was changed. The first series was intended to test the effect of irradiation temperature by lowering the temperature from ambient down to 100 K in 50 K steps. The second group evaluated the effect of the accelerating voltage of the ions from a maximum of 290 keV down to 30 keV in 65 keV steps. The last group used doubly-charged noble gases ions, Kr, Ar and Ne, to test the effect of ion mass. The irradiation conditions for these samples are detailed in Table 3.2.

In a parallel experiment led by another member of my research group, Dr William Iliffe, the superconducting properties of a sample of bulk SuperPower tape had been measured after He-irradiation to a fluence of 10^{16} cm^{-2} at an accelerating voltage of 300 kV at room temperature, and it was reported that this sample was no longer superconducting. I carried out a similar irradiation on a TEM sample for comparison purposes. Lastly, I sacrificed one TEM sample by performing room-temperature Xe-ion irradiation at 350 KeV in several steps up to complete amorphisation, i.e. a point where the diffraction spots in the SAED pattern disappeared.

Table 3.2: Specifications of the second in-situ TEM irradiation experiments at the MIAMI2 facility. In each group of samples there are three irradiation parameters that are fixed and one parameter that varies.

Group number	**1**	**2**	**3**
Number of samples	5	5	3
Fixed conditions:			
Ion	Xe	Xe	
Irradiation temperature [K]		298	298
Energy [keV]	350		350
Fluence [cm^{-2}]	1×10^{13}	1×10^{13}	1×10^{13}
Variable tested:	Irradiation temperature	Energy	Ion-type
Values / ion types	300, 250, 200, 150, 100 [K]	290, 225, 160, 95, 30 [keV]	Kr, Ar, Ne

3.4.4. Real fluence in MIAMI2 experiments

In the second in-situ TEM campaign, the extent of the damage was far beyond what was expected given the experience of from the first campaign. Generally, the maximum error in the flux reading at MIAMI2 is expected to be about 1%, but shortly after the first experiment was carried out the dosimetry device failed. According to the records from the first experiment, it is now believed that the measured current was artificially high, with the real fluence being 7×10^{12}

cm^{-2} compared to the reported fluence of 1×10^{13} cm^{-2}. This 30% dose error would be expected to make considerable differences but one cannot rule out other unidentified reasons that may have contributed, and was not discovered until after the second campaign which took place after the dosimeter had been fixed. This resulted in the actual fluence in the second set of experiments being higher than in the first experimental campaign. This led to the introduction more irradiation damage than was intended.

3.5. Data Analysis

This section details the MATLAB code developed to analyse the images from the STEM/HAADF and HRTEM experiments. In both cases, the aim is to extract quantifiable data on changes in the perfection of the perovskite lattice of the REBCO superconductors from the two kinds of images. For STEM/HAADF images, the MATLAB code gets an output from the StatSTEM [396] program with all the (x,y) atomic coordinates positions without assigning them to specific atomic type. Then my program assigns the StatSTEM atomic positions to each sublattice, extracts graphical representations of the atomic locations, normalises the differences emanating from instrumental alignment and image acquisitions types (section 3.5.1.4.1), and collates the data to extract averages and statistical distributions of the lattice spacings from each image. For the HRTEM images, I have adopted and developed an image quality assessment (IQA) method typically used for analysing normal photographs, which is based on the concept of entropy in information theory [356].

3.5.1. Analysis of STEM/HAADF images

3.5.1.1. Images analysed

STEM/HAADF images were collected using the ARM300CF and ARM-200F aberration-corrected microscopes along the [100]/[010] *zone axis* (ZA). The images selected, in some cases, included intergrowths generated during the sample manufacture, as can be seen in Figure 3.11a. The double Cu layer locally increases the c-axis lattice parameters. In order to exclude this unwanted effect when calculating the c-axis lattice parameters, two approaches can be applied. The first is omitting whole images that include intergrowths from the analysis. My MATLAB code allows this because all images are initially categorised manually and these data files will have been tagged as 'images with intergrowth'. The second approach is to remove values that deviate by more than a certain percentage from the mean c-axis lattice parameter. A 10% maximum deviation is sufficient to remove enlarged lattice parameters in the vicinity of intergrowths without removing most of the extreme outliers that do not link to intergrowths, provided that the neighbouring unit cells in their vicinity are unaffected. The advantage of the latter is that it does not change the number of images that can be used in the analysis. Table 3.3 summarises the irradiation parameters of the samples used for the analysis, and the associated total number of unit cells (usually hundreds to several thousands in one image).

Table 3.3: Summary of the samples used for STEM/HAADF images analysis.

Sample name:	**Pristine**	**Neutron**	**He**	**Xe (T=100 K)**	**Xe (T=298 K)**	**Ne**	**Ar**
Energy [KeV]	-----	-----	300	350	350	350	350
Reported Fluence [cm^{-2}]	-----	3.3×10^{18}	1×10^{16}	1×10^{13}	1×10^{13}	1×10^{13}	1×10^{13}
Irradiation temperature [K]	-----	~333	298	100	298	298	298
# images	84	78	24	8	14	41	21
# unit cells	42201	104656	17065	7231	9003	35272	18357

3.5.1.2. *ReBCO sublattice fitting*

As will be explained below, the purpose of the MATLAB code was not to find the atomic locations from the STEM images but rather to assign these locations, as calculated from the StatSTEM software [396], to a specific atomic type, namely, Ba_1, Ba_2, Gd/Y, Cu_1, Cu_2 and Cu_3 (see REBCO atomic locations in Figure 3.17). The MATLAB StatSTEM software [396] is a model-based estimation algorithm that finds the atomic column locations using Gaussian fitting with a precision of the order of magnitude of a picometre. The interested reader is referred to [396] and the references within for more details about how the algorithm works. In this section, the fitting procedure to detect the separate types of atomic columns is explained.

3.5.1.2.1. Finding projected atomic columns (StatSTEM)

Images taken in the STEM/HAADF, high-angle electron scattering mode corresponds to the real atomic locations in the lattice [397], [398], from which lattice parameters and other properties of the crystal structure can be calculated. For consistency, I increased the peak intensity threshold to the maximum value to ensure fitting of the lower mass Cu sublattice that appears as dimmer spots in the HAADF images, and defined the same width for the Gaussian peaks in a given atomic location. However, the light oxygen atoms could not be detected in STEM/HAADF images and StatSTEM computations. Using StatSTEM means that the fitting of the atomic positions was done before assigning atoms to different sublattices. After running the fitting procedure using the StatSTEM package, the software provides a list of x and y atomic locations, that can be graphically presented, as shown in Figure 3.11b.

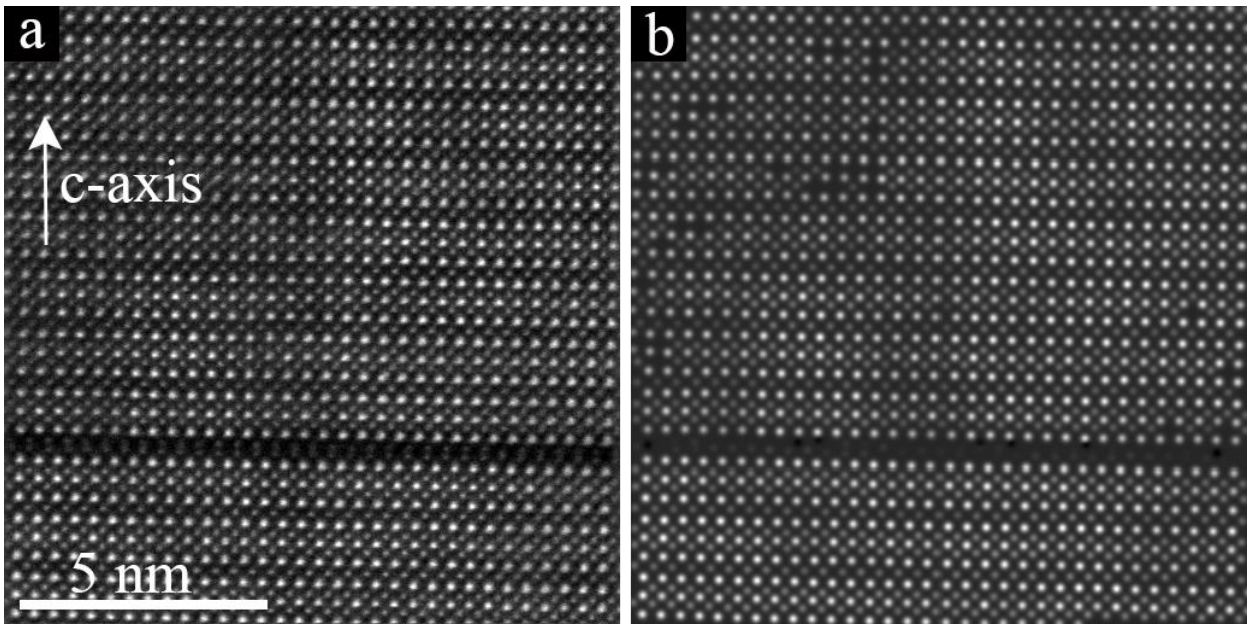


Figure 3.11: (a) STEM/HAADF stack image taken along [100]/[010] ZA from an unirradiated (pristine) SuperPower sample, with the white arrow indicating the growth direction of the REBCO layer. (b) StatSTEM fitting coordinates represented by a grayscale map.

3.5.1.2.2. Model input parameters

After the locations of the atomic columns were fitted using the StatSTEM algorithm, the next step was to assign each to the correct REBCO sublattice, namely, Ba_1, Ba_2, Gd/Y, Cu_1, Cu_2 and Cu3, as shown in Figure 3.17. In order to do so, the program first requires the user to select Ba_1, Ba_2, and Gd/Y atomic columns situated within one unit cell. This step is shown by the 3 red circles in the upper left side of Figure 3.12a, and gives an 'identity' to each sublattice. The REBCO lattice directions are defined by the user's choice of Gd/Y atomic columns along c and a/b directions (Figure 3.12a) with respect to the initial unit cell, as can be seen in Figure 3.12b.

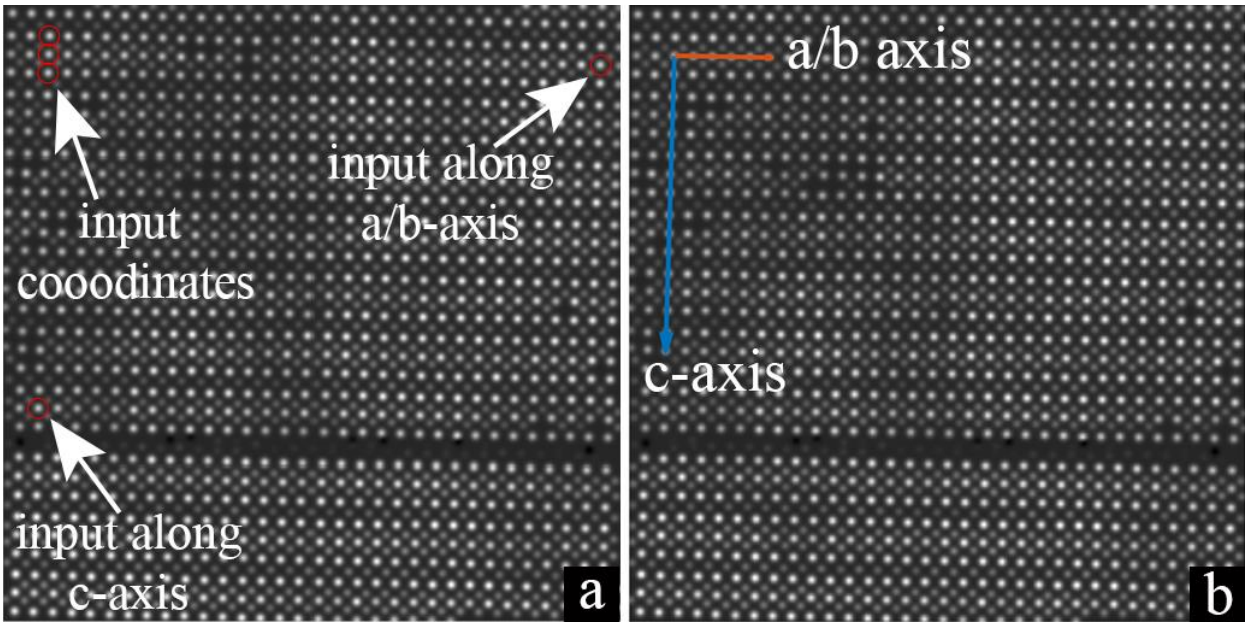


Figure 3.12: initial user inputs and lattice directions. (a) 3 input coordinates of the RE and Ba sublattice chosen from one unit cell. Two Gd/Y atomic column locations along a/b- and c-axis directions are also selected as shown in the figure. (b) Lattice directions determined according the atomic columns input in (a).

3.5.1.2.3. RE and Ba sublattice fitting

Fitting the RE and Ba sublattice is done one atomic column at the time, starting from the initial coordinates inserted by the user. For the purpose of creating a generalised code model that can effectively handle a wide range of defects, orientations and average lattice parameters, the model can be refined by manual user control variables, as shown in Table 3.4. The fitting algorithm involves two loops, the first runs along the a/b direction and the second along the c direction. In each step, the program searches for the next atomic column from the StatSTEM atomic locations output according to the lattice direction unit vector and the lattice parameter defined by the user. The program stores the value of the closest atomic location only if it is located within the radius defined by user (a_axis_threshold / c_axis_threshold variables in Table 3.4) and the distance

normal to scanning direction in a case of a/b direction (Dev_threshold, Table 3.4). Each iteration starts from the current real/forecasted atomic column location. In the case of the real atomic location, the model relies on the atomic location coordinates as showed in the StatSTEM output database. In the forecasted atomic column case however, the model does not rely on real atomic column coordinates but rather on a phantom location that is either deliberately defined by the user in variable Model_anchors (Table 3.4) or as a necessity due to lattice distortion or other image defects. For example, if one of the atomic columns in the RE/Ba sublattice is missing due to distortion, its location would not be fitted, so instead, the model relies on its theoretical coordinates to search for the next column. Figure 3.13a shows an example of the procedure and the result of the fitting of the Ba_2 sublattice. First, the algorithm scans for atomic locations along the a/b direction. When it reaches the end of the image, the algorithm finds the adjacent atomic column along the c-direction and reiterates the scanning along the a/b direction as in step 1. The same procedure runs separately for every atomic column type in the RE and Ba sublattice.

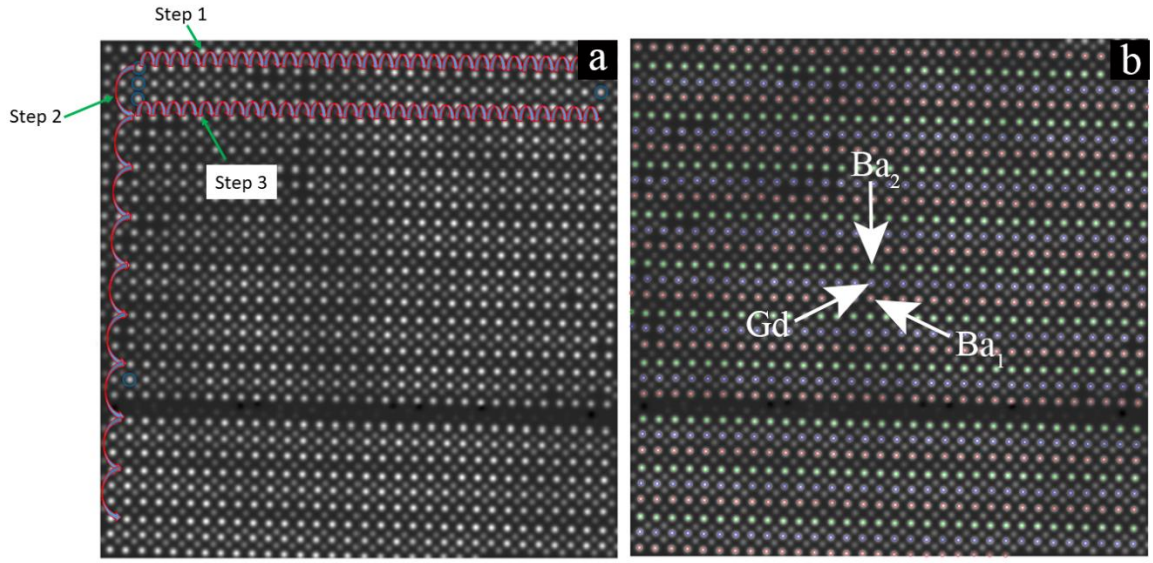


Figure 3.13: RE and Ba sublattice fitting. (a) Fitting algorithm process. Step 1 scans along the a/b-axis until it reaches the end and continues to Step 2 where the adjacent atomic column along c-axis direction is situated. Step 3 runs the same as step 1. (b) The result of the Ba_1, Gd/Y, Ba_2 atomic columns fitting procedure marked by white arrows and represented by red, blue, and green coloured circles, respectively.

Table 3.4: MATLAB program control variables for fitting REBCO sublattices.

Variable name	Functionality
a_axis_length / c_axis_length	Defines the a/b- and c- lattice parameters length.
a_axis_threshold / c_axis_threshold	Upper radius threshold with respect to the lattice parameters when the program scans for the next atomic column.
Model_anchors	An integer that defines how many scans for the next atomic column along a/b-axis direction are performed before the progrma relies on a phantom (theoretical) location to look for the next atomic column.
Dev_threshold	Defines the next atomic location upper threshold with respect to the normal, i.e. 90°, of the scanning direction. Applied when scanning along the a/b direction.

Although the algorithm, with its adjustable user parameters (Table 3.4), is fairly robust, local changes in the lattice structure can cause imperfect fitting e.g. a fitting of Gd/Y instead of Ba atom and/or atomic column that was found by StatSTEM but was not assigned to an atomic type by the program. For this reason, the program allows the user to manually remove and add atomic locations with a mouse click.

Up to this point, this procedure ‘catalogues’ the RE and Ba sublattice atomic column types and location; however in order to measure, for instance, the lattice constants, it is also vital to validate the 2D locations of atomic columns with respect to their neighbours. For this reason, a 2D cell array was created in MATLAB where each cell stores the REBCO unit cell atomic column types and coordinates. Each cell has a two integer address, which represents the a/b and c-locations, respectively. For example, a random cell situated at (4,7) will have neighbours at (4,6) and (4,8) along the a/b direction and (3,7) and (5,7) along the c-direction. In Figure 3.14 every colour stands for a series of unit cells, or in other words, the colours represent neighboring (situated along a specific direction) unit cells rather than atomic columns, along (a) the c-direction or (b) the a/b direction; they show perfect alignment in both directions. In contrast, (c) displays a partially imperfect alignment.

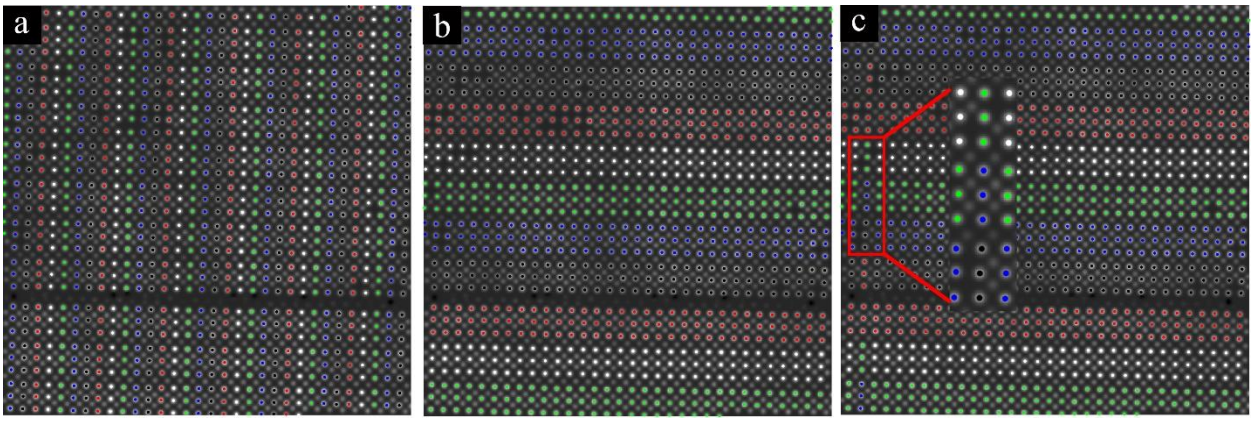


Figure 3.14: Model validation of unit cell alignment. Validation along (a) the c direction and (b) the a/b- direction, where each colour represents adjacent unit cells along the a/b or c-direction. (c) Validation along the a/b direction that shows misalignment emphasised by the enlarged sub image captured from the region noted with red rectangle.

3.5.1.2.4. Cu sublattice and interstitial fitting

To search for the less intense Cu atomic columns, the RE and Ba sublattice locations are used. The code relies on three reference atoms Ba_1, RE, and Ba_2 in a given unit cell. According to its location in a perfect unit cell, a 2D vector from a current reference atom to the experimental atomic location in which the Cu atom should be located is created. Similar to the RE or Ba sublattice fitting, the user defines a radius threshold with respect to the theoretical location of a Cu column. For consistency, a threshold of 1 Å was used throughout this work. Figure 3.15a illustrates the vectors from the reference atoms to the Cu location in one unit cell, and b shows the extracted RE, Ba, and Cu sublattices. The yellow, cyan and magenta vectors (Figure 3.15a) and circles (Figure 3.15b) stand for the Cu_1, and Cu_2 & Cu_3 locations, respectively.

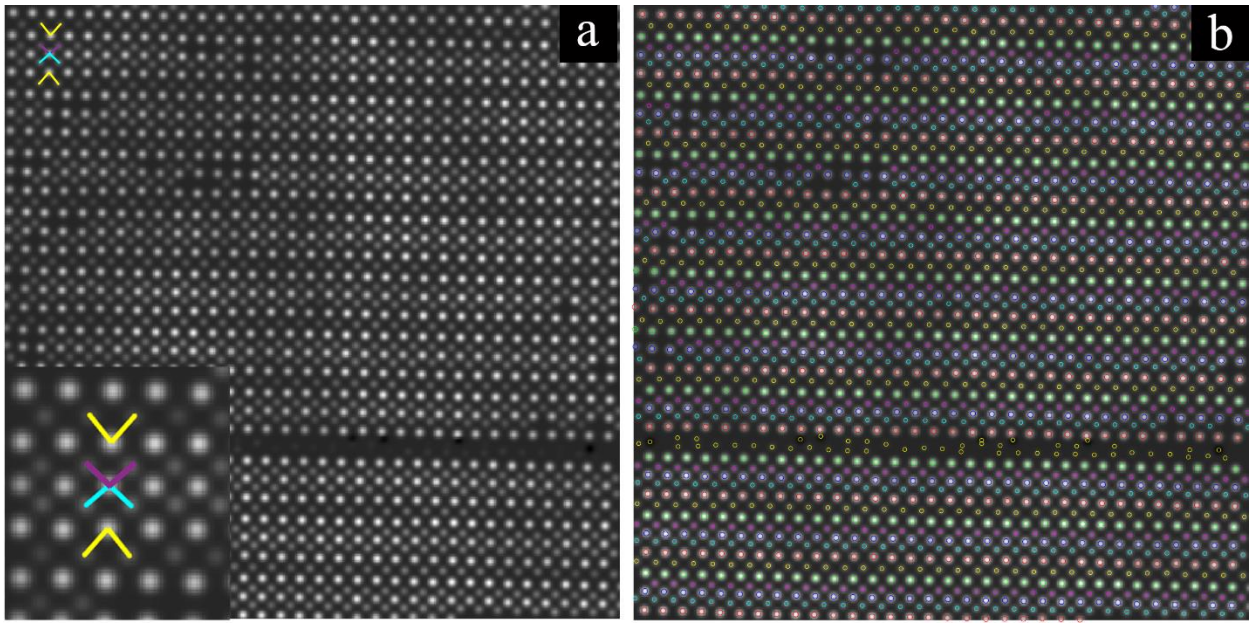


Figure 3.15: Cu sublattice fitting. Cu_1, Cu_2, and Cu_3 are represented by yellow, cyan, and magenta colours, respectively. (a) An example of the vectors from the reference RE or Ba sublattice atoms to the forecasted locations of the Cu atoms. The inset shows the Cu vectors at higher magnification. (b) Fitting of the experimental data to atomic column types, including the Cu sublattice. Red, blue, and green represent the Ba_1, RE, and Ba_2, respectively.

The question arises of how unidentified atomic columns are categorised if they are not matched by the definitions presented above. The answer is divided into two parts. The first is if the user can with confidence define the nature of the atomic column, and the second when the atomic column type cannot be determined for certain. For the former, the user can manually select the atomic columns as a specific atomic type in a case the algorithm did not do a perfect fitting, whereas in the latter case the atoms are defined as 'uncategorised' and thus will not affect the structural parameter calculation described next. A summary of the MATLAB code main assignments is presented in Figure 3.16.

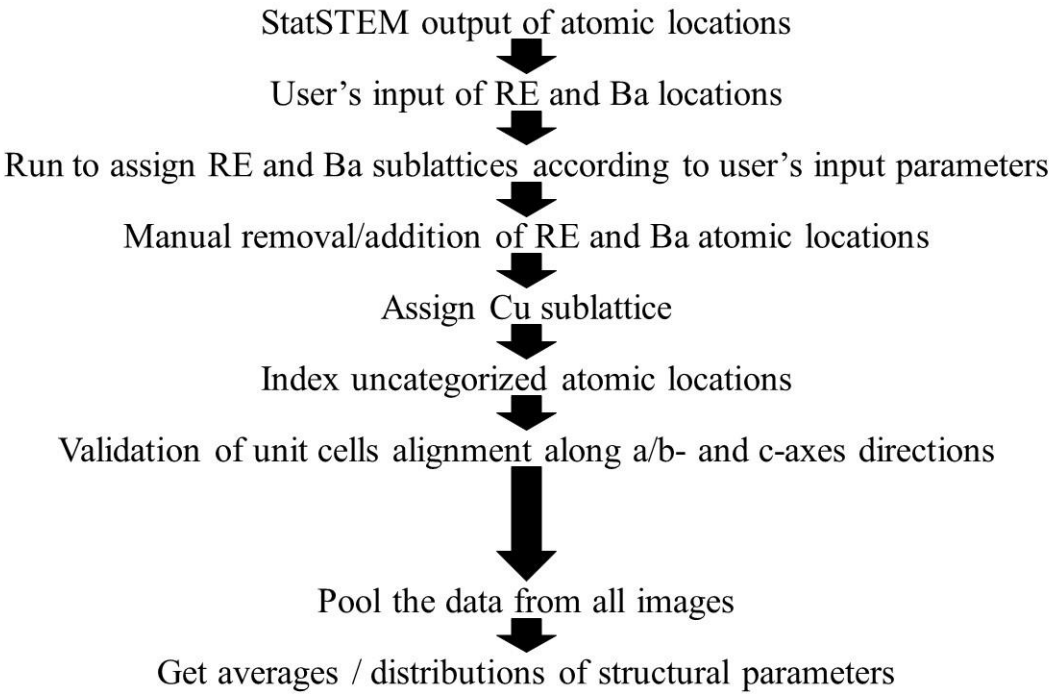


Figure 3.16: A flow chart with the main steps undertaken in the MATLAB program for the STEM/HAADF image analysis.

3.5.1.3. Unit cell definition

The next step is to define the unit cell, as well as how lattice constants are measured. The absolute location of a unit cell, i.e. (0,0) is not defined in the model, instead the distances

between adjacent unit cells are calculated. Figure 3.17 shows an illustration of lattice parameter calculations, where the c-axis lattice parameter is defined as the distance from the Ba_1, RE or Ba_2 atoms in a unit cell to the same atomic column type in a neighbouring unit cell along the c-axis. Similarly, the a/b-axis lattice constant is the distance between identical atomic column types along the a/b-axis direction. The pairwise unit cell lattice parameter is then defined by an average of the Ba_1, RE and Ba_2 column types. In Figure 3.17 the lattice constants were measured with respect to RE atoms. The unit cell marked with the upper red rectangle captures the RE and Ba atoms which belong to a unit cell. Lastly, the Cu sublattice, namely Cu_1, Cu_2 and Cu_3 atoms, is also defined with respect to the representative unit cell.

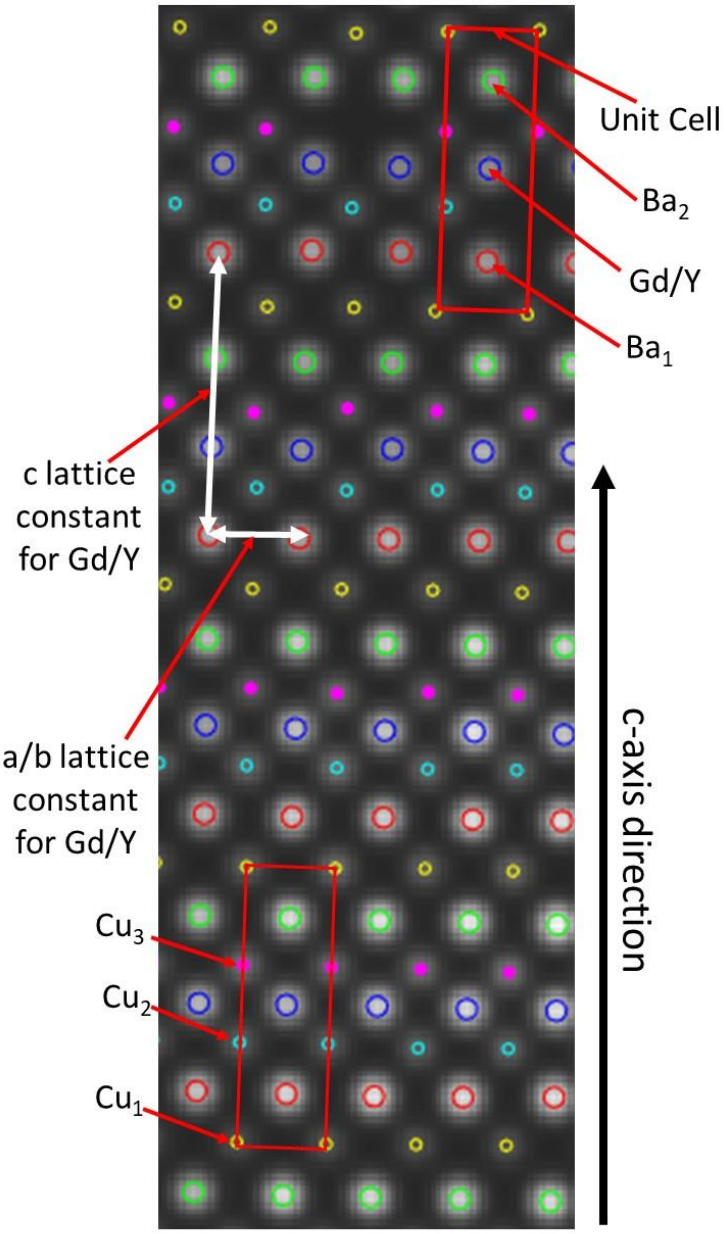


Figure 3.17: Unit cell and lattice constant definition. The growth direction (c-axis) goes from the bottom to the upper part. The conventional unit cell is defined as a 2D cell that contains Ba_1, RE, Ba_2, Cu_1, Cu_2 and Cu_3 columns as shown with red arrows. For convenience, the notification was done on separate unit cells. Lattice constants are measured, in this example, with respect to the Gd/Y atom as shown by the white arrows.

3.5.1.4. Normalising the effects of microscope and image type

There are subtle differences associated with particular instruments and the parameters by which images were acquired. As a case in point, the digital readout of magnification can vary according to changes in the lens strength (scan coils in a case of STEM), and thus in order to get the most accurate magnification, calibration should take place in every session [389], though this protocol is rarely adopted.

There are two conventional modes for acquiring STEM images, the first by capturing one frame with relatively slow scanning to improve the signal to noise ratio, and the second by capturing multiple frames from the same area using faster scanning but without the loss of signal due to the frame summation. For the latter, scripts are used to align precisely the frames to remove the effect of image drift. Image quality is usually worse for one-frame images due to noise and drift. Table 3.5 shows the settings of the image acquisition in both instruments, and for one-frame and stack images. Once the stack images have been acquired, they were aligned using Smart Align [399] to create single-frame image stack.

Table 3.5: Summary of the image acquisition spesifications for each type of microsccpe broken down into one-frame and stack images acquisition methods. The first row displays the total number of images analysed taken from pristine samples.

	ARM300CF (stacks)	**ARM300CF (one-frame)**	**ARM-200f (stacks)**	**ARM-200f (one-frame)**
# images	30	35	12	7
# frames per image	10	---	8	---
Dwell time [µsec^{-1}]	5	20	5	10
Image size [pixels]	512×512	1024×1024	512×512	1024×1024

Figure 3.18 shows the average lattice parameters and standard deviations calculated from pristine sample images for all combinations of microscope and image acquisition types. The total number of images analysed is shown in Table 3.5. Both the calculated a/b- and c-axis values are larger

from images taken on the ARM-200f, and the smallest values are calculated from stacked images from the ARM300CF. It is worth noting that the ARM300CF is remotely control from a separate room whereas the ARM-200f is manually controlled and its surroundings are noisier than the ARM300CF. The magnitude of these effects is discussed in the next section.

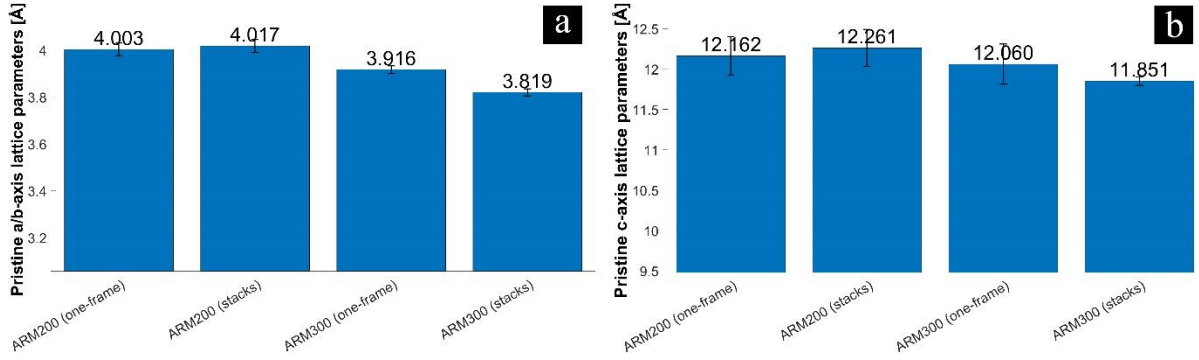


Figure 3.18: Average lattice parameters from pristine samples images calculated as a pair-wise unit cell distances using StatSTEM software and custom algorithm without introducing correction factors. (a) a/b-axis lattice parameters and (b) c-axis lattice parameters.

3.5.1.4.1. Magnification calibration using gold nanoparticles

To accurately calibrate microscope magnifications to explain the discrepancies in lattice parameters in Figure 3.18), one needs a material with well-known lattice parameters, and traditionally Au nanoparticles are used for this purpose [390]. Images of Au nanoparticles were acquired using the highest magnifications possible where FFT signal was strong enough, to try to replicate the experimental conditions used for the REBCO samples. Four different magnifications were selected, ranging from about 2Mx to 5Mx (as a comparison, the range of magnifications for REBCO were usually between 8Mx to 15Mx). A summary of the images used is presented in Table 3.6. Although 8 images were taken from each category, occasionally the data was too weak to fit.

Table 3.6: Number of Au nanoparticle STEM images taken from ARM300CF and ARM200f microscopes in different image acquisition modes.

		# images			
		2Mx	3Mx	4Mx	5Mx
ARM300CF	Stack	8	8	8	8
	One-frame	8	8	8	8
ARM-200f	Stack	6	6	8	6
	One-frame	6	6	8	7

Gold nanoparticles have the *face centered cubic* (FFC) structure with a lattice parameter of 4.0783 Å [390]. When placed on a TEM holder, they are randomly oriented and thus produce a typical concentric ring-pattern when applying FFT on the resulting image [389]. To measure the precise location of the rings from the centre, a HyperSpy Python module was used in several stages: (1) measure the radial intensity from the centre of the FFT image, (2) reduce the background intensity, (3) fitting Gaussians to {111} and {200} rings, as illustrated in Figure 3.19, and extracting the number of pixels from the centre for each family of planes. Then, using the Au d_{hkl} values and the number of pixels, the calibrated magnification was calculated. Figure 3.20 shows the magnification calibration results using the Au-nanoparticles calculated by the following formula:

Equation 3.1: $Diff\ [\%] = \frac{Au(calibrated\ pixel\ size) - digital\ readout}{digital\ readout} * 100$

The correction factors for the calculation of lattice parameters were derived by subtracting the percentage difference from 100%. In practice, because the numbers in the Figure 3.20 are all negative, the scale bars in the images from both microscopes are larger than the calibrated value.

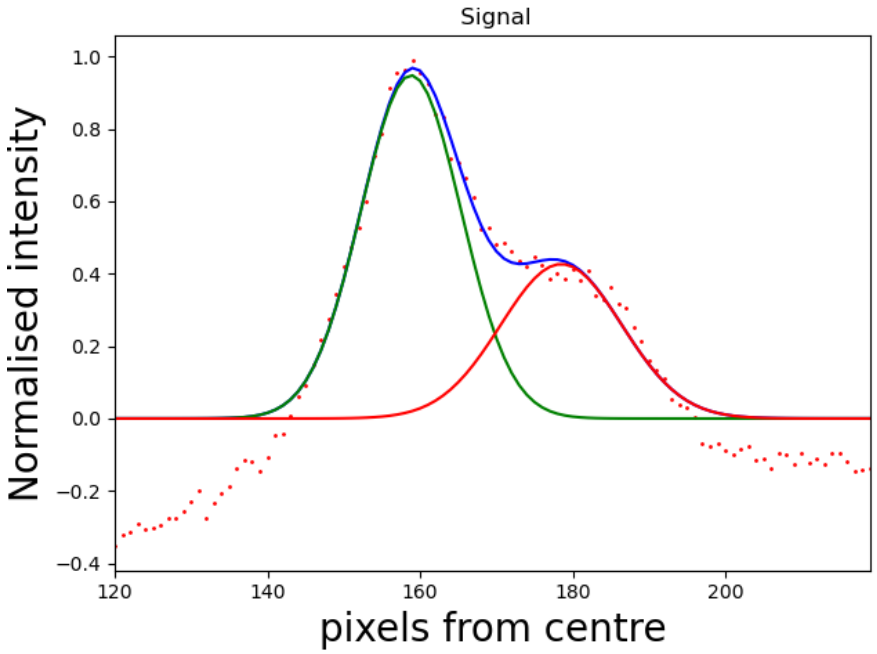


Figure 3.19: Gaussian fitting to find the location of the {111} and {200} rings as was performed using HyperSpy module in Python. X-axis represents the number of pixels from the FFT image centre and the y-axis is the normalized intensity measured radially. The red dots are the measured signal (after subtracting the background intensity), the blue line is the fitting to the measured signal, and the green and blue lines are two Gaussians fitted the measured signal.

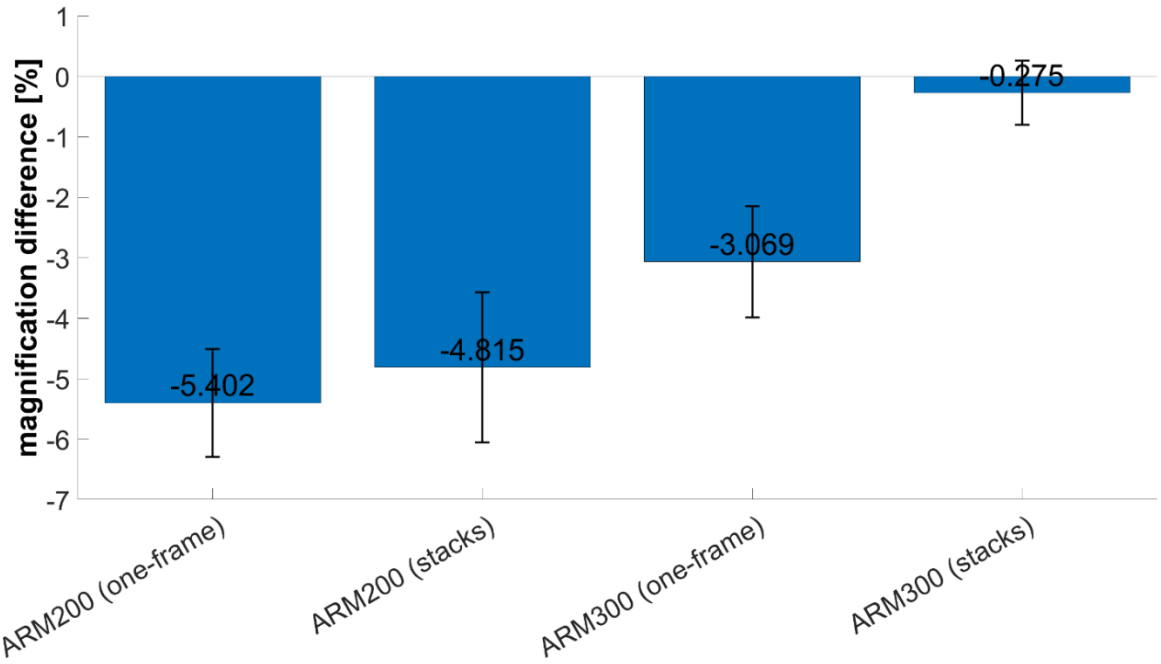


Figure 3.20: Magnification average percentage differences between the digital readout and Au-calibration for the two microscopes, and stack and one-frame image acquisition.

Figure 3.21 shows the pristine sample average lattice parameters after correction using the values presented in Figure 3.20. It can be seen that the calibrated a/b-axis lattice parameters (Figure 3.21a) deviate by less than 1% over all 4 datasets, whereas the c-axis lattice parameters (Figure 3.21b) show increasing values, with the value for the stacked ARM300CF data being nearly 3% higher than for the single ARM200f data. In part this difference could be explained by the orientation of the scanning direction relative to the a/b- and c-axes. The TEM lamellae were always put into the TEM holder such that a/b-axis was aligned roughly horizontally and c-axis vertically in each image. The STEM scans are horizontal, i.e. along the a/b-axis in in the REBCO sample, and when finished a row of pixels, the beam moves one pixel down in the vertical direction and continues scanning along the horizontal direction but this time in the opposite direction, and so on. As a result, the scanning duration for collection of the section of an image necessary to calculate a set of a/b-axis pair-wise lattice parameters is shorter than the time to

complete the scanning for atomic columns along the c-direction, which allows more time for sample drift along this axis.

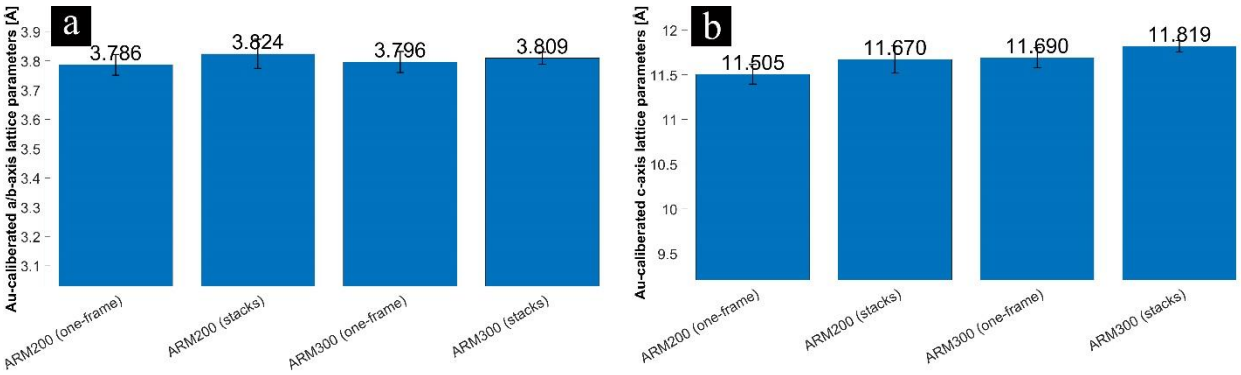


Figure 3.21: Calibrated lattice parameters from the pristine samples after taking into account the difference between the digital readout and the Au-calibrated magnifications.

Figure 3.22 shows an illustration of this idea, the red rectangle defines the minimum region that has be scanned in order to calculate all the pair-wise a/b-axis lattice parameters from this specific layer of REBCO unit cells. On the other hand, in order to calculate the pair-wise c-axis lattice parameters the scanning coils need to scan the blue rectangle which is approximately 3 times larger and thus also triples the time it takes to scan this region. Although stage drift is not a fixed phenomenon, the error in c-axis lattice parameters stems from the fact that it lies along the 'slower' scan direction and thus will be larger compared to a/b-axis.

The reader should note that inaccurate calibration of the magnification is not the only source for the discrepancies between data collected on different microscopes. The image acquisition method selected, systematic/random image drift caused by the microscope environment, and conditions within the stage itself such as thermal gradients can also affect the measured lattice parameters. However the observed convergence in values after calibration of the measured a/b axis lattice parameters from the different microscope/image settings validates the effectiveness of the Au-calibration procedure, and thus will be applied when presenting the lattice parameters

values throughout the thesis, regardless of whether the source of error is a pure magnification calibration or a mix of instrumental factors.

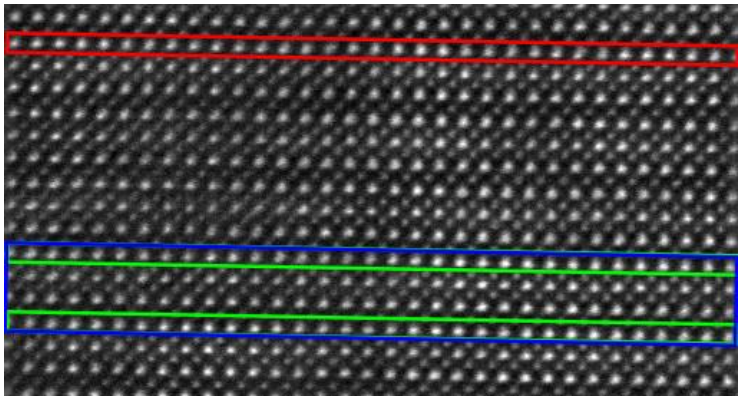


Figure 3.22: REBCO STEM/HAADF image showing the minimum scanning areas for pair-wise lattice parameter measurements of the a/b- and c-axes. The red and blue rectangles show the area of the image that has be scanned in order for the a/b- and c-axes lattice parameters to be calculated, respectively. The two green rectangles contain two neighboring rows of Ba_2 atomic columns.

3.5.1.5. Definition of Inter- and intra-cell fractions and calculation when the images contain intergrowths

Since REBCO has a layered structure, it is instructive to analyse how the interplanar spacings change as a result of irradiation damage. I have chosen to do this by measuring the changes in the spacing of the Ba_1 and Ba_2 layers. Using the conventional unit cell shown in Figure 3.23, it is convenient to consider two different sections of the unit cell: the Ba_1-Ba_2 "intra-cell" region that contains the two Cu(2) planes and the RE plane, and the Ba_1-Ba_2 "inter-cell" region that contains the Cu(1) chains.

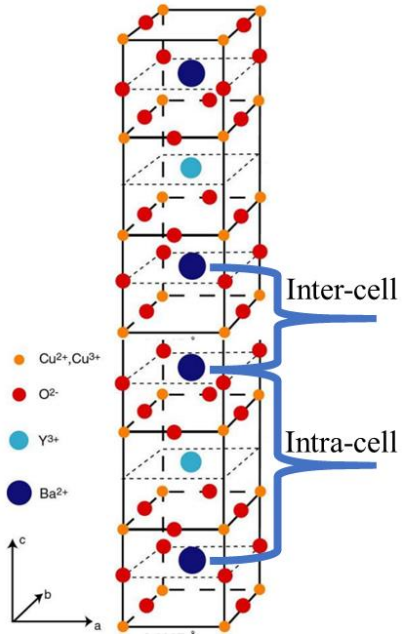


Figure 3.23: Schematic of YBCO two unit-cells with an indication of the Ba_1-Ba_2 inter- and intra-cell distances as defined in this thesis. Reproduced from [400].

Since the characterisation of intergrowths was not the focus of this study, partly because they often exist in the pristine material, it is essential to ignore regions of images that contain intergrowths because the Ba_1-Ba_2 spacings here will not represent the overall inter- and intra-cell fractions. An example of the skewed analysis of the inter-cell fractions where intergrowths are included is shown in Figure 3.24b, and benchmarked against Figure 3.24a where images containing intergrowths are excluded from the analysis. It can be seen that the presence of intergrowths causes a relative expansion of the inter-cell fractions. For this reason, throughout this thesis Ba_1-Ba_2 inter- and intra-cell fraction calculations have not considered local intergrowths regions.

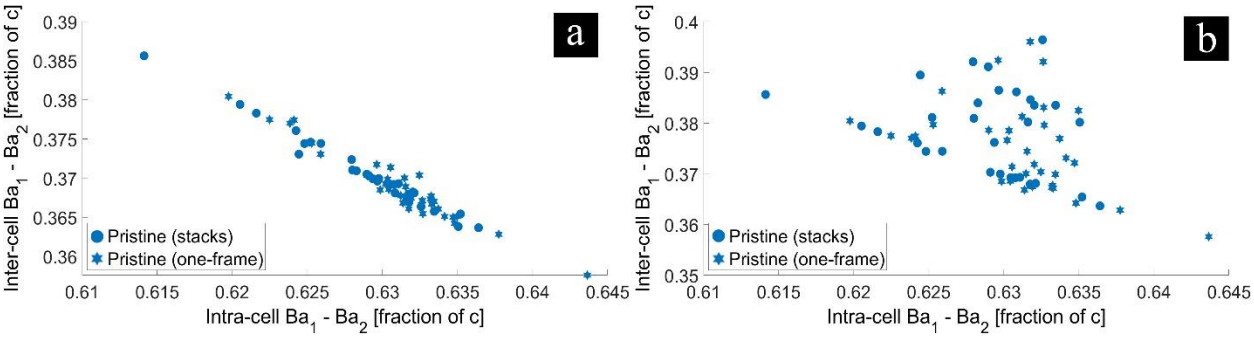


Figure 3.24: Scatter plots presenting the inter- and intra-cell Ba_1-Ba_2 distances as a fraction of average c-axis lattice parameter per image for pristine samples. The scatter on the left (a) does not include images with intergrowths whereas the figure on the right (b) contains all unit-cells in every image that was analysed. The data includes one-frame & stack images taken on the ARM300CF microscope.

3.5.2. HRTEM Quality assessment

3.5.2.1. Images used

For consistency, all the images used were taken along [100]/[010] ZA using the JEOL JEM-3000F field emission gun microscope at magnification of 800K and resolution of 4096X4096 pixels. Images were taken at Scherzer defocus condition [389]. Additionally, all the images were filtered using 2D Wiener filtering [401] to reduce noise. Then, sub-images with 2048X2048 pixels, i.e. ¼ of the original image size, were created using a Digital Micrograph script 'Create Image from ROI' [402] (see Figure 3.25b). In Figure 3.25, the square marked with 'b' is an example of a region from which sub-image was taken. In addition, 512X512 pixel sub-images were extracted from the amorphous edge of various samples as shown in the square marked 'a' in Figure 3.25. A total of 359 amorphous edge sub-images were deliberately taken from pristine samples. Images were captured in many different microscope sessions to examine the impact of differences in microscope and sample conditions, such as electron beam stability, aberrations,

alignment, and edge thickness and wedge angle. Table 3.7 presents the irradiation conditions and the number of sub-images used for this analysis.

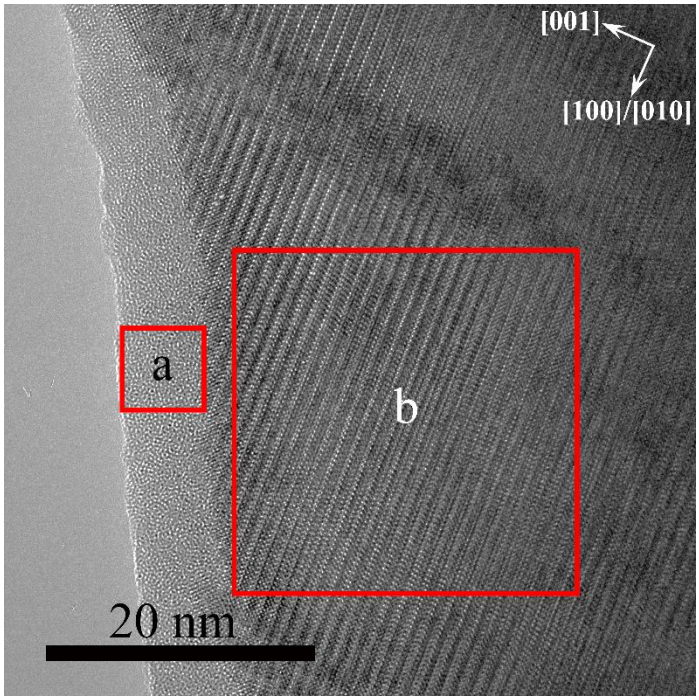


Figure 3.25: HRTEM image taken along [100]/[101] ZA from an unirradiated sample. (a) ROI consists of 512X512 pixels taken from the amorphous edge. (b) 2048X2048 pixel ROI sub-image taken from REBCO crystalline region, avoiding a $BaZrO_3$ rod.

Table 3.7: Irradiation conditions for the samples used for HRTEM analysis.

Sample name:	**Pristine**	**Neutron**	**He**	**Ne**	**Ar**	**Kr**	**Xe (30 keV)**	**Amorphous**	**Xe(T = 298K)**	**Xe(T = 100K)**	**Ar (exp1)**
Sample type	SP*	SP*	SP*	SP*	SP*	SP*	SP*	SP*	SP*	SP*	SP*
Energy [KeV]	-----	-----	300	350	350	350	30	-----	350	350	350
Reported Fluence [cm^{-2}]	-----	3.3×10^{18}	1×10^{16}	1×10^{13}	1×10^{13}	1×10^{13}	1×10^{13}	-----	1×10^{13}	1×10^{13}	1×10^{13}
Irradiation temperature [K]	-----	~333	298	298	298	298	298	-----	298	100	298
# images	409	49	78	110	59	95	67	44	37	46	40

* SuperPower

3.5.2.2. *Dividing the images into blocks*

As already mentioned, image quality assessment (IQA) methods routinely divide images into small, individual blocks, and perform calculations on each separately. In contrast to natural scene images where statistical changes can be found in small blocks when comparing undistorted images with distorted images, in highly periodic HRTEM images, the type of 'distortion', i.e. irradiation damage, is mainly manifested in structural changes that lead to decreasing lattice periodicity. For this reason, I chose to divide the sub-images into 4 quarters (1024X1024 pixel blocks) that are large enough to contain structural information. I then performed entropy calculations for every block as will be explained in the section below.

3.5.2.3. *Entropy in the Discrete Cosine Transformation (DCT) domain*

The following DCT entropy calculations were performed on every selected image block. First, the 2D DCT transformation was performed using the function 'dct2' in the MATLAB code adopted from [316]. Location (1,1), i.e. DC, where the energy (i.e. amplitude squared) is concentrated, received a value of epsilon ('eps' in MATLAB) since it does not represent structural information (refer to section 2.3.2.3.2). For the spectral entropy calculation [362], I first normalised the power spectrum coefficients values ($C_{i,j}$) to reflect their relative frequencies using Equation 3.2.

Equation 3.2: $$P(i,j) = \frac{C(i,j)^2}{\Sigma_i \Sigma_j C(i,j)^2}$$

For the DCT entropy calculation $i, j \neq 0$, I used the following equation:

Equation 3.3: $$E_{PE} = -\Sigma_i \Sigma_j P(i,j) log_2 P(i,j)$$

3.5.2.4. Entropy in the Fourier domain

Similar to the DCT entropy calculations, 2D FFT was performed on every image block using 'fft2' function in MATLAB. To move the zero frequency component to the centre of the image, I used the 'fftshift' function, and then took the absolute values of the complex FFT coefficients. As mentioned, the FFT image represents the frequency components of the original image, and thus can be broken down into different frequency bands. In the current calculation I chose to include the mid-frequency band by applying a circular binary mask to exclude the other bands (see Figure 3.26). The range of the mid-frequency band was deliberately chosen to encompass the halo present in images from amorphous regions (the reasoning for this choice is explained in Appendix C (i)). The inner and outer radii were selected to be 2.5 and 4.6 [1/nm], respectively. Lastly, epsilon value replaced the zero FFT coefficients originating from the binary mask multiplication to avoid division by zero (Equation 3.2). Equation 3.2 & Equation 3.3 were then applied to compute the mid-frequency band spectral entropy of the FFT domain. The figure below summarises the procedure for the entropy calculations in both the DCT and FFT domains.

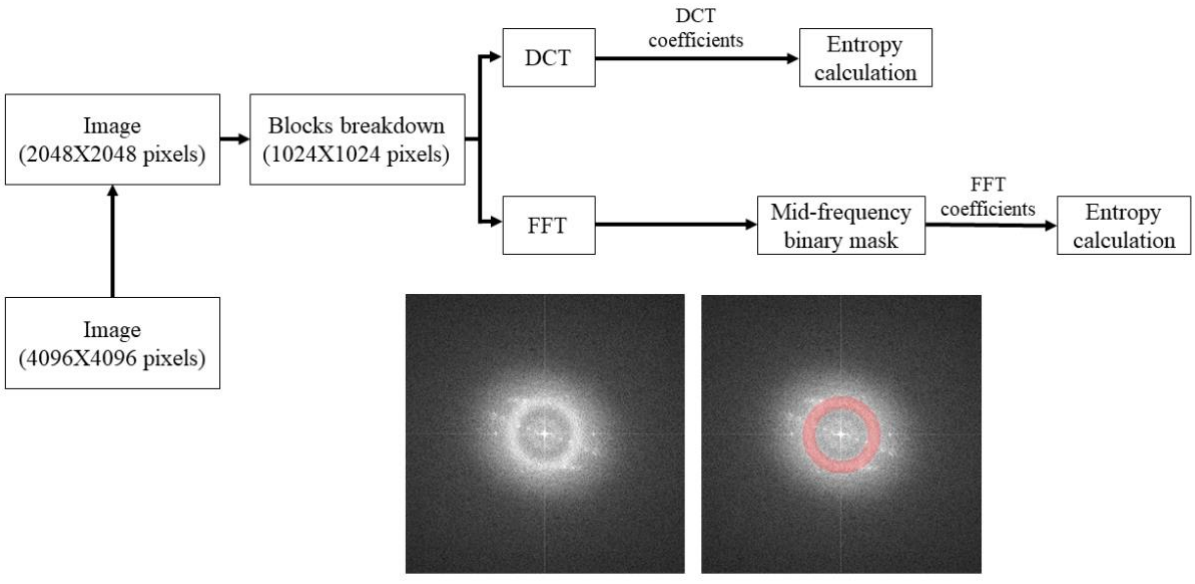


Figure 3.26: A schematic overview of the entropy calculation framework.

4. Irradiation damage mechanisms

The microstructural evolution of radiation-induced damage in REBCO has not been extensively discussed in the literature, but rather the focus has been on measurements of the degradation of transport properties. As already discussed, the nature of irradiation damage can be broadly broken down into two categories; heavy-ions and high energy neutrons which lead to amorphous cascades (refer to section 2.2.2.1.1), and more subtle damage generated by lighter ions and/or lower energy neutrons (2.2.2.1.2). Previous articles that included TEM observations did not reveal much information either on the irradiation damage mechanisms or on the nature of the lattice damage between the isolated cascades. This section focuses on the qualitative aspects of both neutron and ion-irradiation damage as observed using HRTEM. Quantitative assessment of the damage is discussed in sections 5 & 6.

4.1. Neutron-irradiation damage

Figure 4.1a shows a typical HRTEM image taken along [100]/[010] direction of a neutron-irradiated sample (section 3.1.2 for sample details). Two crystalline regions can be identified, (1) the REBCO matrix and (2) a $BaZrO_3$ (BZO) rod presenting Moiré fringes characteristic of interference between electrons diffracted by the orthorhombic REBCO perovskite lattice and the cubic BZO. This is the microstructure expected for these SuperPower samples [403]. The periodicity of the lattice planes in the regions marked by white squares can be demonstrated using FFTs taken from 9.35×9.35 nm windows, as shown in b-d. The crystallinity of both the REBCO matrix and the BZO rod is shown in b & c, respectively. Additionally, ~10 nm diameter amorphous regions marked with white arrows are reminiscent of damage cascades created by ion-irradiation [241], [272]. The lack of long-range order in the amorphous cascades is

highlighted in d, with the characteristic amorphous halo and weak spots from the crystalline matrix at the edge of the amorphous core.

To confirm that these amorphous cascades were not a consequence of electron beam damage in the microscope, sample preparation damage/artefacts, or manufacturing defects, I have used identical sample preparations steps and characterisation methodology on lamella prepared from un-irradiated (i.e. pristine) samples from the same coated conductor material as the neutron-irradiated samples. The amorphous regions detected in the irradiated sample as shown in Figure 4.1a could not be found anywhere in three TEM lift-outs taken from the pristine reference sample. Therefore, I can confidently assign them to neutron-induced damage.

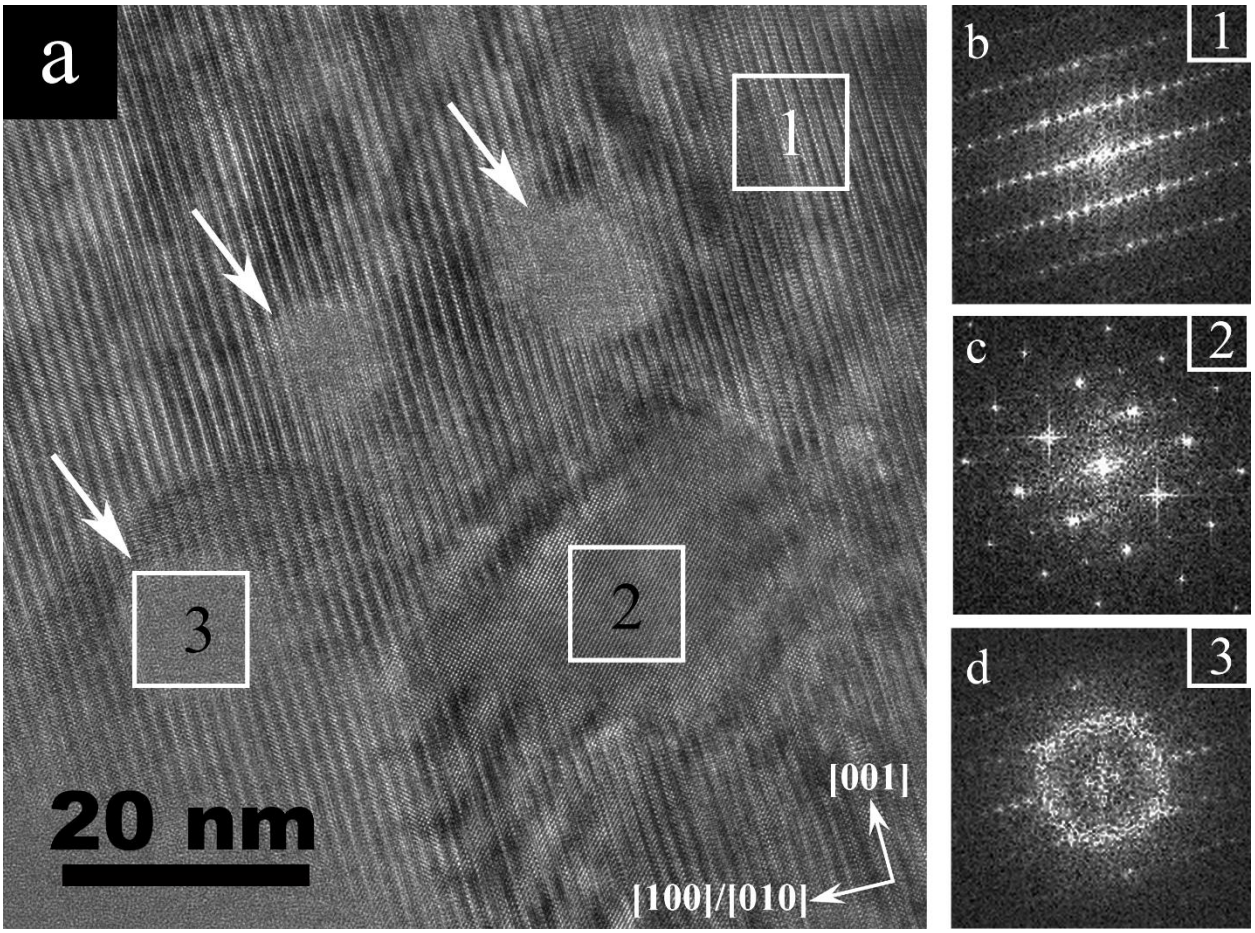


Figure 4.1: A cross-sectional HRTEM image of typical amorphous cascades formed in the neutron-irradiated samples and Fast Fourier Transforms (FFT) from selected regions. (a) A HRTEM image taken at [100]/[010] orientation shows three different phases: the GdBCO matrix identified by the periodic layered structure of the ab-planes (1), crystalline BZO rods (2), and amorphous cascades (3) (arrowed) identified by the loss of the periodic plane structure. (b-d) Fourier Transforms for each phase, (b) for the GdBCO matrix, (c) BZO rod, (d) amorphous cascade, taken from regions 1, 2, and 3, respectively.

Direct observation of these amorphous cascades using HRTEM is a function of the probability of a cascade being present in a given region, absence of the FIB damage often found at the edge of a lift out lamella, and a sample thickness which is small enough to avoid including undamaged, crystalline regions that lie above and below the cascade. Based on a standard lamella of width of 15 µm, estimated foil thickness of ~40 nm, 1 µm superconducting layer thickness and the

observation of 10-30 cascades per lamella, I estimate the density of large cascades (~10 nm in diameter) in the irradiated material to be $3.3 \pm 1.6 \times 10^{19}$ m^{-3}. This estimate corresponds to less than 0.01% of the cross section of the superconducting tape being occupied by the presumably non-superconducting, amorphous cascades. Therefore, much smaller amorphous regions, and the local disorder in the irradiated samples that is also expected to contribute to the observed degradation in J_c and T_c values in this case [404], are difficult to accurately quantify using this kind of TEM analysis.

Frischherz et.al.[253] calculated the defect density of neutron-irradiated sample to a fluence of 8×10^{17} n cm^{-2} to be 3.9×10^{22} m^{-3}. The several orders of magnitude difference between my observations and Frischherz et.al. stems from the fact that the two-beam (TB) condition those authors used is sensitive to the local changes in diffraction conditions created for instance by small defect clusters [405]. This imaging technique works well for the bulk superconductor crystals free from artificial pinning centres (APCs) used by Frischherz et al, but is less suitable for samples that contain high density of $BaZrO_3$ (BZO) nanorods, such as manufactured by SuperPower, which create local distortions due to the lattice parameter mismatch [89]. Furthermore, identifying irradiation damage using TB conditions does not distinguish so clearly between amorphous and distorted regions, but rather captures the lattice strains associated with different kinds of irradiation damage [405]. In addition, Frischherz et.al. also mention the size distribution of what they identify as defect cascades and infer a mean size of 2.5 nm in diameter. Sizes above 5 nm were not found. This emphasises that large cascades in this current study are larger than Frischherz found, and thus their reported density cannot be compared directly with the estimate here.

Chudy et.al. [278] used *positron annihilation lifetime spectroscopy* (PALS) on neutron-irradiated samples up to a fluence of 6×10^{17} n cm^{-2} and reported similar concentration of cascades (defined as several nanometres of local damage) as Frischherz et.al. [253]. In the same study, the concentration of point defects was reported to be a magnitude of order higher. Based on this analysis, and the fact that neutron-irradiation of my samples [37] resulted in a decrease in J_c value (measured at 30 K) of about 30% at a neutron fluence of 3.3×10^{18} n cm^{-2}, it is sensible to assume that other small defects (including point defects) exist between the large cascades.

Figure 4.2 shows a comparison between typical images of the superconducting matrix in un-irradiated (Figure 4.2a) and neutron irradiated (Figure 4.2b) SuperPower samples, showing no signs of an increased density of intercalation defects and/or degradation of the lattice periodicity of the kind reported by Zandbergen et.al. [269]. From the study of more than 50 images, I found no systematic differences between the typical periodic lattice structure of the matrix in irradiated and un-irradiated samples. This observation is somewhat subjective since I do not possess pre & post irradiation images taken from the same region as I have for samples from the in-situ ion-irradiation experiments (section 3.4.1). It is clear, however, that any lattice damage between the cascades in the REBCO matrix is subtle and hard to identify directly from these kinds of images. A similar case will be reported in section 4.2.1.2 for Ne-irradiated samples, where analysis of about a hundred of post-irradiation images did not reveal any signs of lattice degradation.

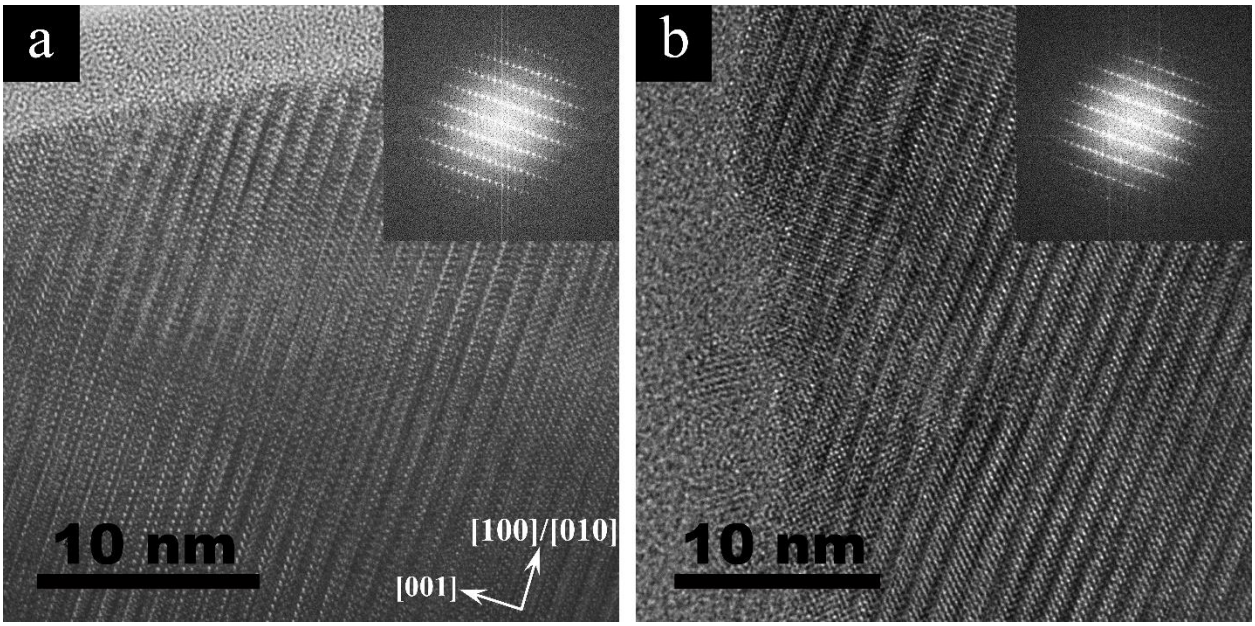


Figure 4.2: Typical HRTEM images taken along [100]/[010] and the corresponding FFT images (shown in insets) from (a) an as-manufactured and (b) neutron-irradiated SuperPower sample, showing no obvious intercalation defects in either material.

Another type of high-resolution image that can be useful to reveal lattice damage in neutron-irradiated samples is those obtained under STEM imaging conditions (section 3.3 & Figure 3.8). Figure 4.3 shows two pairs of typical images; HAADF on the left (a,c) and BF on the right (b,d). For STEM images formation theory, the reader is referred to section 3.3. Regions with this characteristic local contrast change, i.e. lower brightness in HAADF and higher brightness at BF signals with respect to the rest of the image, could not be observed in un-irradiated samples and thus I can infer that these regions are a result of neutron-induced damage. STEM images along specific ZA in samples with local lattice distortions will contain regions with additional elastic scattering when the Bragg conditions are not satisfied so the BF image will look darker (i.e. less electrons collected by the detector) and vice versa for DF. For the case of HAADF contrast, although the main contributor to contrast variation is atomic mass (Z number), Wang et.al. [406] argued that mean atomic displacements from their natural atomic location gives rise to increasing

contrast that behaves similarly to *thermal diffuse scattering* (TDS). Additionally, Cowley and co-authors [407] noted that local de-channelling effects due to lattice distortions also contributes to wide-angle scattering. Thus, this kind of contrast in both imaging modes implies the existence of local lattice disorder that can be seen directly in the STEM mode when fully amorphous cascades are not visible.

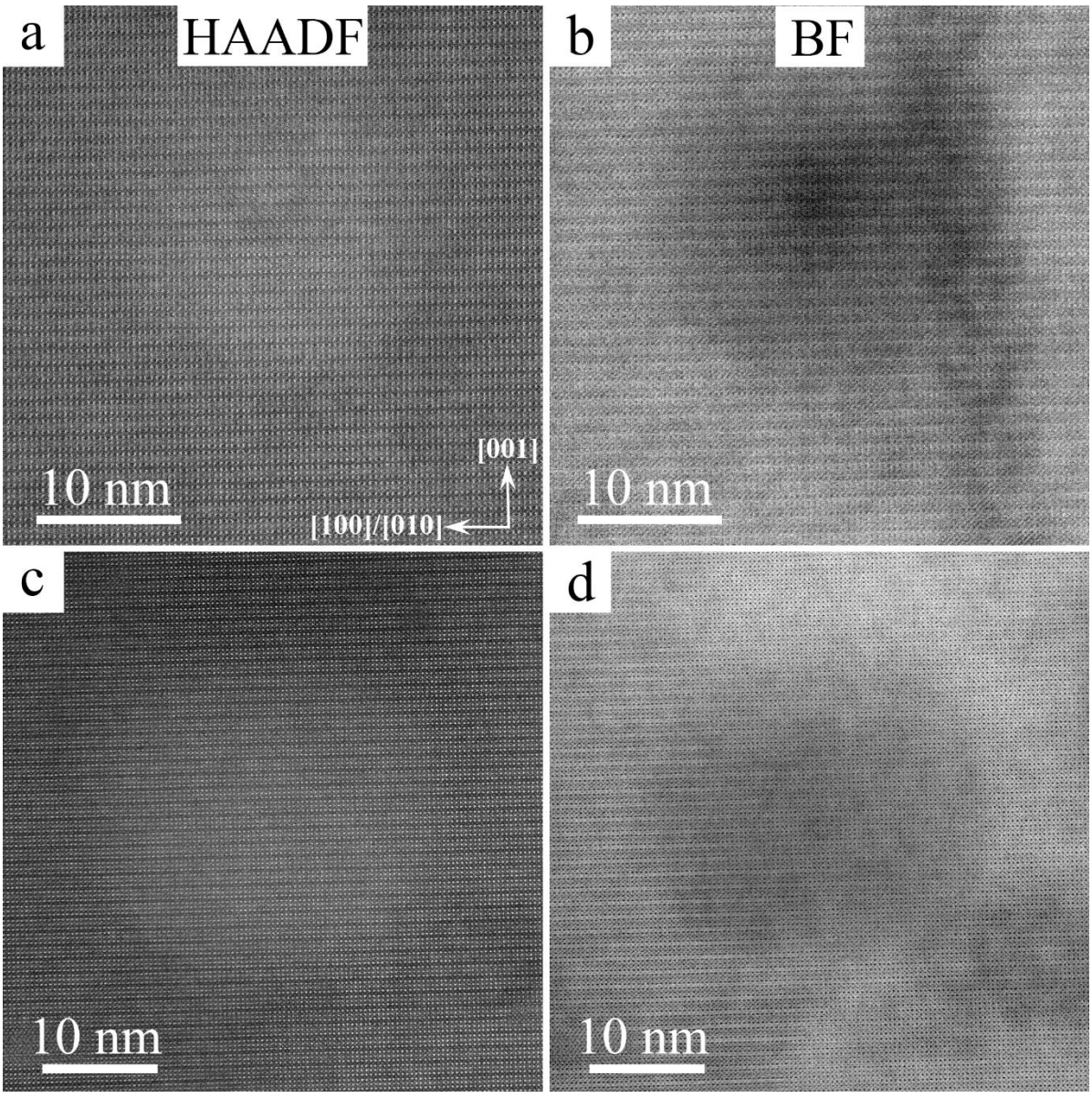


Figure 4.3: BF/HADDF STEM images taken from neutron-irradiated samples along [100]/[010] ZA. (a-b) images at a magnification of 5 Mx showing (a) HADDF and (b) BF signals; (c-d) images taken at magnification of 4 Mx, (c) HADDF and (d) BF.

4.2. Ion-irradiation damage

There are several advantages of using ion-irradiation to reveal damage mechanisms in REBCO, such as the ability to conduct in-situ experiments and to tune the irradiation parameters (e.g. temperature), and to avoid the expense and difficulty of working with neutron-irradiated

materials. This section shows observations of ion-induced irradiation damage studied using HRTEM. For more details on the irradiation conditions the reader is referred to sections 3.4.2 & 3.4.3.

4.2.1. The effect of ion mass

Ion mass plays a crucial role in determining the extent and type of damage; light ion irradiation generates mostly Frenkel pairs (FP) [197], whereas heavy ions generate damage cascades [191]. The number of surviving smaller defects such FP, small clusters, and Schottky defects in a collision cascade scales as a power law with PKA energy [408]. This section compares the irradiation damage created by four types of ions with increasing mass: He being the lightest and Xe the heaviest. The structures of the samples irradiated with the heavier ions are compared at low doses before the REBCO lattice is too heavily damaged.

A common measure for comparing the damage created by different types of ions at different energies and fluences is *displacement per atom* (dpa) (see section 2.2.1.1.2). Figure 4.4 shows the dpa values as a function of depth for the incident ions used above, calculated using Equation 2.3 and the output of SRIM simulations [395]. It can be seen that as the ion mass increases the mean free path (λ) decreases, i.e. both the average number of collisions of the incident ion with the sample and the dpa values increase. Therefore, it is expected that heavier ions will result in more damage near the sample surface. In the case of in-situ TEM ion-irradiation, these small λ values are responsible for efficient irradiation damage accumulation in TEM samples that, in particular those intended for HRTEM, do not exceed 100 nm in thickness. Table 4.1 illustrates this idea by showing the increasing dpa values estimated for 100 nm. It can clearly seen that dpa increases precipitously with the ions mass, which is consistent with the experimental results

shown in this section. For the irradiation experiment that was undertaken on TEM foils rather than on bulk samples it means that the shorter the mean free path is, the higher the expected level of damage. It is worth mentioning that low energy light ions show small λ and thus can be generating irradiation damage effectively; however, for the current experiment chosen energies this is not the case.

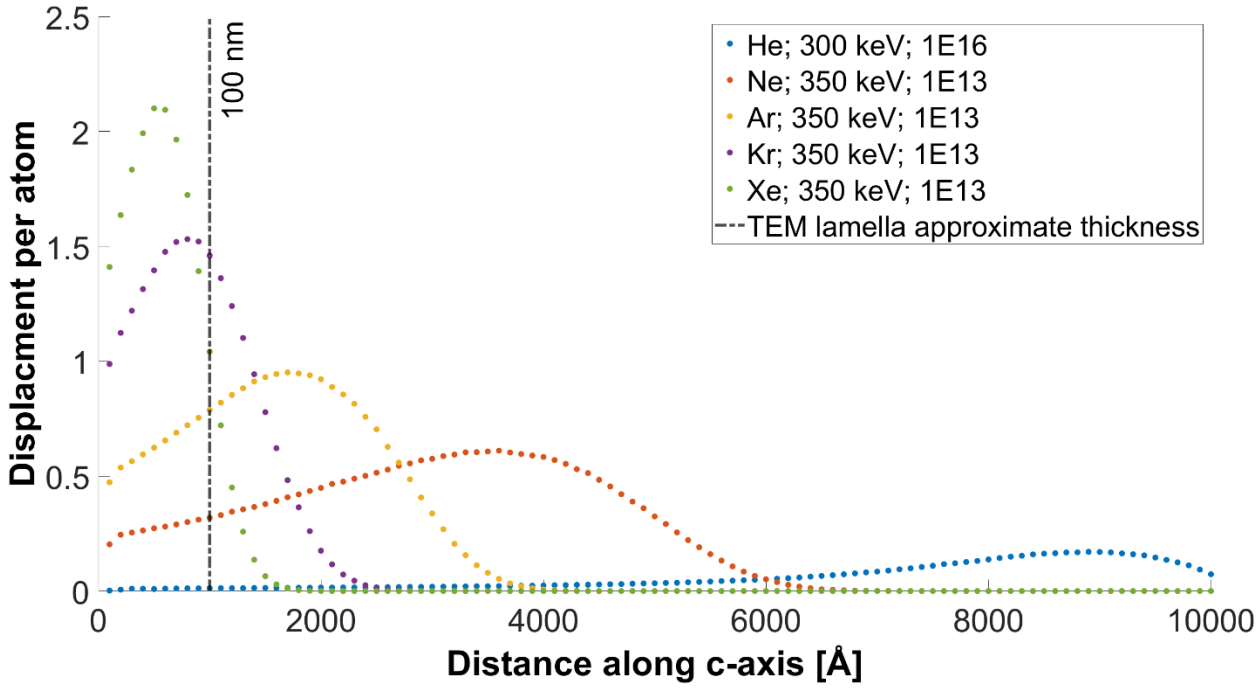


Figure 4.4: Displacement per atom (dpa) as a function of depth in YBCO calculated using threshold displacement energies (TDE) of 40 [207]*, 45* [207]*, 33* [208]*, and 8* [207], [209] *eV for Y, Ba, Cu, and O, respectively. The vertical dotted line marks the approximate thickness of the TEM foil.*

Table 4.1: Average dpa values estimated using SRIM for 100 nm thick YBCO for five types of ions irradiated at 350 keV.

Ion type	**He**	**Ne**	**Ar**	**Kr**	**Xe**
Atomic number (Z)	2	10	18	36	54
Fluence [ion × cm^{-2}]	1×10^{16}	1×10^{13}	1×10^{13}	1×10^{13}	1×10^{13}
Average dpa for 100 nm	0.0095	0.2739	0.6402	1.3547	1.7188

4.2.1.1. He-ions

Figure 4.5 shows two pairs of images taken from the same place on a TEM foil in the pristine state (a,c) and after in-situ He-irradiation (b,d). It worth remembering that FIB sample preparation induces damage even in pristine material (section 3.2.2) so some damage will inevitably be present. This in-situ irradiation took place at room temperature, using an accelerating voltage of 300 kV to a fluence of 10^{16} cm^{-2}. A BZO nanorod can be seen in both of the lower images. It can be seen by comparing both post-irradiation images to the pre-irradiation images that the REBCO layered structure appears less crisp after irradiation (a very subjective observation, but visible even to the untrained eye), but no localised cascades or intercalation defects can be identified in Figure 4.6. This is consistent with observations from dozens of images of He-irradiated samples in this study, and consistent with the concept that He-ion damage results mostly in the formation of Frenkel pairs and other types of point defects that are invisible to this kind of TEM imaging [38].

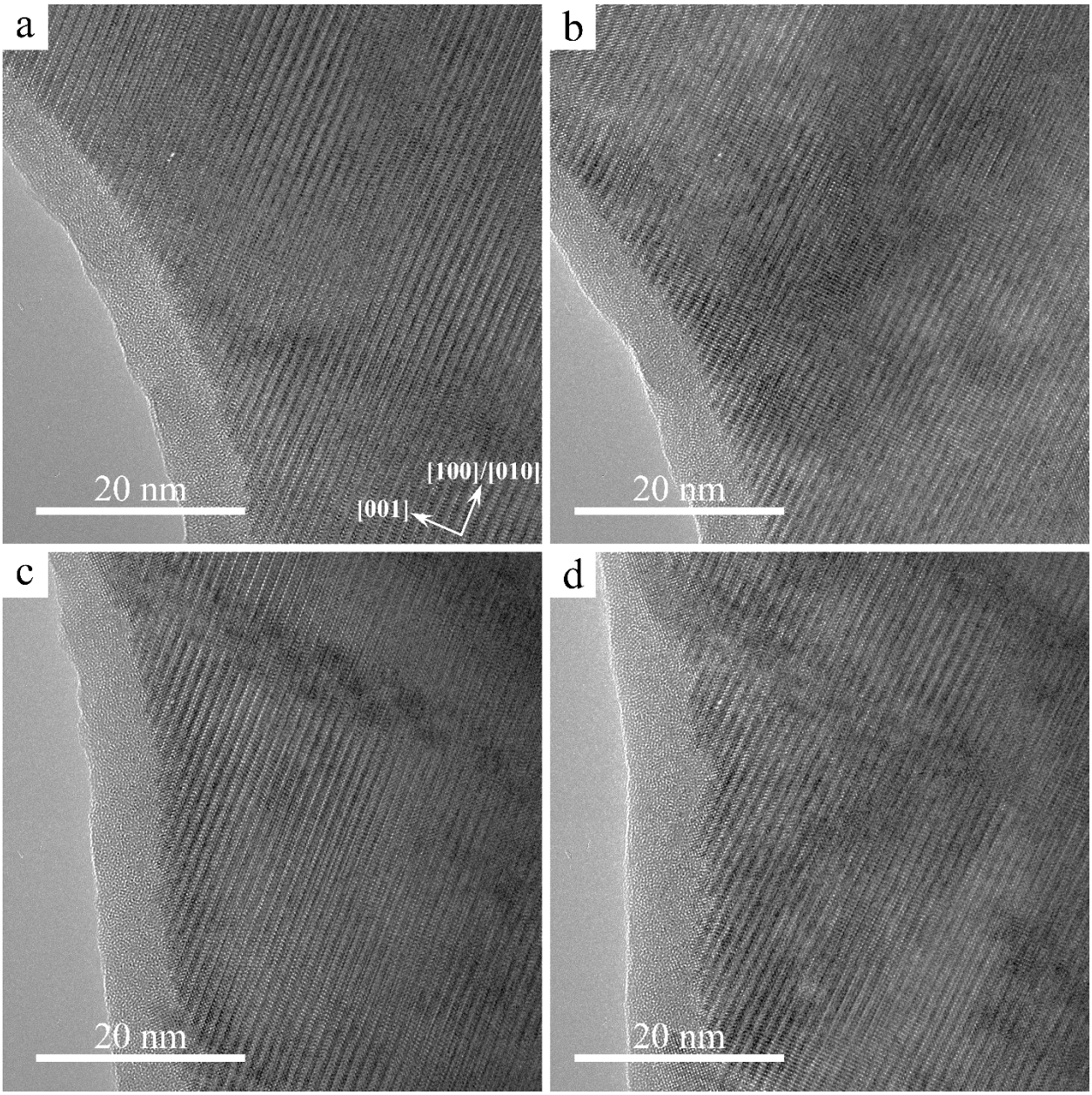


Figure 4.5: Direct HRTEM image comparison, taken along [100]/[010], of (a, c) pre- and (b, d) post-He-irradiation at room temperature, accelerating voltage of 300 kV, and to a fluence of 10^{16} cm^{-2}. The two pairs of images were taken from exactly the same region under the same microscope imaging conditions, i.e. 800 K magnification, [100]/[010] ZA, and 200 kV accelerating voltage.

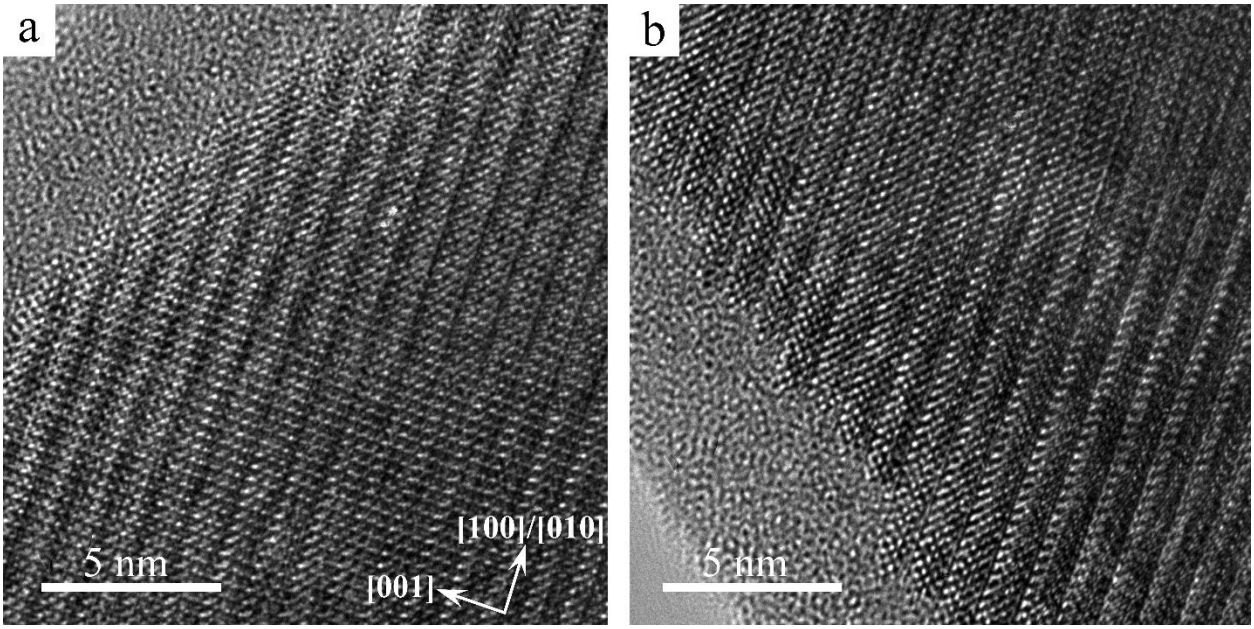


Figure 4.6: High magnification HRTEM images, taken along [100]/[010], of He-irradiated samples show no obvious signs of local cascades or intercalation damage.

4.2.1.2. Ne-ions

Figure 4.7 presents typical images taken from (a) pristine and (b) a sample following 350 keV Ne-irradiation conducted at room temperature to a fluence of 10^{13} cm^{-2}. The Ne-ion fluence was three orders of magnitude lower than the He-irradiated sample shown in Figure 4.5 & Figure 4.6, and so it is not expected that there will be much obvious sign of damage. However, the Ne-ions dpa estimated for the TEM foil, is several times greater compared to He-ions (Table 4.1), due to its larger mass and lower mean free path. A qualitative assessment of about a hundred HRTEM images from this Ne-irradiated sample show no identifiable damage, and a typical image is shown in Figure 4.7.

Despite the fact that clear structural changes were not observed in these Ne-irradiated samples, it cannot be stated explicitly that the damage introduced by these ions is too subtle to be seen in TEM. Van Tendeloo et.al. [272] studied ion-irradiation effects in GdBCO using HRTEM and

showed small amorphous cascades created by Ne-ions accelerated to 200 kV, which is lower than the energy used in the current study. However, Van Tendeloo et.al. experiment design was different and the irradiation took place on a bulk material rather on TEM lamella, which is different to this in-situ experiment where most of the Ne ions are expected to pass through the TEM foil (Figure 4.4).

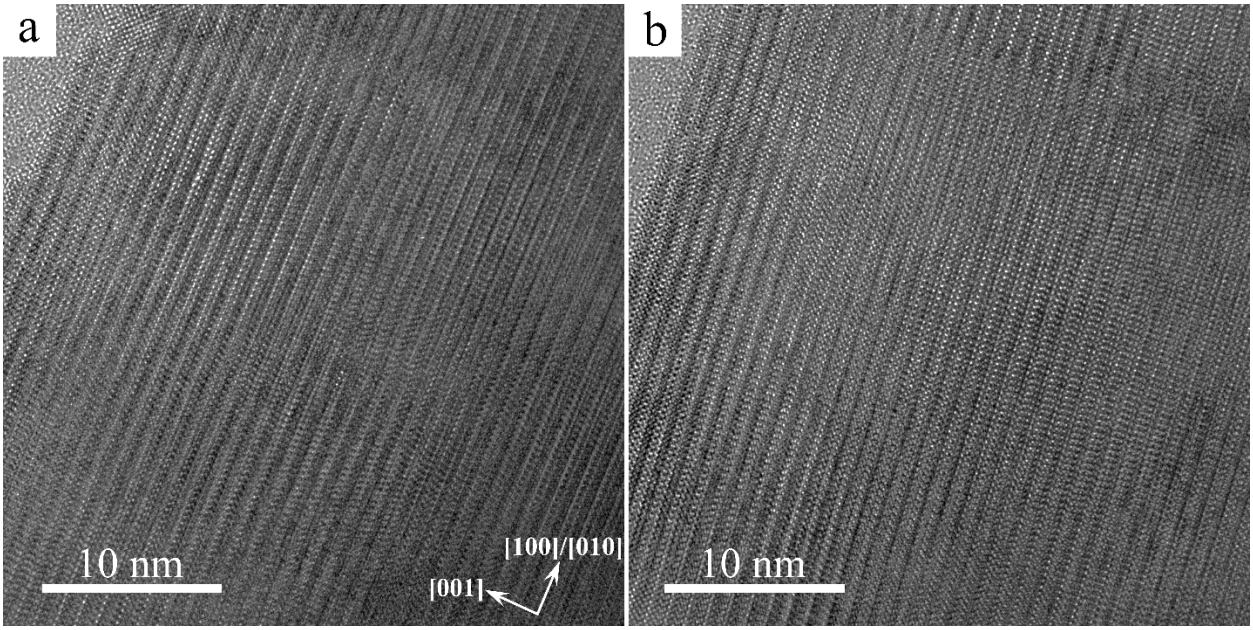


Figure 4.7: Typical HRTEM images taken along [100]/[010] from (a) pristine and (b) Ne-irradiated samples. Note that these images, were not taken from the same sample.

4.2.1.3. Ar-ions

Ar-irradiation was also undertaken with identical accelerating voltage and fluence as the Ne-irradiated sample. Figure 4.8 shows two typical HRTEM images of Ar-irradiated samples. It can be seen that the overall lattice structure is somewhat less regular compared to a pristine sample (e.g. Figure 4.7a), as can be seen from the many images of Ar-irradiated material collected for this study (see Appendix A: Figure S- 1). The arrow in Figure 4.8a points to an amorphous/highly distorted region a few nanometres in diameter that can probably only be seen

clearly because of its proximity to the very edge of the thin foil. The existence of amorphous cascades in this set of samples is expected since Ar-ions are heavier than Ne-ions and the damage is located at lower penetration distances (Figure 4.4). Similarly, the red circles in Figure 4.8b point to local lattice distortion that is less visible due to the higher thickness in these regions and thus the images will be an average of damaged/undamaged regions through the sample thickness (as was described in the case of neutron-irradiated samples). Since the extent of the damage induced by Ar-ions is less visible than that from Kr-ions (shown below - 4.2.1.4) calculating the density of these damage cascades density would be very inaccurate.

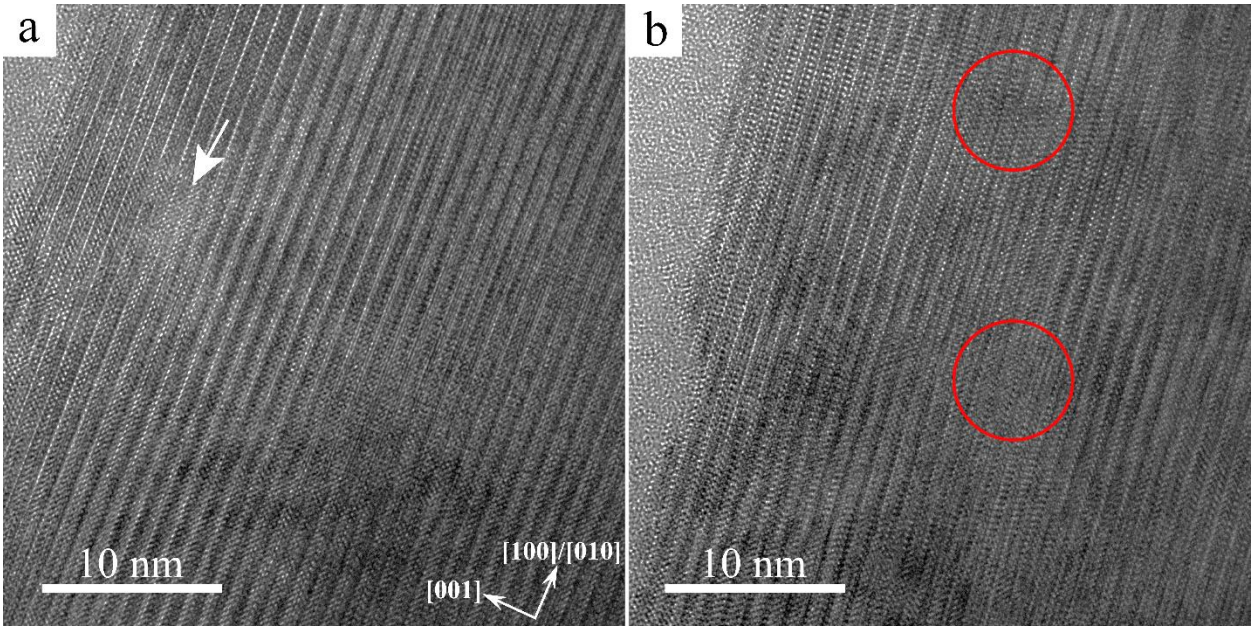


Figure 4.8: HRTEM images of Ar-irradiated samples taken along [100]/[010]. The irradiation took place at room temperature, 350 kV accelerating voltage, and a fluence of 10^{13} cm^{-2}. The white arrow in (a) points to a local amorphous/highly distorted damage cascade, similarly to the circles in (b) that show potentially buried cascades.

4.2.1.4. Kr-ions

A typical HRTEM images after heavier Kr-irradiation to a fluence of 10^{13} cm^{-2} is shown in Figure 4.9b, compared to a pre-irradiated image in Figure 4.9a taken from exactly the same region on the TEM foil using the same imaging conditions. It can be readily seen that the extent of damage is far greater than achieved by Ar-irradiation to the same fluence (Figure 4.8), and that the REBCO matrix is decorated with a very high density of local amorphous cascades. The BZO nanorods seem to show higher durability to irradiation damage as the one in this image retains at least partial crystallinity extending into the amorphous sample edge (see arrows). Though it is not possible to count the number of cascades since they overlap, according to Table 4.1, the average dpa value expected in a 100 nm TEM foil produced by Kr-ions is about two times greater than expected for Ar-ions, so it is not surprising that more damage can be seen.

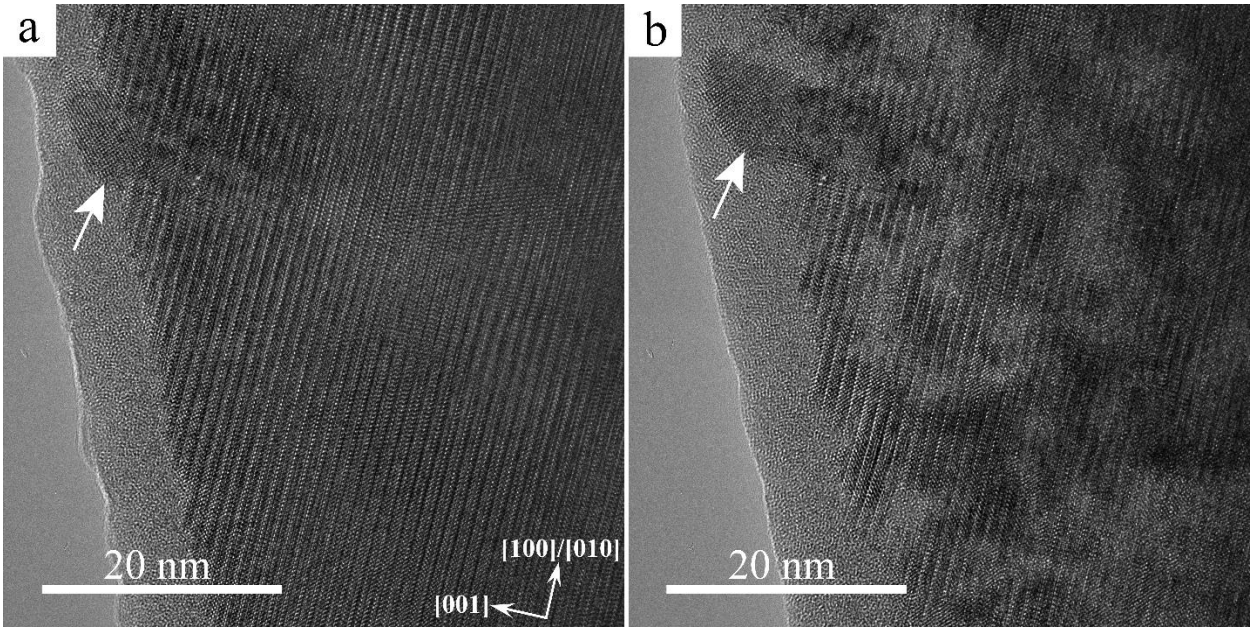


Figure 4.9: Direct HRTEM image comparison, taken along [100]/[010], from (a) pre- and (b) post- Kr-irradiation to a fluence of 10^{13} cm^{-2}. The arrows point to partially-crystalline BZO rod at the fully-amorphous sample edge. The images were taken from exactly the same region under the same microscope imaging conditions, i.e. 800 K magnification, ZA, and 200 kV accelerating voltage.

4.2.1.5. Xe-ions

The last of this series of irradiation experiments was undertaken using Xe-ions starting at 30 keV and increasing at 65 keV intervals up to 350 KeV (used for Ne, Ar, and Kr ions). Lowering the accelerating voltage of the incident ions has several effects on the nature of the irradiation damage. The two principal effects are decreasing the mean free path (λ) that measures the average penetration of the incident ions into the target material (as illustrated in Figure 4.10 for Xe-ion irradiation at two different energies), and the lower energy transferred to the primary knock-on atoms (PKA). Therefore, it is not straightforward to predict whether increasing the energy will lead to more severe damage in a thin TEM foil. In part, this is because the depth at which the damage peak lies in the sample surface depends on the ion energy.

SRIM calculations on 30 and 350 keV Xe-ion implantation into YBCO (see example of 95 and 350 keV in Figure 4.10) show that the mean free path (λ) at the lower energy is small, so the damage created by these low energy ions will lie mostly 20-30 nm from the sample surface. The higher energy Xe ions will create damage to depths in excess of 100 nm, which leaves the irradiated TEM lamella unaffected. Figure 4.11 shows HRTEM images following Xe-irradiation with increasing energies of 30, 95, 160 and 225 keV from (a) to (d), respectively. The other irradiation parameters, temperature and fluence, were kept constant. It can be easily seen that 30 keV ions do not cause visible amorphous regions, whereas the same fluence of higher energy ions first damages the thin regions close to the sample edge, with increasing damage accumulation at thicker regions up to a point of almost compete amorphisation extending to a large distance from the edge (Figure 4.11d).

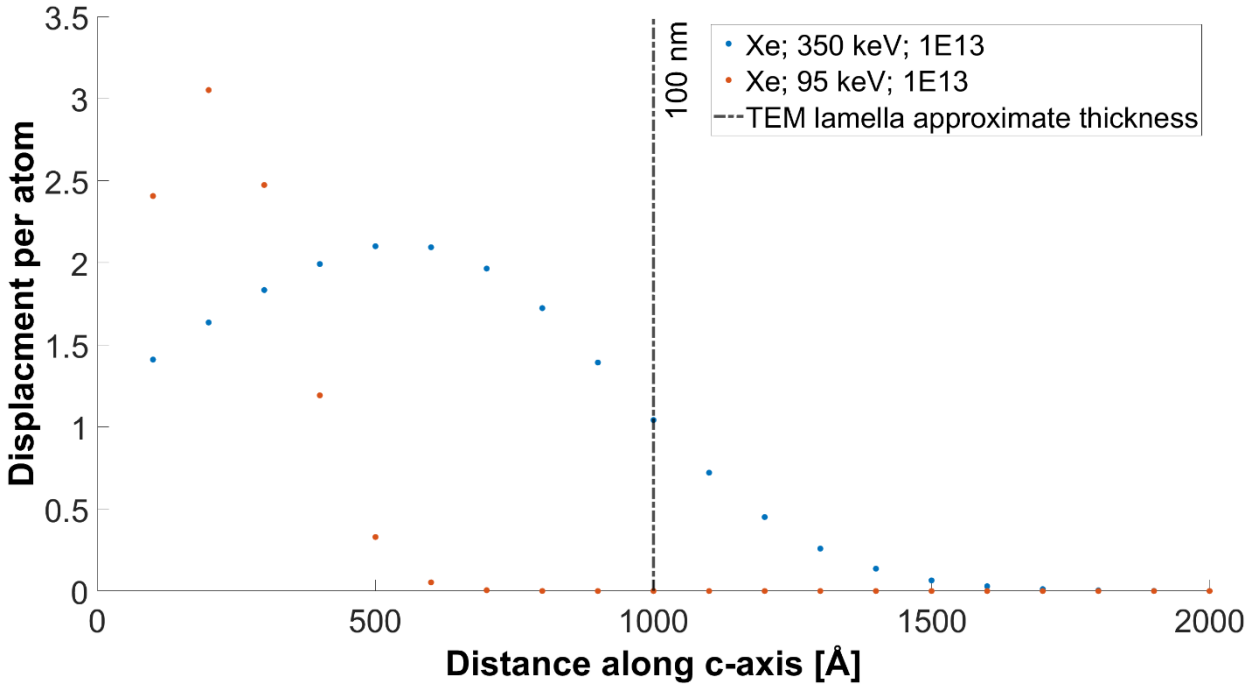


Figure 4.10: Displacement per atom (dpa) as a function of depth. The dpa calculation was performed according to SRIM output with Xe-ion incident into YBCO. The vertical dotted line marks the approximate thickness of the TEM foil.

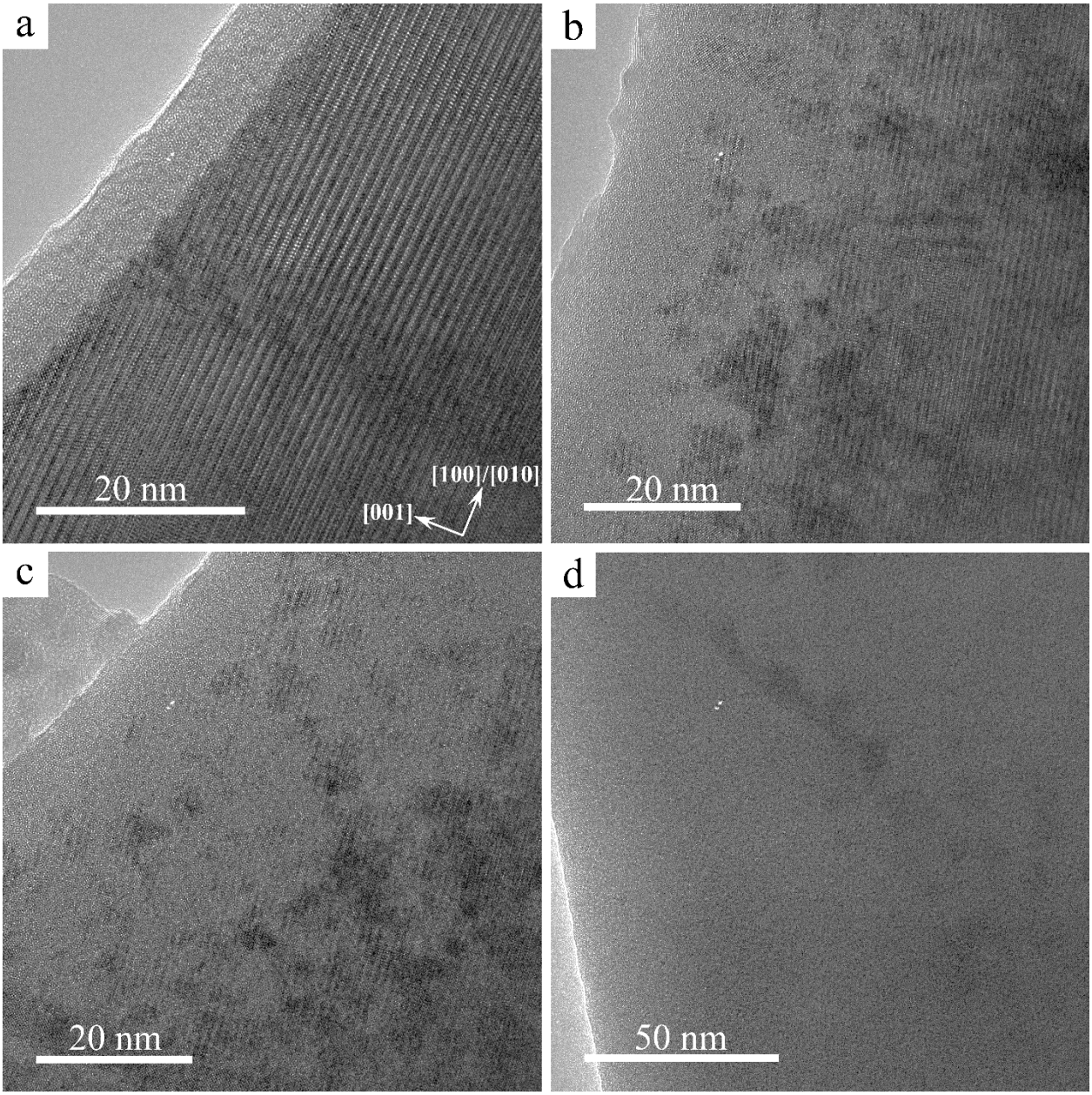


Figure 4.11: HRTEM images taken along [100]/[010] of Xe-ion irradiated samples. The fluence and temperature were kept constant, 10^{13} cm^{-2} and 298 K, whereas the energy was 30, 95, 160, and 225 keV for a, b, c, and d, respectively.

4.2.2. The effect of sample temperature during irradiation

As has been discussed in section 5.4, the sample temperature during irradiation is an important factor that can influence the mechanisms of damage evolution. This is especially important for

fusion applications where the operating temperature of the superconducting materials in the magnets are likely to be around 20 K [27]. In this section, I will focus on in-situ irradiation experiments with heavy Xe ions (where the damage mechanism has been shown above to be primarily by cascade formation) at different irradiation temperatures.

Figure 4.12 shows two pairs of images taken from the same regions of TEM foils pre (left figures) and post (right figures) irradiation, at two sample temperatures. The irradiation parameters were chosen to be Xe-ions accelerated by 350 kV to a nominal fluence of 10^{13} cm^{-2}. As discussed in section 3.4.4, the reported fluence was higher that the real fluence on the sample, but since the experiments were conducted on the same day, one can assume that the fluence was identical and the only difference was the irradiation temperature. Other images from samples at both temperatures during the same experiment are shown in Appendix A: Figure S- 2 & Figure S- 3. It is clear that the damage generated at 100 K (Figure 4.12d) is much more severe than that at room temperature (Figure 4.12b). The arrow in Figure 4.12b points to a single amorphous cascade generated by the Xe-ions. Other brighter patches are also likely to be damage cascades but were generated in regions where the sample is thicker. On the other hand, in Figure 4.12d the overall degree of damage is much higher and it is hard to identify individual cascades. Even the $BaZrO_3$ nanorods appear to be damaged at the lower temperature. These observations will be correlated with lattice parameter measurements (section 5.4) and higher image entropy values (see section 6.4.3).

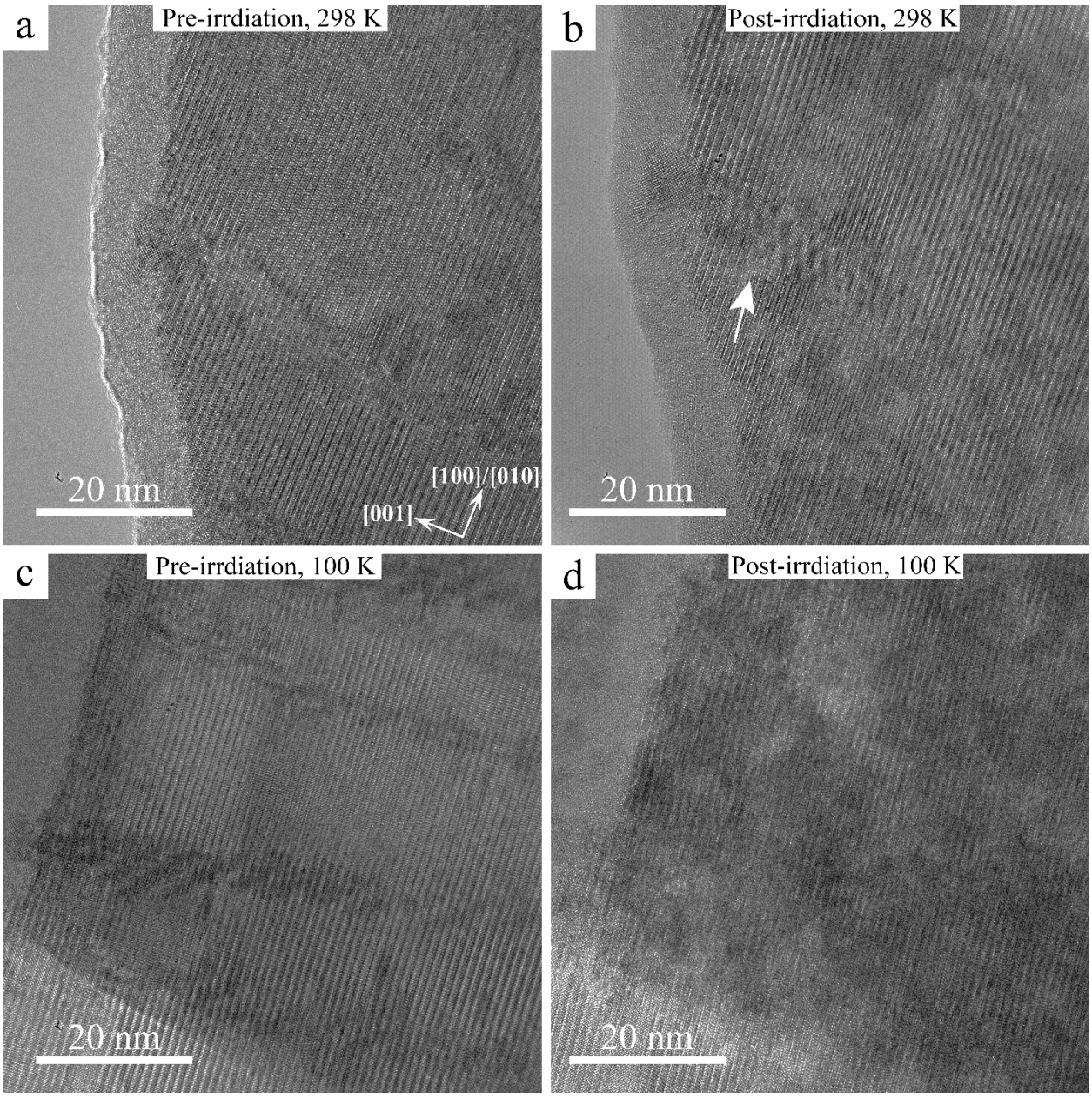


Figure 4.12: Direct HRTEM image comparison, taken along [100]/[010], from pre- (a,c) and post- (b,d) Xe-irradiation experiments conducted at room temperature (298 K) (b) and at 100 K (d). The images were taken from exactly the same regions under the same microscope imaging conditions, i.e. 800 K magnification, [100]/[010] ZA, 300 kV accelerating voltage, and a fluence of 7 × 10^{12} cm^{-2}.

More serious accumulation of damage at lower irradiation temperatures is a well understood phenomenon. Panghal et.al. [409] conducted irradiation experiments on $La_2Zr_2O_7$ at 88 and 300

K at 3 different fluences and found an enhancement in lattice strain at all fluences at 88 K compared to 300 K, measured with *grazing incidence XRD* (GIXRD) and Raman Spectroscopy. The authors hypothesised that sluggish diffusion, migration and recombination of point defects at low temperatures results in more pronounced damage. This is consistent with other irradiation studies conducted on ceramics, such as $SrTiO_3$ under 1 MeV Au irradiation from 150 to 400 K [410], $LiNbO_3$ irradiated with 40 keV He and 350 KeV Ar ions at 15 and 300 K [411], and β-SiC under 1.5 MeV Xe-ions over a temperature range from 40 to 550 K [412]. Gong et.al. [413] also suggest that more severe irradiation-induced damage takes place at lower temperatures due to the contribution of the thermal free energy (ΔG_{therm}) that shifts the thermodynamic stability of the amorphous phase to lower fluences.

So the evidence from the literature supports the qualitative observations from the HRTEM images in Figure 4.12 that irradiation damage at 100 K is more severe than at room temperature due to suppression of dynamic defect recovery mechanisms [232]. This will discussed further in sections 5.5.4 and 6.4.3.

4.2.3. Summary

It is not easy from the images shown above to analyse quantitatively the transition from more homogenous lattice damage with light ions to the formation of local amorphous regions (cascades) following heavy ion irradiation [414]. The former mechanism is dominated by the accumulation of point defects until the whole lattice becomes amorphous to lower the energy of the material [415], [416]. By contrast, the latter mechanism assumes the generation of local amorphous cascades that start overlapping, generating a gradually increasing amorphous fraction [234].

A crucial differentiating factor in the in-situ irradiation experiment presented here compared to bulk samples irradiation is the average dpa in the TEM lamella ~100 nm thickness, which, leads to higher dpa as the ion mass increases, 0.0095 and 1.7188, for He- and Xe-ions, respectively (Table 4.1). In the case of He-irradiation, amorphous cascades are not created but rather small distorted volumes. As the fluence goes up, this kind of damage is manifested in HRTEM images that look degraded with less vivid layer structure and a patchy background intensity, but without clear loss of crystallinity (Figure 4.5). Samples irradiated with slightly heavier Ne ions (Figure 4.7) show neither obvious signs of the creation of amorphous cascades nor a degraded matrix. As discussed earlier [272], 350 keV Ne-ions have sufficient energy to generate small amorphous cascades, but are also likely to degrade the lattice via the accumulation of point defects, i.e. a mixture of homogenous and heterogeneous amorphisation. However, it is very likely that the dpa on the TEM foil was too low since most of the Ne-ions pass through the TEM foil. Lattice degradation following Ar-ion irradiation (Figure 4.8) is dominated by heterogeneous amorphisation (cascades), an intermediate between the damage created by Ne and Kr ions (Figure 4.9). Lastly, the Kr-ion damage mechanism is clearly dominated by heterogeneous amorphisation manifested in amorphous cascades densely scattered across the matrix. Using the heavier Xe-ions at different energies, results in almost complete amorphisation due to overlapping of relatively large amorphous cascades observed (e.g. Figure 4.11b).

In conclusion, this section has presented direct observation by HRTEM of neutron-induced irradiation cascades and discussed the difficulty in visualising the more subtle damage that must be situated in between these amorphous regions. In addition, the transition from homogenous amorphisation mechanisms in the case of He-ion irradiation to the heterogeneous (cascade)

mechanism after irradiation with ions of different mass was presented. Again, the nature of any lattice damage between the cascades is hard to determine in this imaging mode.

5. STEM/HAADF image analysis

5.1. Introduction

Traditionally, crystal structure and lattice parameters are accurately measured using *X-ray diffraction* (XRD), and refinement techniques such as the Rietveld process [417] allow precise quantification of phase content and lattice parameters in multiphase materials from experimental powder XRD data. X-rays have large mean free paths (λ) in many materials, and thus result in poor spatial resolution, and so XRD is typically a bulk analysis method. On the other hand, electron diffraction performed in a TEM is a powerful tool to analyse structure with a spatial resolution of hundreds of nanometers using a *selected area* (SA) aperture and down to a few nanometers using nanodiffraction [418]. However, the relatively poor resolution in electron diffraction does not allow accurate determination of lattice parameters, even with careful calibration.

As mentioned in section 3.3, using the STEM/HAADF imaging mode gives a good identification of atomic locations, and therefore can be utilised to measure local lattice parameters, but the absolute calibration of values is difficult because it is controlled by the settings of the particular microscope, image acquisition mode (one-frame / stacks), and stage drift (section 3.5.1.4). The implementation of mathematical models like that by De Backaer et.al. [396] helps to determine the atomic column positions in lattice images to picometer precision. Using a mixture of state-of-the-art aberration-corrected microscopes operated under carefully controlled conditions with superior mathematical tools opens the door for exploring local changes in lattice parameters in

complex crystals as a result of irradiation damage. In addition, the main advantage of measuring structural properties locally, is the ability to extract and compare different statistical parameters, such as standard deviation, kurtosis, and skewness, that are helpful to understand the specific types of lattice damage that might occur in different samples.

Local variations in atomic positions are inevitably present in images taken from REBCO crystals, and this is particularly true in coated conductor samples which contain a high density of stacking fault defects, small growth artefacts like antisite defects, vacancies and interstitials that are impossible to detect individually, and also the damage introduced during sample preparation [240]. Figure 5.1a shows a typical high-quality, high magnification STEM/HAADF image stack (10 frames), and Figure 5.1b shows the fitted positions of atom columns in the Ba_1 (red), RE (blue), and Ba_2 (green) sublattices. The local variations in the a/b-axis and c-axis lattice parameters, derived from the atom column fitting, are shown as 2D plots in Figures (c) and (d), respectively. It can be seen that local variations of structural parameters always exist even in nominally 'perfect' samples that do not contain any obvious stacking defects, due to a combination of intrinsic sample imperfections, and extrinsic factors like thermal fluctuations, local FIB damage, and computational accuracy. Only by comparing data from the same sample in pristine and irradiated conditions one can factor out the effect of the intrinsic damage landscape on the images. Although the data is inherently scattered as shown, for example, in Figure 5.1, the experimental results presented in this section are statistically significant as they were extracted from a large number of individual unit cells for each sample type (>10,000).

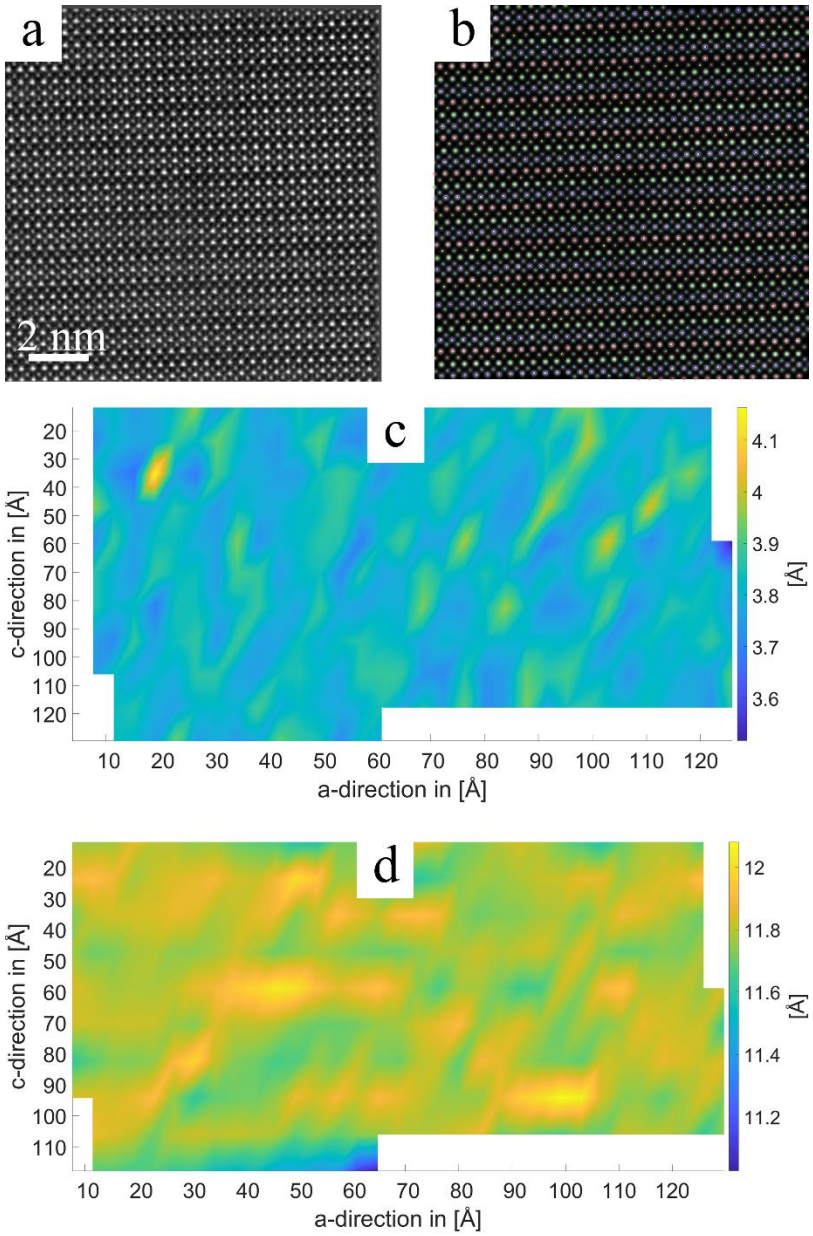


Figure 5.1: Analysis of local variations in lattice parameters extracted from a STEM/HAADF image of an unirradiated REBCO sample. (a) STEM/HAADF 10-frame stack image taken along [100]/[010] ZA. (b) Fitting of Ba-(GdY) sublattices, red, blue, and green colours represent Ba_1, Gd/Y, and Ba_2 atom columns, respectively. (c-d) local colour maps of (c) the a/b and (d) the c lattice parameters calculated from the Ba_1 atom locations.

In order to be confident that the output, i.e. atomic locations, is as accurate as possible [396], the input images should be of the highest quality possible. There are at least two main considerations

that need to be taken into account here: the image acquisition procedure, and the capabilities of the different microscopes on which the images were acquired (see section 3.5.1.4). In the following section, the structural parameters have been corrected using the Au nanoparticles calibration presented in Figure 3.20 in order to take into account these different conditions. Even with this calibration of the microscopes, it is vital to compare images taken under the same conditions, namely on the same microscope and only comparing data from either image stacks or from single-frame images, and not mixing them up. In the rest of this chapter, the dataset used is written in the figure/table caption. Inter- and intra-cell distance presented as a fraction of the c-axis can be directly compared, but only after dividing *each* image by its average c-axis lattice parameter, which presumes that the different magnifications do not change the ratio of the Ba ion distances (see more details in section 3.5.1.5). In this section, I will present the structural parameters directly extracted from STEM/HAADF images, and correlate the statistical changes to the irradiation mechanisms.

5.2. Neutron and ion irradiation mechanisms

5.2.1. Analysing image sets

Figure 5.2 shows a bar chart of how the average lattice parameters change, in percentage terms, compared to an unirradiated (pristine) sample of the same CC, extracted from multiple images of a neutron irradiated sample at a fluence of 3.3×10^{18} cm^{-2}, a sample Xe ion irradiated to a fluence of 7×10^{12} cm^{-2} and a sample He-irradiated to a fluence of 1×10^{16} cm^{-2}. It can be seen that the change of a/b-axis lattice parameters is very small for the Xe-irradiated samples, slightly higher for the neutron-irradiated sample (0.68% increase), and highest for the He-irradiated sample (1.82% increase). The c-axis lattice parameter on the other hand does not display the same trend, expanding a similar amount as a result of both Xe- and He-irradiation, but slightly shrinking as a

result of neutron-irradiation. Table 5.1 shows the absolute lattice parameter values, their ratios $\left(\frac{c}{a}\right)$, and unit cell volume, together with a comparison to XRD measurements on the same sample batch [419]. The XRD results show 2.00% enlargement of the c-axis lattice parameter from 11.725 Å in the pristine sample to 11.960 Å after He-ion irradiation, close to the 1.82% expansion extracted from the STEM images. Additionally, it is interesting to note that following He-ions irradiation, the unit cell becomes more tetragonal and the average a/b-axes lattice parameters converge to what was measured using the STEM images; however, the XRD results for pristine sample are slightly larger than to the measured values. He-irradiated XRD results proximity to the values measured in my analysis give some confidence that the STEM image analysis can give reliable results even though the volume of material studied is so much smaller.

From the unit cell volume of the irradiated samples compared to the pristine sample it can be seen that in all cases the unit cell volume does increase in these samples. However, the REBCO structure is inherently anisotropic, and it is interesting to note that the degree of anisotropy, defined as $\left(\frac{c}{a}\right)$, is also a function of the irradiation species. Also from Table 5.1, it can be seen that the effect of neutron and He-ion irradiation is different to that of the heavy Xe-ions, as the unit cell expansion in the former is dominated by lengthening of the a/b-axis whereas Xe ion damage produces expansion mainly along the c-axis.

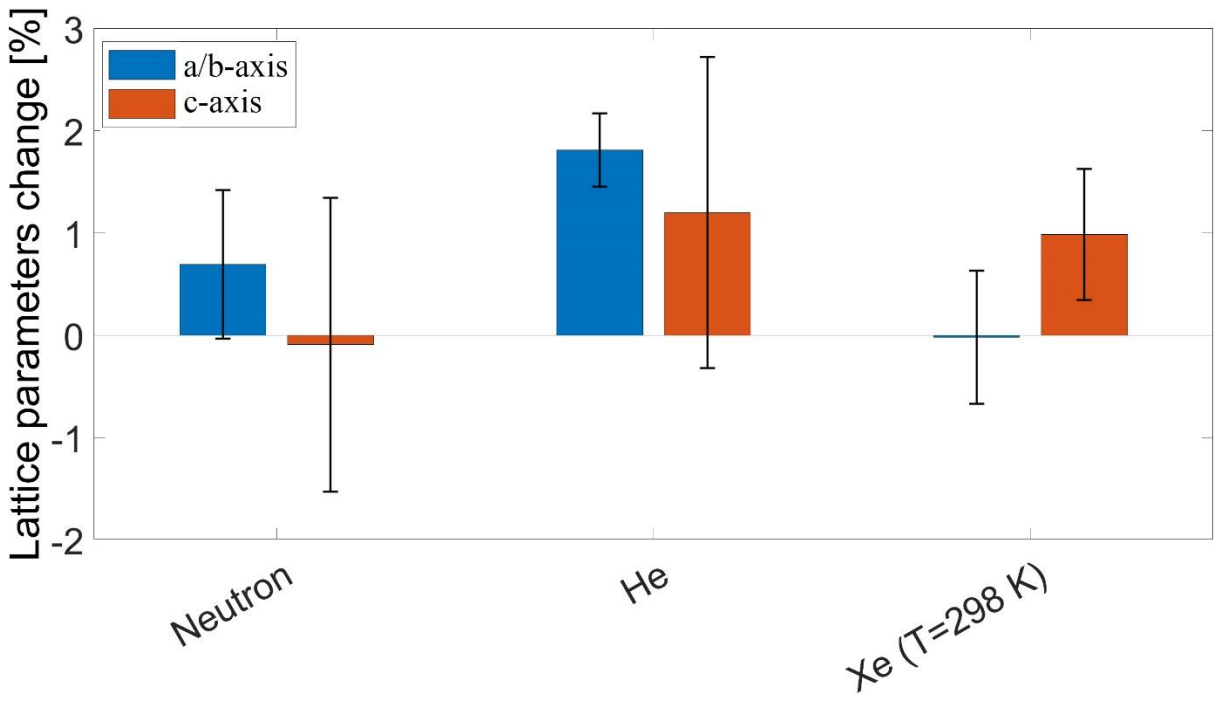


Figure 5.2: Bar charts comparing a/b (blue bars) and c-axis (red figure) lattice parameters of neutron-irradiated to a fluence of 3.3×10^{18} cm^{-2},He-irradiated to 1×10^{16} cm^{-2}, and Xe ion irradiation conducted at room temperature to a fluence of 7×10^{12} cm^{-2}. The data is shown as percentage change compared to pristine sample. The errorbars stand for the standard deviation. The values were extracted from one-frame images taken on the ARM300CF microscope, by the analysis of 62, 14, and 18 images of neutron-irradiated, Xe-irradiated at 298 K and He-irradiated samples, respectively.

Table 5.1: REBCO structural parameters as were extracted from STEM images (one-frame images taken on the ARM300CF microscope) for un-irradiated (pristine) and three irradiated samples; neutron-irradiated, Xe-ion at 298 K and He-ions. The first two rows show the average REBCO lattice parameters (a/b- and c-axis). The third and forth rows present a comparison of unit cell volume and c/a axes lattice parameter ratio (assuming a/b-axes lattice parameters are equal). For the sake of comparison, the c/a ratios taken from the literature are 3.028 and 3.026 for YBCO and GdBCO, respectively. The presented shift from the theoretical values of the a/b-axis compared to c-axis is explained in section 3.5.1.4.1. The last three rows quote the a-, b-, and c-axis lattice parameters extracted from X-ray diffraction (XRD) measurements [419].

	Pristine	**Neutron-irradiated**	**He-ions**	**Xe-ions at 298 K**
a/b-axis lattice parameter [Å]	3.796	3.822	3.865	3.795
c-axis lattice parameter [Å]	11.687	11.676	11.827	11.802
Unit cell volume [Å^3]	168.421	170.596	176.656	169.995
c/a ratio	3.079	3.055	3.060	3.110
XRD results - a-axis lattice parameter [Å] [419]	3.820	---	3.860	---
XRD results - b-axis lattice parameter [Å] [419]	3.890	---	3.870	---
XRD results - c-axis lattice parameter [Å] [419]	11.725	---	11.960	---

Analysis conducted on all images analysed in this section (see Appendix B: Table S- 1) of the intra-cell Ba_1-GdY and GdY-Ba_2 distances as a fraction of c-axis are very similar in all the samples, and can also be summed together to get average Ba_1-Ba_2 inter-cell fractions. These Ba_1-GdY and GdY-Ba_2 distances are identical in the perfect unit cell according to the Wyckoff atomic positions [63], and do not change following the irradiation conditions studied here, which

means that there is no preferential irradiation defects generation in one of the Ba atoms with respect to Gd/Y atom.

Because spacing of each set of planes along the c-axis can be extracted, one can be more specific about which part of the unit cell changes height as a result of irradiation: the portion containing the Cu(2) planes (intra-cell), or the portion containing the Cu(1) chains. Figure 5.3 presents the percentage change (compared to pristine sample) in the breakdown of the c-axis lattice parameter into the intra-cell Ba_1-Ba_2 spacing and the inter-cell Ba_1-Ba_2 spacing, both as a fraction of the average c-axis lattice parameter measured *per image*. These inter- and intra-cell fractions are presented in Table 5.2. Both the intra- and intra-cell fractions are similar for the pristine and neutron-irradiated samples, with intra-cell fractions of 0.630 and 0.626 and inter-cell fractions of 0.370 and 0.374, respectively. It is worth mentioning that the reason why intra-cell and adjacent-cell Ba_1-Ba_2 distances as a fraction of average c-axis lattice parameter sometime deviate slightly from unity, relies on geometrical considerations where the three atoms do not lie on a straight line. On the other hand, the He-irradiated sample shows a smaller intra-cell Ba_1-Ba_2 fraction. Xe-irradiation gives a much more pronounced change in the partitioning of the unit cell, and one can see that the overall expansion of the c-axis lattice parameter is mainly a result of a large increase in the inter-cell fraction. It is worth mentioning that for Xe-irradiated sample (T=298 K) the inter-cell *absolute* distance shrinks compared to pristine sample. The ratios between the intra- and inter-cell Ba_1-Ba_2 fractions are 1.703, 1.674, 1.655 and 1.541 for pristine, neutron-irradiated, He-irradiated and Xe (T=298 K) samples, respectively. From this simple analysis, it can be concluded that irradiation impacts the relative spacing of the Ba_1-Ba_2 planes in the c-axis direction of the REBCO unit cell differently, depending on the projectile.

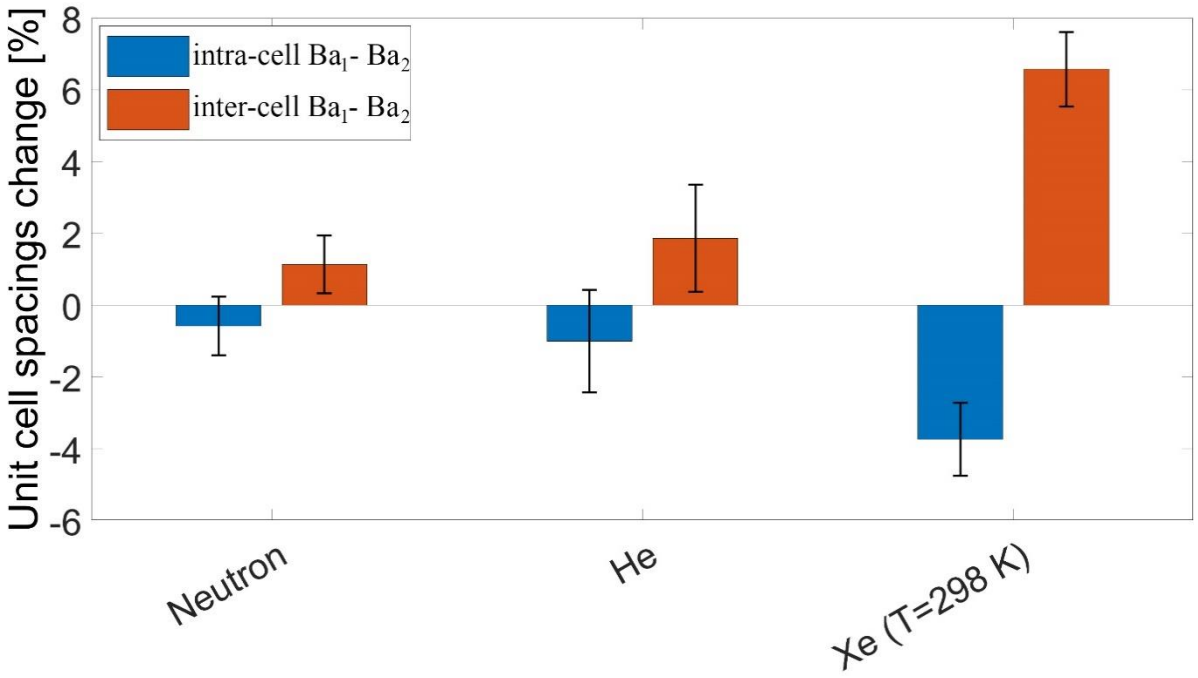


Figure 5.3: Comparison of the inter- (red bars) and intra-cell (blue bars) Ba_1-Ba_2 distances as a fraction of average c-axis lattice parameter in neutron-irradiated, He-irradiated, and Xe-ion (T=298 K) presented as a percentage change compared to pristine sample. The errorbars stand for the standard deviation. The analysis includes one-frame & stacks images taken on the ARM300CF microscope.

Table 5.2: Inter- and intra-cell Ba_1-Ba_2 distances as a fraction of average c-axis lattice parameter for pristine, neutron-irradiated, He-irradiated, and Xe-ion irradiation at 298 K. The numbers are the average of one-frame & stacks images taken on the ARM300CF microscope.

	Pristine	**Neutron-irradiated**	**He-ions**	**Xe-ions (T=298 K)**
Inter-cell Ba_2-Ba_1 [fraction of c-axis]	0.370	0.374	0.377	0.394
Intra-cell Ba_2-Ba_1 [fraction of c-axis]	0.630	0.626	0.624	0.607

Figure 5.4 shows the probability distribution of a/b-axis lattice parameters calculated from individual unit cells in images from pristine, neutron-irradiated (3.3×10^{18} cm^{-2}) and He-irradiated

(1×10^{16} cm^{-2}) samples. All the distributions are fairly symmetric around the mean value (manifested in low skewness values, 0.004, 0.148, and 1.027 for neutron-irradiated, pristine, and He-irradiated, respectively), and roughly display a Gaussian shape. However, the new observation here is that there is a much wider distribution of a/b-axis lattice parameter values in the neutron-irradiated samples compared to the pristine or He irradiated samples. This broadening is due to an existence of inhomogeneous strain, defined as the gradient of the displacement fields [392], and thus it can concluded that the neutron-irradiated sample has large anisotropic microstrain along a/b-axis. This point is further emphasised when comparing the *full width half maximum* (FWHM) of the three sample types as shown in Appendix B: Table S- 2. However, the width of the distribution of the c-axis lattice parameters of these same neutron-irradiated samples is no larger than in the pristine and He-irradiated samples (Figure 5.5), and the slight shortening of the c-axis (Figure 5.2 & Table 5.1) is also shown here. Equivalent graphs containing only stack images also show lower c-axis parameter for the neutron-irradiated sample, which makes the argument of c-axis shrinkage even more statistically significant. The reader is referred to Appendix B (iii) for more details on the analysis on the statistical distribution parameters of the a/b-axis lattice parameters.

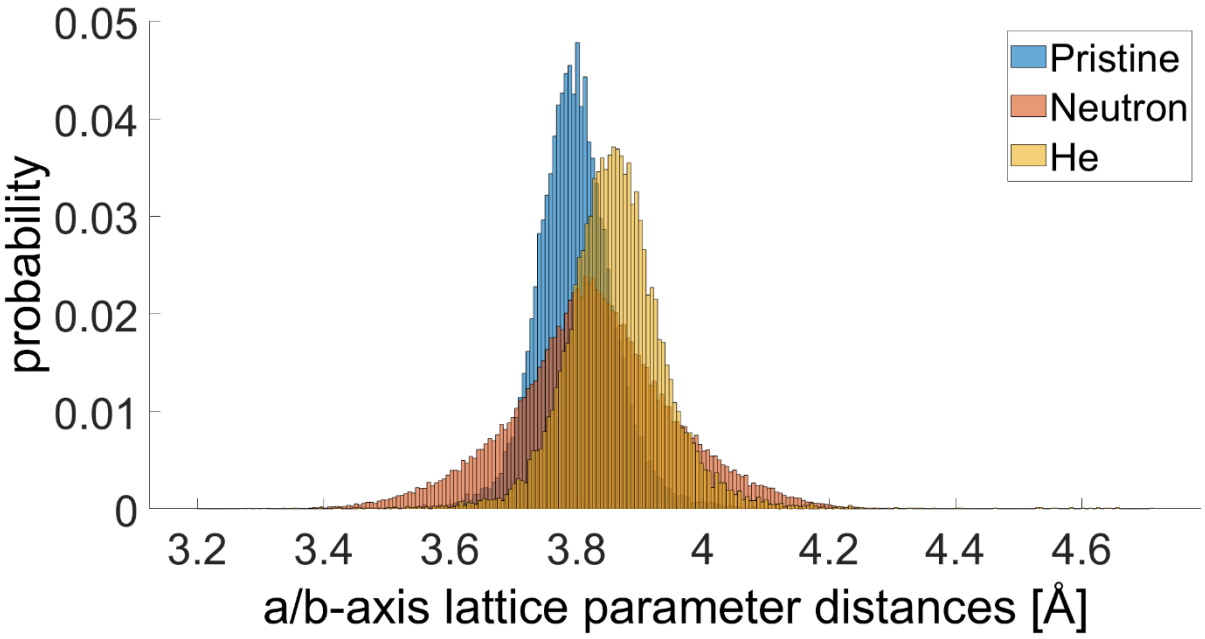


Figure 5.4: Normalised distribution of a/b-axis lattice parameters from pristine (blue bars), neutron-irradiated to a fluence of 3.3×10^{18} cm^{-2} (red bars), and He-irradiated to a fluence of 1×10^{16} cm^{-2} (yellow bars) samples. Data was taken from one-frame images taken on the ARM300CF microscope. 1% of extreme outliers were removed from every image to avoid distortion of the overall distributions.

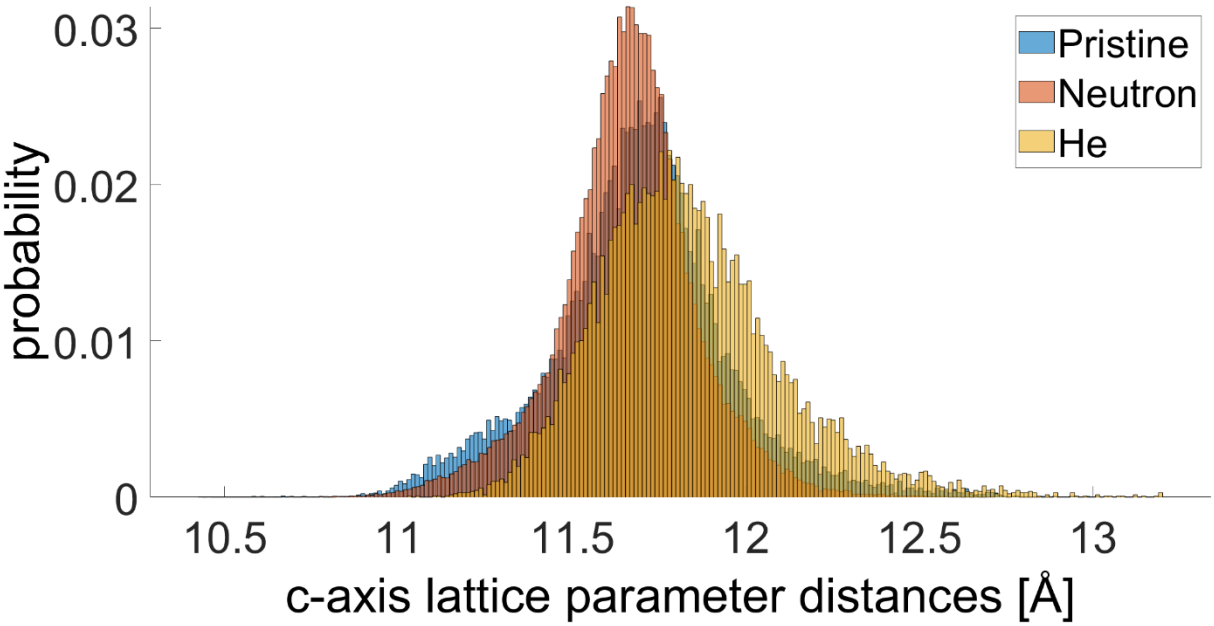


Figure 5.5: Normalised distribution of c-axis lattice parameters from pristine (blue bars), neutron-irradiated (red bars), and He-irradiated (yellow bars) samples. Data was taken from one-frame images taken on the ARM300CF microscope. 1% of extreme outliers were removed from every image to avoid distortion of the overall distributions.

It is also worth noting that the histograms do not show a double-peak of the a- and b-lattice parameters, which are known to be different by about 0.06 Å in pristine REBCO compounds [63]. Recalling that REBCO is characterised by a twinned structure on the scale of a few 10s of nm along a/b-axis [127], it is plausible to assume that STEM images contain regions of material aligned along both [100] and [010]. To analyse this in more detail, Figure 5.6a is a scatter plot of average lattice parameters where each symbol is taken from the average value from one whole image. There is a clear separation into two groups along the horizontal axis representing the a/b-axis lattice parameter, which could result from images that were taken along the [100] and [010] zone axes, respectively. The separation of the values - ~ 3.80 and 3.84 Å is also of approximately the correct magnitude. Figure 5.6b shows the probability density function of the lattice parameters collected from the same images and amounts to about 10,000 individual unit cells

a/b-axis lattice parameter measurements. However, this histogram can be deconvoluted into two Gaussian peaks as shown in Appendix B: Figure S- 5 & Table S- 4.

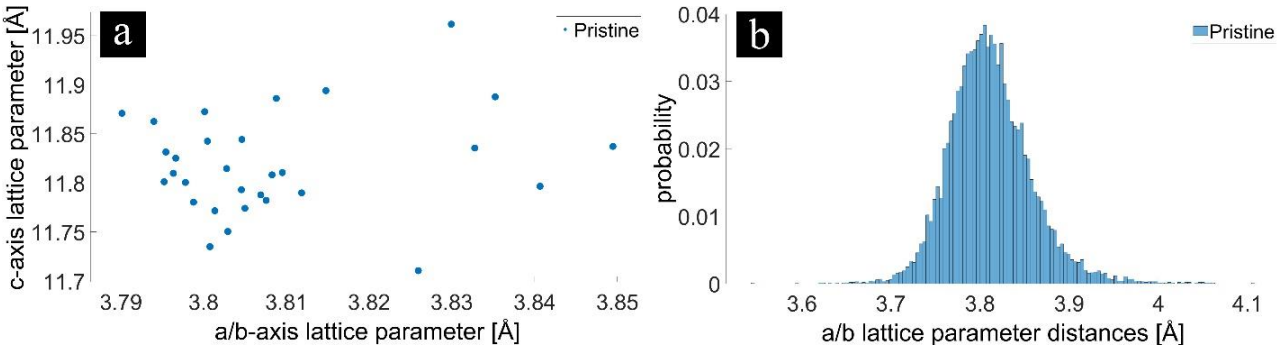


Figure 5.6: Lattice parameters of pristine samples shown as averages on a scatter plot (a) and a pair-wise a/b lattice parameters plotted as a histogram (b). Data was taken from stacks images taken on the ARM300CF microscope.

5.2.2. Analysing individual images

Up to this point, I have mostly analysed the characteristics of all the images together and ignored any variations between individual images taken from different regions of the sample that have not necessarily had exactly the same damage history. The histograms in Figure 5.4 & Figure 5.5 (previous section, 5.2.1) include all the lattice parameters measured *per unit cell*, and a typical image includes hundreds/thousands of data points. To investigate how the lattice parameters change between images, I have plotted the average lattice parameters of pristine, neutron-irradiated and He-irradiated on a scatter plot in Figure 5.7 (as was done in Figure 5.6a, but now for single-frame images). As expected, the a/b-axis lattice parameters of pristine and He-irradiated samples clustered around their averages (shown as cross markers), with the He data showing the systematically expanded lattice parameter described above (see Appendix B: Figure S- 6 for a clearer representation excluding the neutron-irradiated samples). In the case of the neutron-irradiated samples, however, the red symbols can be seen to lie across the whole range

from the lower end of the distribution of pristine lattice parameters to the upper end of the expanded He-irradiated a/b-axis lattice parameters. The two clusters for pristine and He-irradiated samples are emphasised by blue and yellow ellipses, whereas the neutron-irradiated samples scattered at a much greater range of a/b-axis lattice parameters. There could be two potential hypotheses for it, the first is that the neutron-irradiation scatter along a/b-axis accounts for two clusters that are formed, one at about 3.80 Å and the second around 3.84 Å, and each is likely to contain primarily one twin domain, the second is larger variability of the average a/b-axis lattice parameter per image. However, it would be hard to come up with a reasonable explanation why the neutron-irradiated sample domains will be different from pristine or He-irradiated samples and therefore presenting wider spread.

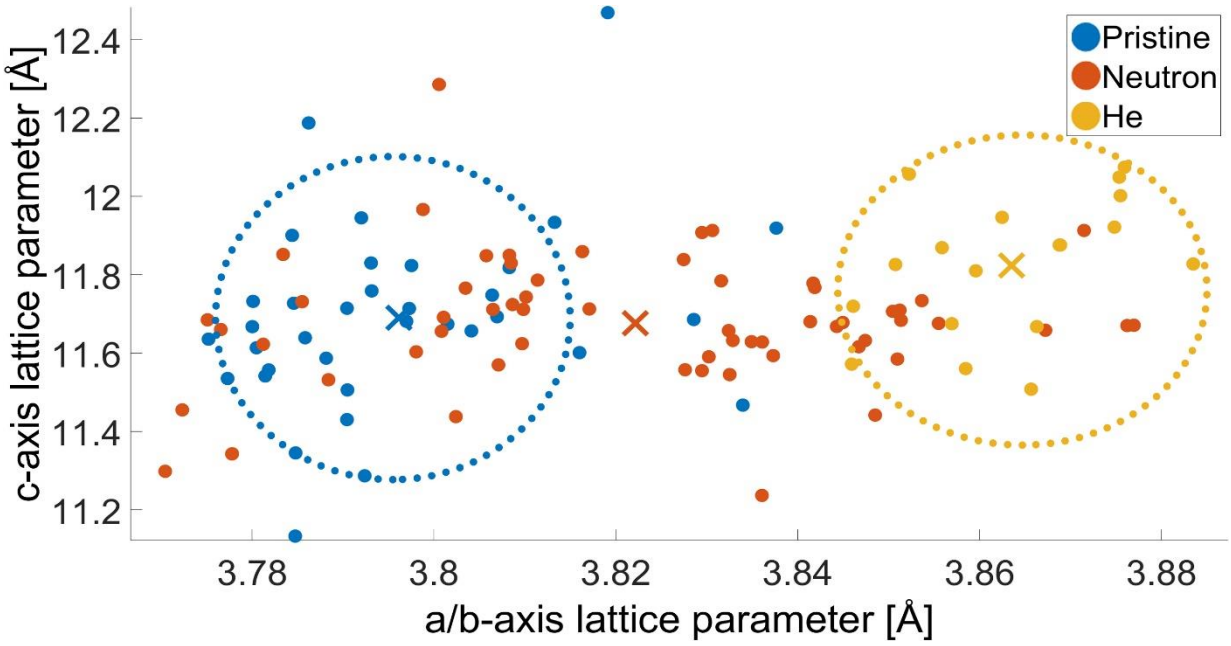


Figure 5.7: Scatter plot presenting the average lattice parameters per image for pristine (blue circles), neutron-irradiated (red circles), and He-irradiated (yellow circles) samples. The blue and yellow ellipses represent the clusters of pristine, and He-irradiated, respectively. The cross markers show the average lattice parameters of every sample type. The data includes one-frame images taken on the ARM300CF microscope.

To explore the length scale of the lattice parameter inhomogeneity, the standard deviation in lattice parameters within each image is shown in Figure 5.8 for pristine, neutron-irradiated and He-irradiated samples. The lattice parameter values for both pristine and He-irradiated sample cluster around relatively low standard deviations, but the neutron-irradiated samples show a second group of points with high standard deviations in a/b-axis lattice parameter only (along the x-axis in the graph). This observation calls for further analysis to determine whether the standard deviation in a/b-axis lattice parameter within an image correlates with the average a/b-axis lattice parameter for that image. To visualise this, Figure 5.9 displays a scatter plot of the average a/b-axis lattice parameters from each image, and their corresponding standard deviation values. The goodness of linear fitting ($R^2 = 0.013$) is very low and convincingly demonstrates that there is no correlation between the two values.

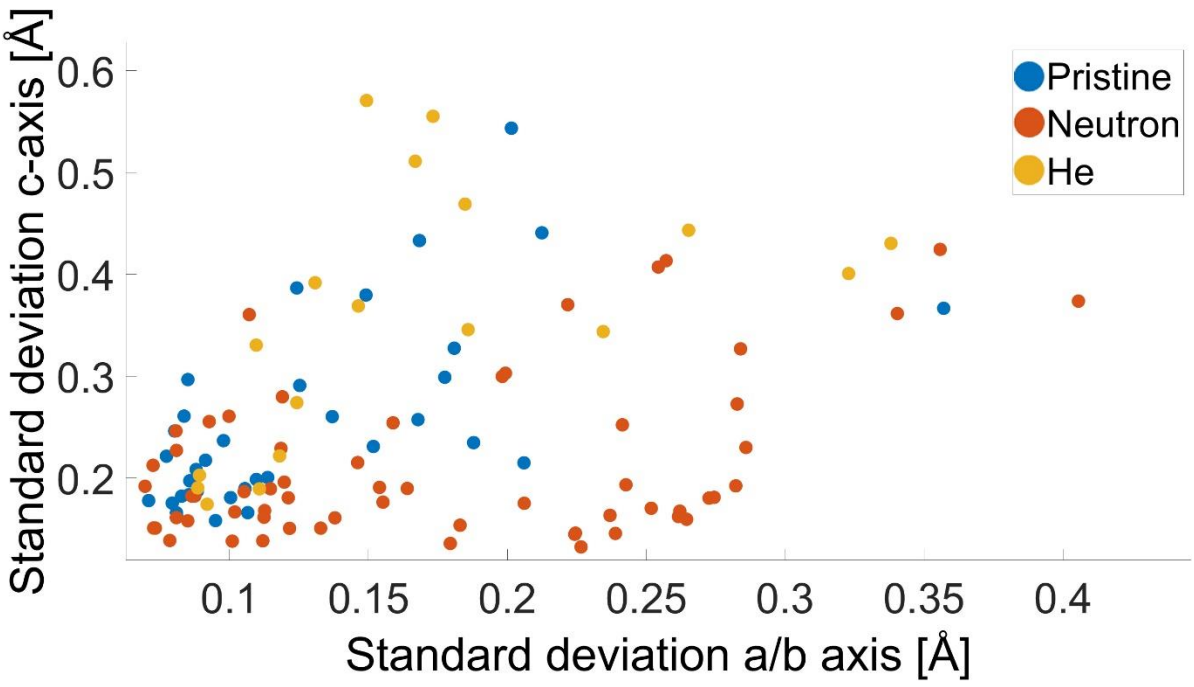


Figure 5.8: Scatter plot of standard deviations of a/b- and c-axes lattice parameters of pristine (blue circles), neutron-irradiated (red circles), and He-irradiated (yellow circles) samples. Data is taken from one-frame images taken on the ARM300CF microscope.

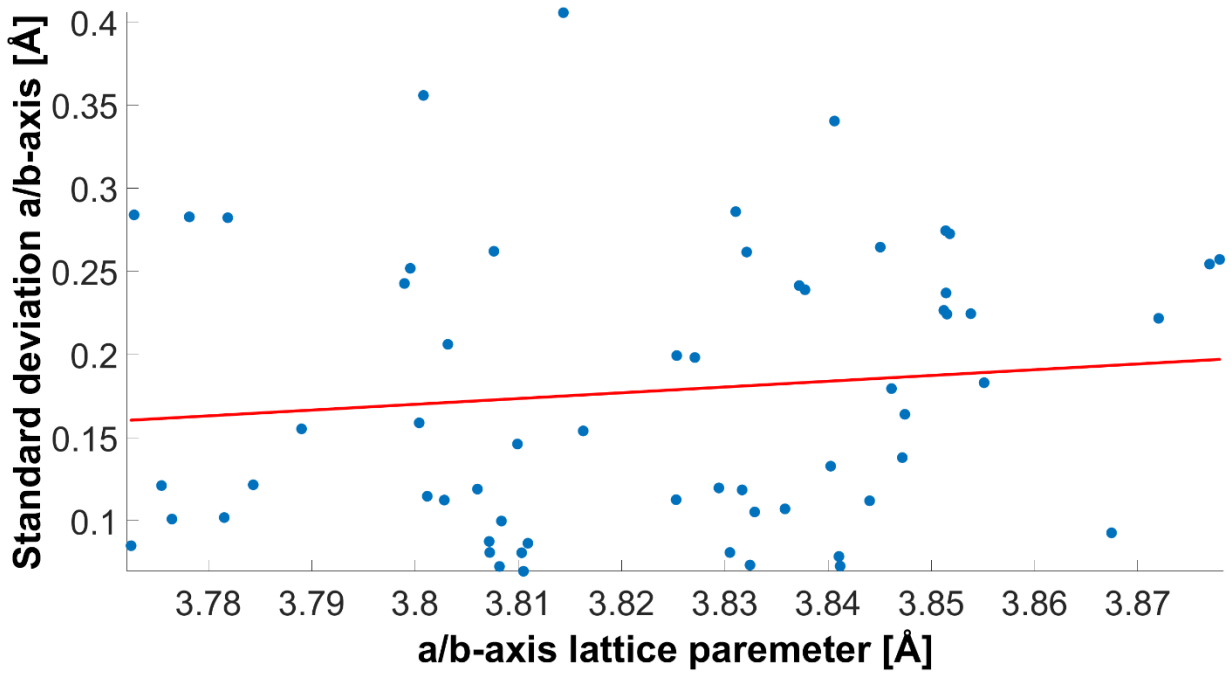


Figure 5.9: correlation between a/b-axis lattice parameters and their corresponding standard deviations in neutron-irradiated samples. The data was taken from one-frame images taken on the ARM300CF microscope.

To explore whether the irradiation-induced average expansion along the c-axis is a regular increase in lattice parameter rather than skewed by certain images, the distribution of the inter-cell and intra-cell Ba_1-Ba_2 fractions have been calculated. The scatter plot distribution of these two fractions in images from pristine, neutron-irradiated and He-irradiated samples does not show any signs of systematic change in the neutron- and He-irradiated samples (Figure 5.10a). However, comparing the data from Xe-irradiated and pristine samples, shows the intra-cell Ba_1-Ba_2 fractions in the Xe-irradiated sample are smaller than the pristine images (Figure 5.10b).

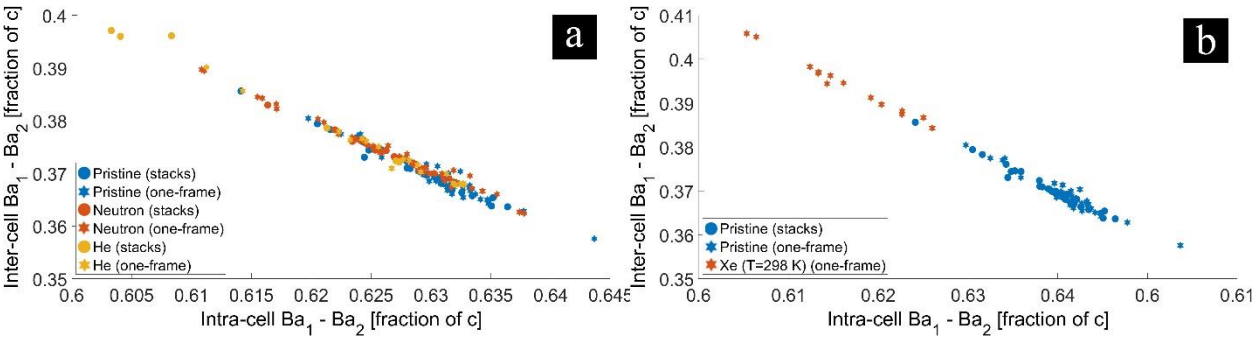


Figure 5.10: Scatter plots presenting the inter- (y-axis) and intra-cell (x-axis) Ba_1-Ba_2 distances as a fraction of average c-axis lattice parameter. (a) for pristine (blue), neutron-irradiated (red) and He-irradiated (yellow) samples showing no distinguishable clustering; (b) for pristine and Xe-irradiated (room temperature) samples presenting two separate clusters, shown in blue and red, respectively. The data includes one-frame & stack images taken on the ARM300CF microscope and unit cells that contain intergrowth were removed from the analysis as elaborated in section 3.5.1.5.

5.2.3. Analysing local variations within images

Hitherto, I have analysed how the average values and distributions of lattice parameters change in apparently perfect regions of crystal following irradiation, and the question now rises as to whether the lattice parameters also change when local damage is sufficiently severe to be easily observed in STEM images. For this purpose, I have chosen selected neutron-irradiated images that were included in the analysis earlier in this section (5.2.1 & 5.2.2).

As already showed and discussed in the section 4.1, several STEM/ABF images of neutron-irradiated samples contain regions of dark contrast, like that seen in Figure 5.11b. STEM/ABF dark contrast can arise due to local strains [420] that change the Bragg conditions and therefore the scattering angles of the transmitted electrons that are collected by the annular detector. In the STEM/HAADF image in Figure 5.11a, these local strains are barely noticeable. The dark contrast in the STEM/ABF image is likely to be a result of damage created by the neutron

irradiation, as it was not observed in pristine samples and resembles the damage observed in Ar-irradiation samples where amorphous cascades are buried in crystalline material (Figure 4.8). An examination of local lattice parameters was carried out on this image for the purpose of shedding light on potential differences between the ‘damaged’ and the ‘undamaged’ regions, and displayed in Figure 5.11c-e. A subtle increase in both average a/b and c lattice parameters was identified when comparing the area with the dark contrast (rectangular region in Figure 5.11c) and the rest of the same image, from 3.847 to 3.856 Å for the a/b-axis, and from 11.675 to 11.707 Å for the c-axis parameters. The distributions of a/b-axis lattice parameters in both regions, shown in (d), appear very similar, but the c-axis data shows a distinct broadening of the distribution to higher values inside the damaged region, which is consistent with the average c-axis increase seen in He- and Xe-ions (Figure 5.2).

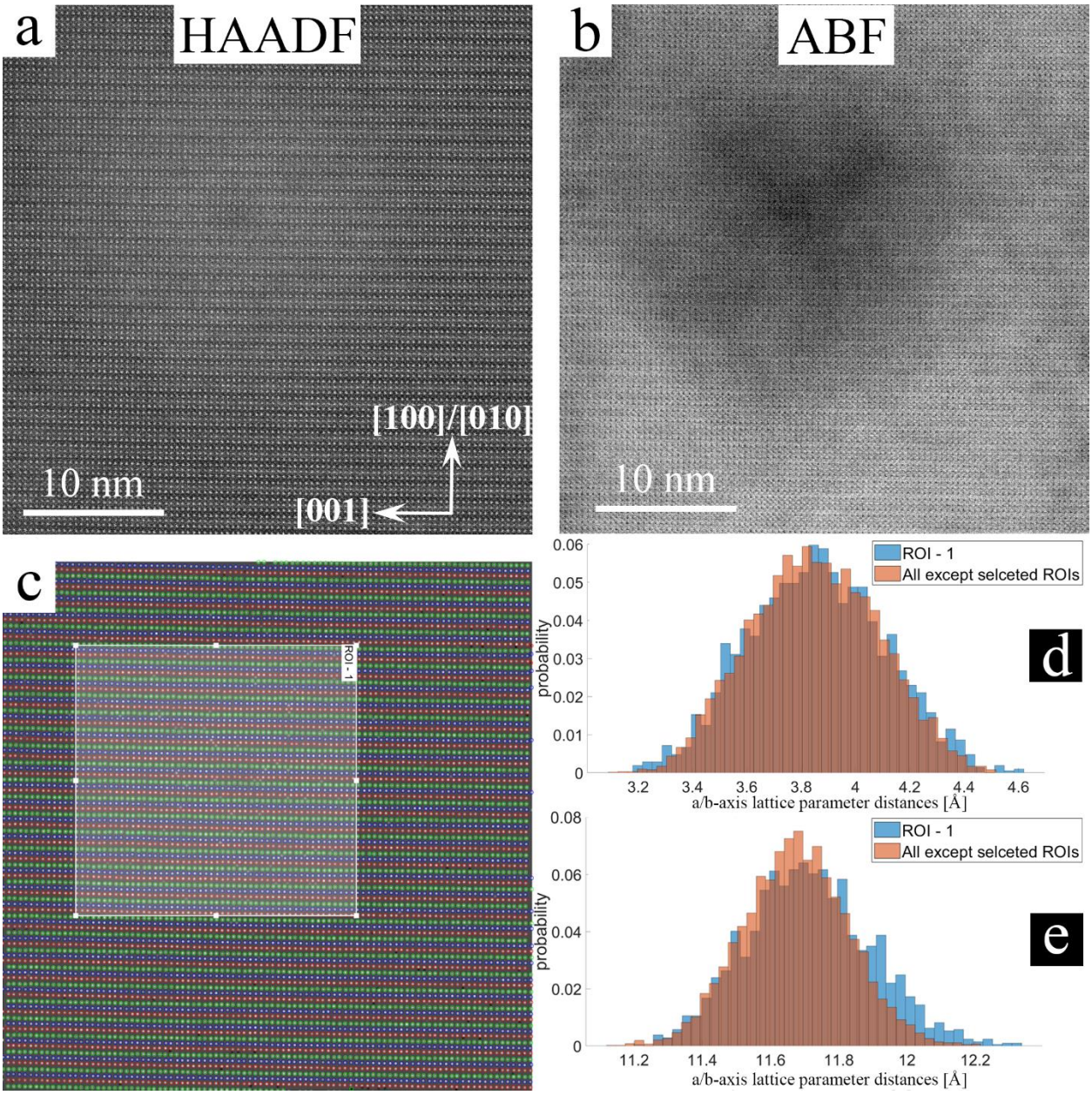


Figure 5.11: STEM images of neutron-irradiated sample and local analysis of lattice parameters. HAADF (a) and ABF (b) images taken along [100]/[010] ZA. a/b-axis (d) and c-axis (e) lattice parameter distributions presented using blue and red colour bars as extracted from inside and outside the Region of Interest (ROI) as shown in the fitted Ba-GdY sublattice image in (c).

To make the analysis more statistically significant, I have analysed 11 STEM images of neutron-irradiated samples where damage is visible under ABF conditions. The resulting scatter plot is shown in Figure 5.12, and with this larger dataset the a/b-axis lattice parameter can be seen to

expand locally in the damaged regions by an average of 0.0025 Å when compared to the undamaged region. Similarly, the damaged regions show an increase in the c-axis by an average of 0.0027 Å. In other words, the average lattice parameters per image is pushed to higher values due to the presence of local irradiation damage, and the apparently undamaged matrix actually has slightly lower lattice parameter values than the image average.

A similar analysis was carried out on the width of the lattice parameter distributions measured from both ‘damaged’ and ‘undamaged’ regions. The average standard deviations of the ‘damaged’ regions with respect to the average standard deviation per image shows a slight increase of 0.0011 and 0.0080 Å for the a/b- and c-axes, respectively. This change can be explained if one considers that a ‘damaged’ region is characterised by inhomogeneous strains associated with a high local concentration of lattice defects. However, the slight change seen here does not account for the wide distribution of a/b-axis lattice parameter (Figure 5.4), and implies that the seemingly undamaged matrix suffers from subtle irradiation damage as will be also discussed in section 6.

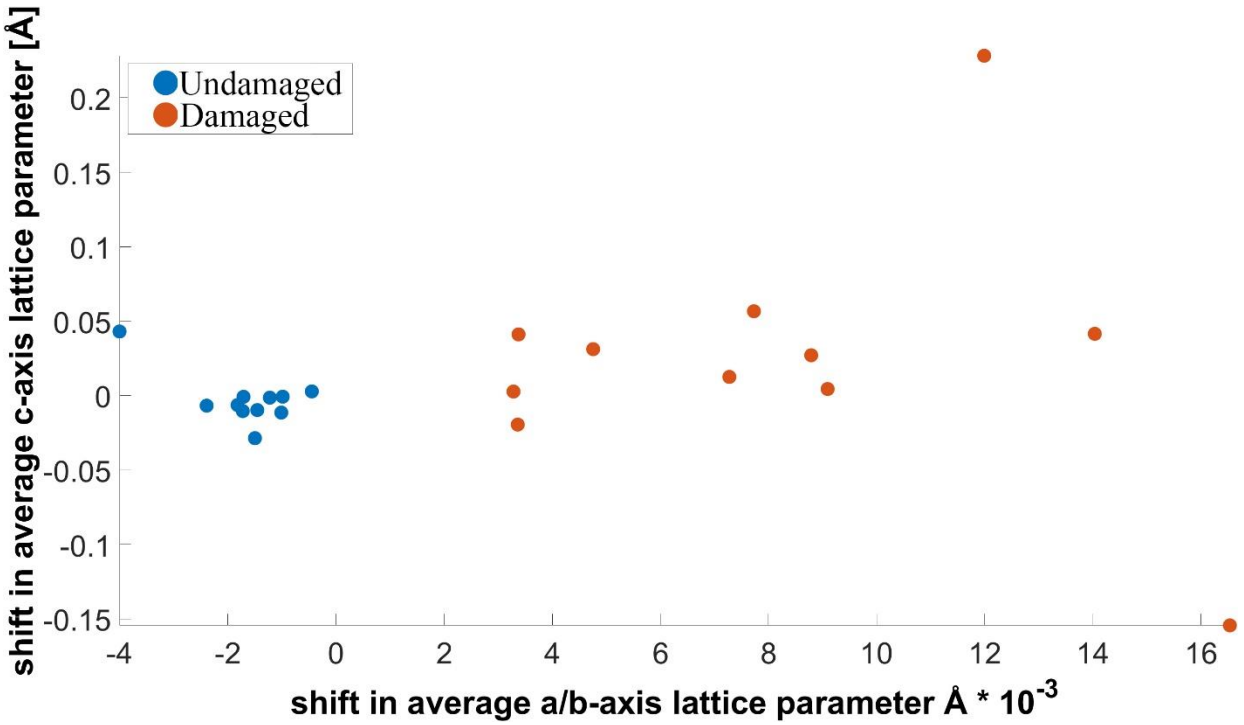


Figure 5.12: Shift in average lattice parameters measured in undamaged (blue circles) vs 'damaged' (red circles) regions in neutron-irradiated samples as identified by dark contrast in STEM/ABF images.

5.3. Effect of projectile on light ion irradiation damage

This section focuses on using the analysis of STEM images to compare the irradiation damage caused by light Ar, Ne and He ions to unirradiated samples. Although He-ions irradiation damage was already discussed in section 5.2, some of the results are shown here again for the sake of comparison with different light ions.

Figure 5.13 shows a comparison of the lattice parameters extracted from STEM images of samples damaged by Ar, Ne and He irradiation to results from pristine (unirradiated) samples. Since the Au-calibration described in section 3.5.1.4.1 is not perfect when comparing results from different microscopes along the a/b- or c-axes, as demonstrated in Figure 3.21, the data was split into two parts according to the instrument on which images were taken, ARM200f on the

left and ARM300CF on the right, and only one-frame images were included. Both are benchmarked against pristine sample images taken under the same conditions. The a/b-axis lattice parameter increases in the case of the He ion irradiation but stays roughly unchanged for Ne and Ar ions (see Appendix B: Figure S- 7 lattice parameters scatter plot of pristine, Ne- and Ar-irradiated samples shows no clustering along a/b-axis). In contrast, the c-axis lattice parameters increased as a result of irradiation by all 3 ions. The heavier Ar ions expanded the c-axis more than the lighter Ne ions, 2.12% and 1.35%, respectively, when irradiated to an identical fluence of 1×10^{13} cm^{-2}. Irradiating with even lighter He ions to a higher fluence of 1×10^{16} cm^{-2} had a similar effect on the c-axis lattice parameter as Ne-ions, resulting in c-axis lattice parameter increase by 1.20%.

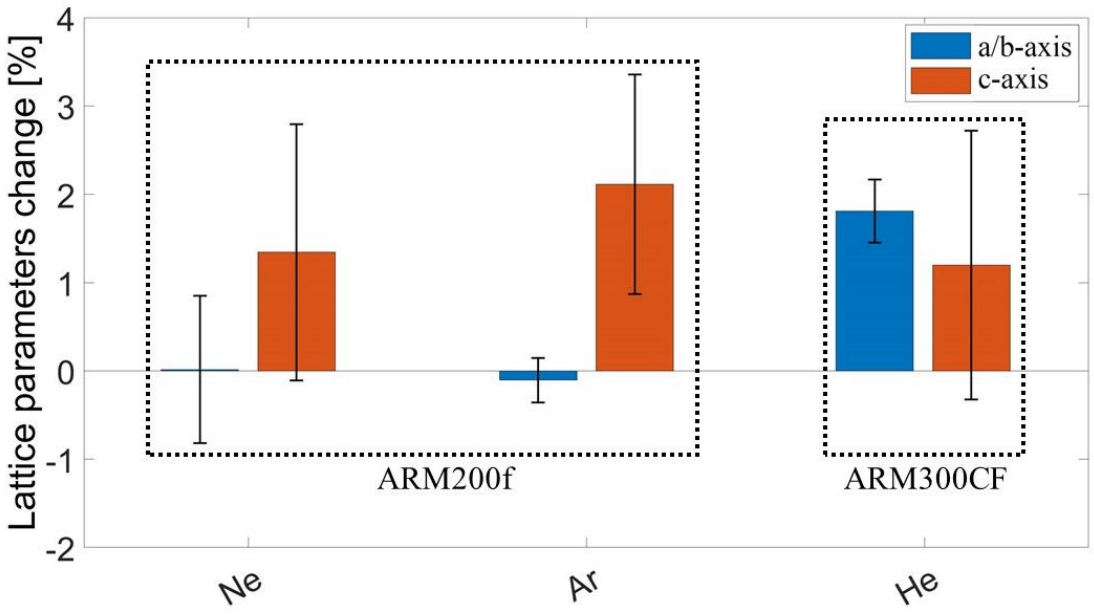


Figure 5.13: Bar chart comparing average percentage change a/b- (blue bars) and c-axes (red bars) lattice parameters of He, Ne and Ar ion irradiated samples compared to pristine samples. The data was extracted from one-frame images taken on the ARM200f microscope on the left and ARM300CF microscope on the right. The errorbars stand for the standard deviation.

This universal increase in c-axis lattice parameters, regardless of the mass of the irradiating ions, was further analysed by breaking the c-axis parameters down into two parts: the intra-cell Ba_1-Ba_2 separation and the Ba_1-Ba_2 inter-cell separation, both as a fraction of average c-axis lattice parameter, as shown in Figure 5.14. In the case of He-ions (right dotted box in Figure 5.14), the data shows a slight decrease in the intra-cell Ba_1-Ba_2 fractions. Ar irradiation (left dotted box) also displays the same trend, and one can recall that following Xe-ion irradiation (Figure 5.3) the trend was similar. In contrast, Ne-ions show the opposite trend, where the inter-cell Ba_1-Ba_2 fractions shrink (Figure 5.14). The numbers of both a/b- and c-axes lattice parameters and inter- and intra-cell fractions for pristine and the three irradiated samples are shown in Table 5.3.

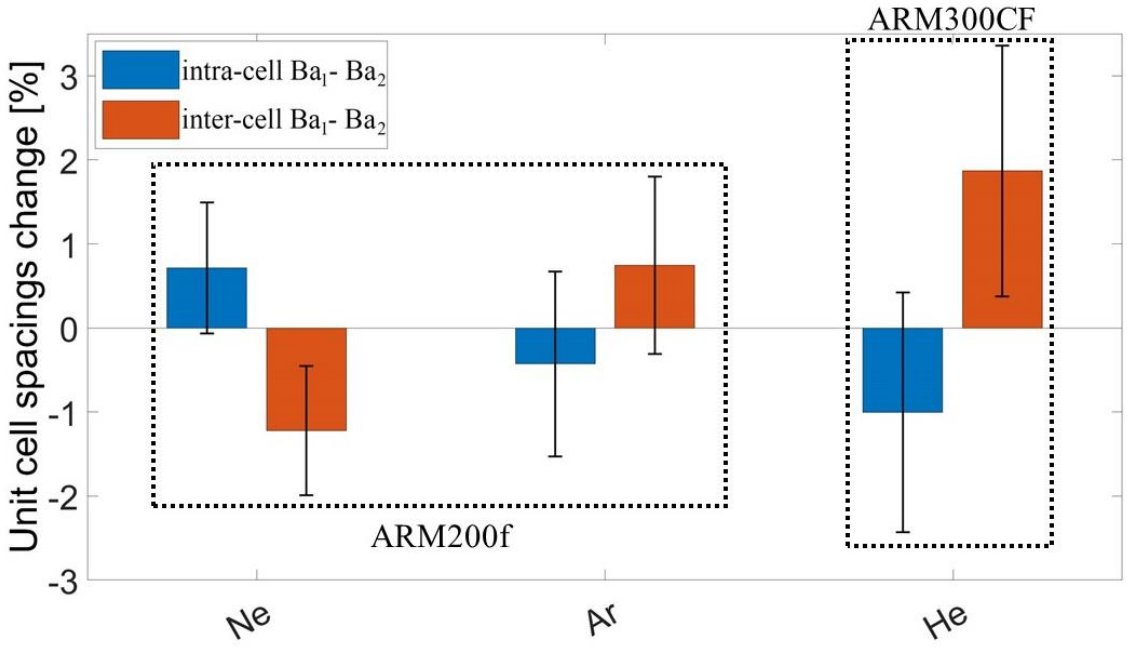


Figure 5.14: Comparison of the inter- (red bars) and intra-cell (blue bars) Ba_1-Ba_2 distances along the c-axis as a fraction of average c-axis lattice parameter for Ne and Ar ion irradiation shown as percentage change compared to pristine sample. The errorbars stand for the standard deviation. Data was extracted from images taken on the ARM200f microscope (left dotted box) and He-irradiated sample taken on the ARM300CF microscope (right dotted box).

Table 5.3: Average REBCO lattice parameters (a/b- and c-axis) and inter- and intra-cell Ba_1-Ba_2 fractions for un-irradiated (pristine) and three irradiated samples; Ne-ions, Ar-ions and He-ions as was measured from STEM images extracted from one-frame images (lattice parameters) and one-frame & stack images (inter- and intra-cell fractions) taken on the ARM200f and ARM300CF microscopes, shown on the left and right side of the table, respectively.

	ARM200f			**ARM300CF**	
	Pristine	Ne-ions	Ar-ions	Pristine	He-ions
a/b-axis lattice parameter [Å]	3.786	3.787	3.782	3.796	3.865
c-axis lattice parameter [Å]	11.505	11.660	11.749	11.687	11.827
Inter-cell Ba_2-Ba_1 [fraction of c-axis]	0.378	0.373	0.381	0.370	0.377
Intra-cell Ba_2-Ba_1 [fraction of c-axis]	0.622	0.626	0.619	0.630	0.624

As will be discussed in more detail later (section 6.4.2), He-ions at a relatively high total fluence create such a lot of lattice damage that local distortions have been observed in about 20 STEM images investigated, and such an example is shown in Figure 5.15. The STEM/HADDF image (Figure 5.15a) and StatSTEM fitting (Figure 5.15b) display distortions that are reminiscent of small damage cascades, but I do not expect individual He ions to create an amorphous cascade (section 4.2.1.1) so this local damage must be a consequence of the accumulation of point defects resulting from the high fluence (1×10^{16} cm^{-2}). An illustration of the presence of heavy atoms lying off the locations of the perfect Ba-GdY and Cu sublattices, defined as about 2 and 1 angstroms deviation from Ba-GdY and Cu positions, respectively, is shown Figure 5.15d. However, it is likely that not all the defects shown are interstitials but rather small stacking faults (examples shown in red circles). Additionally, the interstitials atoms can also be columns of interstitials since the brightness of very few interstitials is not sufficient to be discovered using StatSTEM.

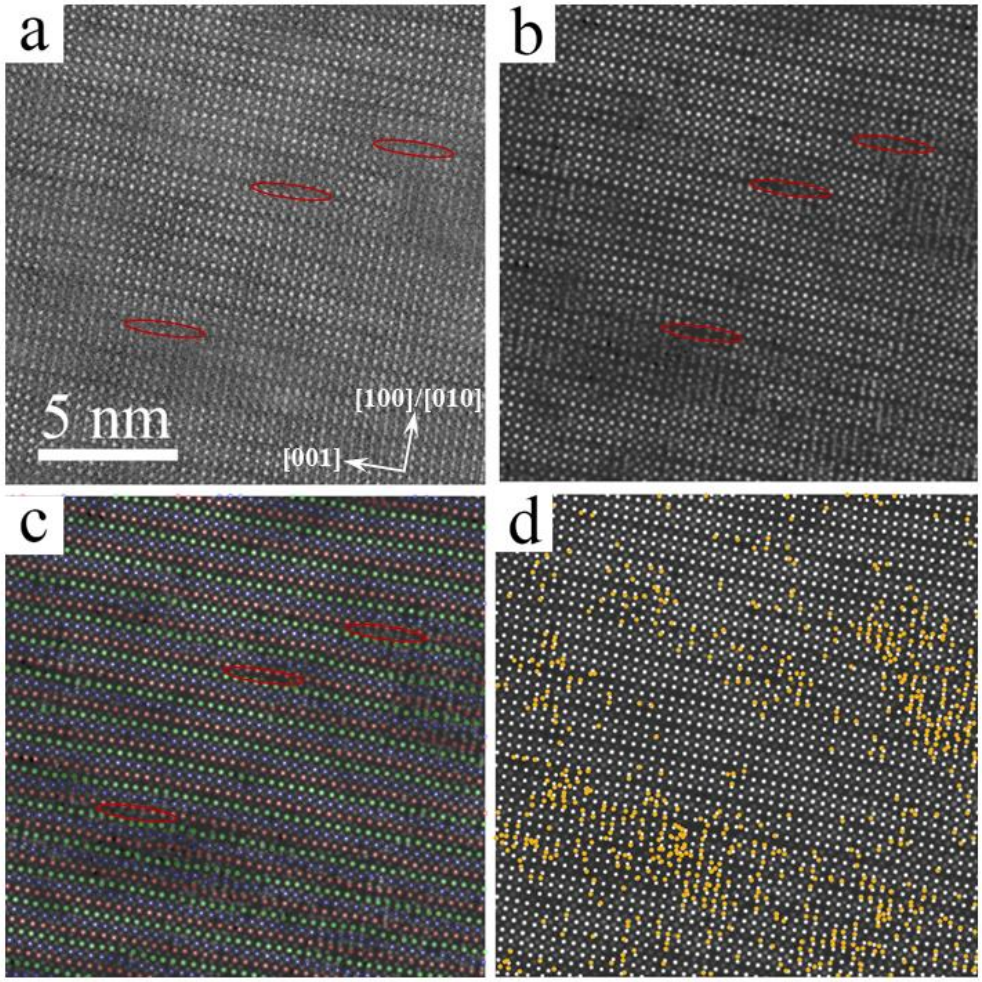


Figure 5.15: STEM/HAADF image and atomic location analysis using StatSTEM of a He-irradiated sample. (a) STEM/HAADF taken along [100]/[010] ZA and the corresponding StatSTEM fitting (b). (c) Fitting of Ba-GdY sublattice, where red, blue, and green colours represent Ba_1, Gd/Y, and Ba_2 atoms, respectively. (d) Ba-GdY sublattice atoms in their perfect lattice sites shown in white and stacking faults/interstitial atoms in orange. Potential extra layers, namely, stacking faults, are shown by red ellipses in a-c.

5.4. Effect of temperature on Heavy ion irradiation

Another category of damage that can be analysed by the analysis of STEM images is Xe-ion irradiation conducted at different temperatures. Two Xe-irradiated samples were analysed, after in-situ irradiation to a fluence of 7×10^{12} cm^{-2} at room temperature and at 100 K. A typical

example of a damage cascade, Ba-GdY sublattice fitting, and local lattice parameter analysis in the sample Xe-irradiated at 100 K, is shown in Figure 5.16. A damage cascade seems to progress from the bottom left corner and towards the centre of the image. Judging by the scale of the damage shown in Figure 5.16a it is possible that it is a result of at least two overlapping damage cascades that could be either spherical or display more a complex shape. Figure 5.16b presents the Ba-GdY sublattice fitting and Figure 5.16c emphasises the location of atoms in orange that could not be assigned to locations characteristic of the Ba-GdY sublattices. It is clear that most of the displaced atoms lie in the darker regions of Figure 5.16 (a) and (b), though it is hard to analyse their nature from these images, it is possible that they create local stacking faults as well as partial ‘columns’ of interstitials that lie in a different depths in the sample.

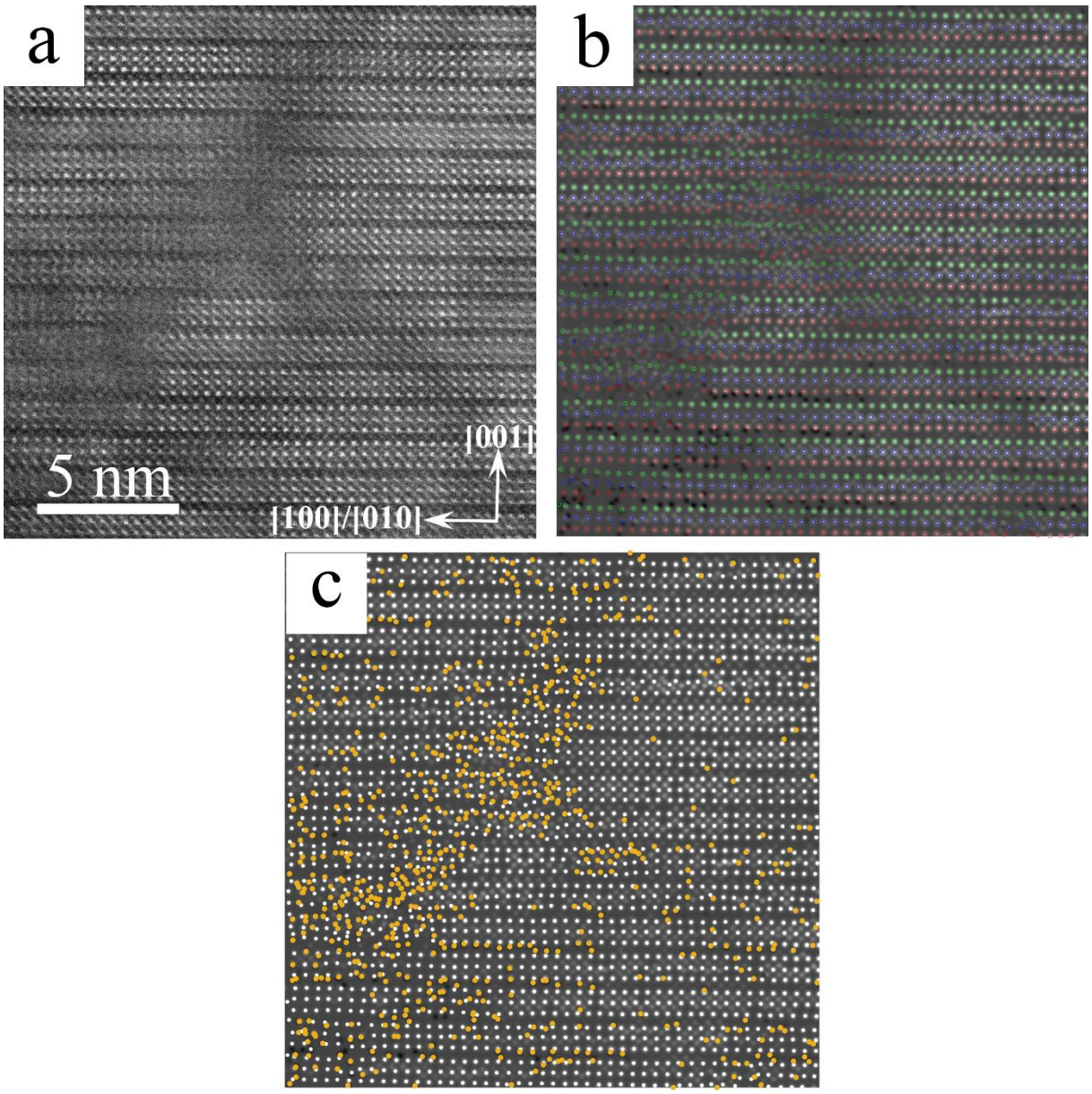


Figure 5.16: STEM/HAADF image and atomic location analysis using StatSTEM of sample Xe-irradiated at 100 K. (a) STEM/HAADF taken along [100]/[010] ZA and the corresponding StatSTEM model with Ba-GdY sublattice, where red, blue, and green colours represent Ba_1, Gd/Y, and Ba_2 atoms, respectively (b). (c) Ba-GdY sublattice atoms in their perfect lattice sites shown in white and incomplete displaced atomic columns atoms in orange.

The average lattice parameters and inter- and intra-cell fractions percentage change for the Xe-irradiated samples compared to pristine samples are shown in Figure 5.17. It can be observed

that the c-axis lattice parameter increases dramatically after irradiation taken place at 100 K, by 4.62%, whereas the a/b-axis lattice parameter increases more moderately, by 1.92%. In contrast, in the Xe-irradiated at 298 K, the a/b-axis lattice parameter did not change and the increase in unit cell along the c-axis was more moderate than at 100 K, at only 0.98%. Analysing the c-axis expansion in terms of the ratio of intra-cell to inter-cell Ba_1-Ba_2 fractions (Figure 5.17b), results in 1.516 and 1.541 for irradiation at 100 K and room temperature, respectively, versus 1.671 for the pristine sample. The conclusion is unambiguous; heavy Xe-ion irradiation results in an increase in the Ba_1-Ba_2 inter cell fraction relative to the intra-cell Ba_1-Ba_2 fraction. Interestingly, when looking on the *absolute* Ba_1-Ba_2 distances, Xe (T = 298 K) intra-cell distance actually shrinks from 7.377 Å in pristine sample to 7.158 Å as opposed to Xe at 100 K that was increased to 7.422 Å, a point which will be discussed further in section 5.5.4. This means that the Cu(1) chain portion takes up a significantly greater proportion of the unit cell after Xe irradiation. The Xe-irradiated sample at 298 K shows similarities to the sample irradiated at 100 K in terms of its relative inter- and intra-cell fractions. However, the a/b-axis lattice parameter was not affected by Xe-ions irradiation when taken place at room temperature.

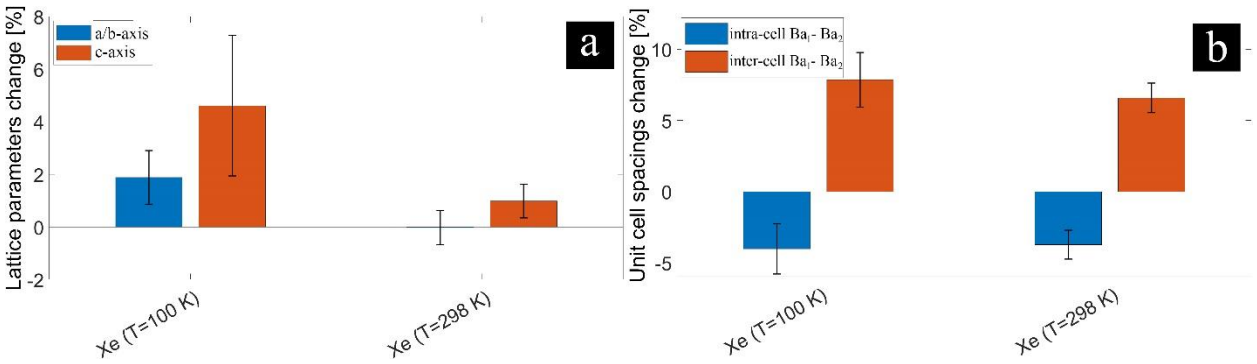


Figure 5.17: Comparison of lattice parameters (a) and inter- and intra-cell Ba_1-Ba_2 fractions (b) of Xe-ion samples irradiated at 298 K and 100 K presented as a percentage change compared to pristine sample. The errorbars in both figures stand for the standard deviation. The one-frame images (a) and one-frame & stacks images (b) used for this analysis taken on the ARM300CF microscope.

Table 5.4: Average REBCO lattice parameters and inter- and intra-cell fractions of Xe-ions irradiated samples at 100 and 298 K benchmarked against un-irradiated (pristine) values. Lattice parameters values were extracted from one-frame and inter- and intra-cell fraction were extracted from both one-frame and stacks images, both taken on the ARM300CF microscope.

	Pristine	**Xe-ions (T=100 K)**	**Xe-ions (T=298 K)**
a/b-axis lattice parameter [Å]	3.796	3.867	3.795
c-axis lattice parameter [Å]	11.687	12.226	11.802
Inter-cell Ba_2-Ba_1 [fraction of c-axis]	0.370	0.399	0.394
Intra-cell Ba_2-Ba_1 [fraction of c-axis]	0.630	0.605	0.607

Another way to visualise the dramatic change of the inter- and intra-cell Ba_1-Ba_2 fractions is to plot the average Ba_1-Ba_2 distances as a fraction of the average c-axis *per image*, and to benchmark them against the values from the pristine sample, as can be seen in Figure 5.18. It is obvious that following Xe-ion irradiation the expansion of the unit cell along the c-axis is mostly

the result of an increase in the inter-cell Ba_1-Ba_2 separation. In terms of the inter- and intra- cell relative change, Xe-irradiation at both temperatures results in a similar effect – i.e. an increase in the inter-cell fraction of the unit cell compared to the pristine samples.

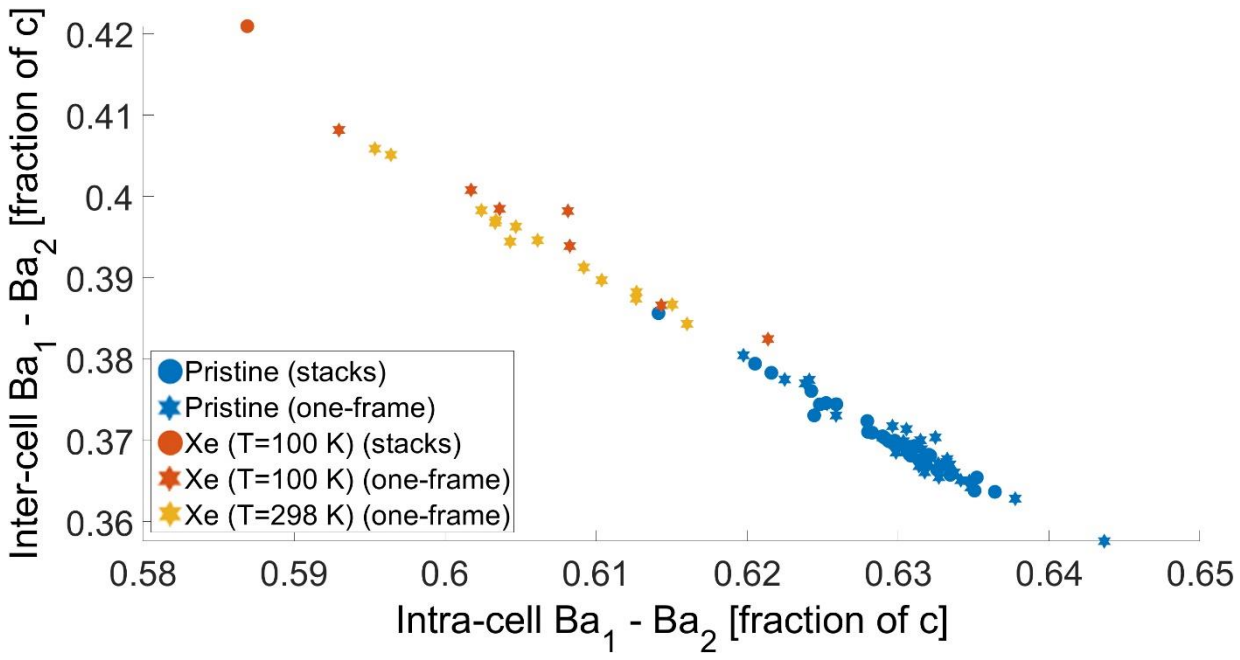


Figure 5.18: Scatter plot presenting the inter- and intra-cell Ba_1-Ba_2 distances as a fraction of average c-axis lattice parameter for pristine and Xe-irradiated at room temperature and 100 K samples. The data includes one-frame & stacks images taken on the ARM300CF microscope.

As discussed above (section 5.2.2), the lattice parameter distributions can also shed light on different types of damage following irradiation. Figure 5.19 and Figure 5.20 show histograms of a/b-axis and c-axis lattice parameters for these Xe-irradiated samples. In Figure 5.19 the sample Xe-irradiated at room temperature shows an almost symmetric distribution with a short tail to higher values, but the sample Xe-irradiated at 100 K displays a much wider distribution with a long tail to higher values. Along the c-axis (Figure 5.20) the shift of the average lattice parameter of the sample Xe-irradiated at T = 100 K to larger values compared to irradiation at 298 K matches the average values shown in Figure 5.17a. In the case of Xe at 100 K, the standard

deviations along both axes measured for a single image, also shift to higher values when compared to Xe at 298 K, as can be seen in Appendix B: Figure S- 8. The evidence shown much more extensive damage in the sample irradiated by Xe at 100 K.

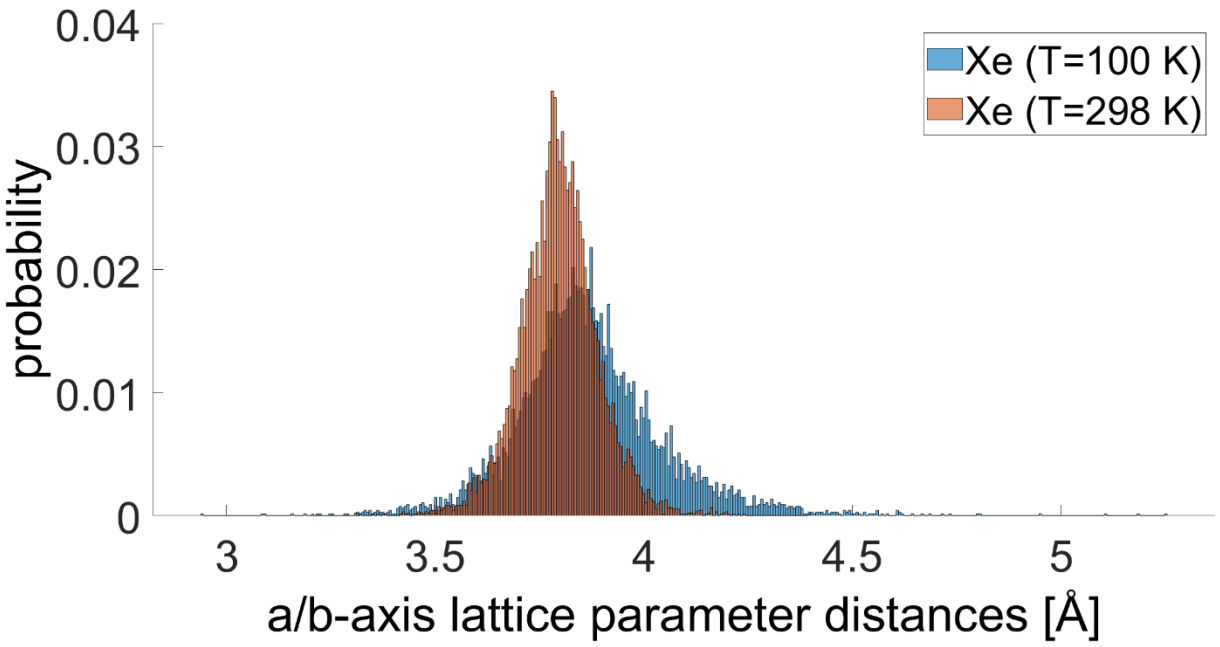


Figure 5.19: Normalised distribution of a/b-axis lattice parameters from a sample Xe-irradiated at 100 K (blue bars) and at room temperature (red bars). 1% of extreme outliers were removed from every image.

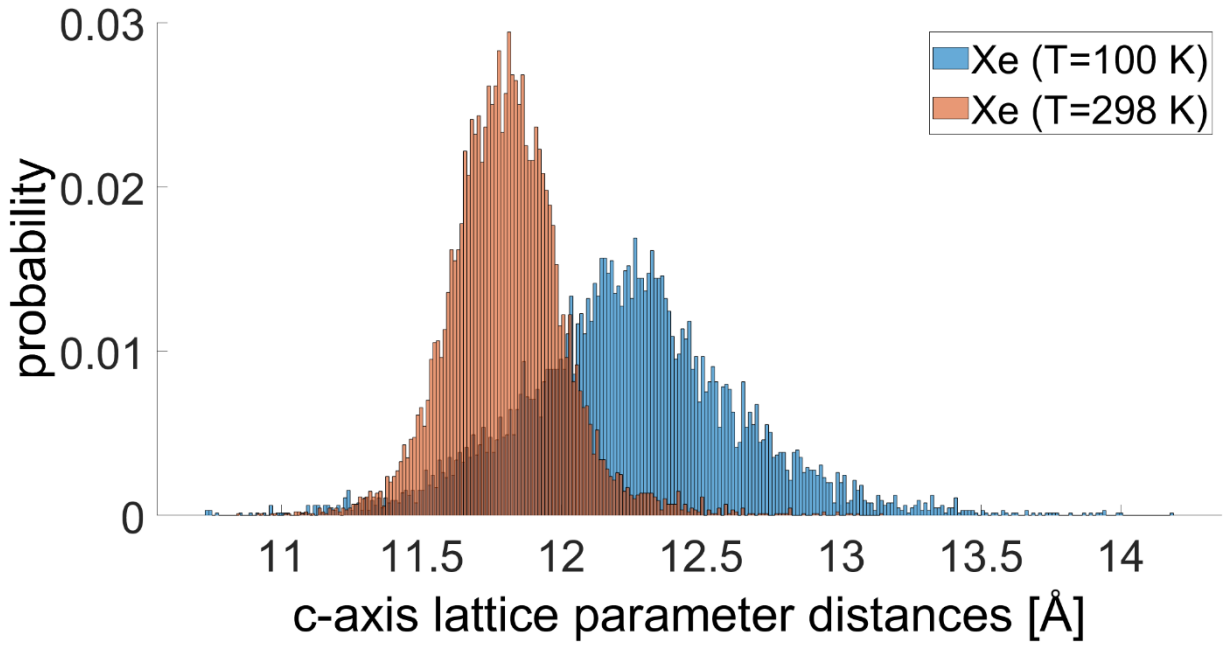


Figure 5.20: Normalised distribution of c-axis lattice parameters from a sample Xe-irradiated at 100 K (blue bars) and at room temperature (red bars). 1% of extreme outliers were removed from every image.

To understand whether localized damage is responsible for the large increase in c-axis lattice parameter in the Xe-irradiated sample at 100 K, one can separate the effect of the damage cascades from the surrounding matrix (see for example Figure 4.12). An example of the local analysis of lattice parameters of regions of interest defined in the damage cascades and the matrix is presented in Figure 5.21a and the results are shown in Figure 5.21b as a scatter plot. It can be seen that the damage cascade regions exhibit enlarged lattice parameters, particularly along the c-axis. The surrounding matrix has an average local c-axis lattice parameter value that is lower by 0.091 Å from the overall average of 12.226 Å (Table 5.4). This is still much larger than 11.687 Å in the pristine sample. I interpret this observation to suggest that not only is there c-axis lattice parameter expansion in the damage cascades, the matrix in their vicinity to display larger lattice parameter compared to pristine sample.

From Figure 5.21 one can calculate that the average increases in a/b- and c-axes lattice parameters in the damaged regions (i.e. the cascade core) amount to 0.0393 Å and 0.1312 Å, respectively. In percentage terms, the lattice parameter expansion is slightly larger along the c-axis: 1.07% versus 1.02% along the a/b-axis. Figure 5.21c compares the deviation of inter-cell and intra-cell Ba_1-Ba_2 fractions in the cascade cores and the surrounding matrix with respect to the average values for the images. It can be seen that two clusters form in inter-cell values (y-axis) but not intra-cell values (x-axis). In the cascade cores, the increase in the inter-cell Ba_1-Ba_2 fractions is 0.1393 Å above the average compared to only 0.0306 Å for the intra-cell values. This analysis is consistent with the average inter- intra-cell fractions for all images shown in Figure 5.18.

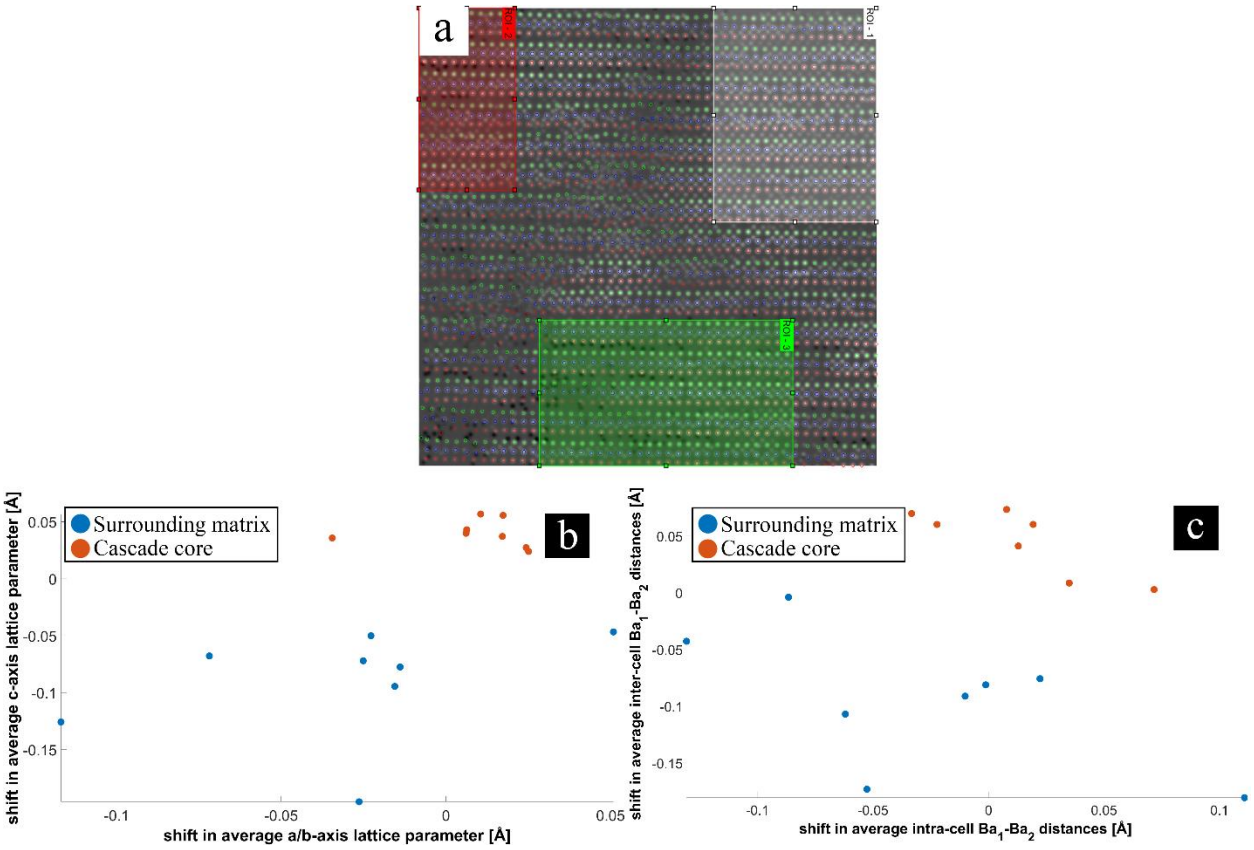


Figure 5.21: Shift from average lattice parameters (b) and inter- and intra-cell fractions (c) as measured in damage cascade regions (The areas in the vicinity to the ROIs shown in (a)) and the surrounding matrix (Three regions of interest (ROIs) shown in (a)) in a sample Xe-ions irradiated at 100 K.

5.5. Discussion

5.5.1. Ba_1-Ba_2 separations

An interesting feature analysed in this chapter is the relative inter- and intra-cell separations of the Ba planes extracted from high quality STEM images. An important piece of extra information was kindly provided by Dr. Samuel Murphy as additional data to his original publication [421] that conducted a *density functional theory* (DFT) study on the stability of point defects (i.e. antisite defect, vacancies and interstitials) in REBCO. The inter- and intra-cell parameters derived from the Ba atom locations in this work are shown in Figure 5.23, where the different subplots represent the defect location: (a) in the CuO chain, (b) in the O(4) (apical)

plane, (c) in the CuO_2 plane and (d) in the RE-plane. The results include point defects, vacancies and interstitials, identified using different symbols. These theoretical calculations impose constant unit cell volume, and so when one distance increases, the other must decrease. Thus within this constraint, the creation of a particular defect type on the Ba_1-Ba_2 inter and intra cell fractions can be predicted. The naming convention follows a 'V' at the beginning to refer to vacancies or 'i' to refer to Cu/O interstitials, and the numbers indicate the site location as defined in the original article (Figure 5.22).

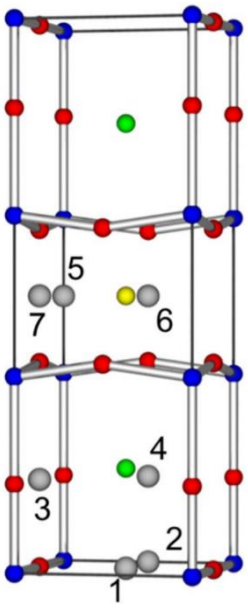


Figure 5.22: Graphical representation of YBCO unit cell. The numbers 1-7 stand for the defects' site locations and the oxygen, copper, barium, and yttrium ions are represented by red, blue, green, and yellow spheres, respectively [421].

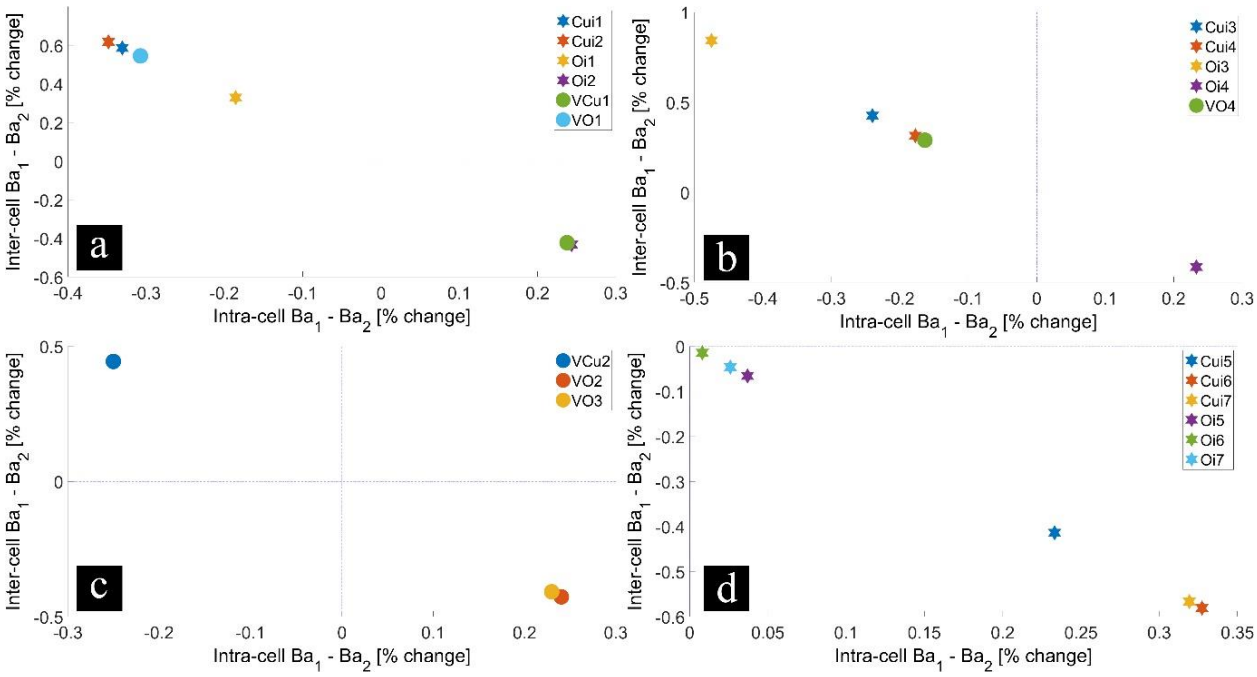


Figure 5.23: DFT theoretical predictions of the percentage change in Ba_1-Ba_2 inter- and intra-cell distances in the presence of Cu/O vacancies and interstitials. The graphs show different defects positions in the REBCO unit cell; CuO chain (sites 1-2), O(4) plane (sites 3-4), CuO_2 planes for O(2) and O(3), and RE-plane (sites 5-7), respectively. Interstitials are marked with hexagrams and vacancies with circles.

Generally speaking, for oxygen vacancies in the CuO_2 plane (O(2), O(3)), the intra-cell Ba_1-Ba_2 fraction increases since these sites are towards the centre of the unit cell, but VO(1) and VO(4) result in inter-cell distance increasing [421]. However, VO(1) and VO(4) have lower formation energy according to Murphy's results [421] and thus oxygen vacancies are predicted to result in inter-cell Ba_1-Ba_2 distance expansion. Cu(2) vacancies in the CuO_2 plane result in a removal of positive charge and thus allows the Ba to move upwards and decrease the Ba_1-Ba_2 intra-cell distance, while the opposite is true for Cu(1) vacancies. Oxygen and copper interstitials situated in the CuO_2 plane and O(4) plane generally cause an increase in the Ba_1-Ba_2 inter-cell fraction, except for oxygen interstitials in sites 2 & 4 that behave the opposite way. As expected,

interstitials lying in the RE-plane (sites 5-7) increase the Ba_1-Ba_2 intra-cell distances, but oxygen interstitials in this plane have little effect on the Ba_1-Ba_2 intra-cell distances.

Further DFT results were provided by Dr. Rebecca Nicholls and co-authors [419], which used robust geometry optimisations, thus tuning the lattice parameters and atom positions within the unit cell to find the minimum in energy. They investigated the following defects: (1) interstitial at (0, 0, 0.5), (2) VO(2) + Interstitial at (0, 0, 0.5), (3) VO(1), (4) VO(2), and (5) VO(4). However, their Ba_1-Ba_2 fractions are not completely consistent with Murphy as they point out on about 2.80% (inter-cell) and -1.65% (intra-cell) change in Ba_1-Ba_2 separation fractions, larger inter-cell fraction increase and intra-cell decrease when compared to Murphy's results. Moreover, it terms of absolute Ba_1-Ba_2 distances, Oxygen vacancies, VO(1), VO(2), and VO(4), lead to decreased intra-cell distance and inter-cell distance expands, while the overall c-axis lattice parameters increase by as little as ~0.015 Å. However, since the unit cell volume was not constrained in this case, it is hard to compare these two theoretical studies directly.

In order to compare Murphy's and Nicholls's DFT results to the experimental results presented in this section, I have plotted the percentage change of inter- and intra-cell fractions on a scatter plot along with the theoretical results, as presented in Figure 5.24. The circles represent the experimental results, excluding the Xe-ions irradiated at 100 and 298 K in order to make the comparison more visible. The inter- and intra-cell percentage change is -4.04, -3.74 and +7.85, +6.58 for irradiation at 100 and 298 K, respectively. This is about X6 and X2 larger than Murphy's and Nicholls's results, respectively. For Murphy's results, only the energetically preferable sites for Cu and oxygen vacancies and interstitials are shown, using squares and hexagrams. Nicholls's results are shown using diamond symbols for vacancies and pentagrams for defects that include interstitials.

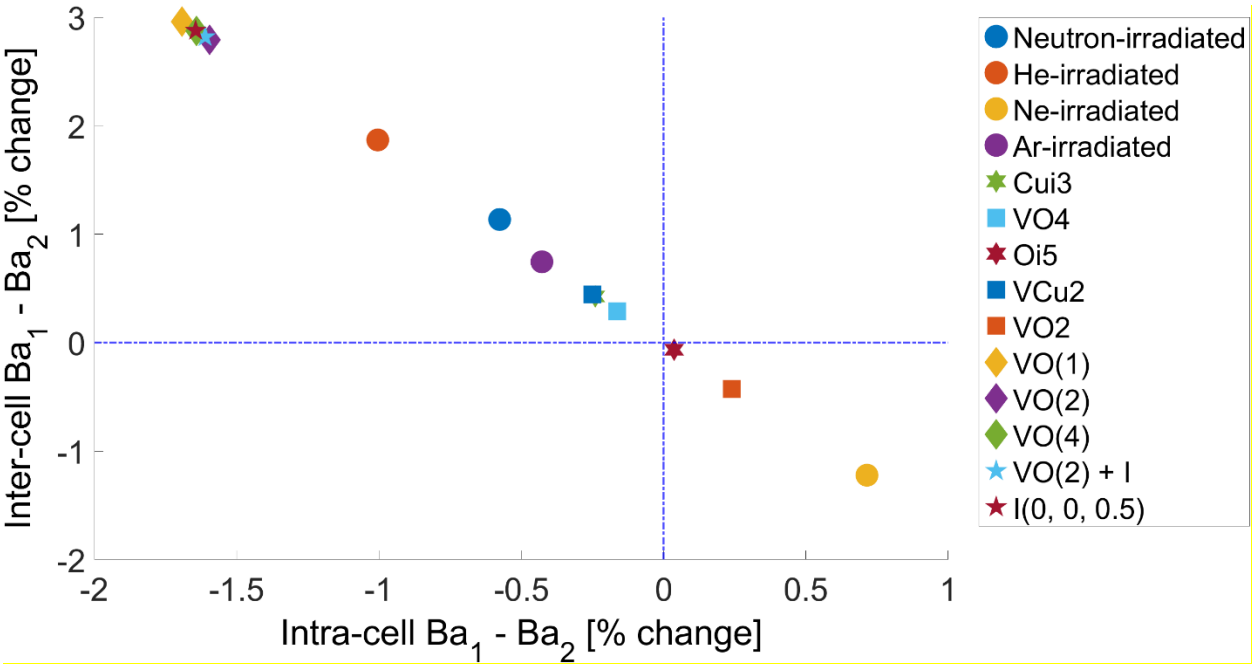


Figure 5.24: Combined scatter plot including DFT theoretical predictions and experimental results of the percentage change in Ba_1-Ba_2 inter- and intra-cell fractions. The DFT theoretical results are shown with hexagrams for interstitials and squares for vacancies as calculated by Murphy [421]*, and pentagrams for defects with interstitials and diamonds for vacancies as analysed by Nicholls et.al.* [419]*. The experimental results are marked with circles and do not include the results of Xe-irradiated samples.*

From the experimental results it can be seen that the Ne-irradiated sample is the only sample that displays a decrease in the Ba_1-Ba_2 inter-cell fraction. In the Ar-irradiated, neutron-irradiated, and He-irradiated samples, the inter-cell fraction gradually becomes expanded on the expense of the intra-cell fraction. The Xe-irradiated samples at both temperatures show dramatic inter-cell fraction expansion. According to Murphy [421], oxygen interstitials prefer to sit in the RE-plane, which has little effect on the Ba_1-Ba_2 separation, and oxygen vacancies prefer to lie around the CuO chain that results in inter-cell Ba_1-Ba_2 distance expansion, which is generally what was observed experimentally.

Oxygen and copper vacancies usually produce a local interstitial; however, apart from the neutron-irradiated sample that was irradiated in its bulk state, all the other sample underwent in-situ irradiation as TEM lamellae, and due to their low thickness net oxygen loss, leading to net vacancies, cannot be ruled out. Thus, it cannot be explicitly stated whether vacancies are present as vacancies-interstitials pairs or as isolated point defects. Murphy argues that in the case of Cu, the lowest energy configuration follows a vacancy that is situated in CuO_2 plane and interstitial that sits in O(4) plane, each one individually causes an increase in inter-cell distances. On the other hand, oxygen vacancies and interstitials have lower effect on the inter- and intra-cell distances. Cu vacancy/interstitial pair has a formation energy about 6 times greater than oxygen vacancy/interstitial pair [421], and their inter-cell expansion gets closer to the neutron-, Ar-, and He-irradiated samples, yet still lower. The Ne-irradiated sample does not fall into either of the Cu/O vacancy-interstitial pair effects and should be investigated further. It is plausible that Ne-irradiated sample shows a combination of several defects that interact with one another and thus presents Ba_1-Ba_2 fractions that cannot be matched to simple Cu/O vacancies/interstitials pair model. Interestingly, by looking on the DFT results of Nicolls and co-workers [419], all defects investigated are associated with an absolute increase in the inter-cell fraction as opposed to a shrinkage of the intra-cell distance. Moreover, the percentage change is about X6 times larger when compared to Murphy's results and clustered at the upper left corner in Figure 5.24.

There are at least two main drawbacks to these theoretical models. (1) They do not include defect clusters (i.e. larger scale than defect-pairs such as Frenkel defect), which presumably will create a larger effect on the inter- and intra-cell fractions due to the greater disruption to the unit cell. (2) Mutual interactions between individual defects can also severely affect the structural parameters in a more complex way and are certainly not a linear combination of two point

defects (see, for example *x-ray absorption spectra* (XANES) spectrum of Frenkel defect in [419]). This emphasises the difficulty of relying on theoretical studies as they are sometimes not consistent with one another; however, they provide an important piece of information in order to discuss the findings.

5.5.2. Neutron and ion-irradiation

DFT calculations [419] performed on REBCO with different types of defects on the oxygen sublattices (e.g. O(1)/O(4) vacancies and Frenkel defects) show that the a/b-axis lattice parameters are essentially unaffected, which were not included as part of Murphy results [421]. However, Lopez et.al. [422] show slightly different results using ab-initio calculations, in a case of complete oxygen removal (YBCO6), average a- and b-axis lattice parameters increase to about 3.90 Å, similar to what was observed in He-irradiated sample (Table 5.1). Many studies (e.g. [54], [77]) correlate between T_c reduction to loss of oxygen from the Cu-O chains; however, although this possibility cannot be ruled out completely, Nicholls et.al. [419] argue that the XANES spectra of He-irradiated samples show changes primarily in the CuO_2 planes and their local environment and not in the CuO chains. Additionally, the enlargement of c-axis seemingly as a results of O(1) vacancies [80], [83] is not aligned with the DFT calculations and thus it is likely that O(1) vacancies (if any) cannot account for all the structural changes occurred in the He-irradiated sample. Actually, experimental XANES spectra matches better the model of Frenkel pair with O(2) vacancy and interstitial at (0,0,0.5), a defect that is also associated with c-axis enlargement. So, only because the superconducting properties were eliminated in this sample, it is hard to point out (let alone given the lack of further literature on this subject) which kind of defects are present as it is likely that superconducting properties can degrade as a result of more than one kind of defect.

The superconducting properties of the neutron-irradiated sample were not as impaired as the He-irradiated sample, showing a T_c reduction to about 82 C° (Figure 2.41a) and a 30% reduction in J_c (Figure 2.44a) [31]. Therefore, it can be said that the irradiation damage (apart from local damage cascades) in this case was not as severe as in the case of He-irradiated samples, an observation that seen qualitatively in observations of damage to the REBCO matrix in Figure 4.1 & Figure 4.5. Despite that, the root-cause that associated with the neutron-irradiated samples characteristics is hard to be stated explicitly. On the one hand, my experimental results show an *absolute* shrinkage of intra-cell distances (from 7.402 to 7.326 Å, for pristine and neutron-irradiated, respectively), aligned with Nicholls et.al. [419] that show a similar ~0.1 Å absolute intra-cell distance decrease due to the presence of oxygen vacancies. These results, although of lesser magnitude, were also observed in Xe-irradiated samples at 298 K (discussed in section 5.5.4). On the other hand, neutron-irradiated samples differ from the rest of the sample types by their: (1) absolute shrinkage of c-axis lattice parameter (Figure 5.2), (2) wide a/b-axis lattice parameters distribution (Figure 5.4), and (3) very scattered a/b-axis lattice parameters and standard deviation values (Figure 5.9). In other words, the neutron-irradiated sample shows more discrepancies than similarities to the other samples investigated.

What could be the potential reasons for the neutron-irradiation sample characteristics? In terms of c-axis lattice parameter shrinkage, it is known that lattice parameters do not change linearly with fluence [423]–[426], and it is possible that with increasing neutron fluence, the measured c-axis lattice parameter would increase in the same way as all the other samples analysed in this section. Another possible explanation is the formation of a different kind of defect altogether that causes, perhaps only over a limited fluence range, the c-axis lattice parameter to decrease, even though they locally increase in the presence of buried damage (Figure 5.12). Although using a

different characterisation technique, evidence supporting the formation of different defect types, in contrast to the dominance of Frenkel defects in He-irradiated sample shown in [419], is reported by analyzing neutron-irradiated REBCO using positron annihilation lifetime spectroscopy (PALS) [278], [427], which concluded that the main defect present is Cu-O divacancy (which is not presented in the DFT calculations discussed). So there are at least two possible mechanisms for the anomalous behavior of the neutron-irradiated sample; the first based on a different distribution of the same kind of defects as formed in the He-irradiated sample, and the second the formation of a different kind of defect, but with the current experimental evidence it is difficult to unequivocally determine which (or a combination of the two) is correct.

The neutron-irradiated sample behavior along a/b-axis implies on large anisotropic microstrains along this axis manifested in wide lattice parameters distribution, whereas the scattered lattice parameters and standard deviations can be a result of damage (excluding local damage cascades) which is not homogenously distributed as in the case of He-irradiated sample. However, due to the unlikelihood of statistical skewness occurred only in the neutron-irradiated samples, I hypothesize that neutron-irradiated REBCO matrix (excluding local damage cascades) is in transition stage, i.e. an intermediate stage between pristine and He-irradiated (or Xe-irradiated at 298 K) state. This transition stage is manifested in two main manifestations: (1) accumulation of defects with relatively low concentration, which is not sufficient to induce inelastic stress relaxation; (2) c-axis lattice parameters shrinkage. Thus, continuation of the irradiation will likely result in an increase of a/b-axis lattice parameters and the release of strain, which then will narrow the a/b-axis lattice parameters distribution similar to what can be seen in the case of He-irradiated samples (Figure 5.4). Additionally, c-axis lattice parameters will increase as was observed for the other samples in this study.

An alternative explanation for the anomalous results from the neutron-irradiated sample is the very high neutron capture cross section of the ^{155}Gd and ^{157}Gd atoms that have natural abundance of about 15% [428], [429]. When a thermal neutron (Ekin < 0.55 eV) is captured, the Gd atom is excited and after returning to its ground state emits an γ-ray with an energy of about 30 eV. This results in momentum transfer which is sufficient to displace this Gd atom and to create a point defect. This phenomenon was suggested to make a contribution for the degradation in Tc values [37]. Although the neutron-irradiated samples in this study contain 100% Gd as the rare-earth element, the effect of the thermal neutrons was eliminated by shielding the sample with cadmium foil, but other interactions with the higher energy neutrons that do not happen in ion-irradiation might contribute to the radiation response of GdBCO.

For Xe-irradiated sample irradiated at 298 K, the interesting observation is the dramatic differences between the Ba_1-Ba_2 inter- and intra-cell fractions when compared to He-irradiated and neutron-irradiated samples (Figure 5.3). Even with this large modification of the lattice, neither were intercalation defects observed in the STEM images (e.g. Figure 4.2), nor was the a/b-axis lattice parameter affected (Figure 5.2 & Table 5.1). By observing the magnitude of the change of the inter- and intra-cell fractions in the Xe-irradiated samples (about X6 times greater than any individual defect predicted by Murphy's model [421] and X2 compared to Nicholls et.al. [423]) - Figure 5.23 & Figure 5.24 - it is likely that these structural changes cannot be generated only by individual defect types and are likely associated with either clusters of defects and/or mutual interactions between several kinds of defects. So in addition to the expected damage cascades (Figure 4.12, section 4.2.2), the matrix in the vicinity of these dense array of vacancies and interstitials must suffer from increasing amount of defect clusters, which leads to the observed magnitude of inter-cell fraction increase.

Summarising the results from Xe, He and neutron irradiated samples: the complete elimination of the superconducting properties in He-irradiated sample is likely to be a combination of oxygen vacancy-interstitial pairs that are associated with T_c and J_c elimination and expanded c-axis lattice parameters. The neutron-irradiated sample, in between the damage cascades, shows some unique characteristics and thus possibly accumulated less lattice damage as also explained by its T_c and J_c reduction compared to He-irradiation sample. Lastly, Xe-irradiated sample behaves differently mainly in its c-axis enlargement nature with large inter-cell fraction increase, and also presents different c/a ratio (Table 5.1), which increases in the case of Xe-ions and decreases for He-ions and neutrons. In all cases, the unit cell volume increases, which is consistent with most of the research conducted on oxides under irradiation [430].

5.5.3. Light ion irradiation

Although I have categorized He, Ne, and Ar ions as 'light' ions, their irradiation-induced damage nature is different. He-irradiation does not generate cascades, whereas Ne-ions at 200 keV result in isolated, small damage cascades [272], and Ar-ions certainly generate cascades as observed in section 4.2.1.3. Thus, one would expect to observe different damage mechanisms when comparing the STEM data from these three sample sets. Also, the reader should note that the fluence is identical for Ne- and Ar-ions, but three orders of magnitude lower than for the He-irradiated sample (10^{13} cm^{-2} compared to 10^{16} cm^{-2} for He-irradiated).

A clear indication of the different nature of the irradiation damage in both the Ne & Ar samples compared to He-irradiated sample is the a/b-axis lattice parameter. He-irradiated sample unequivocally shows expansion in the a/b-axis, in fact, every single image taken from the He-irradiated sample using the ARM300CF microscope (both one-frame and stacks images) has a larger a/b-axis lattice parameter than pristine samples (Appendix B: Figure S- 6). By contrast,

Ne/Ar-ion irradiation does not change the a/b-axis lattice parameter (Figure 5.13). The c-axis lattice parameters, on the other hand, are expanded in all cases, but more in the intra-cell region by Ne-irradiation compared to inter-cell expansion in the case of He- and Ar-ions (Figure 5.14). Based on these observations, and my understanding of the likelihood of generating damage cascades, one should not be surprised that the He-ion damage mechanism is different to that from Ne/Ar irradiation, especially in its effects along a/b-axis. Interestingly, Xe-irradiation also has little effect on the a/b-axis (Figure 5.17a). It is thus consistent that Ne- and Ar-ions, producing small damage cascades, and Xe-ions that produce larger cascades, have little effect on the a/b-axis lattice parameters but do cause an increase along the c-axis. He-ion damage, which generates no cascades, but rather a high density of point defects, affects both the a/b-axis and c-axis lattice parameters.

To conclude, it seems that He-irradiated sample is affected by individual defects that unambiguously cause an increase along a/b-axis; whereas Ar-ions, and to lesser extent Ne-ions, fall outside the realm of individual vacancies 'nature' but rather an accumulation of defects, which has anisotropic effect on c-axis while a/b-axis lattice parameter stays unchanged.

5.5.4. Effect of irradiation temperature

Apart from the a/b-axis lattice parameter discrepancies between the two samples, i.e. at 298 K it retains its initial value but largely increases at 100 K, the irradiation effects nature as measured by c-axis lattice parameters and inter- and intra-cell fractions are similar. However, at 298 K only the inter-cell *absolute* distance increases whereas the intra-cell actually shrinks, a manifestation that intensifies the skewed unit cell distribution along c-axis compared to unirradiated state. This result is consistent with Nicholls et.al. [419] as oxygen vacancies cause

an absolute decrease in intra-cell fraction. Additionally, these defects result in increase of the inter-cell distance while retaining the c-axis lattice parameter value. On the other hand, Frenkel pairs are associated with absolute increase in both inter- and intra-cell distances and large c-axis lattice parameter increase, which nicely illustrated the state of the Xe-irradiated sample at 100 K.

There could be several reasons causing the differences at different temperatures. Due to the fact that the samples were irradiated in-situ as thin TEM lamellae, differences in net oxygen loss due to surface effects are plausible, which can arise from higher mobility of (mainly) oxygen at higher temperature and thus higher net oxygen loss at 298 K compared to irradiation at 100 K. If this manifestation does play a role, it will result in less interstitials atoms at Xe-irradiated at 298 K, which aligned with the DFT results on at least two levels: (1) absolute decrease in intra-cell distance, (2) c-axis lattice parameter change is less substantial compared to what has been predicted given a Frenkel defect. In other words, the larger number of oxygen interstitials in Xe-irradiated at 100 K increases the c-axis lattice parameter while retaining the inter- and intra-cell fractions similar to irradiation at 298 K.

Although the above can explain some of the differences it cannot be accounted for differences observed. A known phenomenon of irradiation at low temperatures is the inhibition of dynamic defects recovery due to low thermal immobility results in a larger number of surviving defects [247]. Although it is known that recovery of REBCO takes place at room temperature, as in the example of Iliffe et.al. [213], the recovery is neither complete nor affects all types of defects. Therefore, one should expect that the excessive defects accumulation will result in increase of stored energy above the minimum energy configuration [430], this energy can then be released using different mechanisms when the material strives to lower its energy [430] since it is above the minimum energy configuration. An evidence for the lattice strain that dominate at low

irradiation temperature can be seen in Figure 5.19 & Figure 5.20 as a wider lattice parameters distribution.

Furthermore, cascade cores (that did not cause full amorphisation throughout the sample thickness) compared the regions in their vicinity of these cascades, as can be seen in Figure 5.21, result in a similar expansion along a/b- and c-axis but the expansion along c-axis takes place primarily in the inter-cell portion. Additionally, in [267] it was reported that the oxygen levels in the cascade cores following 18 MeV Au-ions irradiation are lower compared to the surrounding matrix, which can be one of the reasons for the inter-cell distances growth. Regardless, it is well expected that the cascade cores possess higher lattice parameters and are associated with amorphous phases (that buried in the TEM lamella) [430], chemical changes [267], and residual lattice strains [431].

Lastly, it should be emphasised that the Xe-ions, at both temperatures, damage characteristics are different from both neutrons and lighter ions used in this study. The main reason for deriving this conclusion is the dramatic inter-cell fraction increase, which occurs in both irradiation temperatures (Figure 5.17b). As already been mentioned for Xe-irradiated sample at 298 K, Xe-ions irradiation effects are likely the result of existence of defects clusters and/or reactions between different individual defects. Xe-ions may generate several types of defects that can interact to form a lower energy configuration, an example of such a defect could be a 2VCu + 3VO in the vicinity of Y124 that has lower energy than Cu divacancy [97]. Another possibility than cannot be ruled-out is lattice strains that are associated with amorphous domains.

To conclude, Xe-irradiation at 100 K and 298 K results in similar characteristics in their inter- and intra-cell behaviour but differ in the lattice parameters expansion. It can be attributed to several manifestations: (1) recombination efficiency during irradiation at low temperature, (2)

vary net oxygen loss in the TEM lamellas due to different oxygen mobilisation rates, (3) changes in recombination efficacy at room temperature of the presumably different irradiation damage introduced during irradiation.

5.5.5. Experimental errors

In general, one of the main contributors to the formation of an imperfect image is aberrations, i.e. when rays coming from a unique point in the object plane do not fall on a unique point in the image plane. Aberrations are grouped into two classes, astigmatic and comatic, also known as symmetric and asymmetric, respectively. Specifically, if a point source suffers only from astigmatic aberration, the image formed will be symmetric, and comatic aberrations that form asymmetric images [432]. For the astigmatic aberrations family one can enumerate spherical, astigmatism and defocus, while the comatic family includes coma and distortion. The reader should note that the sometimes ill-defined term distortion refers to an optical system that forms an image with geometrical representation that is differ from the object, regardless the scaling factor. The aberrations in STEM are determined by the shape and size of the electron probe [433] and thus the discussion in this section also applies to probe-forming optical systems such as STEM.

In modern aberration-corrected microscopes, the residual aberration coefficients, namely, their values after corrections, to their different orders are estimated. Among the factors mentioned above, distortion is not estimated directly. In STEM, distortions are mainly associated with scanning distortions and sample drift. Distortions are harder to quantify when compared to other distortions types, but can be dramatically reduced using stack images and rigid followed by non-rigid registration of the image [434]. The former refers to the alignment of the images using

translation, rotation, and scaling, whereas the latter corrects localized geometric differences [435]. This explains why the standard deviation of the lattice parameters measurements presented in this chapter is generally larger when using one-frame acquisition.

Generally speaking, the location of a ray falling on the image plane is a function of the ray location on the object plane, H, and its location on the pupil plane, ρ, and thus its deviation from the ideal image point location can be defined as:

Equation 5.1: $\vec{\epsilon}(\vec{\rho},\vec{H}) = \overrightarrow{\varepsilon_s}(\vec{\rho},\vec{H}) + \overrightarrow{\varepsilon_c}(\vec{\rho},\vec{H})$

Where $\overrightarrow{\varepsilon_s}$ and $\overrightarrow{\varepsilon_c}$ are the astigmatic and comatic aberrations. The 'order' of an aberration, e.g. third, fifth, etc. usually refers to the order of the pupil plane location where symmetric aberrations have odd orders and asymmetric aberrations have even orders. As an example, the following table summarises the typical aberration coefficients in the ARM200f microscope.

Table 5.5: ARM200f microscope typical aberration coefficients in the corrected state at 200 kV. Kindly provided by Dr. Ian Griffiths.

Aberration name	**order**	**Abbreviation coefficient** [436]	**Value**
Defocus	1	C_1	4.1 [nm]
Spherical	3	C_3	198.7 [nm]
Spherical	5	C_5	204.1 [um]
Astigmatism	1	A_1	2.4 [nm]
Astigmatism	3	A_3	1.7 [um]
Astigmatism	5	A_5	518.2 [um]
Coma	2	B_2	8.1 [nm]
Coma	4	B_4	8.3 [um]

The absolute residual aberrations values are less of an interest when discussing the precision of the measurement, but rather their variation between sessions and image acquisitions. An estimate for this variation based on typical microscope operation is about 10% as shown by monitoring the residual aberrations values of ARM300CF microscope overtime. The normal way to combine

the effect of all these aberrations would be to add all the components quadratically to estimate the total measurement error emanating from microscope aberrations, but the coefficients above are a complicated function of ρ and H, and it is mathematically incorrect to sum them up in one equation without proper weighting. Thus, it is also difficult to state which coefficients are contributing the most to defining the precision of the atomic locations.

Another aspect to this discussion is the correlation between the aberration coefficients and the computed atomic locations using the StatSTEM package. In their first publication [396], the authors of StatSTEM discuss only two sources of error to verify the accuracy and precision of the model, namely sample thickness and electron dose. The model precision was proven to be roughly constant with subtle variations from monolayer samples to 75 atoms per column in low ($D=5\times10^2$ $e^-Å^2$) and high ($D=5\times10^5$ $e^-Å^2$) electron dose conditions. Furthermore, from private correspondence with one of the authors, it has been verified that no other factors were assessed, and "[they] *do not expect that the precision will drastically drop within the typically used ranges [e.g., defocus, residual aberration coefficients] for atomic resolution STEM imaging*".

In summary, this short section discusses the sources of experimental errors when STEM images have been acquired. It was concluded that the main factors that lead to image variations are the intrinsic aberrations of the microscope. The atomic locations computations are affected by the typical aberration coefficients and their roughly 10% variation, which impacts accuracy and precision, respectively. The latter is more of an interest when benchmarking irradiated samples to pristine sample, as was done in this chapter. However, it is hard to provide concrete numbers for the effects of aberration coefficients on the computed atomic columns positions without undertaking a separate experiment with modelled STEM images.

5.5.6. Statistical significance analysis

The closing section of this chapter discusses the statistical significance of the results shown above. In some of the figures shown (e.g. Figure 5.2) it looks like the differences between the samples are subtle, while their standard deviations are relatively large. In order to address these changes from a pure statistical point of view two known tests were applied, Kolmogorov-Smirnov test [437], [438] and the Student's T-test [439]. Both tests aim to assess whether two populations are different from each other based on a random set of samples.

The Kolmogorov-Smirnov test (K-S test) is a *non-parametric* statistical test aiming to test the null hypothesis that two samples (in the case of a two sample K-S test) were derived from the same distributions. Being a non-parametric test means that it is not strictly dependent on certain parameters of the distribution. In contrast, the famous Student's T-test is a *parametric* test that is usually applied to populations that have normal distributions. It tests the null hypothesis that data from two samples (in the case of a two sample test) comes from normal distributions with the same mean value. The naming convention for both tests is h=1 when the null hypothesis is rejected and h=0 for the alternative hypothesis.

Both tests were applied to several cases presented in this chapter as a case-in-point. In the first case, pristine samples were compared to neutron-irradiated and to He-irradiated samples in terms of their a/c-axes lattice parameters and inter- and intra-cell distances (refer to Figure 5.2, Figure 5.13), where data was extracted from one-frame images taken on the ARM300CF. In the second case, pristine inter- and intra-cell distances were compared for Ar- and Ne-irradiated samples from one-frame images taken on the ARM200f (Figure 5.14). The results were unambiguous, in all cases both tests showed h=1, which demonstrates that the difference between the samples is statistically significant in terms of their distribution characteristics and means. In addition, the

significance level parameter, α, which is a measure of the strength of the evidence present in the samples before the null hypothesis is rejected, was chosen to be 0.01. In other words, there is a 1% probability that the samples tested have no actual difference although the null hypothesis was rejected. Usually, either $\alpha=0.05$ or $\alpha=0.01$ are used [440], in all cases presented, I deliberately chose to use $\alpha=0.01$ to strengthen the evidence that the samples are indeed different from one another.

The reader should note that the purpose of the above tests is to reject/accept the null hypothesis of the general population based on the distribution characteristics of the random samples chosen, in this case a large though limited number of unit cells taken from a limited number of images when compared to the volume of the entire bulk/TEM sample. Despite the fact that it cannot be ruled out that these differences did not arise due to local variations in the structural parameters of the different samples, based on the evidence above it does seem that all the results shown in this chapter, despite their subtle difference, show a real statistical difference that has not arisen due to chance.

6. HRTEM images analysis

6.1. Introduction

Techniques for analysing the 'quality', i.e. the extent of lattice damage present in TEM/HRTEM images, other than by simple counting of obvious defects, have not been reported extensively in the literature. Among the different studies, perhaps the most researched one is the study of the evolution of the amorphous fraction as a function of irradiation fluence, which can shed light on amorphisation mechanisms [441], [442] (section 2.2.1.1.5). Although for some cases, the damage can be visible to the naked/trained eye (see examples in section 4.2.1), turning this into a quantitative measure is not easy. However, in the field of image processing, extensive research has focussed on matching subjective human 'image quality' scores to a calculated model score. In the following sections, I propose a new quantitative method to apply image processing techniques to the assessment of irradiation damage in HRTEM images. The full details on the images and irradiation conditions can be seen in Table 3.7.

6.2. Why image quality assessment is not likely to succeed in the spatial domain

As already presented in sections 2.3.2.1 & 2.3.2.2, many image quality assessment techniques are based on the statistical properties of images in the spatial domain. However, HRTEM images of crystalline materials are dramatically different to *natural scene* images, and thus quantifying the 'lattice damage' in the spatial domain is not likely to yield satisfactory results, as will be explained in the following section.

It is worth remembering that entropy calculations in the spatial domain are computed directly from the probability density function of the pixel intensities (Equation 2.6), and not from the power spectral density as in the case of spectral entropy, where the amplitude of the signal is

squared (Equation 3.2 & Equation 3.3). As will be shown later, the entropy calculated in the FFT and DCT domains represents the spectral components of the image, and increases in a way consistent with the extent of damage one can estimate from the images; however this is not true for entropy in the spatial domain. Figure 6.1 shows the average entropy values in the spatial domain for all the samples types used for this study, a total of about 1000 images, ordered by increasing values from left to right. To make the visualisation easier, I colour-coded four groups of several samples (as a case in point) according to the expected irradiation damage (see section 4): no damage (pristine), light-medium damage (He-irradiation), severe damage (Kr-irradiation and Xe-ions at 100 K) and amorphous, with the associated colour green, yellow, maroon, and red, respectively. The black colour stands for samples that were not categorised. It can be seen that the 'no damage' and 'amorphous' samples are not situated at the extreme ends of the plot, which makes this analysis unreliable, at least if one expects a simple linear relationship between the extent of damage and extracted entropy values.

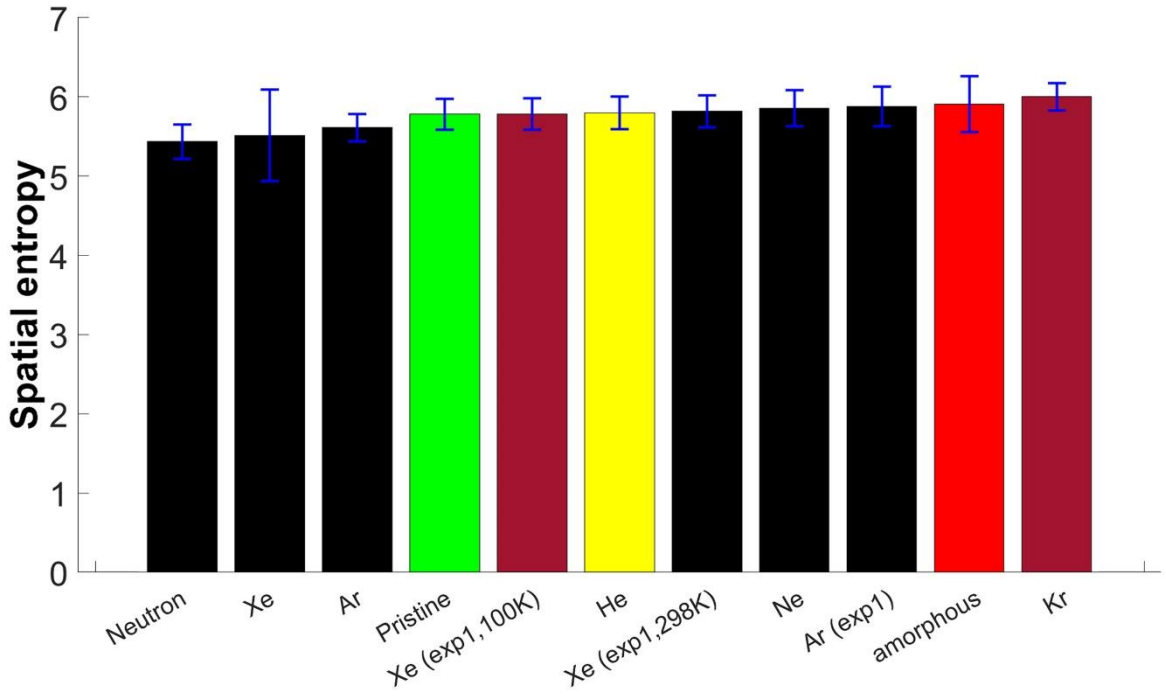


Figure 6.1: Entropy values in the spatial domain extracted from 1024X1024 pixel blocks for all the sample types in the dataset, ordered by increasing values from left to right. Standard deviation values are shown by error bars. The total number of HRTEM images used for this analysis amounts to about 1000. The colour-coding for the bars was chosen according to the observed damage in HRTEM image, no-damage (pristine in green), light-medium damage (He-irradiation in yellow), severe-damage (Kr-irradiation and Xe-ion irradiation undertaken at 100 K) in maroon, and amorphous in red. Black bars belong to samples that were not categorised according to their damage severity.

As an example, Figure 6.2 shows two typical HRTEM images of (a) pristine and (b) 'almost amorphous' regions, and the entropy values in the spatial domain are 5.88 and 6.03, respectively. As a comparison, for the same images the entropy values in the mid-frequency FFT domain are 8.23 and 11.96, and for the DCT domain 9.84 and 12.82, respectively. From this visual illustration (Figure 6.2) as well as the summary statistics from more than 1000 HRTEM images, it can be concluded that entropy in the spatial domain cannot be used effectively to quantify the damage levels in this kind of image.

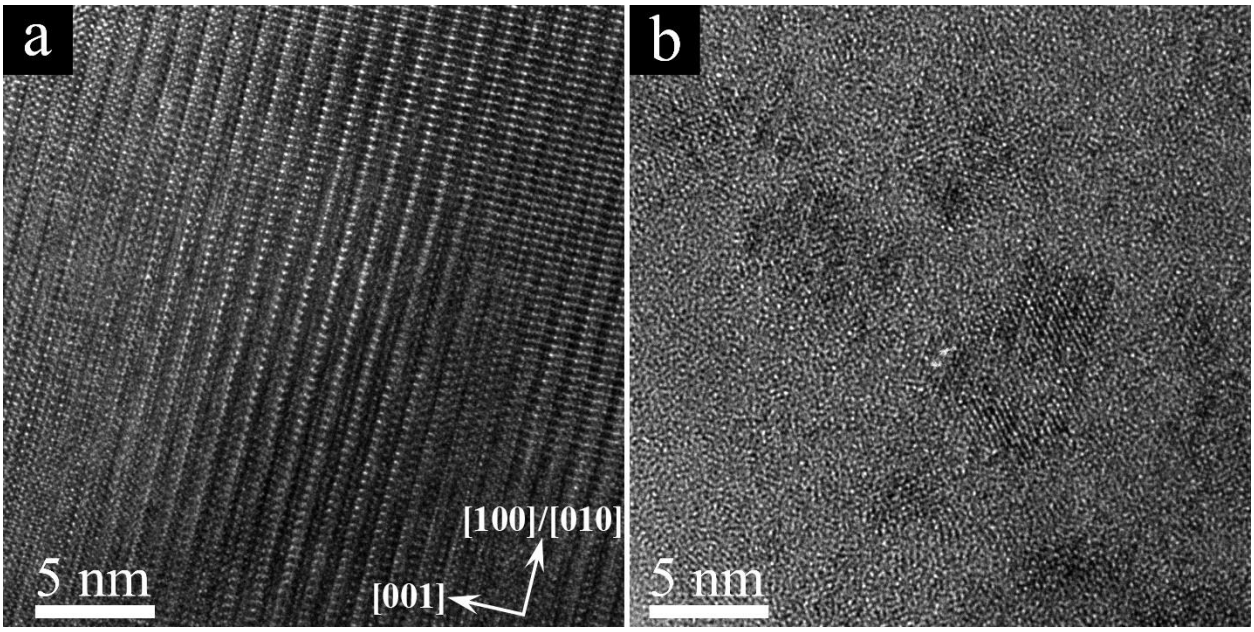


Figure 6.2: examples of (a) pristine and (b) 'almost amorphous' HRTEM images taken along [100]/[010] ZA. The TEM foil in (b) was irradiated in-situ with 350 keV Xe-ions at 100 K to a fluence of 1×10^{13} cm^{-2}.

In order to better understand why the calculated entropy values in the spatial domain from these two extreme examples of lattice perfection do not show much difference, one can look at the probability density function that determines the entropy. Figure 6.3 shows normalised histograms of the pixel intensities calculated from 44 images from both pristine and amorphous samples. In Figure 6.3a it can be seen that the intensities from the amorphous samples are, on average, shifted to higher values (closer to 1), which is manifested in an image that looks, on average, brighter (Figure 6.2b). In order to compare them directly, the centres of the distributions should be aligned as shown in Figure 6.3b. From this example it can be concluded that the two extreme states of pristine and amorphous material have essentially the same pixel intensity distributions, and therefore the entropy values in the spatial domain are very similar, 6.09 and 6.20, respectively, as calculated from the distributions of all the pristine and amorphous 2048X2048 pixel images. Although image corrections (e.g. brightness/contrast) can be applied on these

images to change their pixel intensities, as long as the correction is linear, the entropy value will not change, i.e. the zero-mean distribution will retain its shape.

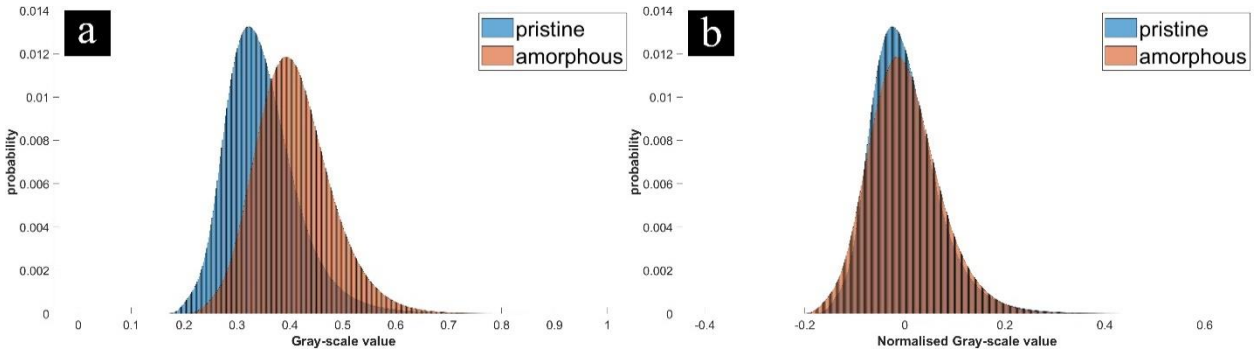


Figure 6.3: Normalised histograms of pixel intensities of 44 HRTEM images of pristine and amorphous samples. (a) Gray-scale (b) gray scales values after shifting the mean values to zero.

So, although HRTEM images of pristine and amorphous material (Figure 6.2) look significantly different, their statistical properties in the spatial domain are essentially the same (although there may be an intensity shift from differing sample thickness or microscope conditions). Therefore, neither entropy nor any other statistical method performed on the spatial domain is likely to differentiate between the damage levels in different HRTEM images without more sophisticated analysis of spatial locations and/or mathematical manipulation to extract small statistical differences.

6.3. Entropy changes in the frequency domain

This section analyses the correlation between *entropy* (defined in section 2.3.2.6 as a measure of the amount of disorder in an image or signal) and lattice damage as seen in HRTEM images. This definition of entropy has the mathematical form that causes it to drop to zero if a signal contains only one value, e.g. an image with equal intensity in all pixels, and reaches a maximum when a signal contains many different values, e.g. lots of random values. Spectral entropy

measures the spectral power distribution, defined as the intensity squared, with the signal being normalised by a measure of power concentration. I will be focusing on spectral entropy in the DCT and FFT domains, hereafter referred to as entropy.

When measuring entropy in this way, it is important to assess its value against a signal with the same number of values because the spectral entropy may increase in absolute terms when the length of the dataset (here number of pixels) increases. Figure 6.4 shows the spectral entropy value of a random series with values between 1 to 1000 measured from a signal length of 6000 up to 150M. What is clear from the figure is that the entropy increases with signal length, namely, the total number of coefficients. For example take [1,2] as two FFT coefficients. In order to get the power spectrum, the power is then [1,4], and when normalised gives [1/5,4/5] = [0.2,0.8], from which the entropy can be calculated using Equation 3.2 & Equation 3.3 (section 3.5.2.3) to be equal to 0.723. If we increase the signal length by a factor of two to give [1,2,1,2], the spectral power will be [1,4,1,4] and after normalisation [0.1,0.4,0.1,0.4], giving a resulting entropy of 1.723.

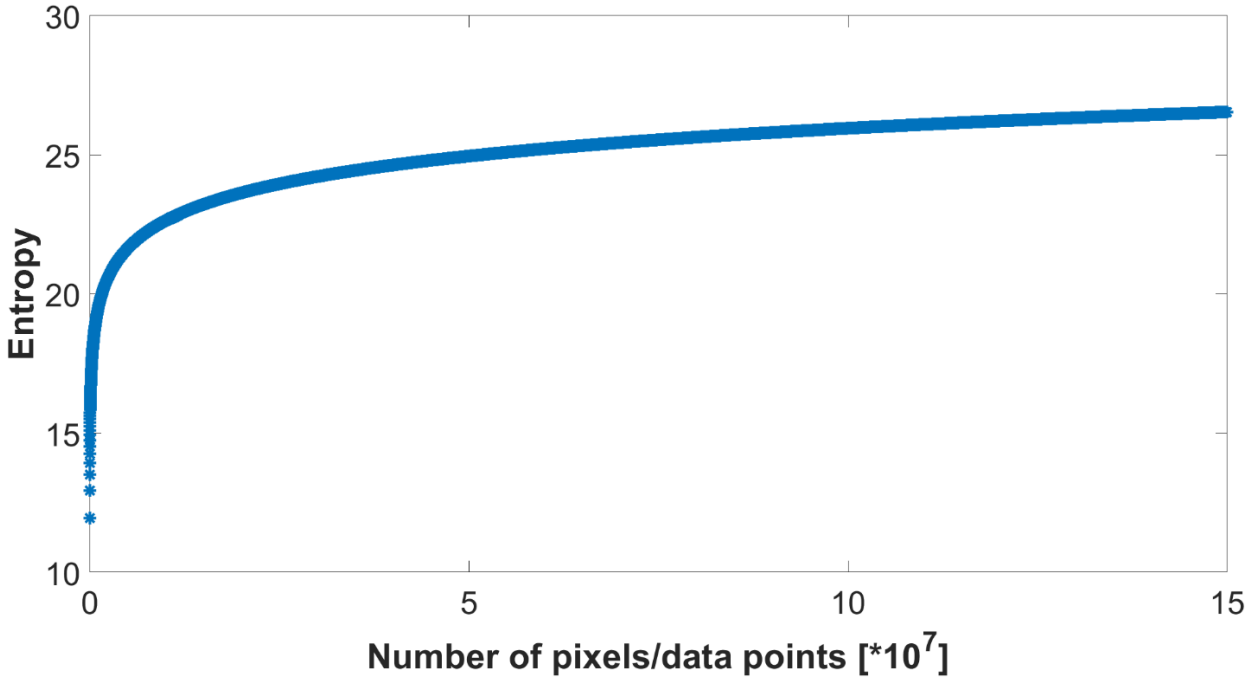


Figure 6.4: Spectral entropy values as measured from a random series of numbers from 1 to 1000 and a signal length from 6000 to 150M with 25000 data points where entropy was calculated.

The following discussion includes two methods for analysing HRTEM images in the frequency domain, i.e. in reciprocal space, and using two mathematical transformations: the *discrete cosine transformation* (DCT) and the *fast Fourier transform* (FFT), introduced in sections 2.3.2.3.1 & 2.3.2.3.2. Figure 6.5 shows a scatter plot of entropy values extracted using DCT (y-axis) and FFT mid-frequency (x-axis) analysis of images from unirradiated (pristine) and amorphous regions created by Xe-ions irradiation and at the sample edge by FIB damage. It is obvious that the entropy values increase in both domains when the REBCO lattice is damaged from the pristine crystalline to the amorphous state, and it is also interesting that the values from the two kinds of amorphous regions align very closely. This section studies the reasons for the entropy increase between those two extremes, and how one might use the intermediate region of less severe damage in between to extract data on more subtle degradation of the REBCO lattice.

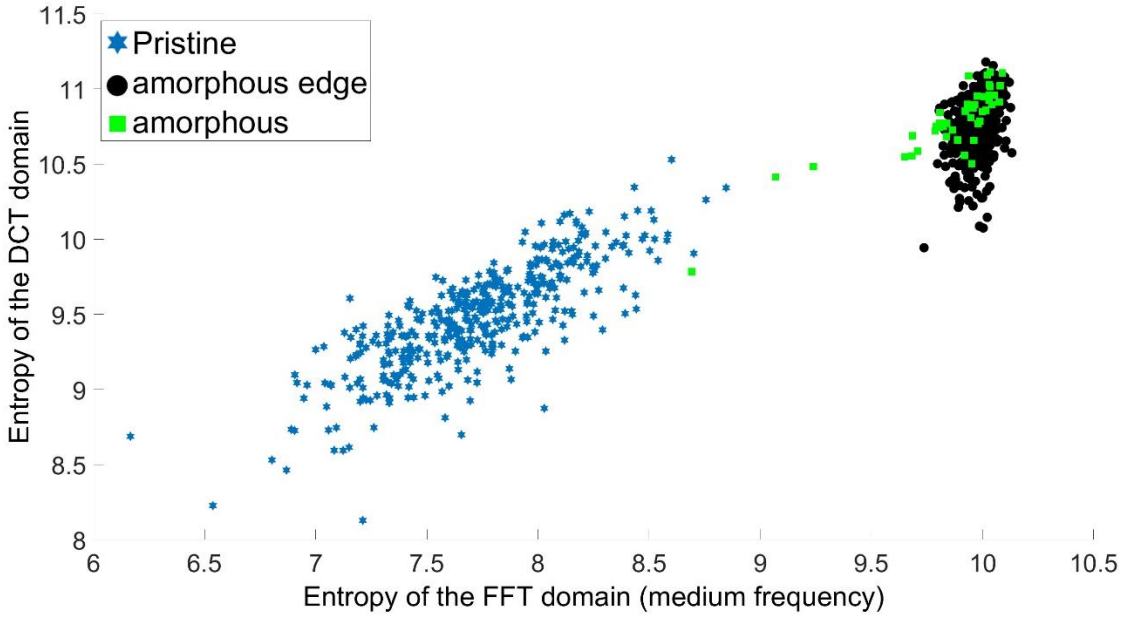


Figure 6.5: A scatter plot of entropy values in the mid-frequency FFT on the x-axis and DCT domain on the y-axis of pristine (blue hexagrams), amorphous edge (black circles) and amorphous (green squares) as extracted from 512X512 pixel image blocks.

6.3.1. Amorphous HRTEM images

Not all the images that defined as amorphous material when the assessing the extent of lattice damage using entropy calculations showed a complete loss of periodic structure. Two examples of 'amorphous' images are shown in Figure 6.6. It can be seen that both images contain some crystalline material, which also contribute to weak spots in the associated FFT images in the insets. To investigate the extent to which the residual crystallinity affects the entropy analysis, the available almost-amorphous entropy values should be compared against those from fully amorphous samples. Since the 1024X1024 pixel blocks used for most of the analysis are not available for the near-amorphous regions, the best proxy would be to compare 512X512 pixel blocks of near-amorphous samples against the amorphous edge images that are considered to represent fully-amorphous material. From the results presented in Table 6.1, it can be seen that

the crystalline regions in the 'almost-amorphous' images dataset has no significant effect on the entropy values, and thus they are a good proxy for amorphous images. Furthermore, the entropy values of the amorphous samples do not affect the analysis when comparing different samples, but only when amorphous samples are used to calculate the amorphous fraction as can be seen, for example, in Figure 6.24.

Table 6.1: Entropy values of 'almost-amorphous' samples used for this study compared to fully-amorphous images taken from the sample edge. To make this comparison, the entropy values were calculated from 512X512 pixel blocks from HRTEM images.

	FFT (mid-frequency) entropy	DCT entropy
'Almost-amorphous' (used for the current analysis)	9.863	10.791
Fully-amorphous (sample edge)	9.976	10.755
Percentage difference (absolute value)	1.15	0.33

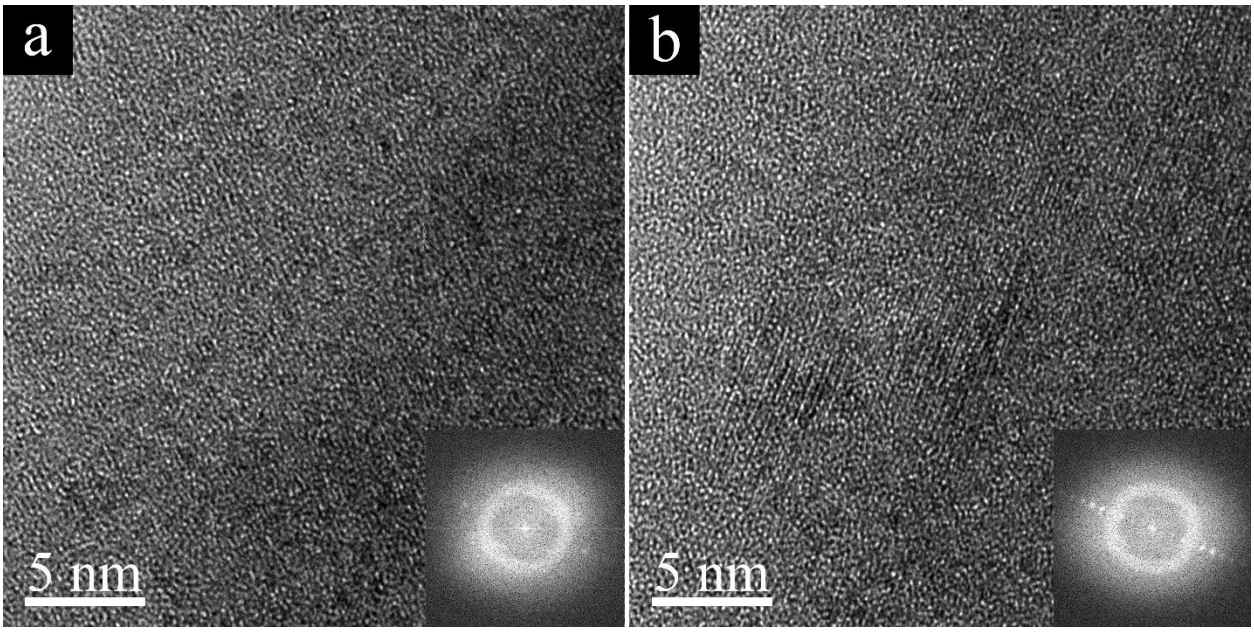


Figure 6.6: Examples of HRTEM images of almost-amorphous REBCO samples. The corresponding FFT images are shown in insets.

6.3.2. Why does FFT entropy increase?

To understand the origin of the major increase in the observed entropy in the FFT domain in the transition from the pristine lattice to amorphous material, one should look at the example in Figure 6.7. Figure 6.7a shows a typical FFT from a REBCO HRTEM image taken along the [100]/[010] zone axis (ZA), whereas Figure 6.7b presents a similar FFT pattern taken from almost fully amorphous REBCO (as discussed above, 6.3.1). The value of the real part of the complex FFT coefficients represents the intensity of the image, namely the brighter the image the larger these FFT coefficients. The major change in the transition from pristine to amorphous material takes place in the mid-frequency band that represent the short/medium-range order [443], i.e. where the amorphous halo is clear in Figure 6.7b. The inner and outer radii of this amorphous halo are at approximately 2.4 and 4.5 1/nm, respectively. In order to capture this change in structure effectively, the entropy values must be calculated from this mid-frequency band (for more details on the different FFT bands entropy the reader is referred to Appendix C (i)). It is also worth mentioning that the calculated entropy values do not vary much with fine tuning of the inner/outer band radius, as presented in Table 6.2, a measure of insensitivity of the methodology to what are necessarily rather subjective decisions on the precise values of the inner and outer mid-frequency band radii.

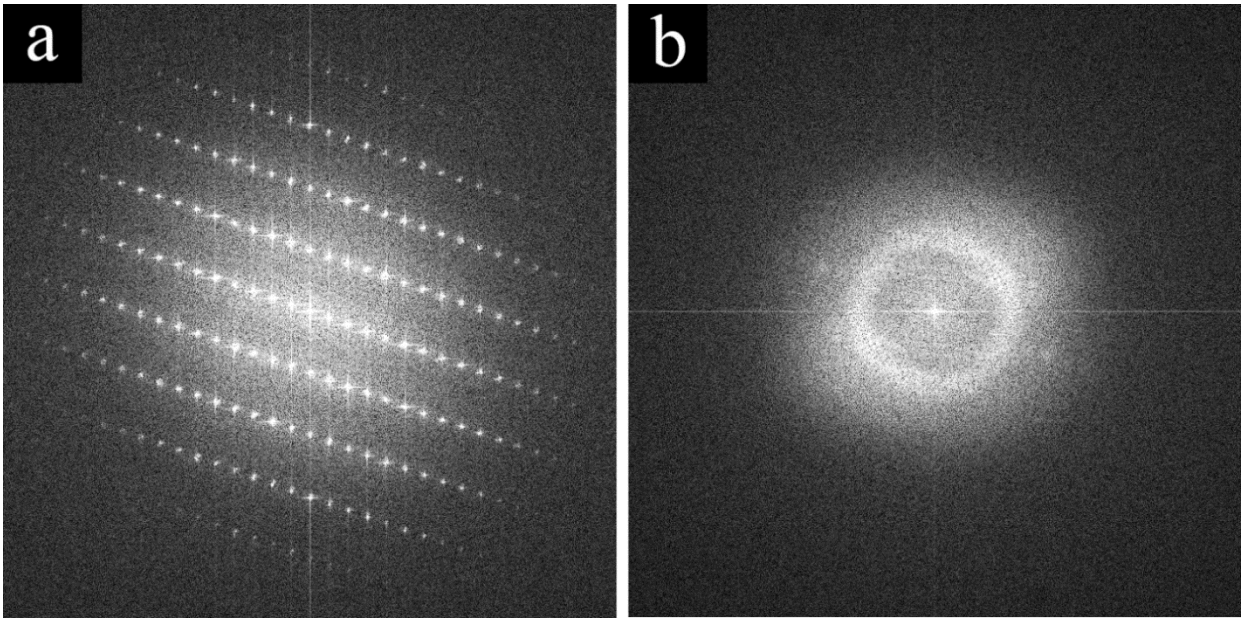


Figure 6.7: Typical examples of FFT patterns taken from [100]/010] ZA HRTEM images. (a) pristine REBCO. (b) almost-amorphous REBCO sample.

Table 6.2: the effect of the choice of inner and outer radii of the medium frequency band on the entropy values calculated from images of pristine and amorphous samples. The entropy values change also due to the change in the number of pixels on which the entropy values were calculated, but the difference in percentage terms is essentially unchanged. The entropy values are averages measured from 410 and 44 HRTEM images of pristine and amorphous material, respectively.

Inner radius [1/nm]	2.4	2.4	2.5	2.5
Outer radius [1/nm]	4.5	4.4	4.6	4.7
Entropy - pristine	8.898	9.095	8.887	8.966
Entropy - amorphous	11.837	12.044	11.847	11.912
% increase from pristine to amorphous	33.03	32.42	33.31	32.86

In order to visually appreciate the change in normalized FFT coefficients and FFT power coefficients, histograms of pristine and amorphous for a set of 44 images from pristine and

amorphous samples are plotted in Figure 6.8. The left histogram presents the shift to higher FFT coefficients, i.e. stronger intensity, when the material becomes amorphous (red bars). After raising the coefficients to the second power and normalising the histogram, the result is even more pronounced (Figure 6.8b), with pristine material results concentrated at low coefficients whereas amorphous coefficients stretch to higher values and are less concentrated. Qualitatively speaking, one would expect higher entropy from the amorphous samples given the shape of the two distributions, and the entropy definition presented in section 2.3.2.6, as the shape of the distribution is flatter and more homogenously distributed.

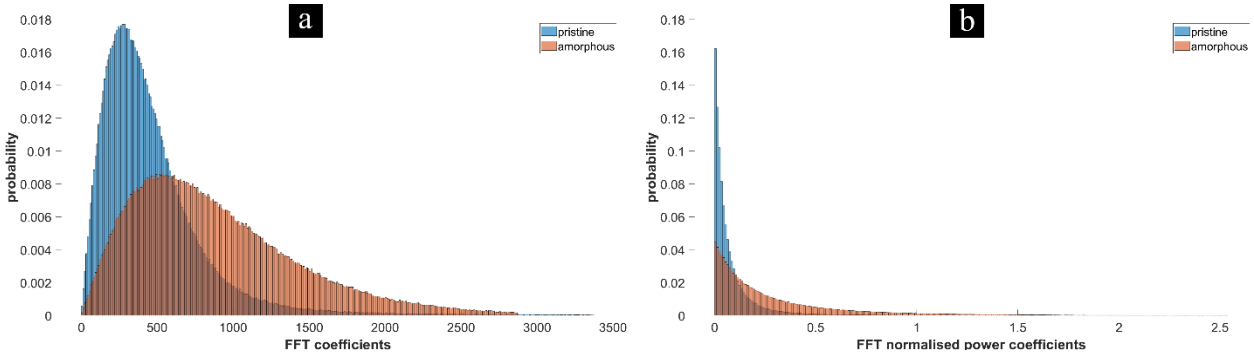


Figure 6.8: Histograms of medium-frequency (2.4 – 4.5 [1/nm]) FFT and power coefficients collected from 44 pristine and amorphous images. (a) probability distribution of the FFT coefficients, (b) power spectral density of the FFT power coefficients.

Summarising this section, when the REBCO is sufficiently damaged to become amorphous, the long range order at specific frequencies and directions in the FFT (see Figure 6.7a) changes to an amorphous halo at medium frequencies (Figure 6.7b). The statistical differences of the values of the FFT coefficients between the two states are captured by a spectral entropy value that increases as the intensity of the amorphous halo increases.

6.3.3. Why does DCT entropy increase?

This section elaborates the reasons why the spectral entropy increases in the DCT domain when the material turns from the pristine to amorphous state. As presented in section 2.3.2.3.2 the frequency equals zero at the upper left side of the DCT image (Figure 6.9i), in contrast to the FFT when it is usually situated at the centre. As DCT is less frequently used to interpret electron microscopy images, and is perhaps less intuitive, I will start this section by introducing the effect of the DCT coefficient on the resulting image.

Figure 6.9 shows the effect of including just the low frequency coefficients on HRTEM images using the *inverse DCT* (IDCT). DCT was first performed on raw HRTEM images of pristine (Figure 6.9a) and amorphous (Figure 6.9e) material to obtain a DCT matrix of the same size as the original image. From the DCT matrix, a square mask, illustrated with red dotted box in Figure 6.9i, with sides equal to 2.5% (b,f), 5.0% (c,g) and 7.5% (d,h) of the original image size were used to build the IDCT images for pristine (upper row) and amorphous (bottom row) material. As expected, the images become more similar to the raw images as the number of coefficients increases, although even with a square side dimension of 7.5% (d,h) the images still look blurry. From this simple analysis one should notice that using just low frequencies components is not enough to create an accurate proxy for the original image.

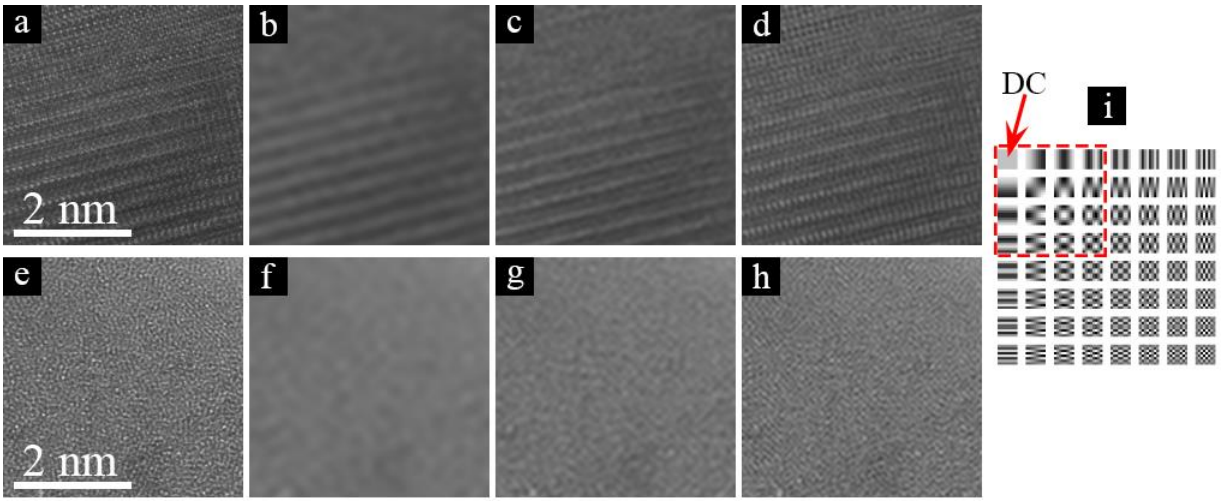


Figure 6.9: Enlarged HRTEM images of pristine (a) and amorphous (e) samples taken along [100]/[010] ZA and the corresponding inverse DCT (IDCT) images. The DCT coefficients from which the IDCT images were built include the lowest frequency components as shown in the red square in (i) and include a square of side with a length equal to about 2.5% (b,f), 5.0% (c,g), and 7.5% (d,h) of the size of the total DCT matrix.

A method that is more widely used, for example in image compression [293], to improve the fidelity of the original image is allowing the DCT coefficients that have high values make a greater contribution to the resulting image. One can recall that the DCT coefficient values stand for their relative weight of a frequency component, which is then multiplied by the cosine function for the relevant DCT pixel. Figure 6.10 shows an example constructed by choosing the high weight DCT coefficients using the same HRTEM raw images from Figure 6.9a,e. The DCT coefficients above a 0.65 threshold were chosen by trial-and-error to give a good resulting image (the quality of the resulting image, or the level of compression in the case of image compression, is determined by this threshold). The resulting images in Figure 6.10b,d for the pristine and amorphous materials, respectively, generated using about 0.06% (in the case of the pristine sample) and 0.53% (in the case of the amorphous sample) of the highest DCT coefficients, are as

not blurry as the images in Figure 6.9d,h, although they lack some of the fine details embedded in the high frequency components.

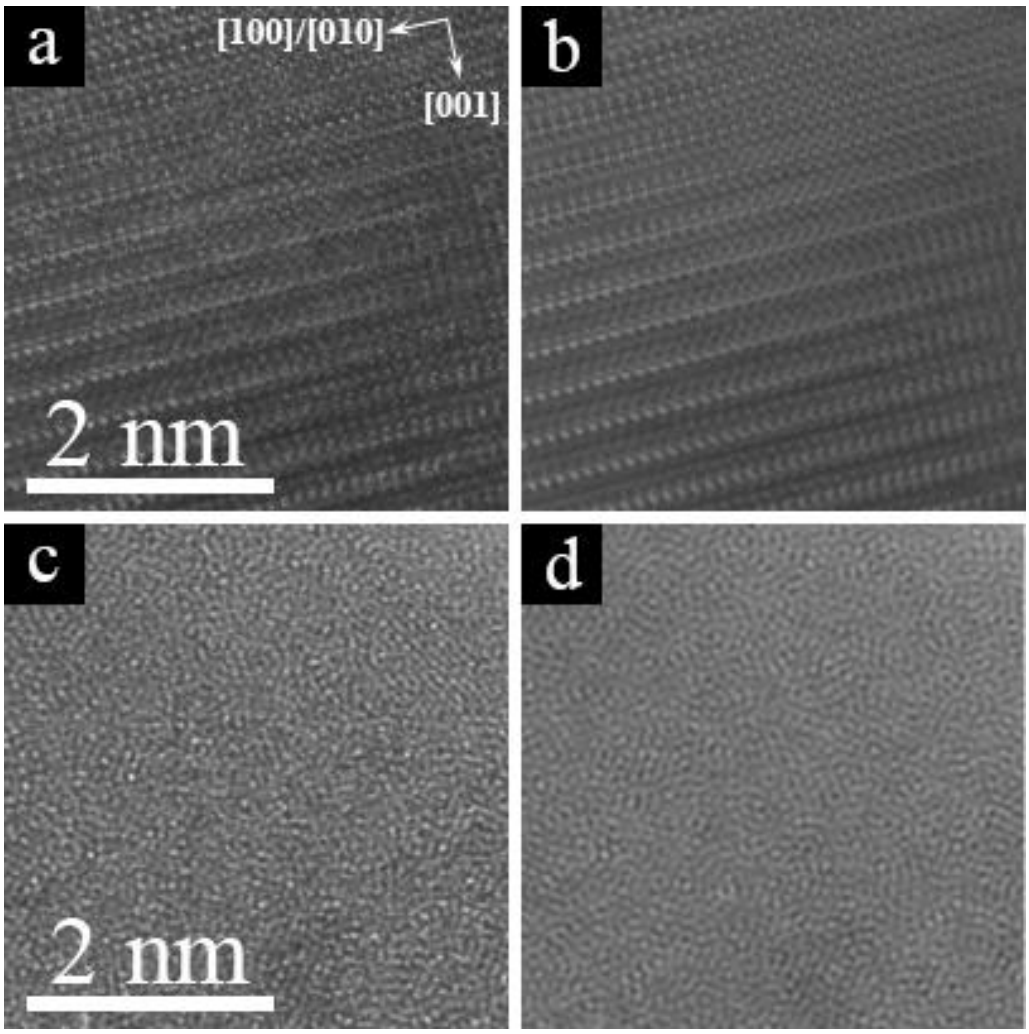


Figure 6.10: Enlarged HRTEM images from pristine (a) and amorphous (c) samples taken along [100]/[010] ZA and the corresponding inverse DCT (IDCT) images (b,d). The IDCT images were extracted from DCT coefficients that are larger than a threshold of 0.65, which accounts to about 0.06% (pristine), and 0.53% (amorphous) of the total number of DCT coefficients.

Up to this point, I have presented the contribution of the DCT coefficients to the resulting image, but the entropy of an image is determined by the distribution of all the DCT coefficients. Due the sheer number of DCT coefficients in 2048X2048 pixel HRTEM images, it is rather intractable to

include all of them. Therefore, Figure 6.11 shows normalised histograms of 150X150 low-frequency DCT coefficients, rather than whole set of 2048X2048 coefficients, from images of the pristine and amorphous materials. The distribution from the pristine samples contains more low weight frequencies, whereas the distribution from the amorphous sample is characterized by more evenly-spread coefficients and less concentration at low values.

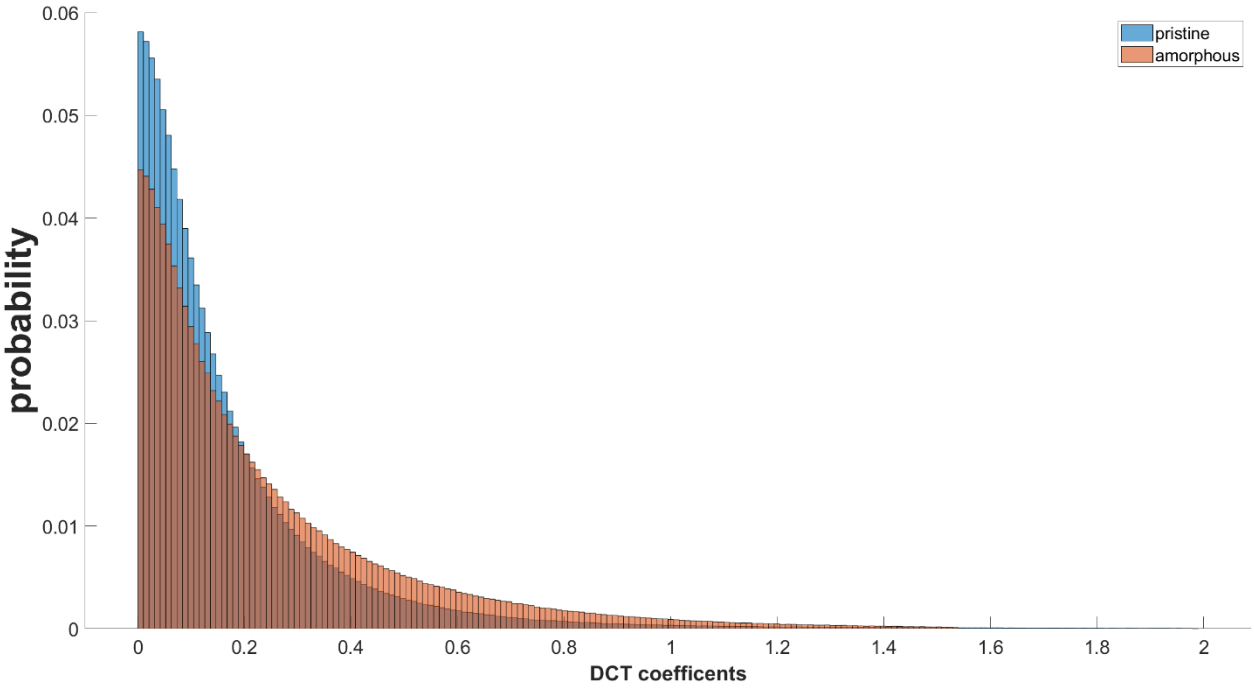


Figure 6.11: Histogram plot showing 150X150 low frequency DCT coefficients extracted from 44 pristine (blue bars) and amorphous (red bars) images. Both histograms are normalised and plotted with equal bin width.

To link the statistical distributions in Figure 6.11 to how these coefficients are spread in the DCT domain, a visual example of pristine and amorphous high-weighted coefficients is shown in Figure 6.12. DCT was taken from 2048 by 2048 pixels of (a) pristine and (c) amorphous HRTEM images using the same 0.65 threshold as before to filter out the low-weighted DCT coefficients. In order to visualise the nature of the difference between the two samples, the contour plots of pristine (Figure 6.12b) and amorphous (Figure 6.12d) material show only the

250X250 low-frequency components. It can be seen that the pristine image shows clusters of high-value coefficients in specific directions (relative to DC, (0,0), point on the upper left) and frequencies, which is expected as the DCT represents a periodic structure. On the other hand, the amorphous high-value coefficients display a random distribution, with an increased concentration in a ring between about 2.5 to 4.0 [1/nm], which is almost equivalent to the mid-frequency band in the FFT domain.

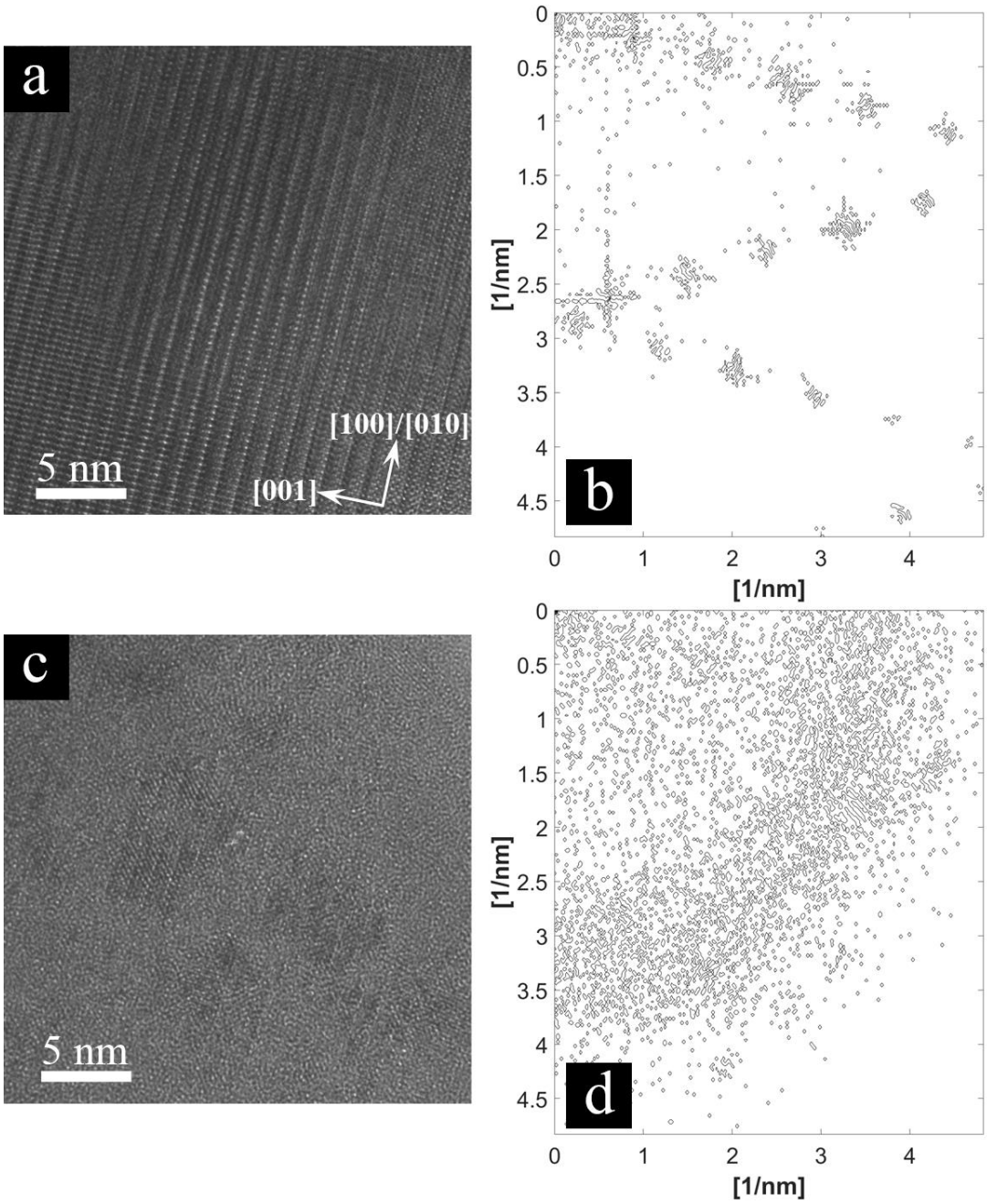


Figure 6.12: Raw HRTEM images from (a) pristine and (c) amorphous materials taken along [100]/[010] ZA and the corresponding representation of the DCT domain, (b) and (d), respectively. DCT contour plots were extracted using a threshold value of 0.65 for high-weighted DCT coefficients and present the 250X250 pixels low-frequency coefficients.

A better way to visualise the nature of the DCT coefficient distribution is looking at two images before and after irradiation taken from exactly the same region. 350 keV Kr-ion irradiation to a fluence of 10^{13} cm^{-2} created patches of amorphous/highly distorted regions but also retained

some of the original structure where ions did not create cascade damage. Figure 6.13 shows HRTEM images of a sample pre- and post-irradiation, as well as their associated DCT contour plots showing the coefficients above 0.65 threshold at the range of 250X250 pixels. The pre-irradiation DCT contour plot (Figure 6.13b) shows an ordered pattern of high coefficients that represent the long range order in the REBCO lattice (Figure 6.13a), whereas the post-irradiation DCT contour is a mix of some of the pre-irradiation ordered pattern as well as disordered pattern similar to that observed for the amorphous sample (Figure 6.12d). This result is expected due to presence of amorphous regions in a crystalline matrix. Red arrows in (b,d) point to a specific plane that changed location in the contour plot following irradiation, i.e. the shift of the high-value coefficients closer to DC (upper left), which is the manifestation of a larger plane spacing in real space. Enlargement of lattice parameters as a consequence of irradiation were also observed in the previous section (5).

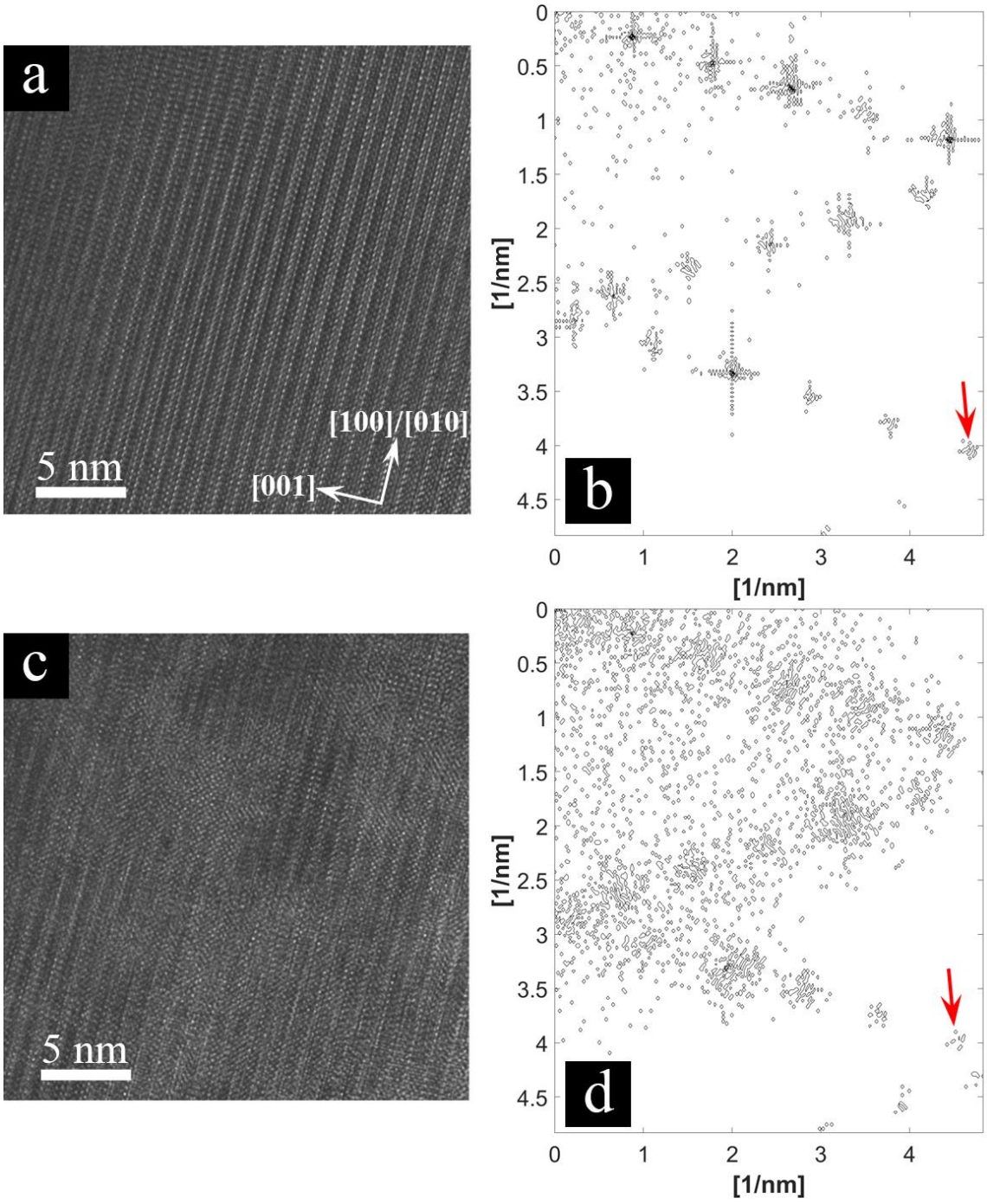


Figure 6.13: Comparison of DCT coefficients from HRTEM images taken along [100]/[010] ZA pre- (a) and post- (c) Kr-ion irradiation. The corresponding DCT coefficients are presented using 250X250 pixel contour plots from high-weighted DCT coefficients defined as above a threshold value of 0.65 for pre-irradiation (b) and post-irradiation (d) conditions.

It is worth mentioning that the zig-zag-like / cosine-like pattern of the high coefficient clusters (see Figure 6.13b) are different from the ordered array of spots shown in FFT patterns. In an FFT, the DC point (zero frequency) is invariably situated in the centre, whereas in DCT the DC point is, by definition, situated at (1,1) at the upper left corner. This difference also makes the pixel size from DCT half the size of the equivalent FFT pattern. Figure 6.14 illustrates why DCT and FFT patterns look different. Figure 6.14b represents the FFT pattern of pristine REBCO in Figure 6.14a that was extracted from the pre-irradiated sample in Figure 6.13a. To 'create' a DCT pattern from the FFT, one needs first to rotate the FFT along the vertical direction (Figure 6.14b) and then along the horizontal direction (Figure 6.14c). Figure 6.14d then shows the zig-zag pattern in the resulting DCT image, with DC situated at the upper left.

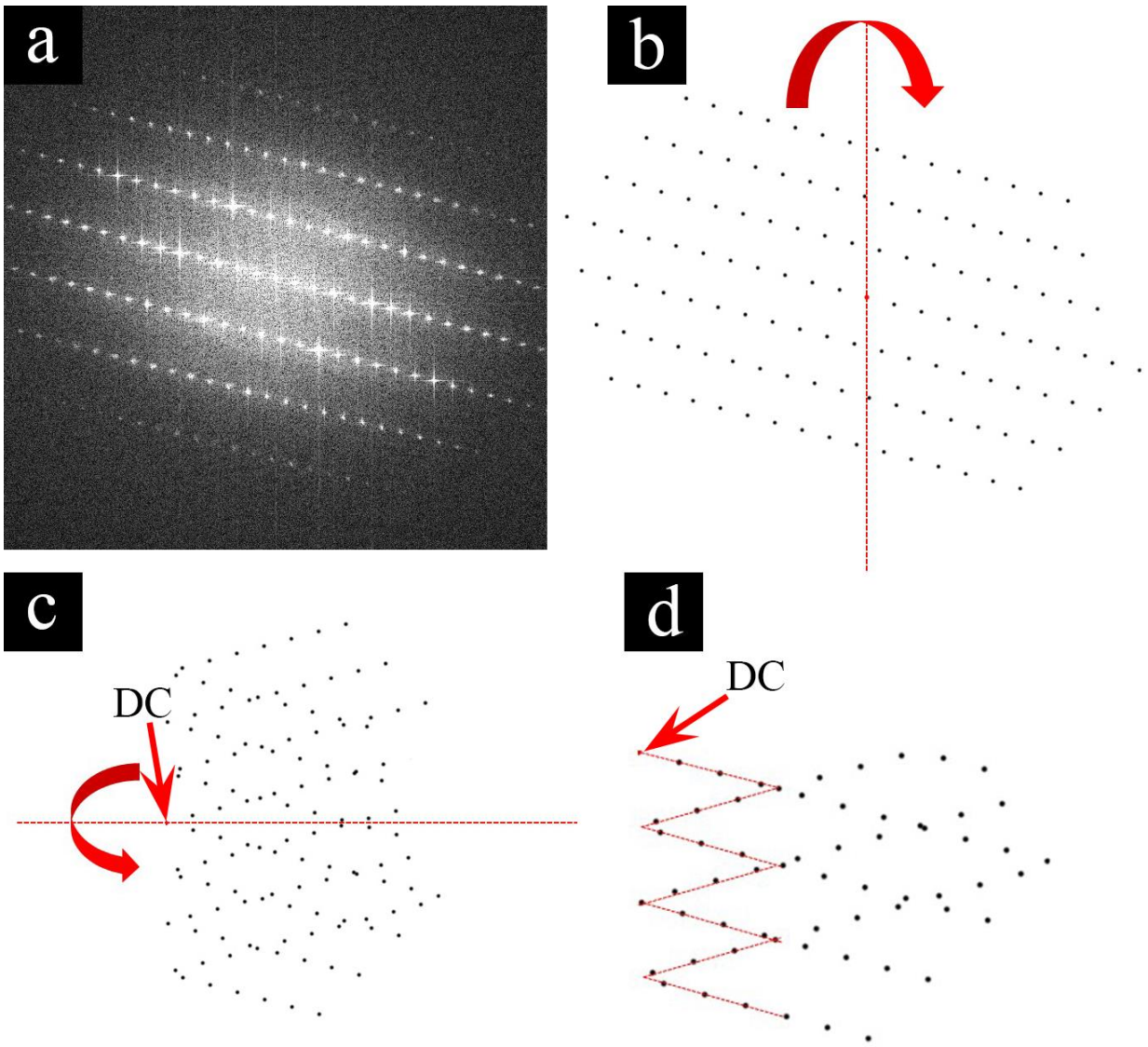


Figure 6.14: An illustration of DCT pattern creation from an FFT using an image of a pristine REBCO sample. (a) FFT pattern with the zero frequency point (DC) situated in the centre and a model of the pattern in (b). The FFT pattern is rotated along the vertical direction (b) and along the horizontal direction (c) to get an example of a DCT pattern with the DC point situated at the upper left corner of the image. The dotted red lines in (d) show the observed zig-zag pattern of the DCT image.

The DCT pattern from a pristine REBCO sample can also be assigned to the lattice planes as usually done for the spots in FFT patterns. Figure 6.15a assigns the main clusters of points in the high DCT coefficients (lower threshold of 0.65) to specific planes. The three red circles stand for regions from which IDCT were taken, and then shown in Figure 6.15b-d. In Figure 6.15e-g IFFT

were taken after applying a mask around a pair of spots, one shown with a red arrow in the inset, and the second is the equivalent point with respect to the symmetry around the centre, e.g. $(\bar{1}0\bar{2})$ and (102). It can be seen that the IDCT and IFFT images display exactly the same pattern both in direction and frequency.

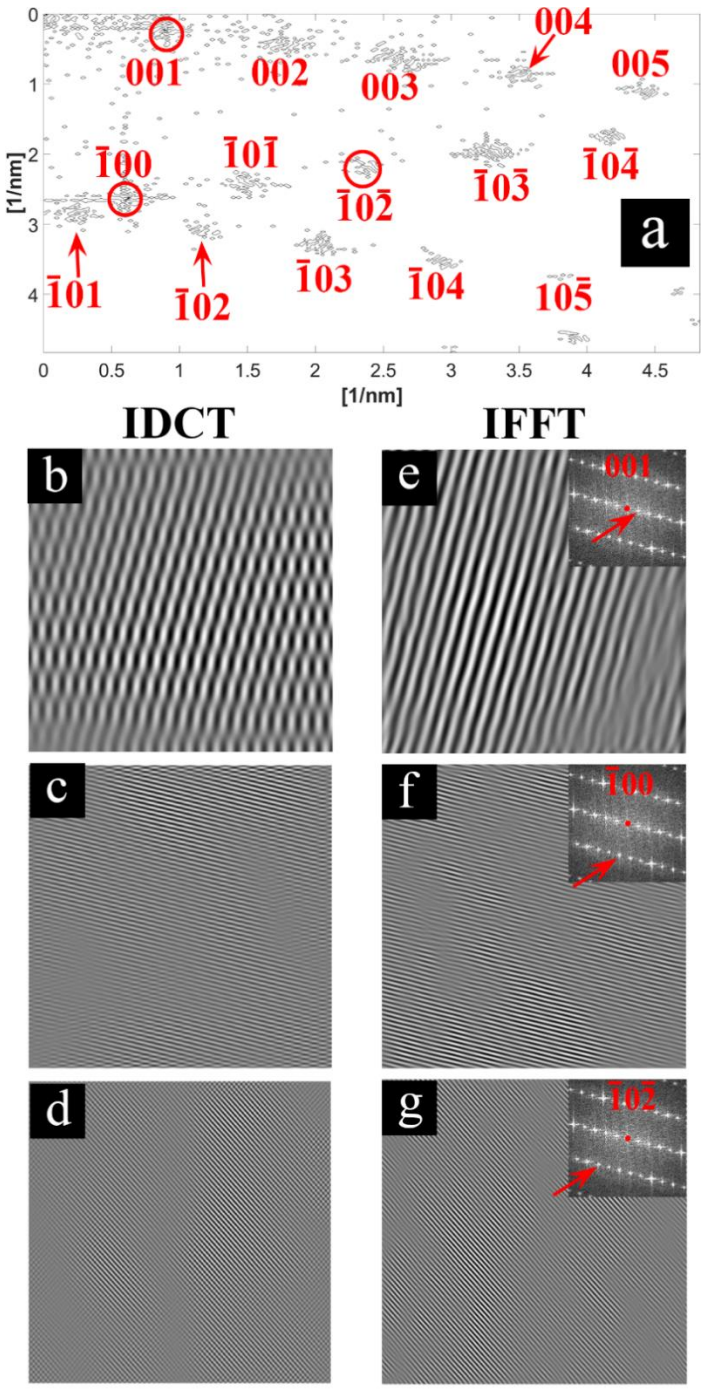


Figure 6.15: DCT patterns from a pristine REBCO sample, and IDCT & IFFT images taken after applying a mask around specific planes. (a) 250X250 low frequency pixels taken from a 2048X2048 pixel DCT image presenting the high coefficients with a lower threshold of 0.65. The 3 digits numbers are Miller indices in the original image (Figure 6.13a). (b-d) IDCT images taken from the clusters of high coefficients marked by red circles in (a). (e-g) the equivalent IFFT images taken after applying a mask on the FFT pattern shown in the inset. The FFT inset also specifies the centre in the red circle, plane indices in red, and the red arrow points to the equivalent spot in the DCT pattern in (a).

To conclude this section, when the extent of lattice damage increases, the distribution of the DCT coefficients gets flatter as more highly-weighted coefficients are introduced at the expense of low-weighted ones, and this phenomenon causes the calculated DCT spectral entropy to increase.

6.3.4. Summary

In this section I have presented the concept of entropy in the FFT and DCT domains and the reasons why lattice damage results in an increase in entropy values. Although similar to each other, they yield different entropy results that are also different in their relative contribution, as presented in Appendix C (ii). The next section presents the results extracted by this methodology from more than a thousand HRTEM images of materials damaged in different ways.

6.4. Quantitative analysis of entropy changes in HRTEM images

6.4.1. Neutron-irradiation damage

According to the findings presented in section 4.1 it is obvious that fast neutron-irradiation (see spectrum in Figure 2.22) creates amorphous cascades with a diameter of about 10 nm. These isolated cascades (Figure 4.1) cannot explain the degradation in the superconducting transition temperature (Figure 2.44a), and some more subtle lattice damage in between these sparse cascades is expected. STEM data analysis (section 5.2.1) also points in this direction by revealing changes in lattice parameters, and individual plane spacings, when compared to a pristine sample. This section shows how the entropy analysis, taken from the matrix and not the damage cascades, can be used to analyse differences in the apparently perfect lattices in pristine and between the cascades in neutron-irradiated samples.

Figure 6.16 shows a scatter plot of the entropy values calculated from 1024X1024 pixel HRTEM images (see Equation 3.3) taken along the [100]/[010] direction for pristine, neutron-irradiated (using only the matrix between the cascades) and amorphous samples, shown by the blue hexagrams, red diamonds and green squares, respectively. The graph shows statistical differences between the three samples in both the FFT and the DCT domains.

If one assumes that the entropy values for the pristine and the amorphous samples represent those characteristic of 'perfect' and fully, 100% damaged respectively, then rescaling the axes from 0 to 1 allows me to estimate the damage in samples with any intermediate entropy values. Based on this linear interpolation (which is a valid assumption judging by the linear-like entropy scatter in Figure 6.22), the average percentage damage values of the matrix of the neutron-irradiated sample calculated from the DCT and FFT (medium-frequency) domains are about 14% and 34%, respectively.

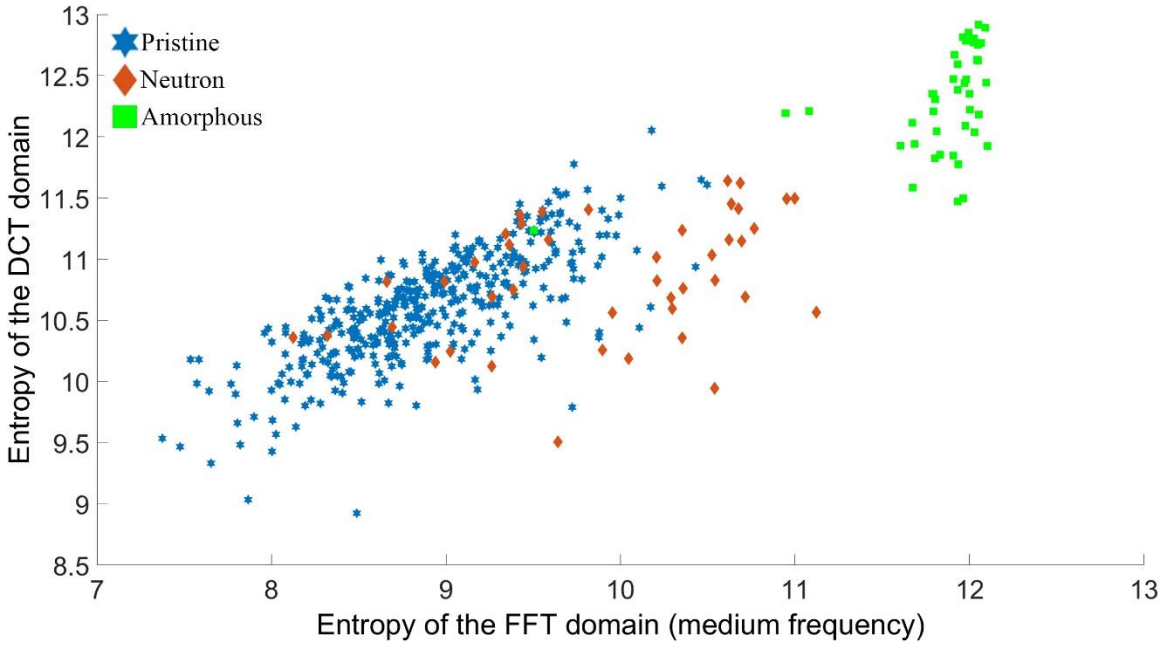


Figure 6.16: A scatter plot showing entropy values calculated from 1024X1024 pixel blocks in HRTEM images both in the mid-frequency band FFT, and DCT domains for pristine (blue hexagrams), neutron-irradiated (red diamonds) and amorphous (green squares).

6.4.2. Ion irradiation

The same methodology is used to compare the entropy values measured in samples damaged in-situ in the MIAMI2 microscope by 4 different ions with increasing mass to those from pristine samples. For all these samples, except that damaged by He-ions with a fluence of 10^{16} cm^{-2}, the irradiation conditions were identical, namely a fluence of 10^{13} cm^{-2}, accelerating voltage of 350 kV and irradiation temperature of 298 K. This allows a direct comparison of the effect of ion mass on the damage process. Figure 6.17 shows the entropy values of samples damaged by all 4 ions on a scatter plot, compared to the pristine sample. This data is taken from the analysis of 750 images taken from about 15 TEM lamellae. Because Ne is a rather a light ion, it is not surprising that this low fluence value was not sufficient to generate significant lattice damage, and thus the values are clustered around the same values as from the pristine material. He-ion

irradiation to a high fluence did seem to create significant lattice damage, as shown by the increased entropy values. The results from the heavier Ar and Kr ion damage clustered further away from the pristine values, and the Kr points are found at the highest DCT and FFT entropy values.

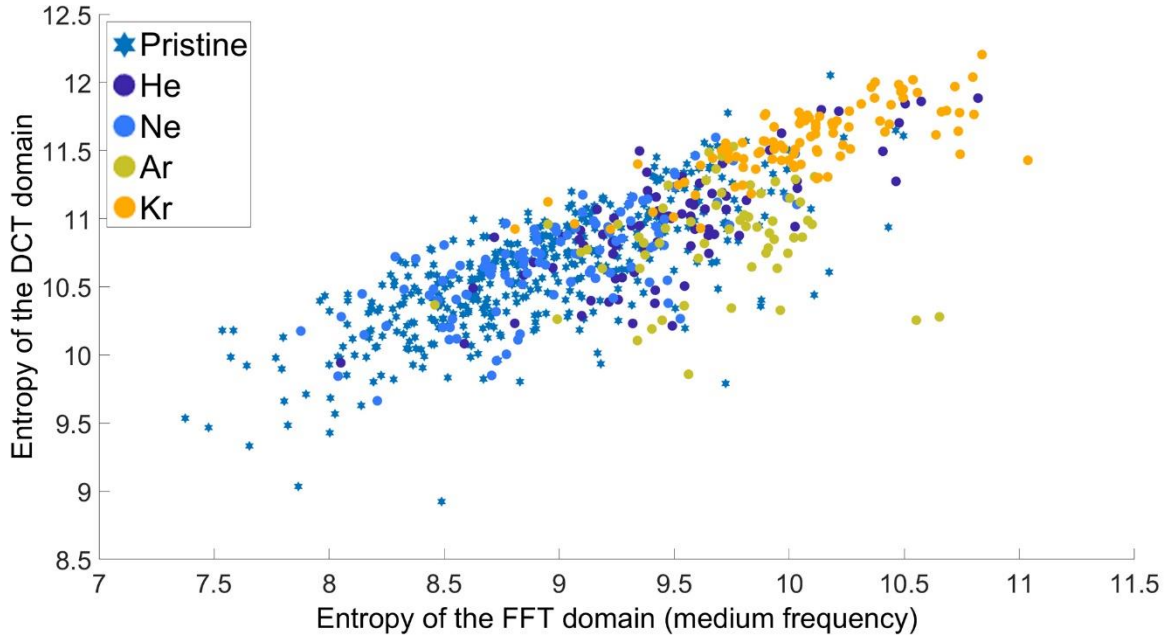


Figure 6.17: Entropy values in the FFT (mid-frequency, x-axis) and DCT (y-axis) domains for pristine and for samples irradiated with He, Ne, Ar and Kr ions shown as a scatter plot. Pristine samples are marked with blue hexagrams, and data for the four different ions marked with circles with different colours as shown in the legend.

To make it easier to see the systematic variations, the average entropy values in both domains are shown in Figure 6.18. The standard deviation is presented using error bars. Generally, the entropy values increase as the ion mass increases, and can be interpreted as demonstrating the production of more severe lattice damage. He-ion irradiation shows larger entropy values in both domains compared to the Ne-ion irradiated samples because the irradiation fluence was three orders of magnitude higher (Table 3.2). This increase of fluence was sufficient to generate enough damage accumulation to be directly visible in the HRTEM images presented in section 4.2.1.1. Similar observation of HRTEM images from the Ne-ion irradiated samples did not show

any visual signs of lattice degradation due to the low fluence (section 4.2.1.2). Therefore, the entropy values shown in Figure 6.18 are consistent with the visual observations in section 4.2.1.

According to the average values in Figure 6.18, the He- and Ar-irradiated samples do not show the same trend of entropy change in the in the DCT and FFT domains. The Ar-irradiated samples display higher entropy in the FFT domain but lower values in the DCT domain compared to the He-ion samples. The entropy value in the FFT domain quantifies only the degree of the medium-range order, while the DCT entropy analysis captures all frequencies and thus takes into account local changes in lattice parameter distributions, loss of high frequency components and random variations at low frequencies, as discussed in section 6.3.3. In addition, the amorphisation process of samples exposed to light ions such as He and heavier ions like Ar is expected to be different (section 2.2.1.1.5), and thus may change the DCT and FFT entropy values in a different fashion.

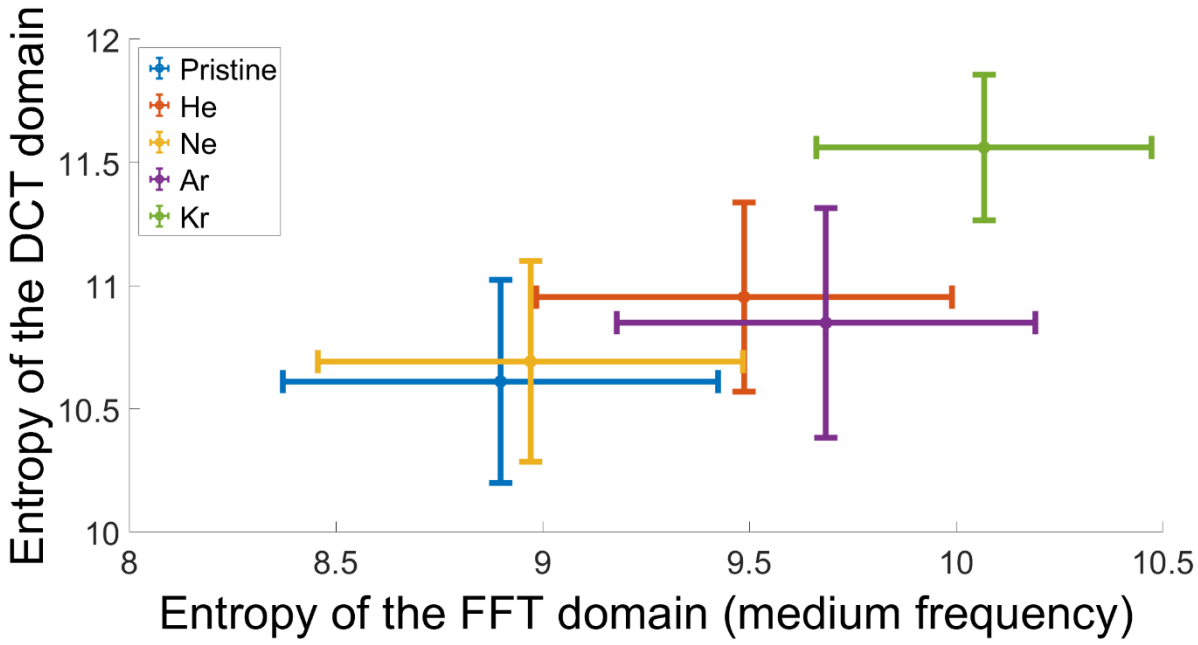


Figure 6.18: A 2D chart presenting the entropy values in the FFT and DCT domains in pristine, He-irradiated, Ne-irradiated, Ar-irradiated, and Kr-irradiated samples. Standard deviations for each domain, FFT on x-axis and DCT on y-axis, are presented by error bars.

Figure 6.19 shows the damage percentages of the four ion-irradiated samples, He, Ne, Ar and Kr. As before, the damage percentage was calculated using linear interpolation, assuming 0% damage in the pristine samples and 100% damage in the amorphous samples. As expected from the entropy values in Figure 6.18, the damage percentage increases from Ne to Kr, and the high fluence He and Ar ions lie in between. Ne-irradiated samples show a slight increase in both entropy values, but more so in the DCT domain. He-irradiated samples display similar increases in both the FFT and DCT domains. The Ar- and Kr-irradiated samples show different behaviour; the Ar samples show more increase in the FFT domain whereas for Kr the entropy increases more in the DCT domain. As explained before, these differences may arise due to the different mathematical representation of the FFT and DCT calculations as well as different amorphisation processes (as presented in section 2.2.1.1.5) in light versus heavy ions that may affect the way the entropy changes as the damage is accumulated. A model that describes the entropy increase as a function of damage accumulation can be seen in Appendix C (iii).

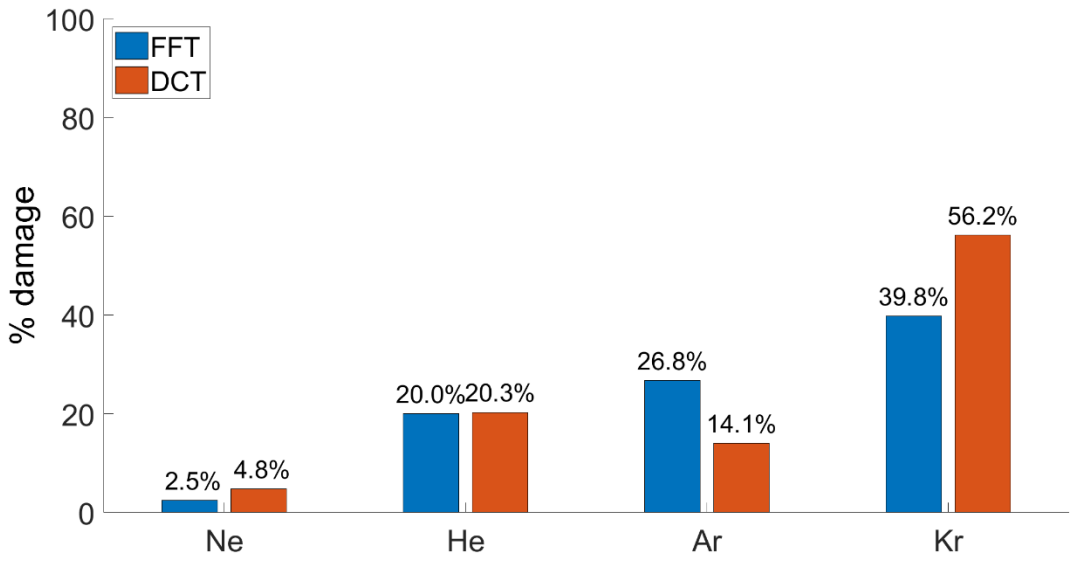


Figure 6.19: Damage percentages calculated from different irradiated samples in the DCT and FFT domains. The percentages were calculated relative to average entropy values in the un-irradiated sample (0% damage) and amorphous samples (100% damage).

6.4.3. Effect of irradiation temperature

Figure 6.20 shows a scatter plot of the entropy values in the DCT and FFT domains for samples Xe-ion irradiated at 298 K (orange triangles) and at 100 K (black triangles) compared to amorphous samples shown as green squares. It can be seen that separate clusters of points have formed for the three types of samples, with data for irradiation with Xe-ions at room temperature clustered at lower entropy values, whereas irradiation at 100 K caused the entropy to shift to higher values, but still nowhere near the data points from the amorphous samples with the highest entropy values at the far right. The statistical analysis clearly shows more severe damage from irradiation at 100 K, with damage percentages of 59.7% and 67.3% compared to 27.9% and 37.7% for irradiation at 298 K for the FFT (mid-frequency) and DCT domains, respectively.

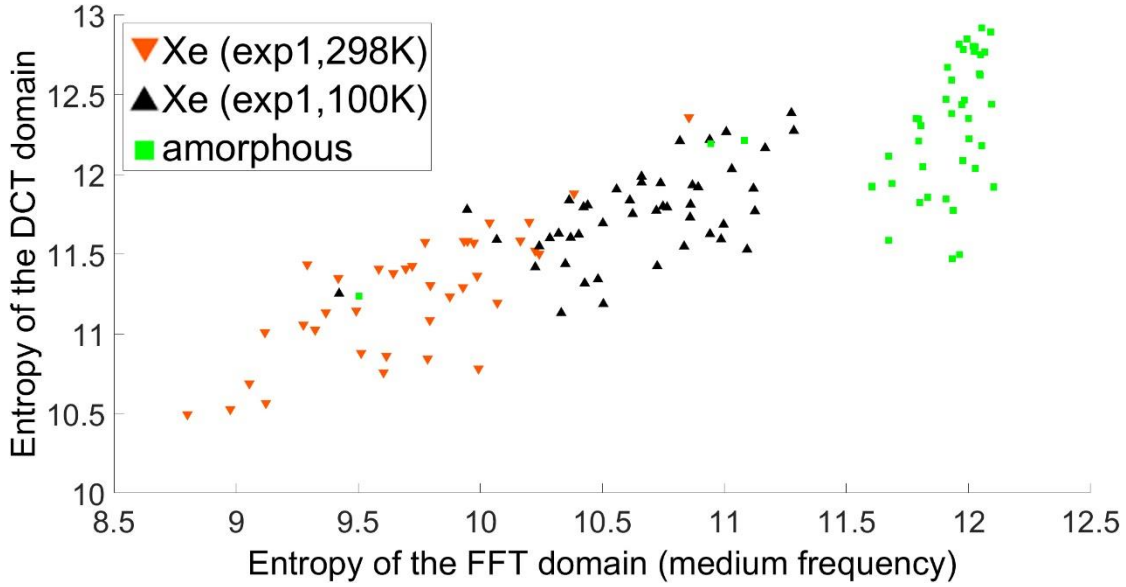


Figure 6.20: Scatter plot of the entropy in the DCT and FFT domains for samples irradiated with Xe ions at 298 K (orange triangles) and 100 K (black triangles), and amorphous samples (green squares).

To support the visual observation of the three clusters of points when comparing the 3 datasets, unsupervised k-mean clustering was undertaken in MATLAB using the squared Euclidean

distance metric [444]. Figure 6.21 shows the allocation of the data to three clusters, as well as the well separated centroids of each cluster. The data points that were designated in this analysis as *misclassified* are shown as green, and there are only 13 of them out of the 127 data points. The detection by this analysis of three distinct clusters means that one can be confident the irradiation temperature plays an important role on the accumulation of lattice damage from heavy ion irradiation. The reader is referred to the supervised k-nearest neighbor confusion matrix in Appendix C: Figure S- 16.

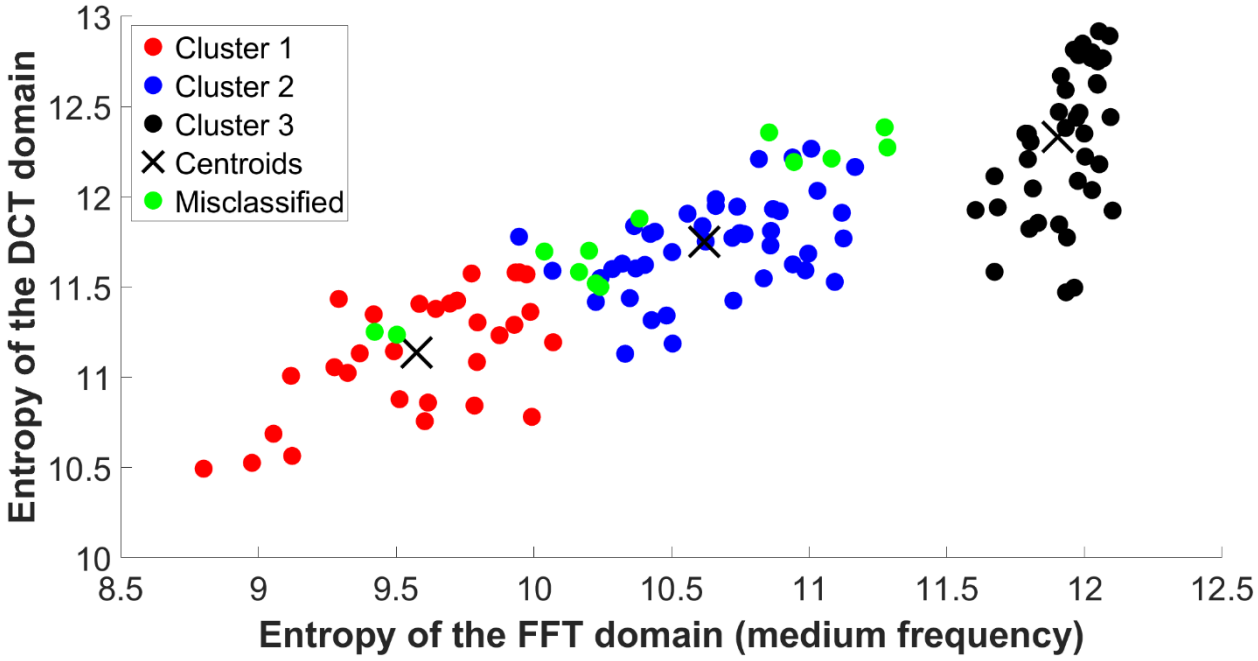


Figure 6.21: Scatter plot of k-mean clustering of Xe-irradiated samples irradiated at 100 K and 298 K, and amorphous samples. The green circles show the misclassified data points.

6.4.4. Comparison of all samples

Up to this point, I have compared groups of samples separately. This section brings together the results on all the samples used for the entropy analysis. Figure 6.22 shows a scatter plot of the entropy values in the FFT (mid-frequency) and DCT domains. It can be seen that the spread of the data can be described as a linear upward trend as the damage increases. The amorphous

samples (green squares) create a distinct group separated from the other samples, showing that a degree of periodicity is retained in all the other samples. However, the number of samples and the large amount of data extracted from the images makes the separation of the other groups rather difficult since many data points are overlapping.

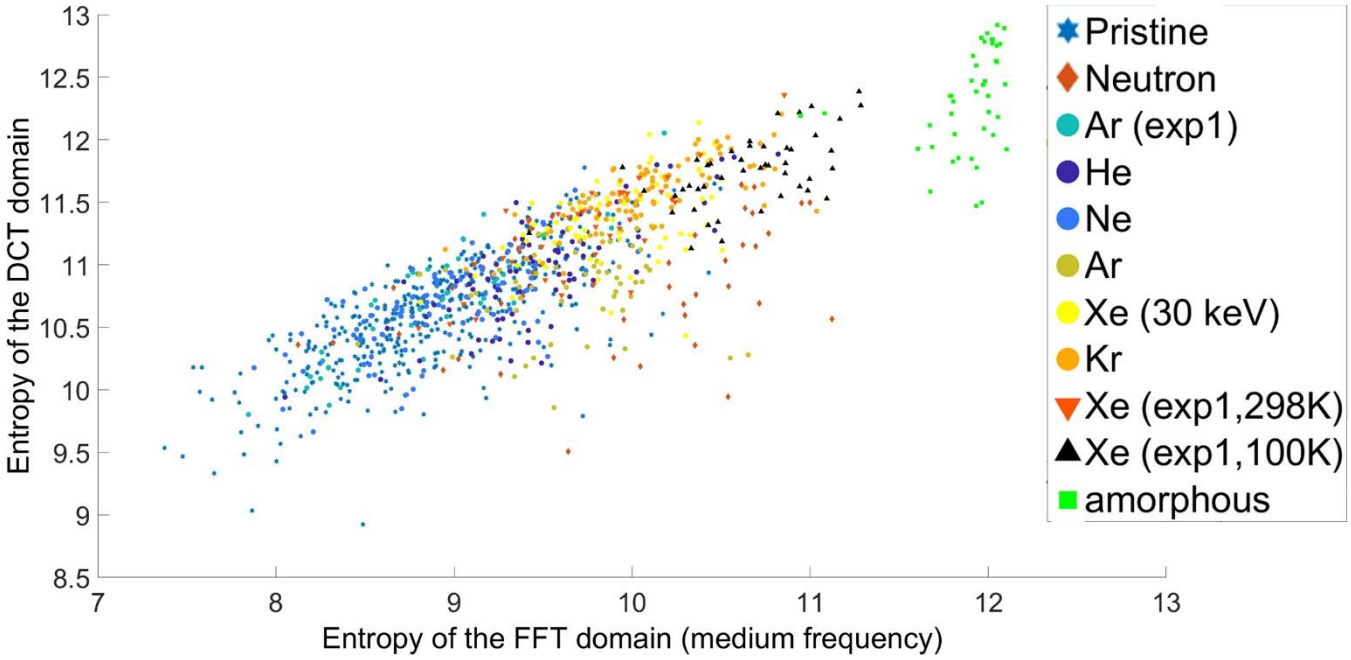


Figure 6.22: scatter plot of the entropy calculated from the DCT and FFT (mid-frequency) domains for all the samples in the dataset.

To make the visualisation easier, Figure 6.23 shows for each sample only the average entropy in both domains as one point on the graph. To illustrate the spread of the data for every group of samples, an ellipse is shown around the average entropy points where the size is determined by two radii with the size of half standard deviation (chosen for easy visualisation) of the FFT and DCT domains along the x-axis and y-axis, respectively. Both the Ar-ion and the neutron-irradiated samples show an increase in entropy values in the FFT domain but a relatively constant DCT entropy. Pristine (blue hexagrams), Ar-irradiated from experiment number one (the low fluence as described in section 3.4.4) and Ne-irradiated samples form a cluster with

similar average entropies and standard deviations because not much lattice damage has been created in these samples.

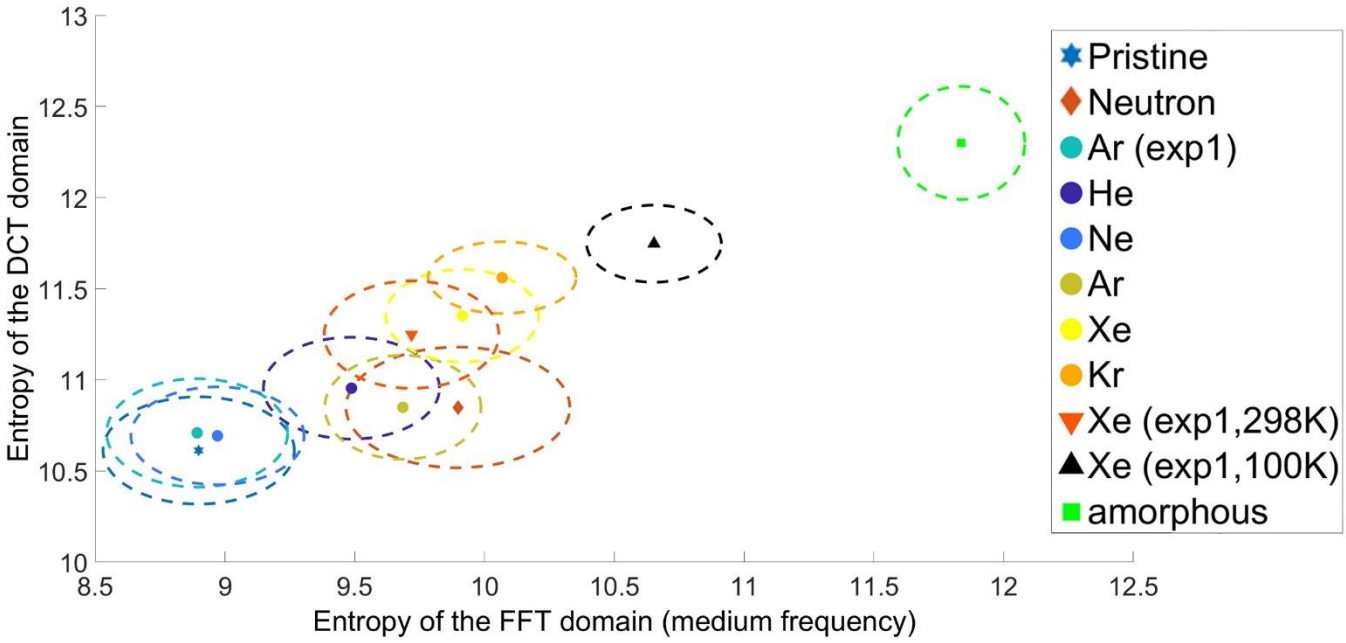


Figure 6.23: A pseudo-scatter plot with the average entropy in the FFT and DCT domains represented by one symbol. The ellipse size is determined by two radii, the half standard deviation of the FFT domain as a radius along the x-axis and the half standard deviation in the DCT domain along the y-axis.

From this data, one can see that the total entropy, i.e. the summation from both FFT and DCT domains, of the amorphous samples increases by about 24% compared to the pristine samples, while the partially-damaged samples are situated in between these two extremes. Figure 6.24 shows the percentage of damage calculated for the different samples assuming an entropy increase from 0% damage in the pristine samples up to 100% damage for the amorphous samples, and Table 6.3 summarises the irradiation conditions for all samples and their entropy values in both domains.

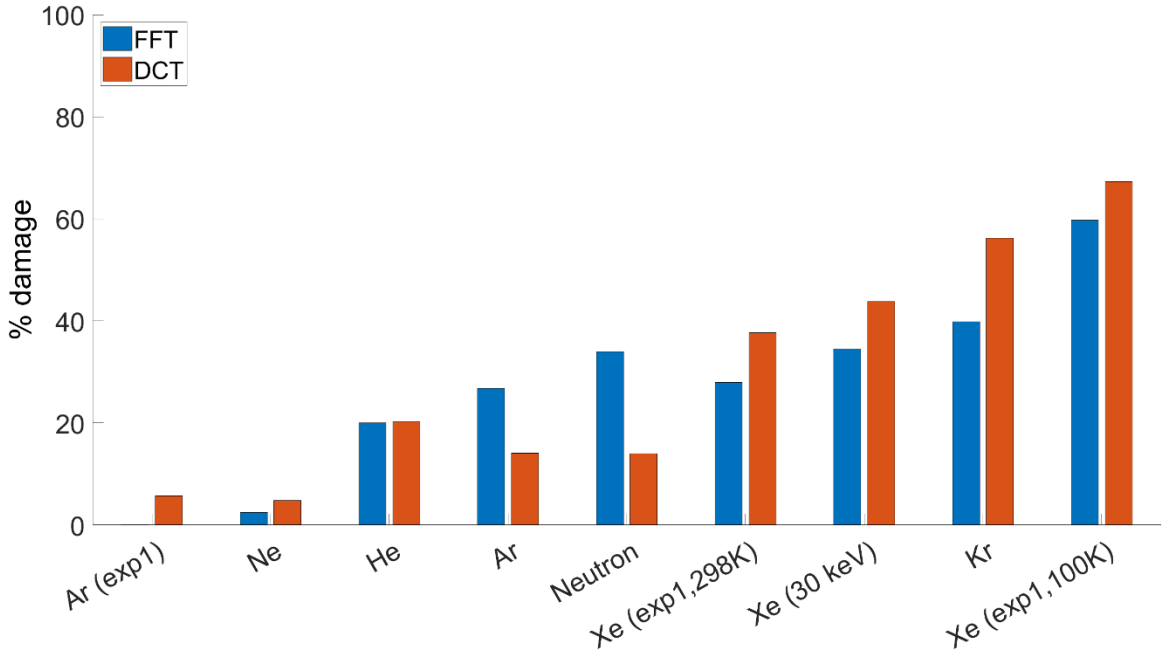


Figure 6.24: Bar chart of the percentage damage in the DCT and FFT domains for all the samples studied here. The calculation is based on the assumption that the entropy increasing linearly from the un-damaged pristine samples with a value of 0% up to the amorphous state with an entropy of 100%.

Table 6.3: Percentage of damage for the samples presented in this study derived from the assumption of 0% damage for pristine samples and 100% for amorphous samples.

	Ar-ions	**Ne-ions**	**He-ions**	**Ar-ions**	**Neutron-irradiated**	**Xe-ions**	**Xe-ions**	**Kr-ions**	**Xe-ions**
Fleunce [cm^{-2}]	7×10^{12}	1×10^{13}	1×10^{16}	1×10^{13}	3.3×10^{18}	1×10^{13}	1×10^{13}	1×10^{13}	1×10^{13}
Irradiation temperature [K]	298	298	298	298	~330	298	298	298	100
Energy [keV]	350	350	350	350	----	350	30	350	350
% damage [FFT domain]	-0.2	2.5	20.2	26.8	34.0	27.9	34.6	39.8	59.7
% damage [DCT domain]	5.8	4.8	20.3	14.1	14.0	37.7	43.8	56.2	67.3

6.5. DCT and FFT comparison

In previous sections, I have presented the idea of measuring the entropy values in the DCT domain as well as the mid-frequency band of the FFT domain. I showed that although these two

methods are mathematically similar, they yield different results and thus offer two approaches to separate samples with different degrees of damage. This short section compares the statistical distributions of the DCT and FFT entropies.

First, the question now arises of whether the spectral entropy concept is reliable enough to use as a quantitative tool for HRTEM image quality assessment of irradiation-induced lattice damage. To address this question, the distribution of the entropy values extracted from the amorphous edges (512X512 pixels) is shown in Figure 6.25 for both (a) FFT and (b) DCT plotted over the range between 7 to 13, which are approximately the lowest and highest entropy values measured from a single image. The 348 images were taken from 12 samples to try to rigorously assess the sensitivity of the extracted entropy values with changing image quality and sample conditions. The amorphous edge around the edge of each TEM lamella is the largest and closest dataset I have to 'fully amorphous material' and in principle should give the same entropy value. This figure shows that the FFT entropy has a narrow distribution with the coefficient of variation ($CV=\sigma/\mu$) equal to 0.0067 whereas the DCT shows a value of 0.0192, approximately 3 times larger. From this analysis, one can assume that entropy change in the FFT domain might be a better proxy for irradiation damage quantification. Speculation as to the origin of the broader distribution in the DCT domain is given in Appendix C (v).

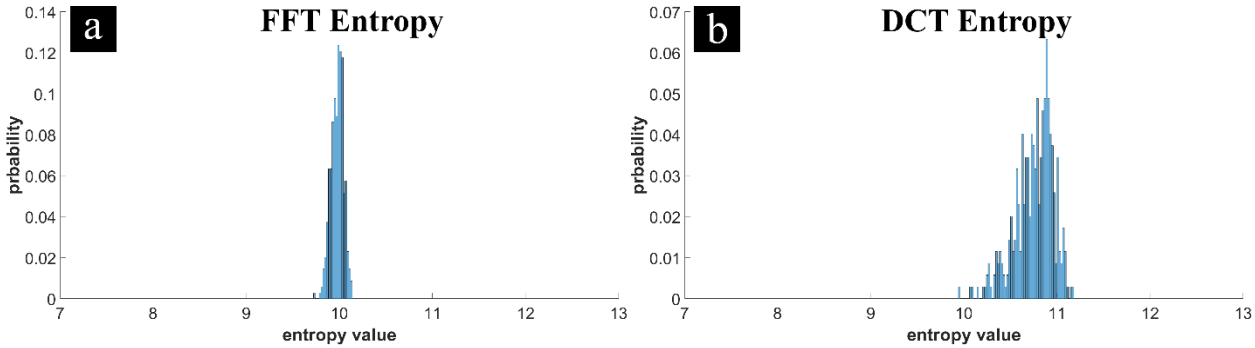


Figure 6.25: Histograms showing the spectral entropy value distribution of 348 HRTEM images (each 512X512 pixels) of the amorphous edge of TEM samples in the mid-frequency FFT (a) and DCT (b) domains.

7. Conclusions and Future Work

7.1. Conclusions

Superconducting wires/tapes are a key component for the magnets in future fusion reactors, and REBCO tapes manufactured by SuperPower Inc were the central focus of this thesis. This work presented a comprehensive electron microscopy investigation of the lattice damage caused by neutron and ion irradiation, with the aim of shedding light on how one can characterise the unique microstructural evolution generated by the different incident particles.

The analytical study taken place in this thesis is based on to two different methodologies applied to different kinds of atomic-resolution electron microscopy images. The first based the principle that STEM/HAADF images are a good proxy of the lattice atomic locations and allowed me the extract the structural parameters and evaluate the damage characteristics from their statistical properties. The second is based on images processing techniques in the frequency domain of HRTEM images that can assess the relative degree of lattice damage based on unirradiated and fully amorphous benchmarks. These methods combined together allow an end-to-end image analysis of irradiated materials from minute local changes in individual STEM/HAADF image

that requires careful interpretation to fast evaluation of relative lattice damage in a large batch of HRTEM images that does not require such intricate interpretation.

Based on my experimental observations, the following conclusions can be drawn:

- Neutron-irradiation induced damage in the form of large, ~10 nm amorphous damage cascades was directly observed using HRTEM. However, these widely separated cascades cannot explain the reduction in T_c as it is known that such a decrease can only occur when the whole superconducting path through the matrix has been damaged. Although amorphous cascades formation was expected from the literature it is the first time direct observation using HRTEM is reported.
- HRTEM direct observations show that the degree of damage increases dramatically when taken at cryogenic temperatures. Some similarities between Xe-ions taken at 100 and 298 K, imply that the damage mechanisms are similar and the main differentiation factor is the rate of dynamic defect recovery during irradiation.
- In Chapter 5, a careful analysis of the structural parameters extracted from STEM/HAADF images has shown several interesting observations:
    - Xe-ion irradiation undertaken at 100 and 298 K causes the Ba_1-Ba_2 inter-cell fractions to increase by a factor 6 times larger than after He, Ne, Ar and neutron-irradiation. Comparing these results to two DFT studies of the formation of individual Cu/O vacancies/interstitial defects, it was concluded that Xe-ions generate damage in the matrix that consists primarily of vacancy/interstitial clusters rather than isolated point defects.
    - He-irradiated samples showed an average increase in a/b-axis lattice parameter in every image when compared to images taken from pristine samples. This unequivocally states

that He-irradiated causes expansion not only along the c-axis but also along the other two axes. Although the c-axis expansion is consistent with the literature (e.g. [419]), the a/b-axis is hardly studied in the literature. It is possible that the He-irradiation characteristics are associated with Frenkel pairs (O(2) vacancies and interstitials at (0,0,0.5)).

- The neutron-irradiated sample showed two distinctive features when compared to the other samples, firstly an average decrease in c-axis lattice parameter, and secondly a wide distribution of a/b-axis lattice parameters, which stems from anisotropic microstrain along these axes. It was concluded that the neutron-irradiation sample is likely to present an intermediate degree of damage between pristine and He-irradiated materials, and that a higher fluence might cause an expansion along c-axis and stress relaxation along the other two axes.
- Overall, it was shown that the c-axis lattice parameters changed following irradiation by all the species studied, whereas along the a/b-axis this does not always happen, for instance in the case of Ne-, Ar-, and Xe (T=298 K)- irradiation. This implies that structural parameter changes do not occur in the same way under all incident projectiles, but rather react to the formation of different types or concentrations of defects in a given material volume.

- From chapter 6, the following conclusions are drawn:
  - I have shown that quantitative analysis in the frequency domain can reveal that the neutron-irradiated matrix (i.e. between the damage cascades) is indeed degraded to a value of about 20% assuming 0% and 100% damage for pristine, and amorphous samples, respectively.

- A comprehensive analysis on more than 1000 HRTEM images showed that spectral entropy values measured in the mid-frequency FFT and DCT domains increases when lattice damage becomes more severe. The mathematical explanation for this relies on the relative strengthening of frequencies that are not associated with REBCO d_{hkl} (i.e. the distances between lattice planes) but rather are a consequence of irradiation damage (e.g. the presence of the amorphous halo in FFTs).

7.2. Suggestions for Future Work

For a more complete understanding of the effects of neutron and ion irradiation on the microstructure of REBCO tapes, I suggest the following:

- Utilising other characterisation techniques such as Ptychography in order to understand the specific point defects associated with the observed structural parameter changes, as was discussed in chapter 5.
- Developing deep learning neural networks dedicated for the purpose of quantifying irradiation damage in HRTEM images. Such a development will be a powerful way to extract quantitative data from images, and have a much more general importance for the field of electron microscopy.
- Continue the development of targeted image feature extraction (such as was presented in chapter 6) in order to improve the quantitative assessment of the quality of HRTEM images.
- Investigate the 'anomalies' of the structural parameters extracted from the neutron-irradiated sample, in particular, the shrinkage of c-axis lattice parameter and the anisotropic lattice stains along a/b directions. One of the techniques to analyse lattice

strain is Williamson–Hall (or other similar models) that can be deduced from XRD of a bulk sample [445]. The shrinkage of lattice parameter can be analysed by plotting the c-axis lattice parameter as a function of fluence to verify whether the hypothesis in this thesis of initial decrease and then expansion holds true.

References

[1] J. Amouroux *et al.*, “Carbon dioxide: A new material for energy storage,” *Prog. Nat. Sci. Mater. Int.*, vol. 24, no. 4, pp. 295–304, 2014.

[2] G. A. Jones and K. J. Warner, “The 21st century population-energy-climate nexus,” *Energy Policy*, vol. 93, pp. 206–212, 2016.

[3] S. Shafiee and E. Topal, “When will fossil fuel reserves be diminished?,” *Energy Policy*, vol. 37, no. 1, pp. 181–189, 2009.

[4] G. Maggio and G. Cacciola, “When will oil, natural gas, and coal peak?,” *Fuel*, vol. 98, no. 2012, pp. 111–123, 2012.

[5] M. Li and Q. Wang, “Will technology advances alleviate climate change? Dual effects of technology change on aggregate carbon dioxide emissions,” *Energy Sustain. Dev.*, vol. 41, pp. 61–68, 2017.

[6] G. Lefebvre, E. Jiménez, and B. Cabañas, *Environment, energy and climate change II: Energies from new resources and the climate change*, vol. 34. Springer, 2015.

[7] R. B. Jackson *et al.*, “Warning signs for stabilizing global CO_2 emissions,” *Environ. Res. Lett.*, vol. 12, no. 11, p. 110202, 2017.

[8] E. Specht, T. Redemann, and N. Lorenz, “Simplified mathematical model for calculating global warming through anthropogenic CO_2,” *Int. J. Therm. Sci.*, vol. 102, pp. 1–8, 2016.

[9] M. T. H.-O. Pörtner, D.C. Roberts, E.S. Poloczanska, K. Mintenbeck and A. O. A. Alegría, M. Craig, S. Langsdorf, S. Löschke, V. Möller, “IPCC, 2022: Summary for Policymakers,” 2022.

[10] S. Ahmed, A. Mahmood, A. Hasan, G. A. S. Sidhu, and M. F. U. Butt, “A comparative review of China, India and Pakistan renewable energy sectors and sharing opportunities,” *Renew. Sustain. Energy Rev.*, vol. 57, pp. 216–225, 2016.

[11] G. McCracken and P. Stott, *Fusion - The Energy of the Universe*, 2nd ed. Academic Press, 2012.

[12] J. Knaster, A. Moeslang, and T. Muroga, “Materials research for fusion,” *Nat. Phys.*, vol. 12, no. 5, pp. 424–434, 2016.

[13] M. S. Yim and J. Li, “Examining relationship between nuclear proliferation and civilian nuclear power development,” *Prog. Nucl. Energy*, vol. 66, pp. 108–114, 2013.

[14] A. Cipollaro and G. Lomonaco, “Contributing to the nuclear 3S’s via a methodology aiming at enhancing the synergies between nuclear security and safety,” *Prog. Nucl. Energy*, vol. 86, pp. 31–39, 2016.

[15] J. P. Freidberg, *Plasma Physics and Fusion Energy*, 1st ed. Cambridge University Press, 2007.

[16] L. A. Artsimovich, "Tokamak devices," *Nucl. Fusion*, vol. 12, no. 2, pp. 215–252, 1972.

[17] P. H. Rebut, R. J. Bickerton, and B. E. Keen Jet, "Magnetic confinement 1. Tokamaks the joint european torus: Installation, first results and prospects," *Nucl. Fusion*, vol. 25, no. 9, p. 1011, 1985.

[18] E. Gibney, "Nuclear-fusion reactor smashes energy record," *Nature*, vol. 602, p. 371, 2022.

[19] D. G. Whyte, J. Minervini, B. LaBombard, E. Marmar, L. Bromberg, and M. Greenwald, "Smaller & Sooner: Exploiting High Magnetic Fields from New Superconductors for a More Attractive Fusion Energy Development Path," *J. Fusion Energy*, vol. 35, no. 1, pp. 41–53, 2016.

[20] B. N. Sorbom *et al.*, "ARC: A compact, high-field, fusion nuclear science facility and demonstration power plant with demountable magnets," *Fusion Eng. Des.*, vol. 100, pp. 378–405, 2015.

[21] A. E. Costley, J. Hugill, and P. F. Buxton, "On the power and size of tokamak fusion pilot plants and reactors," *Nucl. Fusion*, vol. 55, no. 3, 2015.

[22] Y. Zhai, P. Titus, C. Kessel, and L. El-Guebaly, "Conceptual magnet design study for fusion nuclear science facility," *Fusion Eng. Des.*, vol. 135, pp. 324–336, 2017.

[23] J. Zheng, Y. Song, X. Liu, K. Lu, and J. Qin, "Overview of the Design Status of the Superconducting Magnet System of the CFETR," *IEEE Trans. Appl. Supercond.*, vol. 28, no. 3, pp. 11–15, 2018.

[24] R. J. Hawryluk *et al.*, "Principal physics developments evaluated in the ITER design review," *Nucl. Fusion*, vol. 49, no. 6, 2009.

[25] D. Ciazynski, "Review of Nb_3Sn conductors for ITER," *Fusion Eng. Des.*, vol. 82, no. 5–14, pp. 488–497, 2007.

[26] G. Federici *et al.*, "Overview of EU DEMO design and R&D activities," *Fusion Eng. Des.*, vol. 89, no. 7–8, pp. 882–889, 2014.

[27] A. J. H. Donné, "The European roadmap towards fusion electricity," *Philos. Trans. R. Soc. A Math. Phys. Eng. Sci.*, vol. 377, no. 2141, 2019.

[28] W. H. Fietz, R. Heller, M. J. Wolf, and P. V. Gade, "High temperature superconductor cables for EU-DEMO TF-magnets," *Fusion Eng. Des.*, vol. 125, no. August, pp. 290–293, 2017.

[29] R. Heller, P. V. Gade, W. H. Fietz, T. Vogel, and K. P. Weiss, "Conceptual Design Improvement of a Toroidal Field Coil for EU DEMO Using High-Temperature Superconductors," *IEEE Trans. Appl. Supercond.*, vol. 26, no. 4, 2016.

[30] P. Bruzzone, “Pre-conceptual studies and R&D for DEMO superconducting magnets,” *Fusion Eng. Des.*, vol. 89, no. 7–8, pp. 1775–1778, 2014.

[31] F. Romanelli, “Overview of the JET results,” *Nucl. Fusion*, vol. 55, p. 104001, 2015.

[32] A. Sykes *et al.*, “Compact fusion energy based on the spherical tokamak,” *Nucl. Fusion*, vol. 58, p. 016039, 2018.

[33] M. Jirsa, M. Rames, I. Duran, and L. Viererbl, “Effect of neutron irradiation on critical currents of REBaCuO superconducting tapes considered for magnets in fusion reactors,” *IEEE Trans. Appl. Supercond.*, vol. 28, no. 4, 2018.

[34] A. Nishimura *et al.*, “Fast neutron irradiation effect on superconducting properties of Nb_3Sn and Nb_3Al strands,” *AIP Conf. Proc.*, vol. 1435, no. June 2012, pp. 217–224, 2012.

[35] T. Baumgartner, M. Eisterer, H. W. Weber, R. Flükiger, C. Scheuerlein, and L. Bottura, “Performance boost in industrial multifilamentary Nb_3Sn wires due to radiation induced pinning centers,” *Sci. Rep.*, vol. 5, no. January, pp. 1–7, 2015.

[36] M. Jirsa, M. Rameš, I. Ďuran, T. Entler, and L. Viererbl, “Critical currents in REBaCuO superconducting tapes in response to neutron irradiation,” *Supercond. Sci. Technol.*, 2019.

[37] D. X. Fischer, R. Prokopec, J. Emhofer, and M. Eisterer, “The effect of fast neutron irradiation on the superconducting properties of REBCO coated conductors with and without artificial pinning centers,” *Supercond. Sci. Technol.*, vol. 31, p. 044006, 2018.

[38] S. Eley *et al.*, “Decoupling and tuning competing effects of different types of defects on flux creep in irradiated $YBa_2Cu_3O_{7-\delta}$ coated conductors,” *Supercond. Sci. Technol.*, vol. 30, no. 4, pp. 1–13, 2017.

[39] K. J. Leonard, F. A. List, T. Aytug, A. A. Gapud, and J. W. Geringer, “Irradiation performance of rare earth and nanoparticle enhanced high temperature superconducting films based on YBCO,” *Nucl. Mater. Energy*, vol. 9, pp. 251–255, 2016.

[40] ONNES and H. K., “The superconductivity of mercury,” *Comm. Phys. Lab. Univ. Leiden*, vol. 122, p. 124, 1911.

[41] J. G. Bednorz and K. a. Muller, “Possible High T_c Superconductivity in the Ba - La - Cu - O System,” *Phys. B Condens. Matter*, vol. 64, pp. 189–193, 1986.

[42] M. K. Wu *et al.*, “Superconductivity at 93 K in a new mixed-phase Y-Ba-Cu-O compound system at ambient pressure,” *Phys. Rev. Lett.*, vol. 58, no. 9, pp. 908–910, 1987.

[43] A. Schilling, M. Cantoni, J. D. Guo, and H. R. Ott, “Superconductivity above 130K in the Hg-Ba-Ca-Cu-O system,” *Lett. to Nat.*, vol. 363, no. 2 December 1993, pp. 56–58, 1993.

[44] A. P. Drozdov *et al.*, “Superconductivity at 250 K in lanthanum hydride under high pressures,” *Nature*, vol. 569, pp. 528–531, 2019.

[45] M. Somayazulu *et al.*, “Evidence for Superconductivity above 260 K in Lanthanum

Superhydride at Megabar Pressures," *Phys. Rev. Lett.*, vol. 122, no. 2, p. 27001, 2019.

[46] A. D. Grockowiak *et al.*, "Hot Hydride Superconductivity above 550 K," pp. 1–30, 2020.

[47] S. He *et al.*, "Phase diagram and electronic indication of high-temperature superconductivity at 65 K in single-layer FeSe films," *Nat. Mater.*, vol. 12, no. 7, pp. 605–610, 2013.

[48] G. Wu *et al.*, "Superconductivity at 56 K in samarium-doped SrFeAsF," *J. Phys. Condens. Matter*, vol. 21, p. 142203, 2009.

[49] M. J. Rosseinsky *et al.*, "Superconductivity at 28 K in Rb_xC_{60}," *Phys. Rev. Lett.*, vol. 66, no. 21, pp. 2830–2832, 1991.

[50] T. T. M. Palstra, O. Zhou, Y. Iwasa, P. E. Sulewski, R. M. Fleming, and B. R. Zegarski, "Superconductivity at 40 K in Cesium doped C_{60}," *Solid State Commun.*, vol. 93, no. 4, pp. 327–330, 1995.

[51] C. W. Chu, L. Z. Deng, and B. Lv, "Hole-doped cuprate high temperature superconductors," *Phys. C Supercond. its Appl.*, vol. 514, pp. 290–313, 2015.

[52] W. Meissner and R. Ochsenfeld, "Ein neuer Effekt bei Eintritt der Supraleitf??higkeit," *Naturwissenschaften*, vol. 21, no. 44, pp. 787–788, 1933.

[53] F. London and H. London, "The Electromagnetic Equations of the Supreconductor," vol. 85, no. 1933, 1934.

[54] R. Kleiner and W. Buckel, *An intoduction to Superconductivity*, Third. Weinheim: WILEY-VCH, 2016.

[55] V. L. Ginzburg and L. D. Landau, "On the Theory of Superconductivity," *Zh. Eksp. Teor. Fiz.*, vol. 1064, pp. 113–137, 1950.

[56] A. A. Abrikosov, "On the magnetic properties of superconductors of the second group," *Sov. Phys. JETP*, vol. 5, pp. 1174–1182, 1957.

[57] U. Essmann and H. Träuble, "The direct observation of individual flux lines in type II superconductors," *Phys. Lett. A*, vol. 24, no. 10, pp. 526–527, 1967.

[58] C. P. Herring, "THE OBSERVATION OF FLUX LINE PINNING iN SUPERCONDUCTING FOILS," vol. 47, no. 2, pp. 105–106, 1974.

[59] J. Bardeen, L. N. Cooper, and J. R. Schrieffer, "Theory of superconductivity," *Phys. Rev.*, vol. 108, no. 5, pp. 1175–1204, 1957.

[60] H. Fröhlich, "Theory of the superconducting state. I. The ground state at the absolute zero of temperature," *Phys. Rev.*, vol. 79, no. 5, pp. 845–856, 1950.

[61] J. Bardeen, "Wave functions for superconducting electrons," *Phys. Rev.*, vol. 80, no. 4, pp. 567–574, 1950.

[62] R. Wesche and P. Capper, *Springer Handbook of Electronic and Photonic Materials*. Springer, 2017.

[63] J. D. Jorgensen *et al.*, "Oxygen ordering and the orthorhombic-to-tetragonal phase transition in $YBa_2Cu_3O_{7-x}$," *Phys. Rev. B*, vol. 36, no. 7, pp. 3608–3616, 1987.

[64] J. Yuan, L. M. Brown, and W. Y. Liang, "Electron energy-loss spectroscopy of the high-temperature superconductor $Ba_2YCu_3O_{7-x}$," *J. Phys.*, vol. 21, pp. 517–526, 1988.

[65] T. Siegrist, S. Sunshine, D. W. Murphy, R. J. Cava, and S. M. Zahurak, "Crystal structure of the high-T_c superconductor $Ba_2YCu_3O_{9-x}$," *Phys. Rev. B*, vol. 35, no. 13, pp. 7137–7139, 1987.

[66] L. D. L. D. Santos V. *et al.*, "Magnetic Properties of the Superconductor $LaCaBaCu_3O_7$," *Open Supercond. J.*, vol. 2, no. 1, pp. 19–27, 2010.

[67] J. M. Tarascon *et al.*, "Structural and physical properties of the metal (M) substituted $YBa_2Cu_{3-x}M_xO_{7-y}$ perovskite," *Phys. Rev. B*, vol. 37, no. 13, pp. 7458–7469, 1988.

[68] G. Van Tendeloo, H. W. Zandbergen, and S. Amelinckx, "THE VACANCY ORDER - DISORDER TRANSITION IN $Ba_2YCu_3O_{7-\sigma}$ OBSERVED BY MEANS OF ELECTRON DIFFRACTION AND ELECTRON MICROSCOPY," *J. Chem. Inf. Model.*, vol. 63, no. 7, pp. 603–606, 1987.

[69] T. Wu *et al.*, "Incipient charge order observed by NMR in the normal state of $YBa_2Cu_3O_y$," *Nat. Commun.*, vol. 6, no. 96, 2015.

[70] D. E. Farrell, J. P. Rice, D. M. Ginsberg, and J. Z. Liu, "Experimental evidence of a dimensional crossover in $Y_1Ba_2Cu_3O_7$," *Phys. Rev. Lett.*, vol. 64, no. 13, pp. 1573–1576, 1990.

[71] A. R. Armstrong and P. P. Edwards, "Chemistry of Superconducting Oxides," no. 6, 1991.

[72] R. F. Lopes *et al.*, "Low Sr doping effects on critical current density and pinning mechanism of $YBa_2Cu_3O_{7-\delta}$ single crystals," *J. Phys. Conf. Ser.*, vol. 568, 2014.

[73] W. T. Wang *et al.*, "Enhanced flux pinning properties in superconducting $YBa_2Cu_3O_{7-z}$ films by a novel chemical doping approach," *Phys. C Supercond. its Appl.*, vol. 493, pp. 104–108, 2013.

[74] J. Shi *et al.*, "Deposition of REBCO with different rare earth elements on CeO_2 buffered technical substrates by fluorine-free metal organic decomposition route," *J. Eur. Ceram. Soc.*, vol. 41, no. 10, pp. 5223–5229, 2021.

[75] M. Erbe *et al.*, "Comparative study of CSD-grown REBCO films with different rare earth elements: Processing windows and T_c," *Supercond. Sci. Technol.*, vol. 33, p. 094002, 2020.

[76] S. Zhang, S. Xu, Z. Fan, P. Jiang, and Z. Han, "Broad temperature study of RE-substitution effects on the in-field critical current behavior of REBCO superconducting tapes," *Supercond. Sci. Technol.*, vol. 31, p. 125006, 2018.

[77] J. F. Bringley, -M Chen, T, B. A. Averill, K. M. Wong, and P. S. J, "Synthesis and

characterization of $YBa_2(Cu_{1-x}M_x)_3O_{7-\delta}$ (M=Co,Nl): Crystal symmetry, superconductivity, and the role of oxygen," *Phys. Rev. B*, vol. 38, no. 4, pp. 2432–2438, 1988.

[78] G. Xiao, M. Z. Cieplak, A. Garvin, F. H. Streitz, A. Bakhshai, and C. L. Chien, "High-Temperature Superconductivity in Tetragonal Perovskite Structures: Is Oxygen-Vacancy Order Important?," *Phys. Rev. Lett.*, vol. 60, no. 14, pp. 1446–1449, 1988.

[79] S. Mazumder *et al.*, "Structural and superconducting behaviour of Mg- and Zn-substituted $YBa_2Cu_3O_{7-\delta}$," *Phase Transitions*, vol. 19, pp. 97–105, 1989.

[80] J. D. Jorgensen *et al.*, "Structural properties of oxygen-deficient $YBa_2Cu_3O_{7-\delta}$," *Phys. Rev. B*, vol. 41, no. 4, p. 1863, 1990.

[81] J. Bobroff *et al.*, "Absence of static phase separation in the high T_c Cuprate $YBa_2Cu_3O_{6+y}$," *Phys. Rev. Lett.*, vol. 89, no. 15, pp. 157002/1-157002/4, 2002.

[82] R. Liang, D. A. Bonn, and W. N. Hardy, "Evaluation of CuO_2 plane hole doping in $YBa_2Cu_3O_{6+x}$ single crystals," *Phys. Rev. B - Condens. Matter Mater. Phys.*, vol. 73, no. 18, pp. 1–4, 2006.

[83] R. J. Cava *et al.*, "Structural anomalies, oxygen ordering and superconductivity in oxygen deficient $Ba_2YCu_3O_x$," *Phys. C Supercond. its Appl.*, vol. 165, pp. 419–433, 1990.

[84] C. N. R. Rao, R. Nagarajun, A. K. Ganguli, G. N. Subbanna, and V. Bhat, "Nature and stability of the '60-K superconducting phase' in the $YBa_2Cu_3O_{7-\delta}$ system," *Phys. Rev. B*, vol. 42, no. 10, pp. 6765–6768, 1990.

[85] G. Van Tendeloo, H. W. Zandbergen, and S. Amelinckx, "Electron diffraction and electron microscopic of Ba-Y-Cu-O superconducting materials," *Solid State Commun.*, vol. 63, no. 5, pp. 389–393, 1987.

[86] I. K. Schuller *et al.*, "Structural phase transition in $YBa_2Cu_3O_{7-\delta}$: the role of dimensionality for high temperature superconductivity," *Solid State Commun.*, vol. 63, no. 5, pp. 385–388, 1987.

[87] W. E. Farneth, R. K. Bordia, E. M. McCarron III, M. K. Crawford, and R. B. Flippen, "Influence of Oxygen Stoichiometry on the Structure and Superconducting," *Solid State Commun.*, vol. 66, no. 9, pp. 953–959, 1988.

[88] R. Ramesh, S. Jin, and P. Marsh, "Superconductor defect structure," *Nature*, vol. 346. p. 420, 1990.

[89] A. Llordés *et al.*, "Nanoscale strain-induced pair suppression as a vortex-pinning mechanism in high-temperature superconductors," *Nat. Mater.*, vol. 11, no. 4, pp. 329–336, 2012.

[90] P. Mele *et al.*, "High pinning performance of $YBa_2Cu_3O_{7-x}$ films added with Y_2O_3 nanoparticulate defects," *Supercond. Sci. Technol.*, vol. 28, p. 024002, 2015.

[91] D. M. Feldmann *et al.*, "Influence of growth temperature on critical current and magnetic

flux pinning structures in $YBa_2Cu_3O_{7-x}$," *Appl. Phys. Lett.*, vol. 91, p. 162501, 2007.

[92] W. Zhang *et al.*, "Control of flux pinning in MOD YBCO coated conductor," *IEEE Trans. Appl. Supercond.*, vol. 17, no. 2, pp. 3347–3350, 2007.

[93] R. Guzman, J. Gazquez, B. Mundet, M. Coll, X. Obradors, and T. Puig, "Probing localized strain in solution-derived $YBa_2Cu_3O_{7-\delta}$ nanocomposite thin films," *Phys. Rev. Mater.*, vol. 1, p. 024801, 2017.

[94] L. Civale *et al.*, "Angular-dependent vortex pinning mechanisms in $YBa_2Cu_3O_7$ coated conductors and thin films," *Appl. Phys. Lett.*, vol. 84, no. 12, pp. 2121–2123, 2004.

[95] M. Eisterer, R. Fuger, M. Chudy, F. Hengstberger, and H. W. Weber, "Neutron irradiation of coated conductors," *Supercond. Sci. Technol.*, vol. 23, p. 04009, 2010.

[96] A. Ourmazd *et al.*, "Microstructure, oxygen ordering and planar defects in the high-T_c superconductor $YBa_2Cu_3O_{6.9}$," *Nature*, vol. 327, no. 6120, pp. 308–310, 1987.

[97] J. Gazquez *et al.*, "Emerging diluted ferromagnetism in high-T_c superconductors driven by point defect clusters," *Adv. Sci.*, vol. 3, p. 1500295, 2016.

[98] Z. Li, M. Coll, B. Mundet, A. Palau, T. Puig, and X. Obradors, "Suppression of superconductivity at the nanoscale in chemical solution derived $YBa_2Cu_3O_{7-\delta}$ thin films with defective $Y_2Ba_4Cu_8O_{16}$ intergrowths," *Nanoscale Adv.*, vol. 2, no. 8, pp. 3384–3393, 2020.

[99] M. P. A. Fisher, "Vortex-glass superconductivity: A possible new phase in bulk high-T_c oxides," *Phys. Rev. Lett.*, vol. 62, no. 12, pp. 1415–1418, 1989.

[100] A. I. Larkin and Y. N. Ovchinnikov, "Pinning in type II superconductors," *J. Low Temp. Phys.*, vol. 34, no. 3–4, pp. 409–428, 1979.

[101] G. Blatter, M. V. Feigel'Man, V. B. Geshkenbein, A. I. Larkin, and V. M. Vinokur, "Vortices in high-temperature superconductors," *Rev. Mod. Phys.*, vol. 66, no. 4, pp. 1125–1388, 1994.

[102] P. L. Gammel, L. F. Schneemeyer, J. V Waszczak, and D. J. Bishop, "Evidence from Mechanical Measurments for Flux-Lattice Melting in Single-Crystal $YBa_2Cu_3O_7$ and $Bi_{2.2}Sr_2Ca_{0.8}Cu_2O_8$," *Phys. Rev. B*, vol. 61, no. 14, pp. 1666–1669, 1988.

[103] R. Nelson and H. S. Seung, "Theory of flux melted liquids," *Phys. Rev. B*, vol. 39, no. 13, 1989.

[104] P. W. Anderson, "Theory of flux creep in hard superconductors," *Phys. Rev. Lett.*, vol. 9, no. 7, pp. 309–311, 1962.

[105] W. K. Kwok, U. Welp, A. Glatz, A. E. Koshelev, K. J. Kihlstrom, and G. W. Crabtree, "Vortices in high-performance high-temperature superconductors," *Reports Prog. Phys.*, vol. 79, p. 116501, 2016.

[106] N. M. Strickland and S. C. Wimbush, "The magnetic-field dependence of critical current:

What we really need to know," *IEEE Trans. Appl. Supercond.*, vol. 27, no. 4, 2017.

[107] L. F. Goodrich and S. L. Bray, "High T_c superconductors and critical current measurement," *Cryogenics (Guildf).*, vol. 30, pp. 667–677, 1990.

[108] Y. Yeshurun and A. P. Malozemoff, "Giant flux creep and irreversibility in an Y-Ba-Cu-O crystal: An alternative to the superconducting-glass model," *Phys. Rev. Lett.*, vol. 60, no. 21, pp. 2202–2205, 1988.

[109] S. Kang *et al.*, "High-Performance High-T_c Superconducting Wires," *Science (80-.).*, vol. 311, pp. 1911–1913, 2006.

[110] J. W. Ekin, K. Salama, and V. Selvamanickam, "High-transport current density up to 30 T in bulk $YBa_2Cu_3O_7$ and the critical angle effect," *Appl. Phys. Lett.*, vol. 59, no. 3, pp. 360–362, 1991.

[111] L. Piperno *et al.*, "Polymer-assisted surface decoration for critical current enhancement in $YBa_2Cu_3O_{7-x}$ films," *Appl. Surf. Sci.*, vol. 484, pp. 237–244, 2019.

[112] M. Sieger *et al.*, "Thick secondary phase pinning-enhanced YBCO films on technical templates," *IEEE Trans. Appl. Supercond.*, vol. 28, no. 4, pp. 20–24, 2018.

[113] P. Kes and J. Aarts, "Thermally assisted flux flow at small driving forces," *Supercond. Sci. Technol.*, vol. 242, 1989.

[114] V. V. Derevyanko, T. V. Sukhareva, and V. A. Finkel, "Phase Transformations and Vortex Structure Evolution in Two-Level High-Temperature Granular Superconductor $YBa_2Cu_3O_{7-\delta}$ under Temperature and Magnetic Field," *Phys. Solid State*, vol. 59, no. 8, pp. 1492–1500, 2017.

[115] B. D. Josephson, "Possible new effects in superconductive tunnelling," *Phys. Lett.*, vol. 1, no. 7, pp. 251–253, 1962.

[116] D. Dimos, P. Chaudhari, and J. Mannhart, "Superconducting transport properties in $YBa_2Cu_3O_7$ bicrystals," *Phys. Rev. B*, vol. 41, no. 7, pp. 4038–4049, 1990.

[117] N. F. Heinig *et al.*, "Evidence for channel conduction in low misorientation angle [001] tilt $YBa_2Cu_3O_{7-x}$ bicrystal films," *Appl. Phys. Lett.*, vol. 69, no. 4, pp. 577–579, 1996.

[118] M. Miura, M. Yoshizumi, T. Izumi, and Y. Shiohara, "Formation mechanism of $BaZrO_3$ nanoparticles in $Y_{1-x}Sm_xBa_2Cu_3O_y$ -coated conductors derived from trifluoroacetate metal-organic deposition," *Supercond. Sci. Technol.*, vol. 23, p. 014013, 2010.

[119] X. Xiong *et al.*, "High throughput processing of long-length IBAD MgO and Epi-buffer templates at SuperPower," *IEEE Trans. Appl. Supercond.*, vol. 17, no. 2, pp. 3375–3378, 2007.

[120] A. Goyal and M. P. Paranthaman, "The RABiTS approach: Using rolling-assisted biaxially textured substrates for high-performance YBCO superconductors," *MRS Bull.*, no. 29.8, pp. 552–561, 2004.

[121] D. M. Mattox, “Physical vapor deposition (PVD) processes,” *Met. Finish.*, vol. 100, pp. 394–408, 2002.

[122] V. Selvamanickam *et al.*, “High-current Y-Ba-Cu-O superconducting films by metal organic chemical vapor deposition on flexible metal substrates,” *Phys. C Supercond. its Appl.*, vol. 333, pp. 155–162, 2000.

[123] J. O. Willis *et al.*, “Advances in YBCO-coated conductor technology,” *Phys. C Supercond. its Appl.*, vol. 335, no. 1, pp. 73–77, 2000.

[124] V. Matias *et al.*, “YBCO films grown by reactive co-evaporation on simplified IBAD-MgO coated conductor templates,” *Supercond. Sci. Technol.*, vol. 23, no. 1, p. 014018, 2010.

[125] C. Senatore, C. Barth, M. Bonura, M. Kulich, and G. Mondonico, “Field and temperature scaling of the critical current density in commercial REBCO coated conductors,” *Supercond. Sci. Technol.*, vol. 29, no. 1, 2015.

[126] A. Sundaram *et al.*, “2G HTS wires made on 30 μm thick Hastelloy substrate,” *Supercond. Sci. Technol.*, vol. 29, no. 10, 2016.

[127] Y. Zhang *et al.*, “Magnetic field orientation dependence of flux pinning in (Gd,Y)$Ba_2Cu_3O_{7-x}$ coated conductor with tilted lattice and nanostructures,” *Phys. C Supercond. its Appl.*, vol. 469, no. 23–24, pp. 2044–2051, 2009.

[128] R. Guzman *et al.*, “Strain-driven broken twin boundary coherence in $YBa_2Cu_3O_{7-\delta}$ nanocomposite thin films,” *Appl. Phys. Lett.*, vol. 102, p. 081906, 2013.

[129] R. J. Cava *et al.*, “Bulk superconductivity at 91 K in single-phase oxygen-deficient perovskite $Ba_2YCu_3O_{9-x}$,” *Phys. Rev. Lett.*, vol. 58, no. 16, pp. 1676–1679, 1987.

[130] J. E. Greedan, A. O’Reilly, and C. V. Stager, “Oxygen ordering in the crystal structure of the 93-K superconductor $YBa_2Cu_3O_7$ using powder neutron diffraction at 298 and 79.5 K,” *Phys. Rev. B*, vol. 35, no. 16, pp. 8770–8773, 1987.

[131] A. K. Stoyanova-Ivanova *et al.*, “The use of high-temperature superconducting cuprate as a dopant to the negative electrode in Ni-Zn batteries,” *Bulg. Chem. Commun.*, vol. 47, no. 1, pp. 221–228, 2015.

[132] W. Li, S. Li, G. Li, B. Zhang, and P. Chou, “Thickness dependence of structural and superconducting properties of single-crystal-like GdBCO films prepared by photo-assisted MOCVD,” *IEEE Trans. Appl. Supercond.*, vol. 23, no. 2, pp. 0–5, 2013.

[133] U. Welp, W. K. Kwok, G. W. Crabtree, K. G. Vandervoort, and J. Z. Liu, “Magnetic Measurements of the Upper Critical Field of $YBa_2Cu_3O_{7-\delta}$ Single Crystals,” *Phys. Rev. Lett.*, vol. 62, no. 16, pp. 1908–1911, 1989.

[134] K. Iida *et al.*, “Pinning analyses of a $BaHfO_3$-containing $GdBa_2Cu_3O_{7-\delta}$ thin film grown by chemical solution deposition,” *Supercond. Sci. Technol.*, vol. 34, no. 1, 2021.

[135] T. Worthington, W. Gallagher, and T. Dinger, “Anisotropic nature of high-temperature

superconductivity in single-crystal $Y_1Ba_2Cu_3O_{7-x}$," *Phys. Rev. Lett.*, vol. 59, no. 10, pp. 1160–1163, 1987.

[136] M. Erbe *et al.*, "$BaHfO_3$ artificial pinning centres in TFA-MOD-derived YBCO and GdBCO thin films," *Supercond. Sci. Technol.*, vol. 28, no. 11, 2015.

[137] K. Takahashi *et al.*, "Investigation of thick PLD-GdBCO and ZrO2 doped GdBCO coated conductors with high critical current on PLD-CeO2 capped IBAD-GZO substrate tapes," *Supercond. Sci. Technol.*, vol. 19, no. 9, pp. 924–929, 2006.

[138] D. Wu and S. Sridhar, "Pinning forces and lower critical fields in $YBa_2Cu_3O_y$ Crystals: Temperature Dependence and Anisotropy," *Phys. Rev. Lett.*, vol. 65, no. 16, pp. 2074–2077, 1990.

[139] K. X. Xu, X. Da Wu, and H. Fang, "Properties of thermally activated flux motion in MTG-GdBCO measured by AC susceptibility," *J. Phys. Conf. Ser.*, vol. 234, no. PART 1, 2010.

[140] M. C. Marchetti and D. R. Nelson, "Dynamics of flux-line liquids in high-T_c superconductors," *Phys. C Supercond. its Appl.*, vol. 174, no. 1–3, pp. 40–62, 1991.

[141] R. H. Koch, V. Foglietti, W. J. Gallagher, G. Koren, A. Gupta, and M. P. A. Fisher, "Experimental evidence for vortex-glass superconductivity in Y-Ba-Cu-O," *Phys. Rev. Lett.*, vol. 63, no. 14, pp. 1511–1514, 1989.

[142] D. Dew-Hughes, "Flux pinning mechanisms in type II superconductors," *Philos. Mag.*, vol. 30, no. 2, pp. 293–305, 1974.

[143] A. Crisan, V. S. Dang, and P. Mikheenko, "Nano-engineered pinning centres in YBCO superconducting films," *Phys. C Supercond. its Appl.*, vol. 533, pp. 118–132, 2017.

[144] A. M. Campbell and J. E. Evetts, "Flux vortices and transport currents in type II superconductors," *Adv. Phys.*, vol. 21, no. 90, pp. 199–428, 1972.

[145] A. K. Jha *et al.*, "Tailoring the vortex pinning strength of YBCO thin films by systematic incorporation of hybrid artificial pinning centers," *Supercond. Sci. Technol.*, vol. 28, no. 11, 2015.

[146] M. Tachiki and S. Takahashi, "STRONG VORTEX PINNING INTRINSIC IN HIGH-T_c OXIDE SUPERCONDUCTORS," *Solid State Commun.*, vol. 70, no. 3, pp. 291–295, 1989.

[147] E. M. Chudnovsky, "Pinning by Oxygen Vacancies in High-T_c Superconductors," *Phys. Rev. Lett.*, vol. 65, no. 24, pp. 3060–3062, 1990.

[148] T. Haugan, P. N. Barnes, R. Wheeler, F. Meisenkothen, and M. Sumption, "Addition of nanoparticle dispersions to enhance flux pinning of the $YBa_2Cu_3O_{7-x}$ superconductor," *Nature*, vol. 430, no. August, pp. 867–870, 2004.

[149] P. Mele *et al.*, "Systematic study of $BaSnO_3$ doped $YBa_2Cu_3O_{7-x}$ films," *Phys. C Supercond. its Appl.*, vol. 469, no. 15–20, pp. 1380–1383, 2009.

[150] I. A. Sadovskyy, A. E. Koshelev, W. K. Kwok, U. Welp, and A. Glatz, "Targeted evolution of

pinning landscapes for large superconducting critical currents," *Proc. Natl. Acad. Sci. U. S. A.*, vol. 116, no. 21, pp. 10291–10296, 2019.

[151] I. A. Sadovskyy *et al.*, "Toward Superconducting Critical Current by Design," *Adv. Mater.*, pp. 4593–4600, 2016.

[152] V. Selvamanickam *et al.*, "Correlation between in-field critical currents in Zr-added (Gd, Y)$Ba_2Cu_3O_x$ superconducting tapes at 30 and 77 K," *Supercond. Sci. Technol.*, vol. 27, p. 055010, 2014.

[153] J. P. F. Feighan, A. Kursumovic, and J. L. MacManus-Driscoll, "Materials design for artificial pinning centres in superconductor PLD coated conductors," *Supercond. Sci. Technol.*, vol. 30, no. 12, 2017.

[154] M. M. Aye, M. Z. Khan, E. Rivasto, J. Tikkanen, H. Huhtinen, and P. Paturi, "Role of Columnar Defect Size in Angular Dependent Flux Pinning Properties of YBCO Thin Films," *IEEE Trans. Appl. Supercond.*, vol. 29, no. 5, pp. 1–5, 2019.

[155] V. Selvamanickam *et al.*, "Influence of Zr and Ce doping on electromagnetic properties of (Gd,Y)-Ba-Cu-O superconducting tapes fabricated by metal organic chemical vapor deposition," *Phys. C Supercond. its Appl.*, vol. 469, no. 23–24, pp. 2037–2043, 2009.

[156] M. Miura *et al.*, "Mixed pinning landscape in nanoparticle-introduced $YGdBa_2Cu_3O_y$ films grown metal organic deposition," *Phys. Rev. B*, vol. 83, no. 18, p. 184519, 2011.

[157] Y. Zhao, C. H. Cheng, and J. S. Wang, "Flux pinning by NiO-induced nano-pinning centres in melt-textured YBCO superconductor," *Supercond. Sci. Technol.*, vol. 18, no. 2, 2005.

[158] T. Horide, N. Matsukida, M. Ishimaru, R. Kita, S. Awaji, and K. Matsumoto, "Pin potential effect on vortex pinning in $YBa_2Cu_3O_{7-\delta}$ films containing nanorods: Pin size effect and mixed pinning," *Appl. Phys. Lett.*, vol. 110, no. 5, p. 052601, 2017.

[159] T. Horide *et al.*, "Influence of matching field on critical current density and irreversibility temperature in $YBa_2Cu_3O_7$ films with $BaMO_3$ (M = Zr, Sn, Hf) nanorods," *Appl. Phys. Lett.*, vol. 108, p. 082601, 2016.

[160] T. Horide *et al.*, "Control of the glass-liquid transition temperature in $YBa_2Cu_3O_{7-x}$ films," *Phys. Rev. B - Condens. Matter Mater. Phys.*, vol. 79, p. 092504, 2009.

[161] T. Horide *et al.*, "Strong c -axis correlated pinning and hybrid pinning in $YBa_2Cu_3O_{7-\delta}$ films containing $BaHfO_3$ nanorods and stacking faults," *Supercond. Sci. Technol.*, vol. 30, no. 7, p. 074009, 2017.

[162] A. K. Jha *et al.*, "Controlling the Critical Current Anisotropy of YBCO Superconducting Films by Incorporating Hybrid Artificial Pinning Centers," *IEEE Trans. Appl. Supercond.*, vol. 26, no. 3, pp. 2–5, 2016.

[163] D. M. Feldmann, T. G. Holesinger, B. Maiorov, S. R. Foltyn, J. Y. Coulter, and I. Apodaca, "Improved flux pinning in $YBa_2Cu_3O_7$ with nanorods of the double perovskite Ba_2YNbO_6," *Supercond. Sci. Technol.*, vol. 23, p. 095004, 2010.

[164] M. Coll *et al.*, "Size-controlled spontaneously segregated Ba_2YTaO_6 nanoparticles in $YBa_2Cu_3O_7$ nanocomposites obtained by chemical solution deposition," *Supercond. Sci. Technol.*, vol. 27, p. 044008, 2014.

[165] P. Pahlke *et al.*, "Influence of artificial pinning centers on structural and superconducting properties of thick YBCO films on ABAD-YSZ templates," *Supercond. Sci. Technol.*, vol. 31, no. 4, 2018.

[166] A. Xu, J. Jaroszynski, F. Kametani, and D. Larbalestier, "Broad temperature range study of J_c and H_{irr} anisotropy in $YBa_2Cu_3O_x$ thin films containing either Y_2O_3 nanoparticles or stacking faults," *Appl. Phys. Lett.*, vol. 106, p. 052603, 2015.

[167] S. Nariki, N. Sakai, M. Murakami, and I. Hirabayashi, "High critical current density in RE-Ba-Cu-O bulk superconductors with very fine RE_2BaCuO_5 particles," *Phys. C Supercond. its Appl.*, vol. 412–414, pp. 557–565, 2004.

[168] V. F. Solovyov *et al.*, "High critical currents by isotropic magnetic-flux-pinning centres in a 3 μm-thick $YBa_2Cu_3O_7$ superconducting coated conductor," *Supercond. Sci. Technol.*, vol. 20, no. 4, 2007.

[169] G. Majkic *et al.*, "Effect of high BZO dopant levels on performance of 2G-HTS MOCVD wire at intermediate and low temperatures," *IEEE Trans. Appl. Supercond.*, vol. 23, no. 3, pp. 0–4, 2013.

[170] E. Galstyan *et al.*, "In-field critical current and pinning mechanisms at 4.2 K of Zr-Added REBCO coated conductors," *Supercond. Sci. Technol.*, vol. 33, no. 7, 2020.

[171] S. Chen *et al.*, "Generating mixed morphology $BaZrO_3$ artificial pinning centers for strong and isotropic pinning in $BaZrO_3$ – Y_2O_3 double- doped YBCO thin fi lms," *Supercond. Sci. Technol.*, vol. 30, p. 125011, 2017.

[172] Q. P. Meng, D. O. Welch, and Y. Zhu, "Strain-induced changes of oxygen ordering in $YBa_2Cu_3O_{6+\delta}$ cuprates," *Phys. Rev. B - Condens. Matter Mater. Phys.*, vol. 79, p. 134531, 2009.

[173] D. Larbalestier, A. Gurevich, D. M. Feldmann, and A. Polyanskii, "High-T_c superconducting materials for electric power applications," *Nature*, vol. 414, pp. 368–377, 2001.

[174] S. K. Viswanathan *et al.*, "Enhancement of critical current density of $YBa_2Cu_3O_{7-\delta}$ thin films by self-assembly of Y_2O_3 nanoparticulates," *Thin Solid Films*, vol. 515, pp. 6452–6455, 2007.

[175] P. Mele *et al.*, "Insertion of nanoparticulate artificial pinning centres in $YBa_2Cu_3O_{7-x}$ films by laser ablation of a Y_2O_3-surface modified target," *Supercond. Sci. Technol.*, vol. 20, pp. 616–620, 2007.

[176] C. Cantoni *et al.*, "Strain-Driven Oxygen Deficiency in Self-Assembled, Nanostructured, Composite Oxide Films," *ACS Nano*, vol. 5, no. 6, pp. 4783–4789, 2011.

[177] S. Chen *et al.*, "Enhancement of isotropic pinning force in YBCO films with $BaZrO_3$

nanorods and Y_2O_3 nanoparticles," *IEEE Trans. Appl. Supercond.*, vol. 27, no. 4, p. 8000205, 2017.

[178] A. Goyal *et al.*, "Irradiation-free, columnar defects comprised of self-assembled nanodots and nanorods resulting in strongly enhanced flux-pinning in $YBa_2Cu_3O_{7-\delta}$ films," *Supercond. Sci. Technol.*, vol. 18, no. 11, pp. 1533–1538, 2005.

[179] A. K. Jha *et al.*, "Systematic Variation of Hybrid APCs into YBCO Thin Films for Improving the Vortex Pinning Properties," *IEEE Trans. Appl. Supercond.*, vol. 25, no. 3, 2014.

[180] P. Mele *et al.*, "Incorporation of double artificial pinning centers in $YBa_2Cu_3O_{7-d}$ films," *Supercond. Sci. Technol.*, vol. 21, no. 1, p. 15019, 2008.

[181] T. Baumgartner, M. Eisterer, H. W. Weber, R. Flükiger, C. Scheuerlein, and L. Bottura, "Effects of neutron irradiation on pinning force scaling in state-of-the-art Nb_3Sn wires," *Supercond. Sci. Technol.*, vol. 27, no. 1, p. 015005, 2014.

[182] C. G. Windsor and J. G. Morgan, "Neutron and gamma flux distributions and their implications for radiation damage in the shielded superconducting core of a fusion power plant," *Nucl. Fusion*, vol. 57, no. 11, 2017.

[183] J. K. Shultis and R. E. Faw, "An MCNP primer." 2011.

[184] M. Kovari, R. Kemp, H. Lux, P. Knight, J. Morris, and D. J. Ward, "PROCESS: A systems code for fusion power plants - Part 1: Physics," *Fusion Eng. Des.*, vol. 89, no. 12, pp. 3054–3069, 2014.

[185] K. Maki, S. Sato, K. Hayashi, K. Yamada, and H. Takatsu, "Evaluation of dose rate and reactor core and nuclear properties for superconductive magnets in ITER," *Fusion Eng. Des.*, vol. 42, no. 1–4, pp. 173–185, 1998.

[186] B. G. Hong and T. H. Kim, "On the optimal radial build of a normal aspect ratio tokamak fusion system," *Fusion Eng. Des.*, vol. 139, no. 2019, pp. 148–154, 2019.

[187] K. Nordlund, M. Ghaly, and R. Averback, "Defect production in collision cascades in elemental semiconductors and fcc metals," *Phys. Rev. B - Condens. Matter Mater. Phys.*, vol. 57, no. 13, pp. 7556–7570, 1998.

[188] D. J. Bacon, F. Gao, and Y. N. Osetsky, "Primary damage state in fcc, bcc and hcp metals as seen in molecular dynamics simulations," *J. Nucl. Mater.*, vol. 276, no. 1, pp. 1–12, 2000.

[189] G. H. Kinchin and R. S. Pease, "Displacement of Atoms in Solid by Radiation," *Rep. Prog. Phys.*, vol. 18, pp. 1–51, 1955.

[190] J. A. Brinkman, "On the nature of radiation damage in metals," *J. Appl. Phys.*, vol. 25, no. 8, pp. 961–970, 1954.

[191] G. S. Was and T. Allen, "Intercomparison of microchemical evolution under various types of particle irradiation," *J. Nucl. Mater.*, vol. 205, no. C, pp. 332–338, 1993.

[192] H. W. Weber, H. Böck, E. Unfried, and L. R. Greenwood, “Neutron dosimetry and damage calculations for the TRIGA MARK-II reactor in Vienna,” *J. Nucl. Mater.*, vol. 137, pp. 236–240, 1986.

[193] C. W. Allen, “In situ ion- and electron-irradiation effects studies in transmission electron microscopes,” *Ultramicroscopy*, vol. 56, no. 1–3, pp. 200–210, 1994.

[194] P. Bhattacharyya *et al.*, “Proton irradiation studies on Al and Al5083 alloy,” *Radiat. Phys. Chem.*, vol. 139, no. April, pp. 132–140, 2017.

[195] A. Dutta Gupta *et al.*, “Proton irradiation studies on pure Ti and Ti-6Al-4V,” *Nucl. Instruments Methods Phys. Res. Sect. B Beam Interact. with Mater. Atoms*, vol. 387, pp. 63–72, 2016.

[196] G. S. Was *et al.*, “Emulation of neutron irradiation effects with protons: Validation of principle,” *J. Nucl. Mater.*, vol. 300, no. 2–3, pp. 198–216, 2002.

[197] L. E. Rehn, P. R. Okamoto, and R. S. Averback, “Relative efficiencies of different ions for producing freely migrating defects,” *Phys. Rev. B*, vol. 30, no. 6, pp. 3073–3080, 1984.

[198] M. R. Gilbert, J. Marian, and J. C. Sublet, “Energy spectra of primary knock-on atoms under neutron irradiation,” *J. Nucl. Mater.*, vol. 467, pp. 121–134, 2015.

[199] S. Jumel and J. C. Van-Duysen, “INCAS: An analytical model to describe displacement cascades,” *J. Nucl. Mater.*, vol. 328, no. 2–3, pp. 151–164, 2004.

[200] G. S. Was and T. Allen, “Radiation-induced segregation in multicomponent alloys: Effect of particle type,” *Mater. Charact.*, vol. 32, no. 4, pp. 239–255, 1994.

[201] R. M. More and J. A. Spitznagel, “Primary recoil spectra and subcascade effects in ion bombardment experiments,” *Radiat. Eff.*, vol. 60, no. 1–4, pp. 27–33, 1982.

[202] R. S. Averback, “Atomic displacement processes in irradiated metals,” *J. Nucl. Mater.*, vol. 216, no. C, pp. 49–62, 1994.

[203] D. J. Bacon and T. Diaz de la Rubia, “Molecular dynamics computer simulations of displacement cascades in metals,” *J. Nucl. Mater.*, vol. 216, no. C, pp. 275–290, 1994.

[204] A. International, “ASTM E521, Standard Practice for Neutron Radiation Damage Simulation by Charged-Particle Irradiation,” in *Annual Book of ASTM Standards*, vol. 12.02, West Conshohocken, PA, 2009.

[205] D. J. Bacon, H. F. Deng, and F. Gao, “Computer simulation of threshold displacement events in alloys,” *J. Nucl. Mater.*, vol. 205, no. C, pp. 84–91, 1993.

[206] A. F. Calder and D. J. Bacon, “A molecular dynamics study of displacement cascades in α-iron,” *J. Nucl. Mater.*, vol. 207, no. C, pp. 25–45, 1993.

[207] V. V. Kirsanov, N. N. Musin, and H. J. Shamarina, “Displacement threshold energy in high-temperature superconductors. II. Thresholds for O, Ba and Y in $YBa_2Cu_3O_7$,” *Phys. Lett. A*, vol. 171, no. 3,4, pp. 223–233, 1992.

[208] K. Nordlund *et al.*, “Improving atomic displacement and replacement calculations with physically realistic damage models,” *Nat. Commun.*, vol. 9, no. 1, pp. 1–8, 2018.

[209] A. Legris *et al.*, “Effects of electron irradiation on YBCO superconductor,” *J. Phys. I*, vol. 3, pp. 1605–1615, 1993.

[210] ASTM International, “E693, Standard Practice for Characterizing Neutron Exposures in Ferritic Steels in Terms of Displacements per Atom (dpa),” in *Annual Book of ASTM Standards*, vol. 12.02, West Conshohocken, PA, 2012.

[211] M. J. Norgett, M. T. Robinson, and I. M. Torrens, “A proposed method of calculating displacement dose rates,” *Nucl. Eng. Des.*, vol. 33, pp. 50–54, 1975.

[212] R. E. Stoller, M. B. Toloczko, G. S. Was, A. G. Certain, S. Dwaraknath, and F. A. Garner, “On the use of SRIM for computing radiation damage exposure,” *Nucl. Instruments Methods Phys. Res. Sect. B Beam Interact. with Mater. Atoms*, vol. 310, pp. 75–80, 2013.

[213] W. Iliffe *et al.*, “In-situ measurements of the effect of radiation damage on the superconducting properties of coated conductors,” *Supercond. Sci. Technol.*, vol. 34, no. 9, p. 09LT01, 2021.

[214] A. Tundwal, V. Kumar, N. S. Raghaw, and A. Datta, “Monte Carlo simulation of radiation damage produced in iron and vanadium by primary knock on atom ‘PKA,’” *Radiat. Eff. Defects Solids*, vol. 171, no. 7–8, pp. 658–667, 2016.

[215] D. J. Bacon, A. F. Calder, F. Gao, V. G. Kapinos, and S. J. Wooding, “Computer-Simulation of Defect Production by Displacement Cascades in Metals,” vol. 102, no. 1–4, pp. 37–46, 1995.

[216] M. T. Robinson, “Basic physics of radiation damage production,” *J. Nucl. Mater.*, vol. 216, no. C, pp. 1–28, 1994.

[217] R. Dierckx, “The Importance of the PKA Energy Spectrum for Radiation Damage Simulation,” *J. Nucl. Mater.*, vol. 144, pp. 214–227, 1987.

[218] S. Furuno, H. Otsu, K. Hojou, and K. Izui, “Tracks of high energy heavy ions in solids,” *Nucl. Instruments Methods Phys. Res. Sect. B Beam Interact. with Mater. Atoms*, vol. 107, no. 1–4, pp. 223–226, 1996.

[219] H. Wiedersich, “Effects of the primary recoil spectrum on microstructural evolution,” *J. Nucl. Mater.*, vol. 179–181, no. PART 1, pp. 70–75, 1991.

[220] A. Meftah, N. Merrien, N. Nguyen, F. Studer, H. Pascard, and M. Toulemonde, “High-energy irradiation of magnetic insulators by lead ions: appearance of a plateau in the damage efficiency,” *Nucl. Inst. Methods Phys. Res. B*, vol. 59–60, no. PART 1, pp. 605–608, 1991.

[221] A. F. Calder, D. J. Bacon, A. V. Barashev, and Y. N. Osetsky, “On the origin of large interstitial clusters in displacement cascades,” *Philos. Mag.*, vol. 90, no. 7–8, pp. 863–884, 2010.

[222] A. V. Korchuganov, K. P. Zolnikov, D. S. Kryzhevich, V. M. Chernov, and S. G. Psakhie, "Generation of shock waves in iron under irradiation," *Nucl. Instruments Methods Phys. Res. Sect. B Beam Interact. with Mater. Atoms*, vol. 352, pp. 39–42, 2015.

[223] C. H. Woo and B. N. Singh, "Production bias due to clustering of point defects in irradiation-induced cascades," *Philos. Mag. A Phys. Condens. Matter, Struct. Defects Mech. Prop.*, vol. 65, no. 4, pp. 889–912, 1992.

[224] E. Zarkadoula *et al.*, "The nature of high-energy radiation damage in iron," *J. Phys. Condens. Matter*, vol. 25, no. 12, 2013.

[225] C. R. F. Azevedo, "A review on neutron-irradiation-induced hardening of metallic components," *Eng. Fail. Anal.*, vol. 18, no. 8, pp. 1921–1942, 2011.

[226] T. Diaz De La Rubia, R. S. Averback, H. Hsieh, and R. Benedek, "Molecular dynamics simulation of displacement cascades in Cu and Ni: Thermal spike behavior," *J. Mater. Res.*, vol. 4, no. 3, pp. 579–586, 1989.

[227] V. G. Kapinos and D. J. Bacon, "Influence of ion-electron interaction on the formation mechanism of depleted zones in displacement cascades in metals," *Phys. Rev. B*, vol. 50, no. 18, pp. 194–203, 1994.

[228] A. M. Rutherford and D. M. Duffy, "The effect of electron-ion interactions on radiation damage simulations," *J. Phys. Condens. Matter*, vol. 19, no. 49, 2007.

[229] A. De Backer, A. E. Sand, K. Nordlund, L. Luneville, D. Simeone, and S. L. Dudarev, "Subcascade formation and defect cluster size scaling in high-energy collision events in metals," *Epl*, vol. 115, no. 2, 2016.

[230] A. J. E. Foreman, W. J. Phythian, and C. A. English, "The molecular dynamics simulation of irradiation damage cascades in copper using a many-body potential," *Philos. Mag. A Phys. Condens. Matter, Struct. Defects Mech. Prop.*, vol. 66, no. 5, pp. 671–695, 1992.

[231] E. I. Suvorova *et al.*, "Energy dependent structure of Xe ion tracks in YBCO and the effect on the superconductive properties in magnetic fields," *Phys, J Appl*, vol. 126, p. 145106, 2019.

[232] A. . Motta, "Amorphization of intermetallic compounds under irradiation - A review," *J. Nucl. Mater.*, vol. 244, pp. 227–250, 1996.

[233] L. W. Hobbs, F. W. Clinard, S. J. Zinkle, and R. C. Ewing, "Radiation effects in ceramics," *J. Nucl. Mater.*, vol. 216, pp. 291–321, 1994.

[234] F. F. Morehead and B. L. Crowder, "Model for the formation of amorphous Si by ion bombardment," *Radiat. Eff.*, vol. 6, no. 1–2, pp. 27–32, 1970.

[235] J. F. Gibbons, "Ion implantation in semiconductors—Part II: Damage production and annealing," *Proc. IEEE*, vol. 60, no. 9, pp. 1062–1096, 1972.

[236] P. D. Edmondson, D. J. Riley, R. C. Birtcher, and S. E. Donnelly, "Amorphization of

crystalline Si due to heavy and light ion irradiation," *J. Appl. Phys.*, vol. 106, no. 4, 2009.

[237] Y. Zhu, Z. X. Cai, R. C. Budhani, M. Suenaga, and D. O. Welch, "Structures and effects of radiation damage in cuprate superconductors irradiated with several-hundred-MeV heavy ions," *Phys. Rev. B*, vol. 48, no. 9, pp. 6436–6450, 1993.

[238] J. C. Yang *et al.*, "High Intensity heavy ion Accelerator Facility (HIAF) in China," *Nucl. Instruments Methods Phys. Res. Sect. B Beam Interact. with Mater. Atoms*, vol. 317, no. PART B, pp. 263–265, 2013.

[239] G. Greaves, A. H. Mir, R. W. Harrison, M. A. Tunes, S. E. Donnelly, and J. A. Hinks, "New Microscope and Ion Accelerators for Materials Investigations (MIAMI-2) system at the University of Huddersfield," *Nucl. Instruments Methods Phys. Res. Sect. A Accel. Spectrometers, Detect. Assoc. Equip.*, vol. 931, no. December 2018, pp. 37–43, 2019.

[240] D. Kiener, C. Motz, M. Rester, M. Jenko, and G. Dehm, "FIB damage of Cu and possible consequences for miniaturized mechanical tests," *Mater. Sci. Eng. A*, vol. 459, pp. 262–272, 2007.

[241] M. C. Frischherz, M. A. Kirk, J. P. Zhang, and H. W. Weber, "Transmission electron microscopy of defect cascades in $YBa_2Cu_3O_{7-\delta}$ produced by ion irradiation," *Philos. Mag. A*, vol. 67, no. 6, pp. 1347–1363, 1993.

[242] J. Giapintzakis *et al.*, "Production and identification of flux-pinning defects by electron irradiation in $YBa_2Cu_3O_{7-x}$ single crystals," *Phys. Rev. B*, vol. 45, no. 18, pp. 10677–10683, 1992.

[243] M. J. Kramer, Q. Qian, D. Finnemore, and L. Snead, "Time evolved defects in proton-irradiated single-crystal $YBa_2Cu_3O_{7-\delta}$," *Phys. C*, vol. 203, pp. 83–90, 1992.

[244] R. Wheeler, M. a. Kirk, a. D. Marwick, L. Civale, and F. H. Holtzberg, "Columnar defects in $YBa_2Cu_3O_{7-\delta}$ induced by irradiation with high energy heavy ions," *Appl. Phys. Lett.*, vol. 63, no. 11, p. 1573, 1993.

[245] H. Watanabe, B. Kabius, K. Urban, B. Roas, S. Klaumünzer, and G. Saemann-Ischenko, "The influence of 173 MeV Xe-ion irradiation on the microstructure of $YBa_2Cu_3O_7$ thin films," *Phys. C Supercond. its Appl.*, vol. 179, no. 1–3, pp. 75–84, 1991.

[246] K. C. Russell and R. W. Powell, "Dislocation loop nucleation in irradiated metals," *Acta Metall.*, vol. 21, no. 3, pp. 187–193, 1973.

[247] S. J. Zinkle and C. Kinoshita, "Defect production in ceramics," *J. Nucl. Mater.*, vol. 251, no. 97, pp. 200–217, 1997.

[248] G. J. Clark, A. D. Marwick, F. Legoues, R. B. Laibowitz, R. Koch, and P. Madakson, "Radiation effects in thin films of high T_c superconductors," *Nucl. Instruments Methods Phys. Res. Sect. B Beam Interact. with Mater. Atoms*, vol. 32, no. 1–4, pp. 405–411, 1988.

[249] V. Hardy, D. Groult, M. Hervieu, J. Provost, B. Raveau, and S. Bouffard, "Latent track formation induced by high energy heavy ions in superconductive copper oxides," *Nucl.*

Inst. Methods Phys. Res. B, vol. 54, no. 4, pp. 472–481, 1991.

[250] M. Toulemonde, S. Bouffard, and F. Studer, "Swift heavy ions in insulating and conducting oxides: tracks and physical properties," *Nucl. Instruments Methods Phys. Res. B*, vol. 91, pp. 108–123, 1994.

[251] M. Gorley *et al.*, "The EUROfusion materials property handbook for DEMO in-vessel components—Status and the challenge to improve confidence level for engineering data," *Fusion Eng. Des.*, vol. 158, no. May, p. 111668, 2020.

[252] G. Mikhailova *et al.*, "Radiation resistance and generation of pinning centers in composite HTSC under heavy ion irradiation," *Phys. Status Solidi*, vol. 10, no. 4, pp. 677–680, 2013.

[253] M. C. Frischherz, M. A. Kirk, J. Farmer, L. R. Greenwood, and H. W. Weber, "Defect Cascades Produced by Neutron-Irradiation in $YBa_2Cu_3O_{7-\delta}$," *Phys. C-Superconductivity Its Appl.*, vol. 232, pp. 309–327, 1994.

[254] L. Civale *et al.*, "Reducing vortex motion in $YBa_2Cu_3O_7$ crystals with splay columnar defects," *Phys. Rev. B*, vol. 50, no. 6, pp. 4102–4105, 1994.

[255] Y. Yan and M. A. Kirk, "Observation and mechanism of local oxygen reordering induced by high-energy heavy-ion (U^+, Au^+, Xe^+) irradiation in the high-T_c superconductor $YBa_2Cu_3O_{7-\delta}$," *Phys. Rev. B*, vol. 57, no. 10, pp. 6152–6164, 1998.

[256] R. Biswal *et al.*, "Point defect creation by low fluence swift heavy ion irradiation-induced low energy electrons in $YBa_2Cu_3O_{7-y}$," *Supercond. Sci. Technol.*, vol. 21, p. 085016, 2008.

[257] D. Behera, T. Mohanty, S. K. Dash, T. Banerjee, D. Kanjilal, and N. C. Mishra, "Effect of secondary electrons from latent tracks created in YBCO by swift heavy ion irradiation," *Radiat. Meas.*, vol. 36, no. 1-6 SPEC., pp. 125–129, 2003.

[258] D. Bourgault *et al.*, "Modifications of the physical properties of the high-Tc superconductors $YBa_2Cu_3O_{7-\delta}$ by 3.5-GeV xenon ion bombardment," *Phys. Rev. B*, vol. 39, no. 10, pp. 6549–6554, 1989.

[259] H. Matsui *et al.*, "4-fold enhancement in the critical current density of $YBa_2Cu_3O_7$ films by practical ion irradiation," *Appl. Phys. Lett.*, vol. 101, no. 23, p. 232601, 2012.

[260] E. I. Suvorova *et al.*, "Structure analysis of the YBCO layer in Ag/YBCO/metal oxide buffer/Hastelloy composite tape before and after 107 MeV Kr^{17+} irradiation," *Acta Mater.*, vol. 75, pp. 71–79, 2014.

[261] A. M. Petrean, L. M. Paulius, Y. Yan, M. A. Kirk, W. K. Kwok, and G. W. Crabtree, "Thermal stability of correlated defects introduced by heavy ion irradiation in $YBa_2Cu_3O_{7-\delta}$," *Phys. Rev. B - Condens. Matter Mater. Phys.*, vol. 64, no. 13, pp. 1–5, 2001.

[262] Y. Yan, "Modulated structure and local oxygen reordering induced by high-energy Au-ion irradiation in $YBa_2Cu_3O_{7-}$," *Philos. Mag. Lett.*, vol. 73, no. 6, pp. 299–308, 1996.

[263] Y. Zhu, Z. X. Cm, and D. O. Welch, “Strain field and strain contrast of columnar defects in heavy-ion irradiated superconductors,” *Philos. Mag. A*, vol. 73, no. 1, pp. 1–10, 1996.

[264] Y. Yan and M. A. Kirk, “‘Nanotwin’ networks connecting columnar defects in $YBa_2Cu_3O_{7-\delta}$ and implications for magnetic vortex interactions,” *Philos. Mag. Lett.*, vol. 79, no. 10, pp. 841–848, 1999.

[265] M. A. Kirk, M. C. Frischherz, J. Z. Liuft, L. R. Greenwood, and J. Z. Liuft, “The structure of neutron-irradiation damage in $YBa_2Cu_3O_{7-x}$,” *Philos. Mag. Lett.*, vol. 62, no. 1, pp. 41–49, 1990.

[266] F. Vasiliu, V. Sandu, P. Nita, S. Popa, E. Cimpoiasu, and M. Carman Bunescu, “The role of radiation damage structure and fine scale precipitation in the pinning improvement of thermal neutron irradiated lithium floride-doped $YBa_2Cu_3O_{7-x}$,” *Phys. C*, vol. 303, pp. 209–219, 1998.

[267] Y. Zhang, M. W. Rupich, V. Solovyov, Q. Li, and A. Goyal, “Dynamic behavior of reversible oxygen migration in irradiated-annealed high temperature superconducting wires,” *Sci. Rep.*, vol. 10, no. 1, pp. 1–8, 2020.

[268] Y. Zhu, H. Zhang, M. Suenaga, and D. O. Welch, “Planar defects induced by heavy-ion irradiation,” *Philos. Mag. A Phys. Condens. Matter, Struct. Defects Mech. Prop.*, vol. 68, no. 5, pp. 1079–1089, 1993.

[269] H. W. Zandbergen, J. Kulik, and B. Nieuwendijk, “Limitations on the monitoring with electron microscopy of the formation of defects in $YBa_2Cu_3O_7$ by neutron irradiation,” *Phys. C Supercond. its Appl.*, vol. 179, pp. 43–51, 1991.

[270] M. F. Yan, R. L. Barns, H. M. O’Brtan, P. K. Gallagher, R. C. Sherwood, and S. Jin, “Water interaction with the superconducting $YBa_2Cu_3O_7$ phase,” *Appl. Phys. Lett.*, vol. 51, pp. 532–534, 1987.

[271] R. Janam *et al.*, “Electron microscopic investigations on neutron irradiated $YBa_2Cu_3O_{7-x}$ high temperature superconducting single crystals,” *Solid State Commun.*, vol. 77, no. 4, pp. 259–263, 1991.

[272] G. Van Tendeloo, M.-O. Ruault, H. Bernas, and M. Gasgnier, “High resolution electron microscopy of ion-irradiated $GdBa_2Cu_3O_7$,” *J. Mater. Res*, vol. 6, no. 4, pp. 677–681, 1991.

[273] H. Matsui *et al.*, “Enhancement of critical current density in $YBa_2Cu_3O_7$ films using a semiconductor ion implanter,” *J. Appl. Phys.*, vol. 117, no. 4, pp. 0–5, 2015.

[274] D. Huang *et al.*, “Enhancement in the critical current density of $BaTiO_3$-doped YBCO films by low-energy (60 keV) proton irradiation,” *Supercond. Sci. Technol.*, vol. 34, p. 045001, 2021.

[275] Y. Jia *et al.*, “Doubling the critical current density of high temperature superconducting coated conductors through proton irradiation,” *Appl. Phys. Lett.*, vol. 103, no. 12, 2013.

[276] J. R. Liu, J. Kulik, Y. J. Zhao, and W. K. Chu, “Radiation damage and flux pinning in high

temperature superconductors," *Nucl. Instruments Methods Phys. Res. Sect. B Beam Interact. with Mater. Atoms*, vol. 80–81, pp. 1255–1258, 1993.

[277] N. M. Strickland *et al.*, "Enhanced flux pinning in MOD second generation HTS wires by silver- and copper-ion irradiation," *IEEE Trans. Appl. Supercond.*, vol. 17, no. 2, pp. 3306–3309, 2007.

[278] M. Chudy, M. Eisterer, H. W. Weber, J. Veterníková, S. Sojak, and V. Slugeň, "Point defects in $YBa_2Cu_3O_{7-x}$ studied using positron annihilation," *Supercond. Sci. Technol.*, vol. 25, p. 075017, 2012.

[279] R. Prokopec, D. X. Fischer, H. W. Weber, and M. Eisterer, "Suitability of coated conductors for fusion magnets in view of their radiation response," *Supercond. Sci. Technol.*, vol. 28, p. 014005, 2015.

[280] J. R. Cost, J. O. Willis, J. D. Whompson, and D. E. Peterson, "Fast-neutron irradiation of $YBa_2Cu_3O_x$," *Phys. Rev. B*, vol. 37, no. 4, pp. 1563–1568, 1988.

[281] M. Chudy, Z. Zhong, M. Eisterer, and T. Coombs, "N-Values of commercial YBCO tapes before and after irradiation by fast neutrons," *Supercond. Sci. Technol.*, vol. 28, no. 3, 2015.

[282] H. W. Weber, "Flux pinning in neutron irradiated high-T_c single crystals," *Supercond. Sci. Technol.*, vol. 5, pp. S19–S24, 1992.

[283] M. Chudy, R. Fuger, M. Eisterer, and H. W. Weber, "Characterization of commercial YBCO coated conductors after neutron irradiation," *IEEE Trans. Appl. Supercond.*, vol. 21, no. 3 PART 3, pp. 3162–3165, 2011.

[284] N. M. Strickland *et al.*, "Flux pinning by discontinuous columnar defects in 74 MeV Ag-irradiated $YBa_2Cu_3O_7$ coated conductors," *Phys. C Supercond. its Appl.*, vol. 469, pp. 2060–2067, 2009.

[285] M. LeRoux *et al.*, "Rapid doubling of the critical current of $YBa_2Cu_3O_{7-\delta}$ coated conductors for viable high-speed industrial processing," *Appl. Phys. Lett.*, vol. 107, no. 19, 2015.

[286] N. M. Strickland *et al.*, "Effect of annealing high-dose heavy-ion irradiated high-temperature superconductor wires," *Nucl. Instruments Methods Phys. Res. Sect. B Beam Interact. with Mater. Atoms*, vol. 409, pp. 351–355, 2017.

[287] R. Unterrainer, D. X. Fischer, A. Lorenz, and M. Eisterer, "Recovering the performance of irradiated high-temperature superconductors for use in fusion magnets," *Supercond. Sci. Technol.*, vol. 35, no. 4, p. 04LT01, 2022.

[288] A. C. Bovik, "Chapter 1: Introduction to Digital Image Processing," in *The Essential Guide to Image Processing*, 2009, pp. 1–21.

[289] V. M. Potdar, H. Song, and C. Elizabeth, "A survey of digital image watermarking techniques," in *IEEE Third International Conference on Industrial Informatics (INDIN)*, 2005, pp. 709–716.

[290] W. Zhao, R. Chellappa, P. J. Phillips, and A. Rosenfeld, “Hierarchical ensemble of global and local classifiers for face recognition,” *ACM Comput. Surv.*, vol. 35, no. 4, pp. 399–458, 2003.

[291] A. Buades, B. Coll, and J. M. Morel, “A REVIEW OF IMAGE DENOISING ALGORITHMS, WITH A NEW ONE,” *MULTISCALE Model. SIMUL.*, vol. 4, no. 2, pp. 490–530, 2005.

[292] A. K. Hrechak and J. A. McHugh, “Automated fingerprint recognition using structural matching,” *Pattern Recognit.*, vol. 23, no. 8, pp. 893–904, 1990.

[293] G. K. Wallace, “THE JPEG STILL PICTURE COMPRESSION STANDARD,” *IEEE Trans. Consum. Electron.*, vol. 38, no. 1, 1992.

[294] Z. Wang and A. C. Bovik, “Why is image quality ASSESSMENT SO DIFFICULT ?,” *Quality*, pp. 3313–3316, 2002.

[295] Y. Liu, K. Gu, G. Zhai, X. Liu, D. Zhao, and W. Gao, “Quality assessment for real out-of-focus blurred images,” *J. Vis. Commun. Image Represent.*, vol. 46, pp. 70–80, 2017.

[296] H. . Sheikh, Z. Wang, L. Cormack, and A. C. Bovik, “LIVE image quality assessment database release 2,” 2006. [Online]. Available: http://live.ece.utexas.edu/research/quality.

[297] D. Ghadiyaram and A. C. Bovik, “Massive online crowdsourced study of subjective and objective picture quality,” *IEEE Trans. Image Process.*, vol. 25, no. 1, pp. 372–387, 2016.

[298] R. M. Haralick, I. Dinstein, and K. Shanmugam, “Textural Features for Image Classification,” *IEEE Trans. Syst. Man Cybern.*, vol. SMC-3, no. 6, pp. 610–621, 1973.

[299] R. M. Haralick, “Statistical and structural approaches to texture,” *Proc. IEEE*, vol. 67, no. 5, pp. 786–804, 1979.

[300] A. Humeau-Heurtier, “Texture feature extraction methods: A survey,” *IEEE Access*, vol. 7, pp. 8975–9000, 2019.

[301] M. M. Galloway, “Texture analysis using gray level run lengths,” *Comput. Graph. Image Process.*, vol. 4, no. 2, pp. 172–179, 1975.

[302] T. Ojala, M. Pietikäinen, and D. Harwood, “A comparative study of texture measures with classification based on feature distributions,” *Pattern Recognit.*, vol. 29, no. 1, pp. 51–59, 1996.

[303] L. P. Horwitz and J. Shelton, “Pattern Recognition Using Autocorrelation,” *Proc. IRE*, pp. 175–185, 1961.

[304] J. Zhang, J. Liang, and H. Zhao, “Local energy pattern for texture classification using self-adaptive quantization thresholds,” *IEEE Trans. Image Process.*, vol. 22, no. 1, pp. 31–42, 2013.

[305] G. Matheron, “Principles of Geostatistics,” *Econ. Geol.*, vol. 58, pp. 1246–1266, 1963.

[306] A. B. L. Larsen, J. S. Vestergaard, and R. Larsen, “HEp-2 cell classification using shape index histograms with donut-shaped spatial pooling,” *IEEE Trans. Med. Imaging*, vol. 33, no. 7, pp. 1573–1580, 2014.

[307] A. R. Backes, W. N. Gonçalves, A. S. Martinez, and O. M. Bruno, “Texture analysis and classification using deterministic tourist walk,” *Pattern Recognit.*, vol. 43, no. 3, pp. 685–694, 2010.

[308] A. Ramola, A. K. Shakya, and D. Van Pham, “Study of statistical methods for texture analysis and their modern evolutions,” *Eng. Reports*, vol. 2, no. 4, pp. 1–24, 2020.

[309] M. Tüceryan and A. K. Jain, “Texture Segmentation Using Voronoi Polygons,” *IEEE Trans. Pattern Anal. Mach. Intell.*, vol. 12, no. 2, pp. 211–216, 1990.

[310] D. Blostein and N. Ahuja, “Shape from Texture: Integrating Texture-Element Extraction and Surface Estimation,” *IEEE Trans. Pattern Anal. Mach. Intell.*, vol. 11, no. 12, pp. 1233–1251, 1989.

[311] X. Miao, H. Chu, H. Liu, Y. Yang, and X. Li, “Quality assessment of images with multiple distortions based on phase congruency and gradient magnitude,” *Signal Process. Image Commun.*, vol. 79, no. September 2018, pp. 54–62, 2019.

[312] L. Jia, C. Chen, S. Xu, and J. Shen, “Fabric defect inspection based on lattice segmentation and template statistics,” *Inf. Sci. (Ny).*, vol. 512, pp. 964–984, 2020.

[313] K. Y. Song, J. Kittler, and M. Petrou, “Defect detection in random colour textures,” *Image Vis. Comput.*, vol. 14, no. 9, pp. 667–683, 1996.

[314] L. Liu, Y. Hua, Q. Zhao, H. Huang, and A. C. Bovik, “Blind image quality assessment by relative gradient statistics and adaboosting neural network,” *Signal Process. Image Commun.*, vol. 40, pp. 1–15, 2016.

[315] A. Laine and J. Fan, “Texture Classification by Wavelet Packet Signatures,” *IEEE Trans. Pattern Anal. Mach. Intell.*, vol. 15, no. 11, pp. 1186–1191, 1993.

[316] L. Liu, B. Liu, H. Huang, and A. C. Bovik, “No-reference image quality assessment based on spatial and spectral entropies,” *Signal Process. Image Commun.*, vol. 29, no. 8, pp. 856–863, 2014.

[317] G. Van de Wouwer, P. Scheunders, and D. Van Dyck, “Statistical Texture Characterization from Discrete Wavelet Representations,” *IEEE Trans. Image Process.*, vol. 8, no. 4, pp. 592–598, 1999.

[318] L. Cohen, “Time-Frequency Distributions-A Review,” *Proc. IEEE*, vol. 77, no. 7, 1989.

[319] J. W. Cooley and J. W. Tukey, “An Algorithm for the Machine Calculation of Complex Fourier Series,” *Math. Comput.*, vol. 19, pp. 297–301, 1965.

[320] A. C. Bovik, “Chapter 5: Basic Tools for Image Fourier Analysis,” in *The Essential Guide to Image Processing*, 2009, pp. 97–121.

[321] F. Zhou, J. Feng, and Q. Shi, “Texture feature based on local fourier transform,” *IEEE Int. Conf. Image Process.*, vol. 2, pp. 610–613, 2001.

[322] B. Josso, D. R. Burton, and M. J. Lalor, “Texture orientation and anisotropy calculation by Fourier transform and Principal Component Analysis,” *Mech. Syst. Signal Process.*, vol. 19, no. 5, pp. 1152–1161, 2005.

[323] N. Ahmed, T. Natarajan, and K. R. Rao, “Discrete Cosine Transform,” *IEEE Trans. Comput.*, pp. 90–93, 1974.

[324] C. Florea, M. Gordan, B. Orza, and A. Vlaicu, “Compressed Domain Computationally Efficient Processing Scheme for JPEG Image Filtering,” *Adv. Eng. Forum*, vol. 8–9, no. March 2016, pp. 480–489, 2013.

[325] A. Haar, “Zur Theorie der orthogonalen Funktionensysteme,” *Math. Ann.*, vol. 69, pp. 331–371, 1910.

[326] K. Amolins, Y. Zhang, and P. Dare, “Wavelet based image fusion techniques - An introduction, review and comparison,” *ISPRS J. Photogramm. Remote Sens.*, vol. 62, no. 4, pp. 249–263, 2007.

[327] J. N. Bradley, C. M. Brislawn, and T. Hopper, “FBI wavelet/scalar quantization standard for gray-scale fingerprint image compression,” *Vis. Inf. Process. II*, vol. 1961, pp. 293–304, 1993.

[328] B. E. Usevitch, “A tutorial on modern lossy wavelet image compression: Foundations of JPEG 2000,” *IEEE Signal Process. Mag.*, vol. 18, no. 5, pp. 22–35, 2001.

[329] L. Zhang and P. Bao, “Edge detection by scale multiplication in wavelet domain,” *Pattern Recognit. Lett.*, vol. 23, no. 14, pp. 1771–1784, 2002.

[330] J. B. Weaver, Y. Xu, D. M. Healy, and L. D. Cromwell, “Filtering noise from images with wavelet transforms,” *Magn. Reson. Med.*, vol. 21, no. 2, pp. 288–295, 1991.

[331] R. B. Gomez, A. Jazaeri, and M. Kafatos, “Wavelet-based hyperspectral and multispectral image fusion,” *Geo-Spatial Image Data Exploit. II*, vol. 4383, pp. 36–42, 2001.

[332] A. Graps, “An Introduction to Wavelets,” *IEEE Comput. Sci. Eng.*, vol. 2, no. 2, pp. 50–61, 1995.

[333] I. Daubechies, “Orthonormal bases of compactly supported wavelets,” *Commun. Pure Appl. Math.*, vol. 41, no. 7, pp. 909–996, 1988.

[334] I. Daubechies, “The Wavelet Transform, Time-Frequency Localization and Signal Analysis,” *IEEE Trans. Inf. Theory*, vol. 36, no. 5, pp. 961–1005, 1990.

[335] M. Vetterli, “Multi-dimensional sub-band coding: Some theory and algorithms,” *Signal Processing*, vol. 6, no. 2. pp. 97–112, 1984.

[336] Z. Xiong and K. Ramchandran, “Chapter 18: Wavelet Image Compression,” in *The Essential Guide to Image Processing*, 1st ed., Elsevier, 2009, pp. 463–493.

[337] S. Zope-Chaudhari, P. Venkatachalam, and K. M. Buddhiraju, “Assessment of distortion in watermarked geospatial vector data using different wavelets,” *Geo-Spatial Inf. Sci.*, vol. 18, no. 2–3, pp. 124–133, 2015.

[338] P. J. Burt and E. H. Adelson, “The Laplacian Pyramid as a Compact Image Code,” *IEEE Trans. Commun.*, vol. COM-31, no. 4, pp. 532–540, 1983.

[339] D. D. Y. Po and M. N. Do, “Directional multiscale modeling of images using the contourlet transform,” *IEEE Work. Stat. Signal Process. Proc.*, vol. 15, no. 6, pp. 1610–1620, 2006.

[340] K. I. Laws, “Textured Image Segmentation,” University of Southern California, 1980.

[341] D. Gabor, “A Theory of Communication. Part 1. The Analysis of Information,” *J. Inst. Electr. Eng. - Part III Radio Commun. Eng.*, vol. 93, no. 26, pp. 429–441, 1945.

[342] J. He, H. Ji, and X. Yang, “Rotation Invariant Texture Descriptor Using Local Shearlet-Based Energy Histograms,” *IEEE Signal Process. Lett.*, vol. 20, no. 9, pp. 905–908, 2013.

[343] L. Liu, H. Dong, H. Huang, and A. C. Bovik, “No-reference image quality assessment in curvelet domain,” *Signal Process. Image Commun.*, vol. 29, no. 4, pp. 494–505, 2014.

[344] B. Mandelbrot, “How long is the coast of Britain? Statistical self-similarity and fractional dimension,” *Science (80-.).*, vol. 156, no. 3775, pp. 636–638, 1967.

[345] J. Mao and A. K. Jain, “Texture classification and segmentation using multiresolution simultaneous autoregressive models,” *Pattern Recognit.*, vol. 25, no. 2, pp. 173–188, 1992.

[346] R. Chellappa and R. L. Kashyap, “Texture Synthesis Using 2-D Noncausal Autoregressive Models,” *194 IEEE Trans. Acoust. SPEECH, SIGNAL Process.*, vol. 33, no. 1, pp. 194–203, 1985.

[347] J. J. De Mesquita Sá Junior and A. Ricardo Backes, “A simplified gravitational model to analyze texture roughness,” *Pattern Recognit.*, vol. 45, no. 2, pp. 732–741, 2012.

[348] A. R. Backes, D. Casanova, and O. M. Bruno, “Texture analysis and classification: A complex network-based approach,” *Inf. Sci. (Ny).*, vol. 219, pp. 168–180, 2013.

[349] F. Liu, R. W. Picard, and E. C. Society, “Peropdicity, Directionality, and Randomness: Wold Features for Image Modeling and Retrieval,” *IEEE Trans. Pattern Anal. Mach. Intell.*, vol. 18, no. 7, pp. 722–733, 1996.

[350] A. Rosenfeld, “Mosaic Models for Textures,” *IEEE Trans. Pattern Anal. Mach. Intell.*, vol. PAMI-3, no. 1, pp. 1–11, 1981.

[351] R. F. Thompson, *The brain: a neuroscience primer*. New York: Freeman and Co, 1993.

[352] I. A. Basheer and M. Hajmeer, “Artificial neural networks: fundamentals, computing, design, and application,” *J. Microbiol. Methods*, vol. 43, pp. 3–31, 2000.

[353] V. Andrearczyk and P. F. Whelan, “Using filter banks in Convolutional Neural Networks

for texture classification," *Pattern Recognit. Lett.*, vol. 84, pp. 63–69, 2016.

[354] S. Fujieda, K. Takayama, and T. Hachisuka, "Wavelet Convolutional Neural Networks for Texture Classification," 2017.

[355] H. Zhang, J. Xue, and K. Dana, "Deep TEN Poster : Texture Encoding Network Encoding Layer :," *Cvpr*, p. 2016, 2017.

[356] C. . Shannon, "A Mathematical Theory of Communication," *Bell Syst. Tech. J.*, vol. 27, pp. 379–423, 1948.

[357] H. Azami, J. Escudero, and A. Humeau-Heurtier, "Bidimensional Distribution Entropy to Analyze the Irregularity of Small-Sized Textures," *IEEE Signal Process. Lett.*, vol. 24, no. 9, pp. 1338–1342, 2017.

[358] G. Liu and X. Zheng, "Fabric defect detection based on information entropy and frequency domain saliency," *Vis. Comput.*, vol. 37, no. 3, pp. 515–528, 2021.

[359] M. E. Jernigan and F. D'astous, "Entropy-Based Texture Analysis in the Spatial Frequency Domain," *IEEE Trans. Pattern Anal. Mach. Intell.*, vol. PAMI-6, no. 2, pp. 237–243, 1984.

[360] E. Avci, "Comparison of wavelet families for texture classification by using wavelet packet entropy adaptive network based fuzzy inference system," *Appl. Soft Comput. J.*, vol. 8, no. 1, pp. 225–231, 2008.

[361] M. Ribeiro *et al.*, "The entropy universe," *Entropy*, vol. 23, no. 2, pp. 1–35, 2021.

[362] J. N. Kapur and H. K. Kesavan, "Entropy Optimization Principles and Their Applications," in *Entropy and Energy Dissipation in Water Resources*, vol. 9, Springer, 1992, pp. 3–20.

[363] J. W. Sleigh, D. A. Steyn-Ross, M. L. Steyn-Ross, C. Grant, and G. Ludbrook, "Cortical entropy changes with general anaesthesia: Theory and experiment," *Physiol. Meas.*, vol. 25, no. 4, pp. 921–934, 2004.

[364] A. K. Moorthy and A. C. Bovik, "Visual Importance Pooling for Image Quality Assessment," *IEEE J. Sel. Top. Signal Process.*, vol. 3, no. 2, pp. 193–201, 2009.

[365] A. K. Moorthy and A. C. Bovik, "A two-stage framework for blind image quality assessment," *Proc. - Int. Conf. Image Process. ICIP*, vol. 17, no. 5, pp. 2481–2484, 2010.

[366] Y. Cui, "No-reference image quality assessment based on dual-domain feature fusion," *Entropy*, vol. 22, no. 3, 2020.

[367] S. Gabarda and G. Cristóbal, "Blind image quality assessment through anisotropy," *J. Opt. Soc. Am. A*, vol. 24, no. 12, p. B42, 2007.

[368] W. . Williams, M. . Brown, and A. . Hero, "Uncertainty, information and time-frequency distributions," *Adv. Signal Process. Algorithms, Archit. Implementations II*, vol. 1566, pp. 144–156, 1991.

[369] A. Rényi, *ON MEASURES OF ENTROPY AND INFORMATION*. California, CA, USA: The

Regents of the University of California, 1961.

[370] K. Gu, W. Lin, G. Zhai, X. Yang, W. Zhang, and C. W. Chen, “No-Reference Quality Metric of Contrast-Distorted Images Based on Information Maximization,” *IEEE Trans. Cybern.*, vol. 47, no. 12, pp. 4559–4565, 2017.

[371] M. J. Hÿtch, E. Snoeck, and R. Kilaas, “Quantitative measurement of displacement and strain fields from HREM micrographs,” *Ultramicroscopy*, vol. 74, no. 3, pp. 131–146, 1998.

[372] J. . Nye, *Physical properties of crystals: their representation by tensors and matrices*. Oxford : Clarendon Press Publication, 1957.

[373] B. Li, H. Liu, X. Lu, L. Kang, Y. Sheng, and A. Xiong, “Atomic configurations of basal stacking faults and dislocation loops in GaN irradiated with Xe^{20+} ions at room temperature,” *Appl. Surf. Sci.*, vol. 486, no. February, pp. 15–21, 2019.

[374] F. Liu, C. Zhang, C. He, H. S. Zhou, F. Ding, and G. N. Luo, “Characterization of radiation defects in quasi-homogeneously damaged tungsten by PALS and TEM,” *Nucl. Instruments Methods Phys. Res. Sect. B Beam Interact. with Mater. Atoms*, vol. 439, no. August 2018, pp. 17–21, 2019.

[375] S. Park *et al.*, “Swift heavy ion irradiation-induced amorphization of $La_2Ti_2O_7$,” *Nucl. Instruments Methods Phys. Res. Sect. B Beam Interact. with Mater. Atoms*, vol. 326, pp. 145–149, 2014.

[376] I. Nikishin, R. Dulimov, G. Skryabin, S. Galetsky, E. Tchevkina, and D. Bagrov, “ScanEV – A neural network-based tool for the automated detection of extracellular vesicles in TEM images,” *Micron*, vol. 145, no. August 2020, p. 103044, 2021.

[377] C. K. Groschner, C. Choi, and M. C. Scott, “Machine Learning Pipeline for Segmentation and Defect Identification from High-Resolution Transmission Electron Microscopy Data,” *Microsc. Microanal.*, pp. 1–8, 2021.

[378] A. A. Ezzat and M. Bedewy, “Machine learning for revealing spatial dependence among nanoparticles: Understanding catalyst film dewetting via gibbs point process models,” *J. Phys. Chem. C*, vol. 124, no. 50, pp. 27479–27494, 2020.

[379] C. M. Anderson, J. Klein, H. Rajakumar, C. D. Judge, and L. K. Béland, “Automated Detection of Helium Bubbles in Irradiated X-750,” *Ultramicroscopy*, vol. 217, no. July, p. 113068, 2020.

[380] G. D. Brittles, T. Mousavi, C. R. M. Grovenor, C. Aksoy, and S. C. Speller, “Persistent current joints between technological superconductors,” *Supercond. Sci. Technol.*, vol. 28, no. 9, 2015.

[381] H. Li and L. Salamanca-Riba, “The concept of high angle wedge polishing and thickness monitoring in TEM sample preparation,” *Ultramicroscopy*, vol. 88, no. 3, pp. 171–178, 2001.

[382] N. Ünlü, “Preparation of high quality Al TEM specimens via a double-jet electropolishing technique,” *Mater. Charact.*, vol. 59, pp. 547–553, 2008.

[383] A. Reza and P. R. Swann, “Precision Ion Polishing System -A New Instrument for TEM Specimen Preparation of Materials,” *MRS Proc.*, vol. 254, 1991.

[384] R. M. Langford and A. K. Petford-Long, “Preparation of transmission electron microscopy cross-section specimens using focused ion beam milling,” *J. Vac. Sci. Technol. A Vacuum, Surfaces, Film.*, vol. 19, no. 5, pp. 2186–2193, 2001.

[385] S. Lozano-Perez, “A guide on FIB preparation of samples containing stress corrosion crack tips for TEM and atom-probe analysis,” *Micron*, vol. 39, no. 3, pp. 320–328, 2008.

[386] S. Rubanov and P. R. Munroe, “FIB-induced damage in silicon,” *J. Microsc.*, vol. 214, no. 3, pp. 213–221, 2004.

[387] J. Mayer, L. a Giannuzzi, T. Kamino, and J. Michael, “TEM Sample Preparation and FIB-Induced Damage,” *MRS Bull.*, vol. 32, pp. 400–407, 2007.

[388] J. Liu *et al.*, “In-situ TEM study of irradiation-induced damage mechanisms in monoclinic-ZrO_2,” *Acta Mater.*, vol. 199, pp. 429–442, 2020.

[389] D. B. Williams and C. B. Carter, *Transmission Electron Microscopy: A Textbook for Materials Science*. Springer, 2009.

[390] L. Reimer and H. Kohl, *Transmission Electron Microscopy Physics of Image Formation, Fifth Edition*, Fifth. New York: Springer Verlag, 2008.

[391] P. D. Nellist and S. J. Pennycook, *The principles and interpretation of annular dark-field Z-contrast imaging*, vol. 113. Elsevier, 2000.

[392] S. J. Pennycook, “Z-contrast stem for materials science,” *Ultramicroscopy*, vol. 30, no. 1–2, pp. 58–69, 1989.

[393] E. Abe, “Electron microscopy of quasicrystals – where are the atoms?,” *Chem. Soc. Rev.*, vol. 41, no. 20, pp. 6787–6798, 2012.

[394] Z. Li, *Scanning transmission electron microscopy studies of mono- and bimetallic nanoclusters*, 1st ed., vol. 3, no. 1. Elsevier Ltd, 2012.

[395] J. F. Ziegler, M. D. Ziegler, and J. P. Biersack, “SRIM - The stopping and range of ions in matter (2010),” *Nucl. Instruments Methods Phys. Res. Sect. B Beam Interact. with Mater. Atoms*, vol. 268, no. 11–12, pp. 1818–1823, 2010.

[396] A. De Backer, K. H. W. van den Bos, W. Van den Broek, J. Sijbers, and S. Van Aert, “StatSTEM: An efficient approach for accurate and precise model-based quantification of atomic resolution electron microscopy images,” *Ultramicroscopy*, vol. 171, no. 2016, pp. 104–116, 2016.

[397] D. E. Jesson and S. J. Pennycook, “Incoherent imaging of crystals using thermally scattered electrons,” *Proc. R. Soc. London. Ser. A. Math. Phys. Sci. A*, vol. 449, pp. 273–

293, 1995.

[398] P. D. Nellist and S. J. Pennycook, “Direct imaging of the atomic configuration of ultradispersed catalysts,” *Science (80-.).*, vol. 274, no. 5286, pp. 413–415, 1996.

[399] L. Jones *et al.*, “Smart Align—a new tool for robust non-rigid registration of scanning microscope data,” *Adv. Struct. Chem. Imaging*, vol. 1, no. 8, pp. 1–16, 2015.

[400] A. Khoryushin, “Improvement of current-carrying capabilities of high- temperature superconducting thin films and heterostructures,” Denmark: Technical University of Denmark (Department of Physics), 2011.

[401] J. S. Lim, *Two-Dimensional Signal and Image Processing*. Englewood Cliffs, NJ, Prentice Hall, 1990.

[402] D. R. G. Mitchell, “Create image from ROI,” 2009. [Online]. Available: http://www.dmscripting.com/create_image_from_roi.html.

[403] V. Selvamanickam *et al.*, “Enhanced and uniform in-field performance in long (Gd, Y)-Ba-Cu-O tapes with zirconium doping fabricated by metal-organic chemical vapor deposition,” *Supercond. Sci. Technol.*, vol. 23, p. 014014, 2010.

[404] M. A. Kirk, “Structure and flux pinning properties of irradiation defects in $YBa_2Cu_3O_{7-x}$,” *Cryogenics (Guildf).*, vol. 33, no. 3, pp. 235–242, 1993.

[405] M. L. Jenkins, “Characterisation of radiation-damage microstructures by TEM,” *J. Nucl. Mater.*, vol. 216, no. C, pp. 124–156, 1994.

[406] Z. L. Wang and J. M. Cowley, “Dynamic theory of high-angle annular-dark-field stem lattice images for a Ge/Si interface,” *Ultramicroscopy*, vol. 32, pp. 275–289, 1990.

[407] J. M. Cowley and Y. Huang, “De-channelling contrast in annular dark-field STEM,” *Ultramicroscopy*, vol. 40, no. 2, pp. 171–180, 1992.

[408] D. Simeone, J. M. Costantini, L. Luneville, L. Desgranges, P. Trocellier, and P. Garcia, “Characterization of radiation damage in ceramics: Old challenge new issues?,” *J. Mater. Res.*, vol. 30, no. 09, pp. 1495–1515, 2015.

[409] A. Panghal, Y. Kumar, P. K. Kulriya, P. M. Shirage, and N. L. Singh, “Structural assessment and irradiation response of $La_2Zr_2O_7$ pyrochlore: Impact of irradiation temperature and ion fluence,” *J. Alloys Compd.*, vol. 862, p. 158556, 2021.

[410] Y. Zhang, J. Lian, C. M. Wang, W. Jiang, R. C. Ewing, and W. J. Weber, “Ion-induced damage accumulation and electron-beam-enhanced recrystallization in $SrTiO_3$,” *Phys. Rev. B - Condens. Matter Mater. Phys.*, vol. 72, no. 9, pp. 1–8, 2005.

[411] F. Schrempel, T. Gischkat, H. Hartung, E. B. Kley, and W. Wesch, “Ion beam enhanced etching of $LiNbO_3$,” *Nucl. Instruments Methods Phys. Res. Sect. B Beam Interact. with Mater. Atoms*, vol. 250, no. 1-2 SPEC. ISS., pp. 164–168, 2006.

[412] W. J. Weber and L. M. Wang, “The temperature dependence of ion-beam-induced

amorphization in β-SiC," *Nucl. Inst. Methods Phys. Res. B*, vol. 106, no. 1–4, pp. 298–302, 1995.

[413] W. Gong, L. Wang, R. Ewing, and J. Zhang, "Electron-irradiation- and ion-beam-induced amorphization of coesite," *Phys. Rev. B - Condens. Matter Mater. Phys.*, vol. 54, no. 6, pp. 3800–3808, 1996.

[414] W. J. Weber, "Models and mechanisms of irradiation-induced amorphization in ceramics," *Nucl. Instruments Methods Phys. Res. Sect. B Beam Interact. with Mater. Atoms*, vol. 166, pp. 98–106, 2000.

[415] M. L. Swanson, J. R. Parsons, and C. W. Hoelke, "Damaged regions in neutron-irradiated and ion-bombarded Ge and Si," *Radiat. Eff.*, vol. 9, no. 3–4, pp. 249–256, 1971.

[416] J. Freidberg, *Plasma Physics and Fusion Energy*, vol. 1. 2007.

[417] H. M. Rietveld, "A profile refinement method for nuclear and magnetic structures," *J. Appl. Crystallogr.*, vol. 2, no. 2, pp. 65–71, 1969.

[418] J. M. Cowley, "Electron nanodiffraction methods for measuring medium-range order," *Ultramicroscopy*, vol. 90, pp. 197–206, 2002.

[419] R. J. Nicholls *et al.*, "Understanding irradiation damage in technological high temperature superconductors using high resolution x-ray absorption spectroscopy [Manuscript submitted for publication]," 2022.

[420] J. Kwon *et al.*, "Extended electronic structure inhomogeneity created by double chain layer defects surrounding columnar tracks in heavy-ion irradiated $YBa_2Cu_3O_{7-\delta}$," *Supercond. Sci. Technol.*, vol. 31, p. 105006, 2018.

[421] S. T. Murphy, "A point defect model for $YBa_2Cu_3O_7$ from density functional theory," *J. Phys. Commun.*, vol. 4, no. 11, p. 115003, 2020.

[422] G. M. Lopez, A. Filippetti, M. Mantega, and V. Fiorentini, "First-principles calculation of electronic and structural properties of $YBa_2Cu_3O_{6+y}$," *Phys. Rev. B - Condens. Matter Mater. Phys.*, vol. 82, no. 19, pp. 1–13, 2010.

[423] P. Budzyński, M. Kamiński, Z. Surowiec, M. Wiertel, V. A. Skuratov, and E. A. Koroneeva, "Effects of xenon-ion irradiation on the tribological properties and crystal structure of titanium and its alloy Ti_6Al_4V," *Tribol. Int.*, vol. 156, no. September 2020, 2021.

[424] N. V. Gushchina *et al.*, "Effect of Medium-Energy Ar+ Ion Irradiation on the Structure of Austenitic Chromium–Nickel Steel," *Phys. Met. Metallogr.*, vol. 122, no. 3, pp. 307–313, 2021.

[425] N. R. Jitkar *et al.*, "Effects of 6 MeV energy electrons on lattice parameters of $CaSO_4$:Eu nanophosphor," *AIP Conf. Proc.*, vol. 2335, no. March, 2021.

[426] M. N. Mirzayev *et al.*, "Investigation of the formation of defects under fast neutrons and gamma irradiation in 3C–SiC nano powder," *Phys. B Condens. Matter*, vol. 611, no.

October 2020, p. 412842, 2021.

[427] J. Veterníková *et al.*, "Positron annihilation lifetime spectroscopy study of neutron irradiated high temperature superconductors $YBa_2Cu_3O_{7-\delta}$ for application in fusion facilities," *J. Fusion Energy*, vol. 31, no. 1, pp. 89–95, 2012.

[428] J. Emhofer, M. Eisterer, and H. W. Weber, "Stress dependence of the critical currents in neutron irradiated (RE)BCO coated conductors," *Supercond. Sci. Technol.*, vol. 26, no. 3, p. 035009, 2013.

[429] K. E. Sickafus *et al.*, "Neutron-radiation-induced flux pinning in Gd-doped $YBa_2Cu_3O_{7-x}$ and $GdBa_2Cu_3O_{7-x}$," *Phys. Rev. B*, vol. 46, no. 18, pp. 11862–11870, 1992.

[430] W. J. Weber *et al.*, "Radiation effects in crystalline ceramics for the immobilization of high-level nuclear waste and plutonium," *J. Mater. Res.*, vol. 13, no. 6, pp. 1434–1484, 1998.

[431] M. R. Daymond, M. A. M. Bourke, and R. B. Von Dreele, "Use of Rietveld refinement to fit a hexagonal crystal structure in the presence of elastic and plastic anisotropy," *J. Appl. Phys.*, vol. 85, no. 2, pp. 739–747, 1999.

[432] R. Kingslake and R. Barry Johnson, "Chapter-4---Aberration-Theory," in *Lens Design Fundamentals*, Academic Press, 2010, pp. 101–135.

[433] M. Haider, S. Uhlemann, and J. Zach, "Upper limits for the residual aberrations of a high-resolution aberration-corrected STEM," *Ultramicroscopy*, vol. 81, no. 3–4, pp. 163–175, 2000.

[434] M. Nord, P. E. Vullum, I. MacLaren, T. Tybell, and R. Holmestad, "Atomap: a new software tool for the automated analysis of atomic resolution images using two-dimensional Gaussian fitting," *Adv. Struct. Chem. Imaging*, vol. 3, no. 1, pp. 1–12, 2017.

[435] A. Goshtasby, L. Staib, C. Studholme, and D. Terzopoulos, "Nonrigid image registration: Guest editors' introduction," *Comput. Vis. Image Underst.*, vol. 89, no. 2–3, pp. 109–113, 2003.

[436] S. Uhlemann and M. Haider, "Residual wave aberrations in the first spherical aberration corrected transmission electron microscope," *Ultramicroscopy*, vol. 72, no. 3–4, pp. 109–119, 1998.

[437] A. Kolmogorov, "Sulla Determinazione Empirica di una Legge di Distributione," *G. dell'Istituto Ital. degli Attuari*, vol. 4, pp. 1–11, 1933.

[438] N. Smirnoff, "Sur les écarts de la courbe de distribution empirique," *Mat. Sb.*, vol. 48, no. 1, pp. 3–26, 1939.

[439] S. William, "The probable error of a mean," *Biometrika*, vol. 6.1, pp. 1–25, 1908.

[440] L. V Manderscheid, "Significance Levels-0.05, 0.01, or?," *J. Farm Econ.*, vol. 47, no. 5, pp. 1381–1385, 1965.

[441] O. Camara, M. A. Tunes, G. Greaves, A. H. Mir, S. Donnelly, and J. A. Hinks, "Understanding amorphization mechanisms using ion irradiation in situ a TEM and 3D damage reconstruction," *Ultramicroscopy*, vol. 207, no. August, p. 112838, 2019.

[442] P. D. Edmondson *et al.*, "An in situ transmission electron microscopy study of the ion irradiation induced amorphisation of silicon by He and Xe," *Scr. Mater.*, vol. 113, pp. 190–193, 2016.

[443] S. Ríos, E. K. H. Salje, M. Zhang, and R. C. Ewing, "Amorphization in zircon: Evidence for direct impact damage," *J. Phys. Condens. Matter*, vol. 12, no. 11, pp. 2401–2412, 2000.

[444] S. Vassilvitskii and A. David, "K-means++: The Advantages of Careful Seeding," in *SODA '07: Proceedings of the Eighteenth Annual ACM-SIAM Symposium on Discrete Algorithms*, 2007, pp. 1027–1035.

[445] P. Bindu and S. Thomas, "Estimation of lattice strain in ZnO nanoparticles: X-ray peak profile analysis," *J. Theor. Appl. Phys.*, vol. 8, no. 4, pp. 123–134, 2014.

[446] M. C. Bryson, "Heavy-Tailed Distributions: Properties and Tests," *Technometrics*, vol. 16, no. 1, pp. 61–68, 1974.

[447] J. H. McCulloch, "Simple consistent estimators of stable distribution parameters," *Commun. Stat. - Simul. Comput.*, vol. 15, no. 4, pp. 1109–1136, 1986.

[448] S. Wold, K. Esbensen, and P. Geladi, "Principal Component Analysis," *Chemom. Intell. Lab. Syst.*, vol. 2, pp. 37–52, 1987.

Appendices

Appendix A Chapter 4 Supplementary Information

i. Ar-irradiated HRTEM images

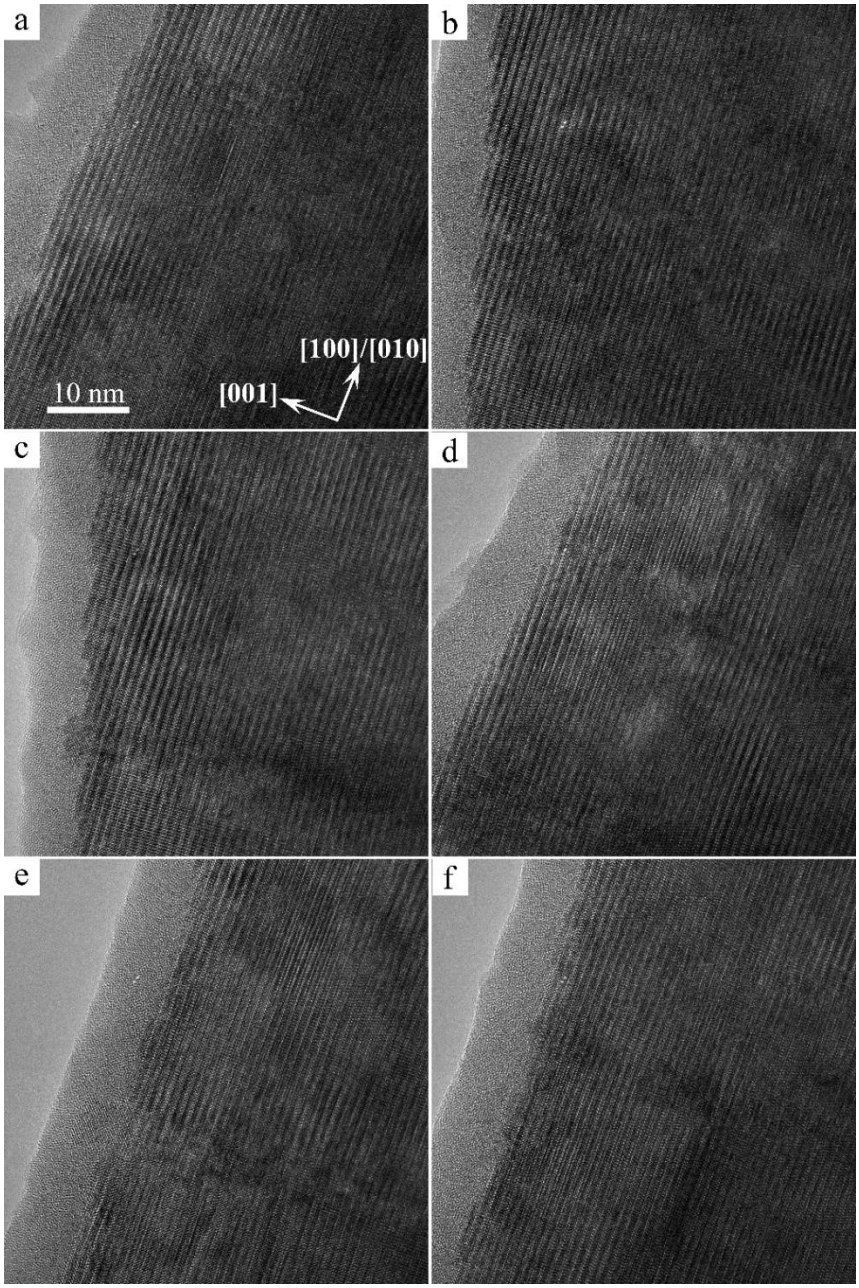


Figure S- 1: (a-f) HRTEM images taken along [100]/[010] from Ar-irradiated samples. The irradiation took place at room temperature, accelerating voltage of 350 kV, and a fluence of 1×10^{13} cm^{-2}.

ii. Xe-ions pre- and post-irradiation HRTEM images

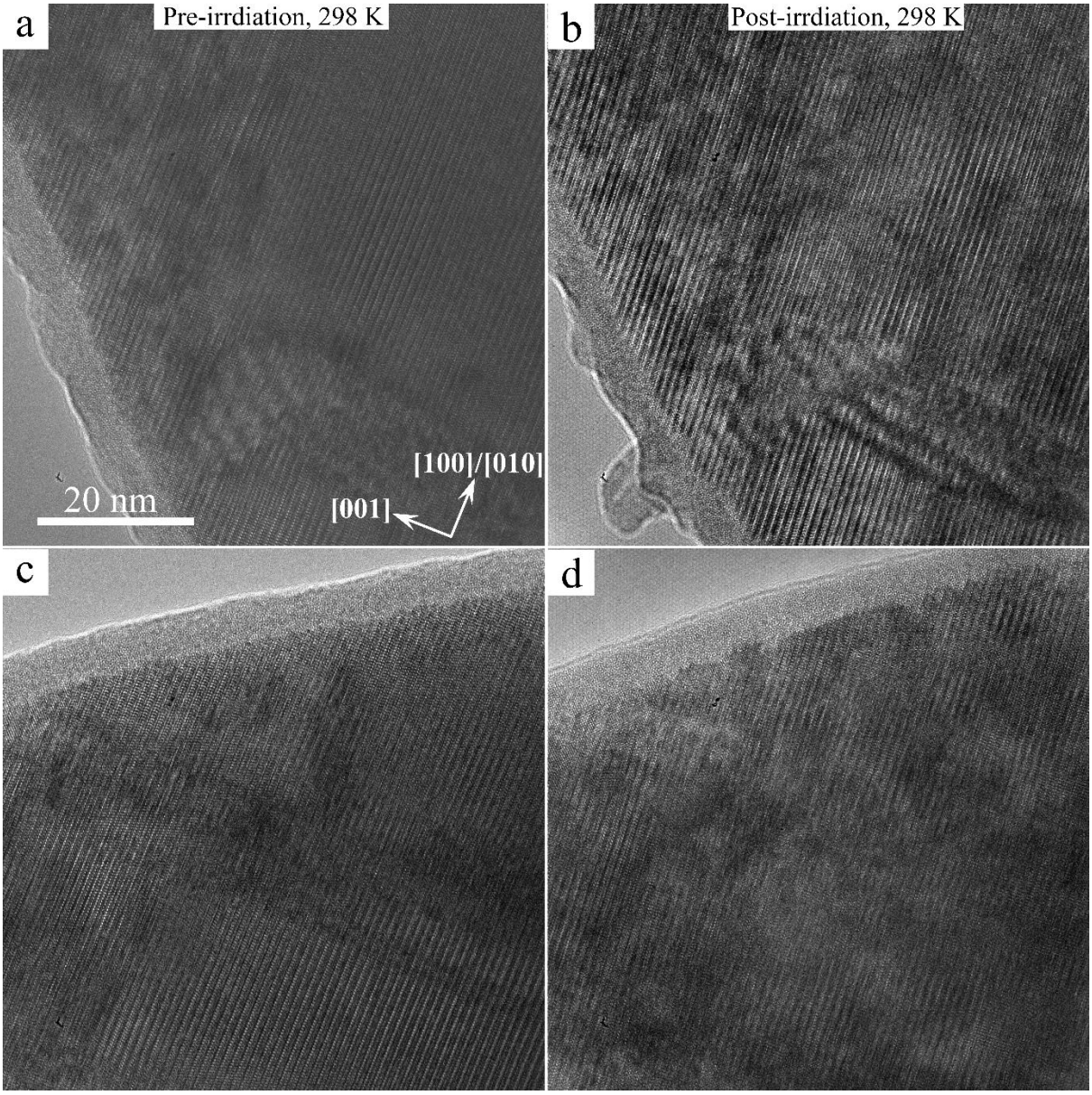


Figure S- 2: Direct HRTEM image comparison, taken along [100]/[010], from pre- (a,c) and post- (b,d) Xe-irradiation. The irradiation took place at room temperature, 350 kV accelerating voltage to a fluence of 7×10^{12} cm^{-2}. The images were taken from exactly the same region under the same microscope imaging conditions, i.e. 800 K magnification, ZA, and 200 kV accelerating voltage.

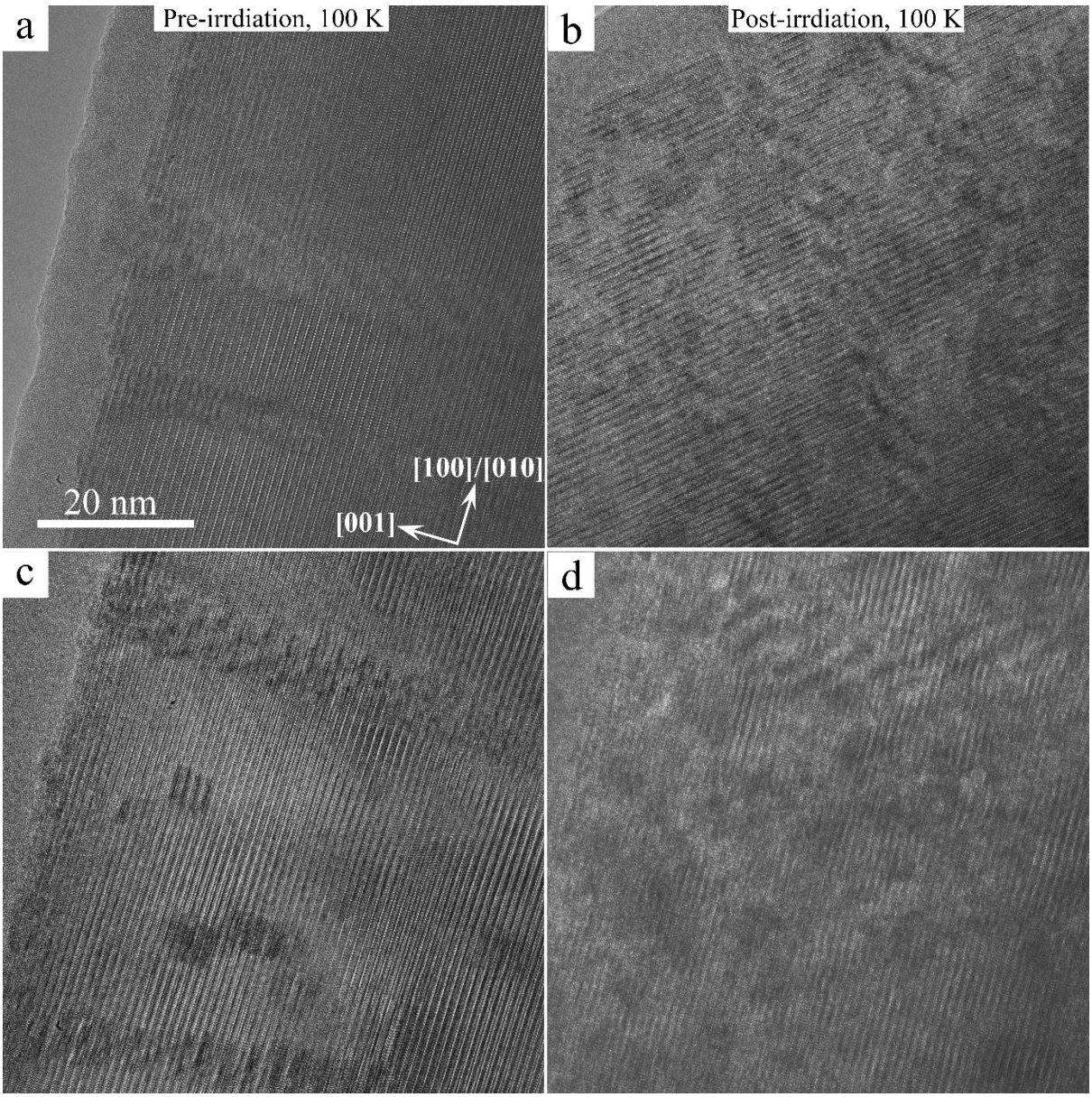


Figure S- 3: Direct HRTEM image comparison, taken along [100]/[010], from pre- (a,c) and post- (b,d) Xe-irradiation. The irradiation took place at 100 K, 350 kV accelerating voltage to a fluence of 7×10^{12} cm^{-2}. The images were taken from exactly the same region under the same microscope imaging conditions, i.e. 800 K magnification, ZA, and 200 kV accelerating voltage.

Appendix B Chapter 5 Supplementary Information

i. REBCO cation sublattice distance fractions

Table S- 1: Intra-cell distances, as a fraction of c-axis lattice parameters, for the different samples analysed in this thesis. Ne- and Ar-irradiated images were collected using the ARM200f microscope and the rest were captured using the ARM300CF microscope.

Sample type	Pristine	Neutrons	He	Xe (T =100 K)	Xe (T = 298 K)	Ne	Ar
Ba_1 - RE	0.319	0.318	0.316	0.309	0.309	0.324	0.320
RE - Ba_2	0.317	0.318	0.317	0.308	0.308	0.324	0.321

ii. Analysis of full width half maximum (FWHM) in pristine and irradiated samples

Table S- 2: Full width half maximum (FWHM) of unit cells lattice parameters along a/b- and c-axis for pristine, neutron-irradiated, and He-irradiated samples. The values were extracted from histograms of individual unit cells values. The results are presented in two different units: (1) in angstroms, (2) in 2ϑ, which is usual for XRD results. For the latter, the angstrom units where converted to degrees using Cu(K)-α wavelength of 1.5406 Å and Bragg's law.

	Pristine	Neutron-irradiated	He-irradiated
FWHM – a/b-axis [Å]	0.205	0.338	0.232
FWHM – c-axis [Å]	0.562	0.486	0.684
FWHM – a/b-axis [2θ]	1.146	2.113	1.224
FWHM – c-axis [2θ]	0.338	0.299	0.4519

iii. Analysis of a/b-axis distribution in neutron-irradiated samples

There is no single parameter that can quantify the different shape of pristine, He-, and neutron-irradiated samples distributions. In the case of normal distributions, it is common to look at the second and fourth moments, i.e. the standard deviation and kurtosis, as a measure for the scale and weight of the tails, respectively. Although the standard deviation of neutron-irradiated samples, as indicated in Table S- 3, is the highest by a wide margin, the kurtosis value is the lowest and implies the presence of light-tails (i.e. lighter-than-exponential tails) [446], which

seemingly stands in contrast to the neutron-irradiated distribution. A reasonable explanation for this abnormality can be the goodness of fitting to normal distribution.

Table S- 3: Parameters of normal, stable, and t location-scale distributions as fitted for the a/b-axis lattice parameters of pristine, neutron-irradiated and He-irradiated samples.

Distribution type	Parameters	Pristine	Neutron-irradiated	He-irradiated
Normal	Standard deviation (σ) [Å]	0.062	0.128	0.084
	Kurtosis	6.539	3.516	13.946
T location-scale	Scale (σ) [Å]	0.051	0.116	0.060
	Shape (ν)	6.185	10.245	4.226
Stable	First shape (α)	1.842	1.967	1.754
	Scale (γ) [Å]	0.039	0.089	0.048

In order to evaluate the distribution characteristics in more depth, I have fitted *stable* and *t location-scale* distributions to the data of the three sample types as shown in Figure S- 4. These two distributions can also indicate the goodness of fitting to the normal distribution. A stable distribution is defined by four parameters, first (α) and second (β) shape parameters, scale parameter (γ), and location parameter (δ) [447]. The first shape parameter determines the probability for heavy tails (i.e. heavier-than-exponential tails) [446] and has values of $0 < \alpha \leq 2$, where $\alpha = 2$ represents a normal distribution and lower values indicate tail-heavy distributions. The scale parameter stands for the dispersion of the distribution (similar to standard deviation) and the location parameter represents the median when $\alpha < 1$, and equals the mean when $\alpha > 1$. The stable distribution helps to determine the proximity to a normal distribution and the degree of the existence of heavy tails. The T location-scale distribution is characterised by three parameters, location (μ), sigma (σ), and shape (ν), which represent the mean, dispersion and the degree of heavy tails, respectively. The shape parameter approaches infinity when the distribution is normal, whereas smaller values indicate heavier tails.

The fitting of normal, stable, and t location-scale distributions to the experimental data of the measured a/b-axis lattice parameter is presented in Figure S- 4. One can notice than none of the fittings is perfect and thus the experimental data cannot be simply represented by any of these distributions. Table S- 3 shows the fitting parameters for the different distributions. The first shape parameter in the stable distribution is close to $\alpha = 2$ in the case of neutron-irradiated sample, and thus has the closest proximity to a normal distribution. Similarly, the t location-scale shape parameter (ν) also indicates that the neutron-irradiated sample distribution is the closest to normal due to its high value. In the three distribution types, the dispersion is the highest for neutron-irradiated sample, reflecting its wider overall distribution.

From this analysis one can derive three conclusions. Firstly, in the case of pristine and He-irradiated samples, the distributions have high peak since values are concentrated around the mean and because the distributions are relatively narrow. The *interquartile range* (IQR) represents the range from 25% up to 75% of the values, and is lower in the pristine sample compared to He-irradiated, 0.072 Å and 0.184 Å, respectively. Secondly, the neutron-irradiated distribution is close to normal, and the high standard deviation does not indicate heavy tails but rather a smooth distribution which is wider compared to the pristine and He-irradiated samples, and therefore has lower probability of tails. Lastly, kurtosis is heavily skewed by the extreme values and therefore the standard deviation is in this case more suitable to measure the width of the distribution.

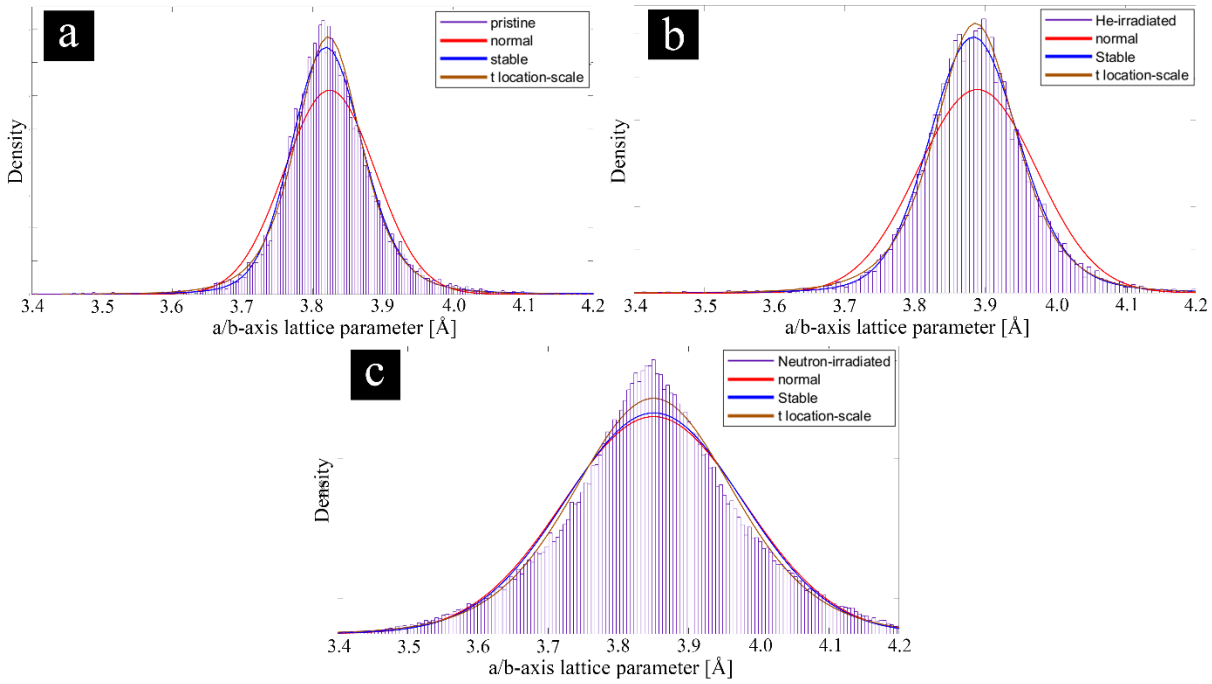


Figure S- 4: Normal (red curve), stable (blue curve), and t location-scale (brown curve) distribution fitting to the experimental a/b-axis lattice parameters in pristine (a), He-irradiated (b), and neutron-irradiated (c) samples.

iv. Deconvolution of pristine a/b-axis lattice parameter distribution

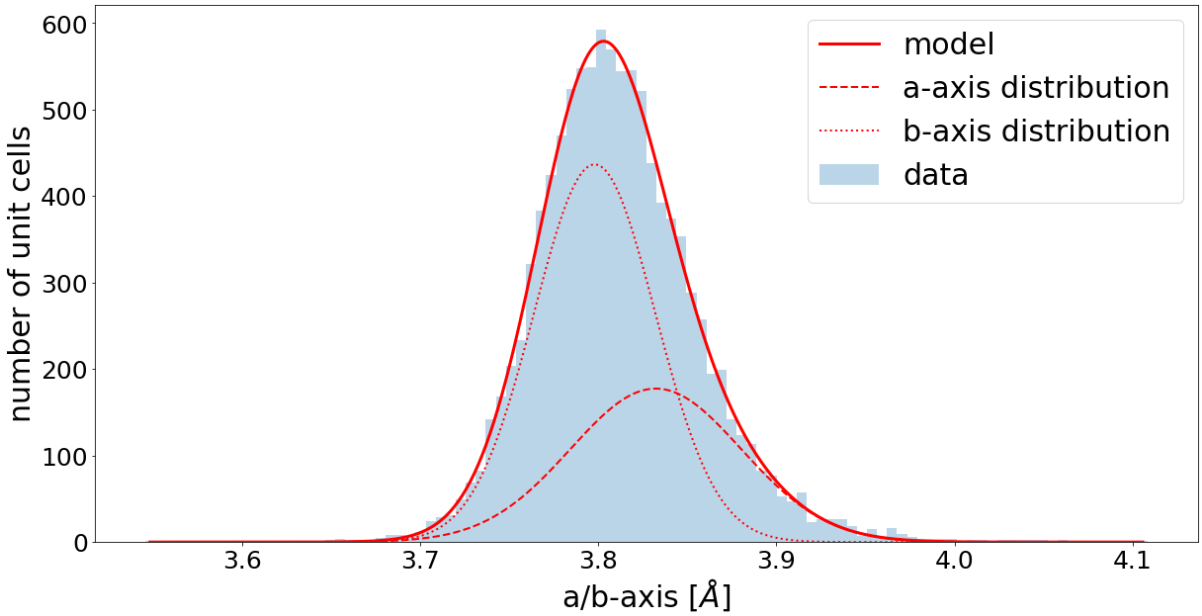


Figure S- 5: Gaussian bimodal fitting for a/b-axis lattice parameters taken from ARM300 stack images. The deconvolution was performed by fitting to a Gaussian model using Python.

Table S- 4: Fitting parameters for two peaks Gaussian model.

Sample type	Parameters	Sigma
μ (a-axis)	3.832	0.015
σ (a-axis)	0.048	0.003
A1	177.451	68.864
μ (b-axis)	3.798	0.001
σ (b-axis)	0.034	0.002
A2	436.661	84.729

v. Lattice parameters scatter plot of pristine and He-irradiated samples

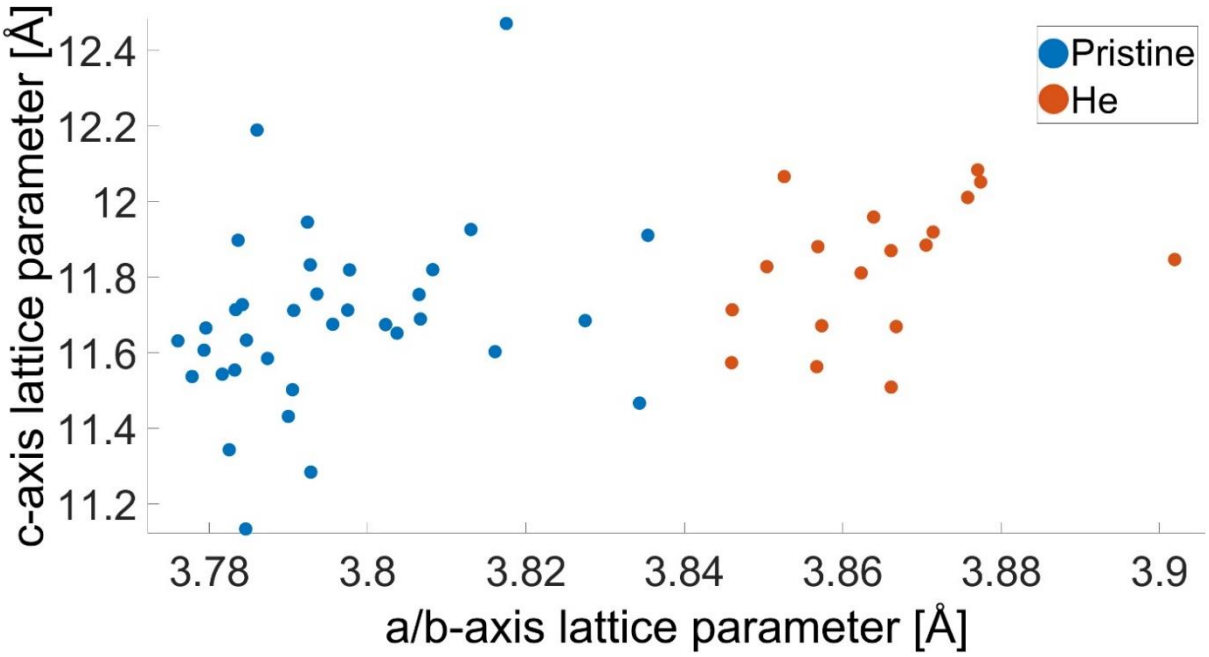


Figure S- 6: Lattice parameter scatter plot for pristine (blue circles) and He-irradiated samples (red circles). The one-frame images used for this analysis were taken on the ARM300CF microscope.

vi. Lattice parameters scatter plot of pristine, Ne- and Ar-irradiated samples

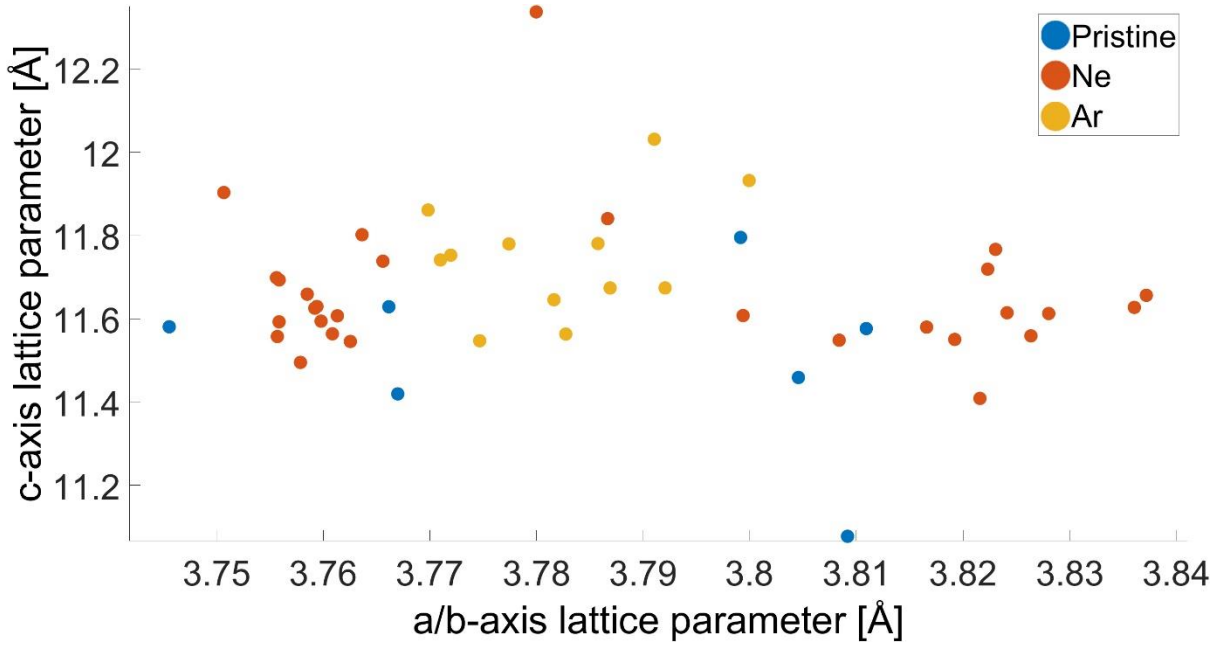


Figure S- 7: Lattice parameter scatter plot for pristine (blue circles), Ne-ion (red) and He-irradiated samples (yellow). The data includes one-frame images taken on the ARM200f microscope.

vii. Standard deviation of lattice parameters of Xe-irradiated samples at 100 and 298 K

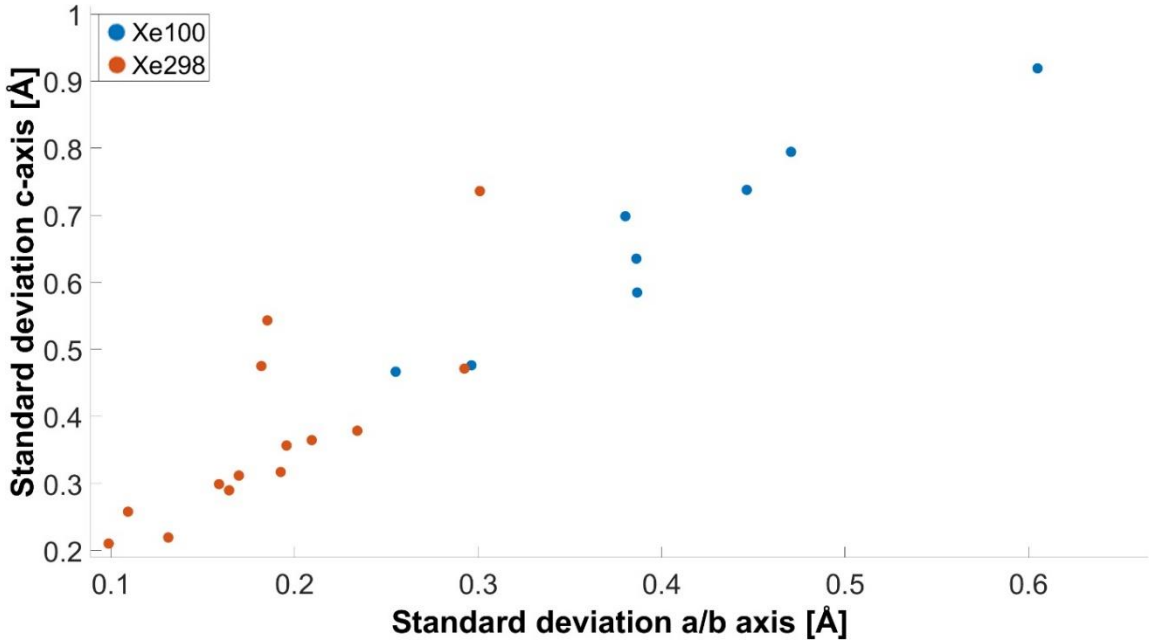


Figure S- 8: Scatter plot of lattice parameter standard deviations along a/b- and c-axes of Xe-irradiated samples at 100 K (blue circles) and at room temperature (red circles).

Appendix C Chapter 6 Supplementary Information

i. Why choose medium subband FFT as a proxy for the extent of damage?

As shown in section 6.3.2, in the analysis of my images using the frequency domain, the entropy is calculated from the FFT domain using only the mid-frequency, 2.4 - 4.5 1/nm band. The idea behind this choice is that the halo characterising scattering from fully amorphous material will be found at about the same frequency range as the damage generated in crystalline materials by displacement of atoms from perfect lattice sites by irradiation. This short supplementary section addresses the question why other frequencies have not been chosen for this analysis.

Figure S- 9 shows a typical FFT pattern taken from an HRTEM image of pristine REBCO along the [100]/[010] direction. The zero in the frequency domain is situated in the centre, and the frequency increases radially. Low frequencies up to 2.4 1/nm (0.417 nm in real space) are shown

in red, medium frequencies from 2.4 to 4.5 1/nm (0.417 to 0.222 nm) in green, and high frequencies, 4.5 to 15.0 1/nm (0.222 to 0.067 nm) in blue. The very high frequencies beyond 15.0 1/nm are truncated from the image.

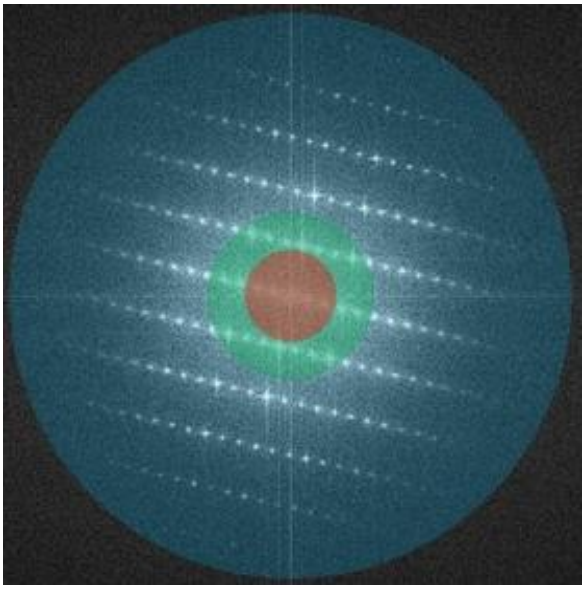


Figure S- 9: FFT pattern of REBCO matrix taken along [100]/[010] ZA with low, medium and high frequencies shown in red, green and blue concentric rings, respectively.

By looking only at the FFT pattern in Figure S- 9, one can eliminate the low-frequency band that contains very little information about the 3D crystalline structure because no information along the a/b-axis is included. Similarly, the very-high frequencies, above 15.0 1/nm, can also be ignored because the absence of spots in the FFT shows that there is not much information on the lattice periodicity at such high frequencies. Therefore, the FFT coefficients in the high frequency band (4.5 to 15.0 1/nm (blue)) need to be compared to the accuracy of the medium frequency (2.4 to 4.5 1/nm (green)), as discussed in chapter 6.

Figure S- 10 shows the spectral entropy values for (a) all frequencies and (b) the high-frequency band, i.e. between 4.5 to 15.0 1/nm. When measured over all frequencies, the standard deviation shown by error bars is very large compared to the mean values. In addition, the damage extent

estimated from the subjective study of the raw images (and captured by the colour-coding) is not consistent with the trend in the entropy values. In the high-frequency band, the standard deviations are smaller and the values seem to show an increasing trend better aligned with the visual assessment of lattice damage from the images. However, according to the HRTEM observations (section 4), I can roll-out the possibility that neither neutron-irradiated sample has more severe damage than Xe-ions at 100 K nor 30 keV Xe-ions create more noticeable damage than Kr-ions.

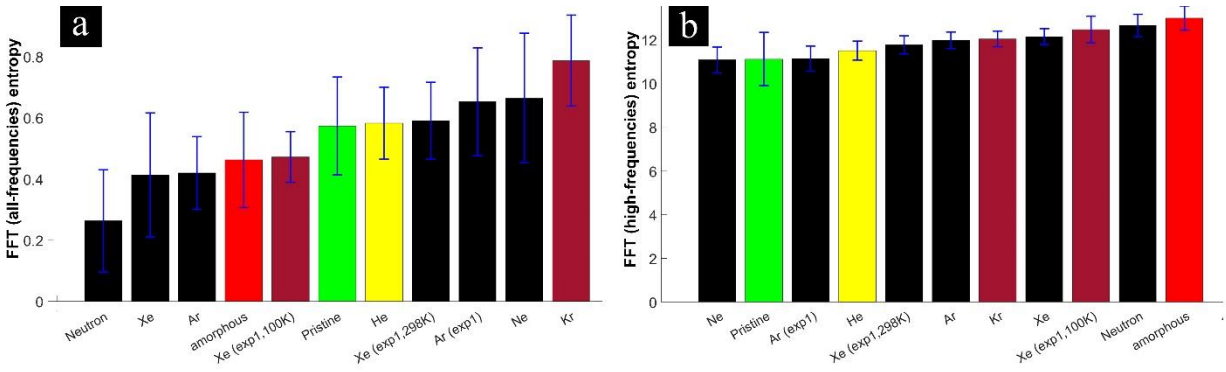


Figure S- 10: Entropy values in the FFT domain for all the sample types in the dataset. Spectral entropy values (ordered by increasing values from left to right) were calculated for (a) all frequencies and (b) the high-frequency band from 4.5 – 15.0 1/nm. The colour-coding shown for the bars is according to the subjective assessment of damage from HRTEM images; no-damage (pristine), light-medium damage (He-irradiation), severe-damage (Kr-irradiation and Xe-ion irradiation undertaken at 100 K), and amorphous, shown in green, yellow, maroon and red, respectively. The black bars belong to samples that were not categorised according to their damage severity.

ii. The relative contribution of FFT/DCT entropies

A question one may ask is which measurement, i.e. FFT or DCT, has a heavier weight when describing the spread of data on a 2D scatter plot. There is an easy-to-implement mathematical method that quantifies which variable is the most valuable for clustering the data, *principal*

component analysis (PCA), which is the most commonly used approach for dimensionality reduction. For a simple 2D graph, the case is relatively easy, but what happens when there are hundreds of variables and hundreds of observations for each variable? PCA computes the relative weight, called the loading scores, of every variable to describe the data. For more details about this method the reader is referred to other sources (e.g. [448]).

For illustration consider the example in Figure S- 11, that presents a scatter plot of two variables and 100 observations for each variable. In Figure S- 11a, it is very obvious that the only variable that causes the clusters to separate is variable1; thus PCA gives almost 100% of the loading score to variable1, which means that variable2 has no importance for the data spread. On the other hand, in Figure S- 11b variable2 affects the data clustering, but still less than variable 1 (the separation between the two clusters is larger along the x-axis); therefore, PCA accounts about 76% of the data spread to variable1 compared to 24% in the case of variable2.

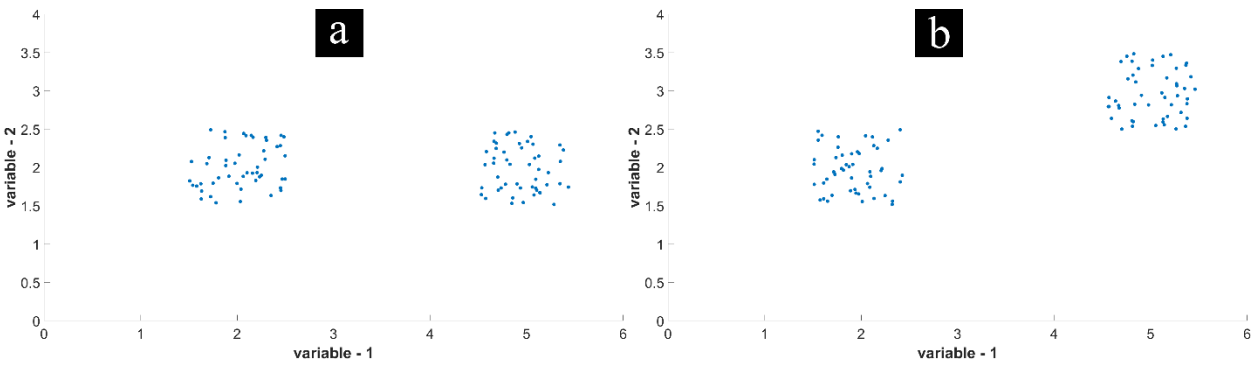


Figure S- 11: An example of two variables (variable1 and variable2) and 100 observations for each one plotted on a scatter plot. The PCA analysis loading scores are heavily weighted to variable1 in (a) but less so in (b).

The same PCA methodology can be applied to the FFT and DCT entropy values. To calculate the loading factors for the DCT and FFT values, the data includes two variables, i.e. FFT mid-frequency and DCT entropy values, and for clarity the data only includes the two extremes of

pristine and amorphous states (in total 454 observations). Figure S- 12 shows the entropy values for both samples. PCA analysis computes the principal direction in which the data spread reaches a maximum, and is shown by the black vector. The unit vector of the black vector is called the PC1 vector or Eigenvector for PC1, and the loading scores are represented by its components, namely 0.8485 along the x-axis and 0.5292 along the y-axis. Accordingly, the loading factor for PC2 are -0.5292 and 0.8485, for the x- and y-axes, respectively. The ratio of each component to the sum of the two components gives the relative contribution of each variable, which accounts for about 61.5% and 38.5% for FFT and DCT domains entropy, respectively.

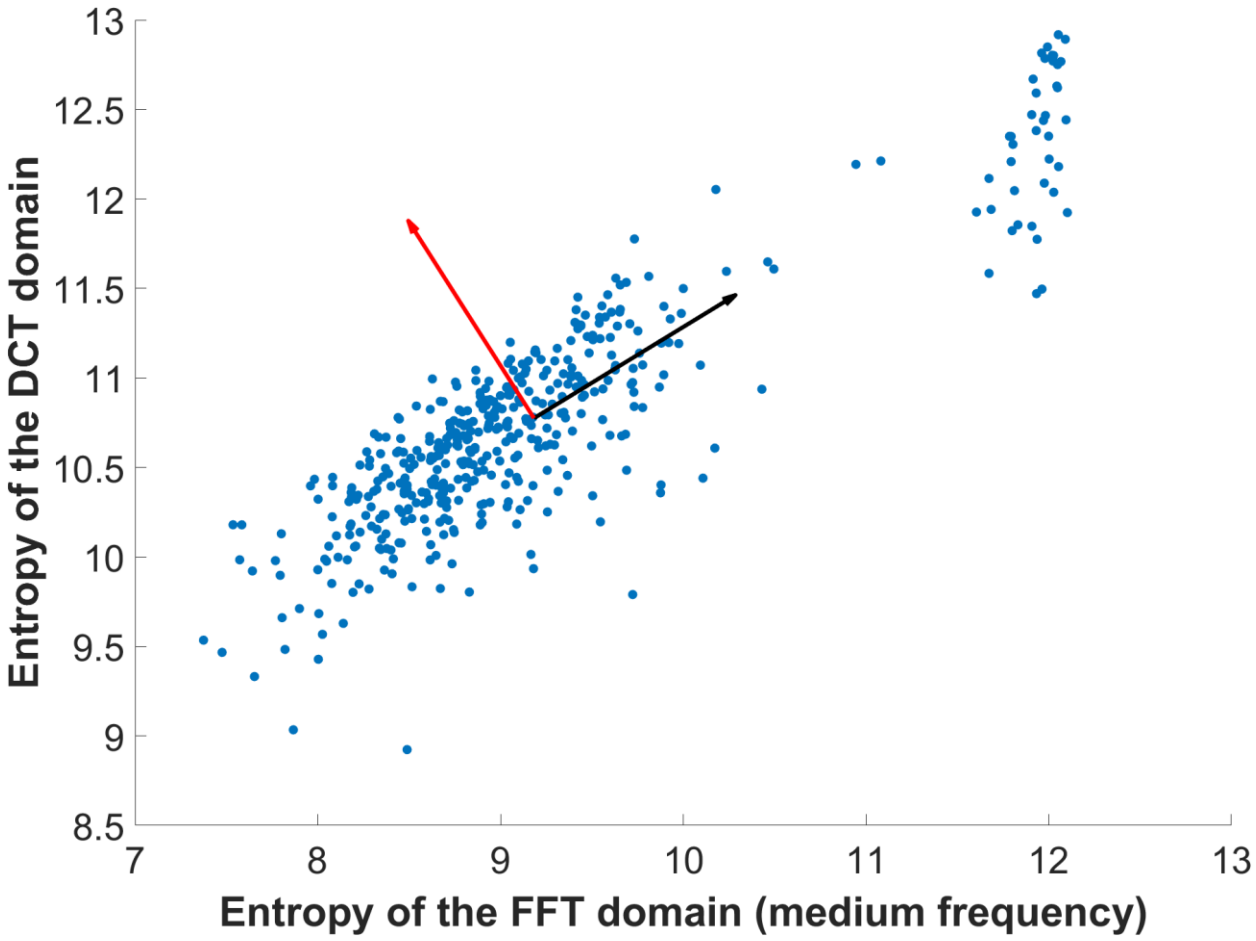


Figure S- 12: Combined data of FFT mid-frequency and DCT entropy values for 1024X1024 pixel images gathered from pristine and amorphous samples. The black vector represents the PC1 vector, i.e. Eigenvector for PC1, the direction in which the spread of the data is maximum, the red vector represents the PC2 vector, which is orthogonal to PC1.

This relative contribution of the entropies in the DCT and FFT domain remains even when including all the sample types (Figure S- 13). The PC1 eigenvector linear combination loadings are 0.8371 and 0.5371 for the x- and y-axes, respectively; for PC2 eigenvector the values are -0.5471 and 0.8371 for the x- and y-axes, respectively. Thus, the relative contribution of the entropy of the FFT domain accounts for 60.5% and DCT 39.5%. This result states that the entropy in the FFT domain increases more rapidly when compared to entropy values of the DCT

domain, and may help to distinguish between samples with different extents of lattice damage simply because the change in the values is larger.

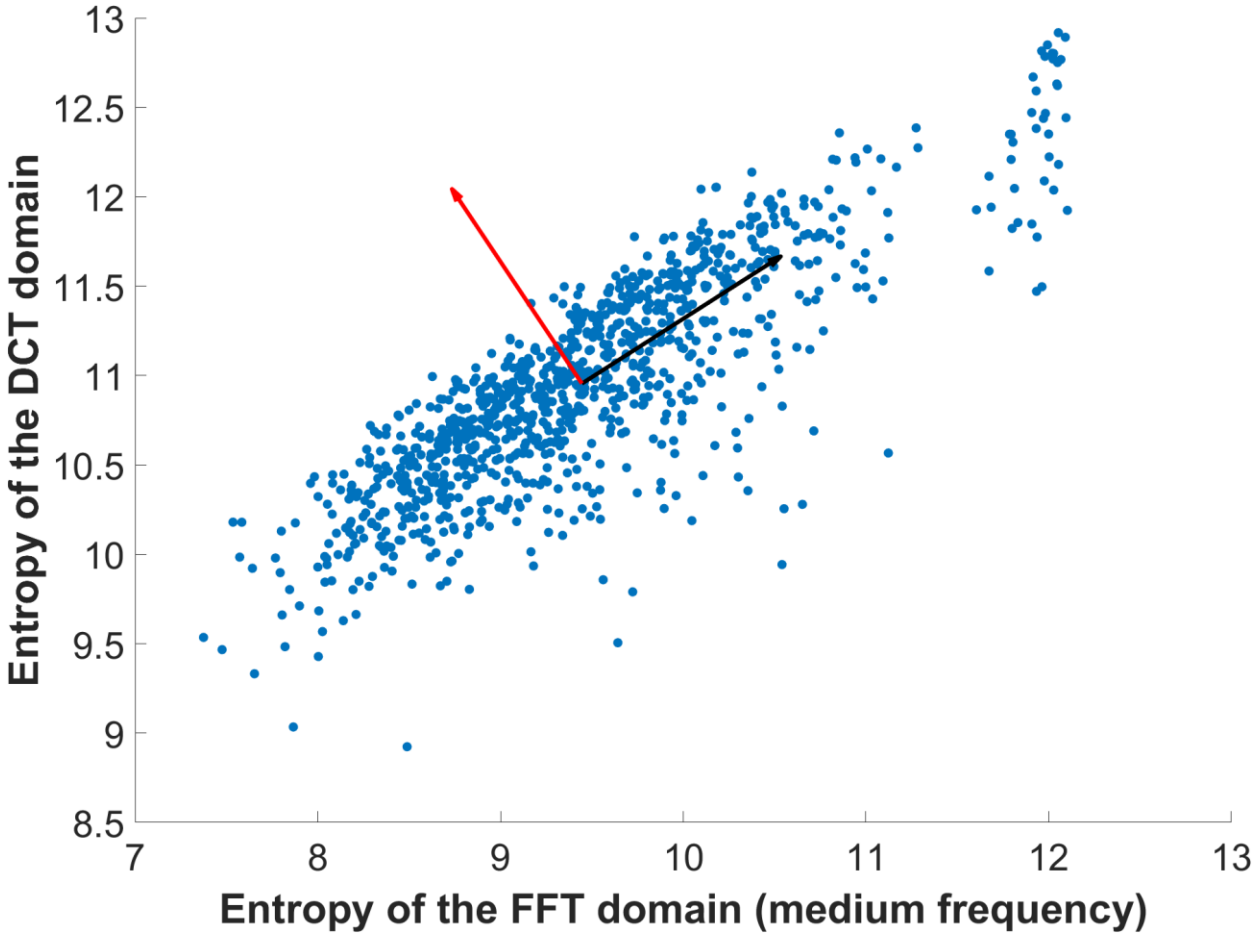


Figure S- 13: Combined data of FFT mid-frequency and DCT entropy values for 1024X1024 pixel images gathered from all the samples analysed. The black vector represents the PC1 vector, i.e. Eigenvector for PC1, the direction in which the spread of the data is maximum, the red vector represents the PC2 vector, which is orthogonal to PC1.

iii. Master curve of entropy increase with fluence

When experimental data is presented, or where theoretical model is built to describe the accumulation of lattice damage or amorphisation under irradiation as discussed in section 2.2.1.1.5, it is convenient to show the amorphous fraction as a function of irradiation fluence

[441]. Here however the entropy values in the FFT and DCT domains are assessed against other methods used to determine the amorphous fraction, such as XRD [443], convergent-beam electron diffraction [413], or directly from SAED diffraction patterns [441]. This supplementary section discusses the usage of entropy change as a metric for determining the amorphous fraction in materials investigated by HRTEM.

Experimental observations following the transition between the pristine and amorphous states as a function of fluence have not been collected in this work, so a simple model was built to evaluate the entropy change between the pristine and heavily-damaged states in order to fill-in the missing raw HRTEM images of intermediate lattice damage degradation. In order to build this model, 44 pristine and almost-amorphous images were taken. The value of each pixel (i.e. image intensity) in the pristine grayscale image was subtracted from the same pixel in the almost-amorphous image to get a quantitative pixel-wise difference between the images. A MATLAB code was then used to calculate the entropy of the intermediate states between the two extremes (i.e. pristine and almost-amorphous) by linearly changing the value of every pixel, iteration number 1 for the pristine pixel values up to iteration number 1000 to get the almost-amorphous pixel values, using the equation below for the intensity value at a given iteration k:

$$\textit{Equation S- 1:}\quad I_{Pixel}(k) = I_{pristine} + k \times \frac{I_{amorphous} - I_{pristine}}{Total\ number\ of\ iterations}$$

where the letter I represents the intensity of a pixel. In other words, each intermediate step, namely, iteration k, makes a further evolution step towards an amorphous state.

From the resulting images of each intermediate step in the spatial domain, the entropy in the DCT and FFT domains was calculated. Figure S- 14 shows the average entropy change in the DCT (red solid line) and FFT (blue solid line) as a function of the fraction of damage extracted

from the analysis of 44 pairs of images. The standard deviation associated with the entropy calculation of the 44 images was also calculated for both domains and shown in broken red and blue lines for DCT and FFT, respectively. It can be seen that both the FFT and DCT curves display the same sigmoidal shape and similar standard deviation values. This result is not unexpected since FFT and DCT operations are similar in nature and thus yield a similar curve shape.

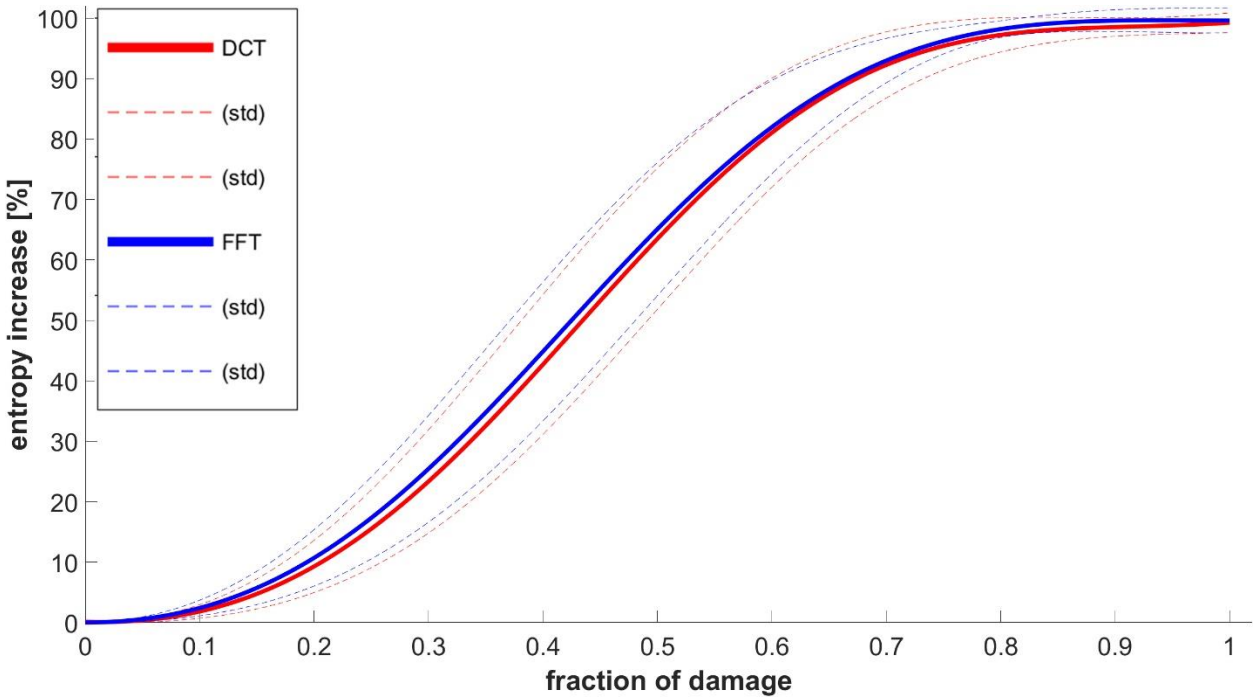


Figure S- 14: Entropy change as a function of irradiation damage fraction (0 in pristine and 1 in almost-amorphous images) calculated as an average of 44 pairs of HRTEM images where pixel intensity values were changed linearly from the pristine to the almost-amorphous states. The solid red line shows the entropy change in the DCT domain and the solid blue line presents the entropy increase in the FFT domain, the dotted red and blue lines present the standard deviation for DCT and FFT entropies, respectively.

The entropy curves shown in Figure S- 14 can be fitted to the heterogeneous amorphisation model shown below [235] for each number of overlapping damage events (m) that create an amorphous region:

Equation S- 2: $f_a = 1 - \sum_{k=0}^{m} \frac{(V*D)^k}{k!} * exp\ (-V * D)$

where f_a is the amorphous fraction, V is the average damage volume per incident ion, D is the total fluence, and m is the number of overlapping damage cascades required to form an amorphous volume, which depends on the mass on the incident ion [442]. Figure S- 15 shows the DCT curve from Figure S- 14, and the fitting curves for m overlapping cascades that trigger amorphisation. It can be seen the m=1 fitting is the least accurate whereas as the number of overlaps increases, the curve fits better. The R^2 values for the goodness of fit, are presented in Table S- 5 for both FFT and DCT domains with m=1 to m=5. These fitting values confirm what can be seen in Figure S- 15, that from m=3 and above the goodness of fit is very close to unity and thus it can be concluded that both FFT and DCT entropies extracted from the pristine and almost-amorphous samples can be fitted to the heterogeneous overlap model [235] with an m value that is between 3 to 4. To get a general idea of the meaning of *m* Camara et.al. [441] showed results from an in-situ irradiation study where germanium samples were irradiated with ions with increasing Z number, and reported m=1 for krypton and m=3 for helium.

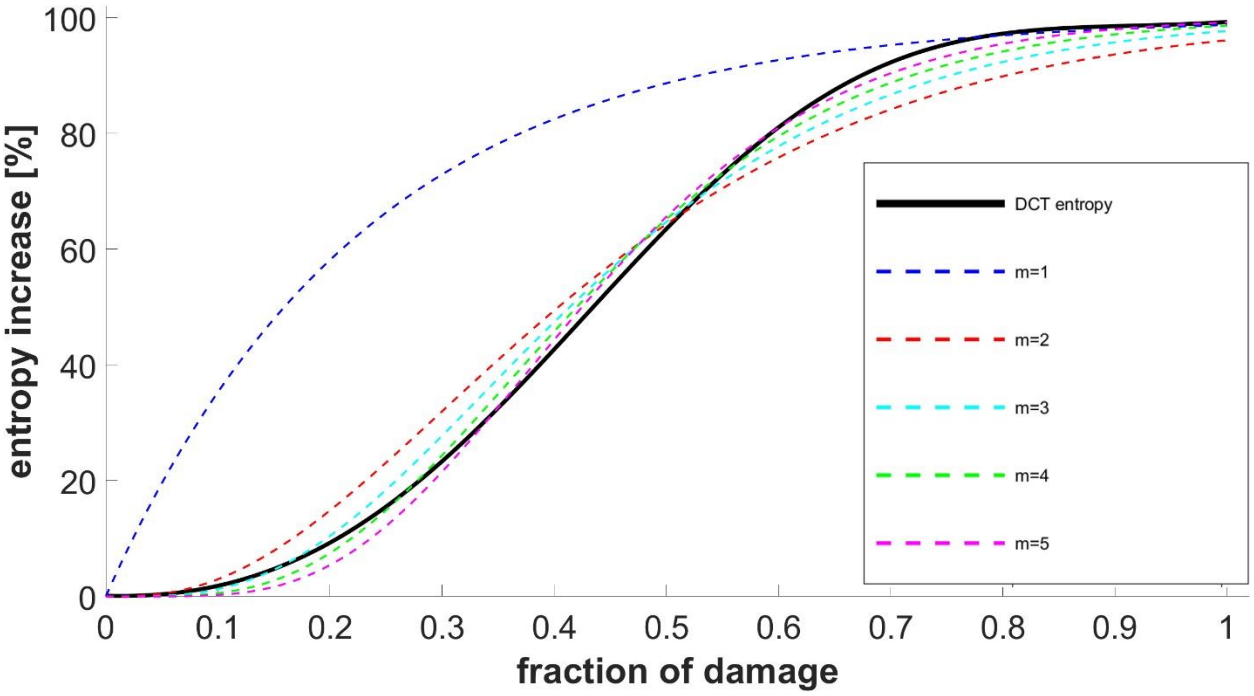


Figure S- 15: Heterogeneous amorphisation model fitted to the DCT entropy increase in 44 pairs of pristine and almost-amorphous images. The solid black line shows the entropy change data as a function of irradiation damage fraction (0 in pristine and 1 in almost-amorphous), the broken lines represent the best fit to the data with the number of overlaps, m, changing from 1 to 5.

Table S- 5: The goodness of fitting (R^2) of the FFT and DCT entropy curves to the heterogeneous amorphisation model (as shown in Figure S- 15) with number of overlaps increasing from m=1 to m=5.

Number of overlaps	R^2 (FFT entropy)	R^2 (DCT entropy)
m=1	0.546	0.551
m=2	0.979	0.977
m=3	0.993	0.992
m=4	0.997	0.997
m=5	0.996	0.998

It must be remembered that my model built to illustrate the transition from pristine to amorphous states is not based on real observations but rather on a linear, pixel-by-pixel comparisons. Thus, a model based on linearised changes in pixel intensity changes might be expected to predict a more

homogenous damage accumulation. Therefore, it is hypothesised that based on the amorphisation curve (Figure S- 14), entropy values both in the FFT and DCT domains are a good proxy for amorphisation fraction.

iv. Confusion matrix of supervised k-nearest neighbour classifier for Xe-irradiated and amorphous samples

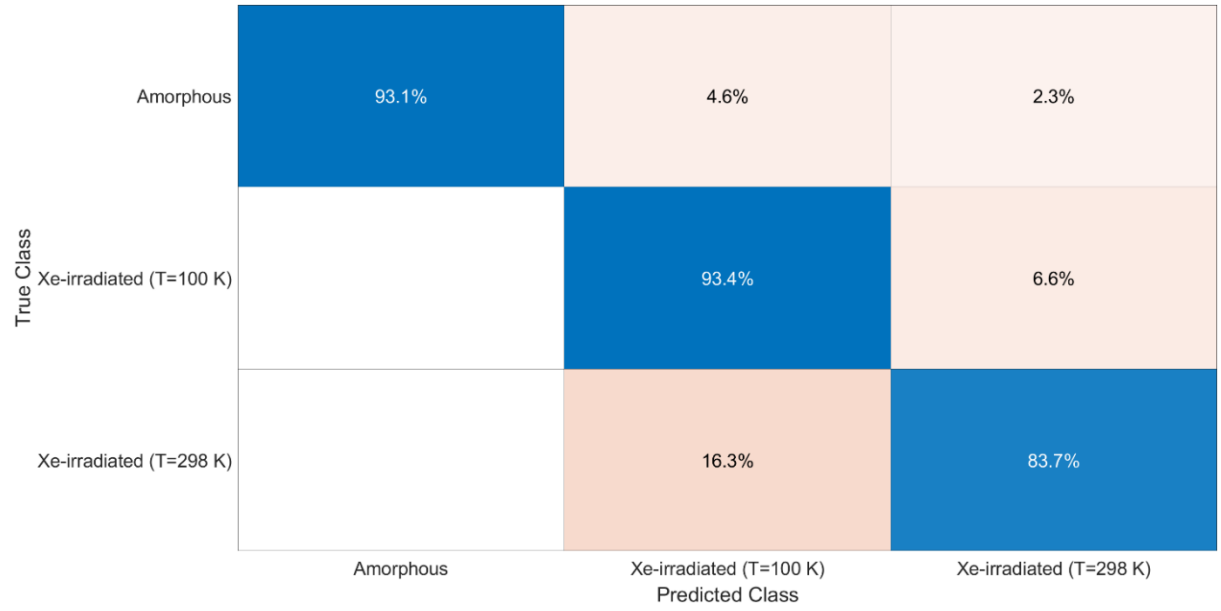


Figure S- 16: Mean confusion matrix calculated across 100,000 trials using MATLAB's supervised k-nearest neighbor classifier of irradiated samples irradiated at 100 K and 298 K, and amorphous samples. The model was trained on 80% of the total images for every sample, using 5-nearest neighbors, and Chebychev distance.

v. Possible reasons as to the origin of the broader distribution in the DCT domain

The first question is where does the larger deviation in a case of DCT entropy come from (Figure 6.25, section 6.5)? To address this question DCT coefficients were taken from the amorphous edge of all these HRTEM images. To analyse which frequencies in the DCT matrix are

responsible for the large standard deviation, the DCT coefficient matrices were broken into blocks that contain 32X32 coefficients and the entropy value was computed from each block. Then the average (μ), standard deviation (σ) and coefficient of variation (CV=μ/σ) were calculated for every block that associated with the 348 HRTEM images. Figure S- 17 shows the coefficient of variation values for every image block, and it can be seen that the largest change of the entropy values between the images takes place at the upper left side of the heatmap where the DCT coefficients stand for the lowest frequency components. It is also noted that the CV values shows a decreasing trend from the upper left block radially towards higher frequency components.

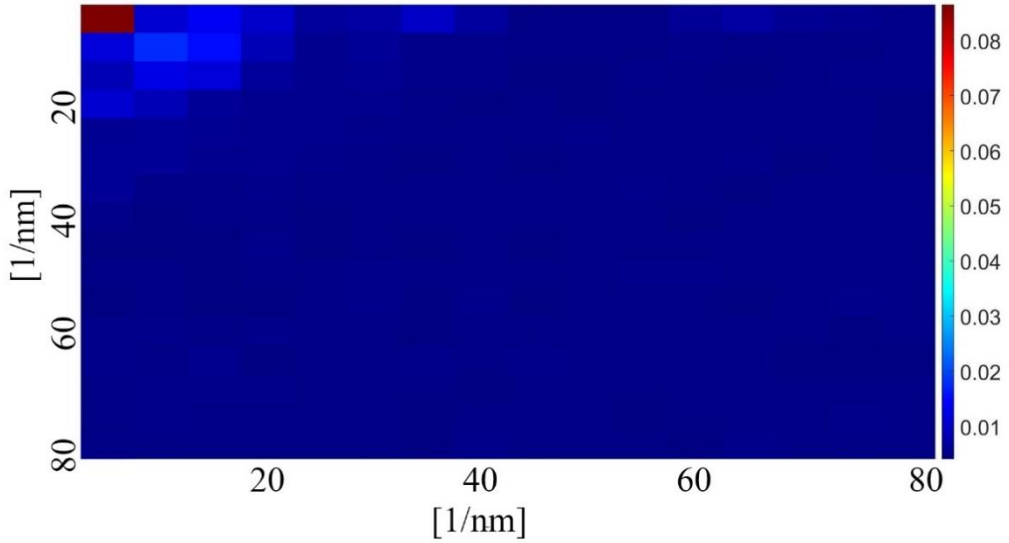


Figure S- 17: Heatmap of the coefficient of variation (CV) calculated from 348 HRTEM images taken from the amorphous edge of the samples. First, DCT was performed on every 512X512 pixel image, then the DCT coefficient matrix was broken into 32X32 pixel blocks and the entropy value was calculated from every block, and finally statistical parameters were computed from every block across all the images.

To investigate further why the low frequency components have high variability, I took the two HRTEM images from the amorphous edge that have the lowest and highest entropy values of the

32X32 pixel low-frequency coefficients (block (1,1) in Figure S- 17) to try to spot visual differences. Figure S- 18a and c show the HRTEM images taken from the amorphous sample edge with the lowest and highest entropy values of the low-frequency 32X32 pixels blocks, 4.40 and 8.85, respectively; (b,d) display the IDCT image taken from these low-frequency 32X32 pixels blocks. It can be seen that the images do not show clear visual differences, and nor can the IDCT images be easily distinguished from each other. Lastly, the entropy of the full-sized images is 9.88 and 10.87 in the DCT domain and 9.86 and 9.81 in the mid-frequency FFT domain for images Figure S- 18a and Figure S- 18c, respectively.

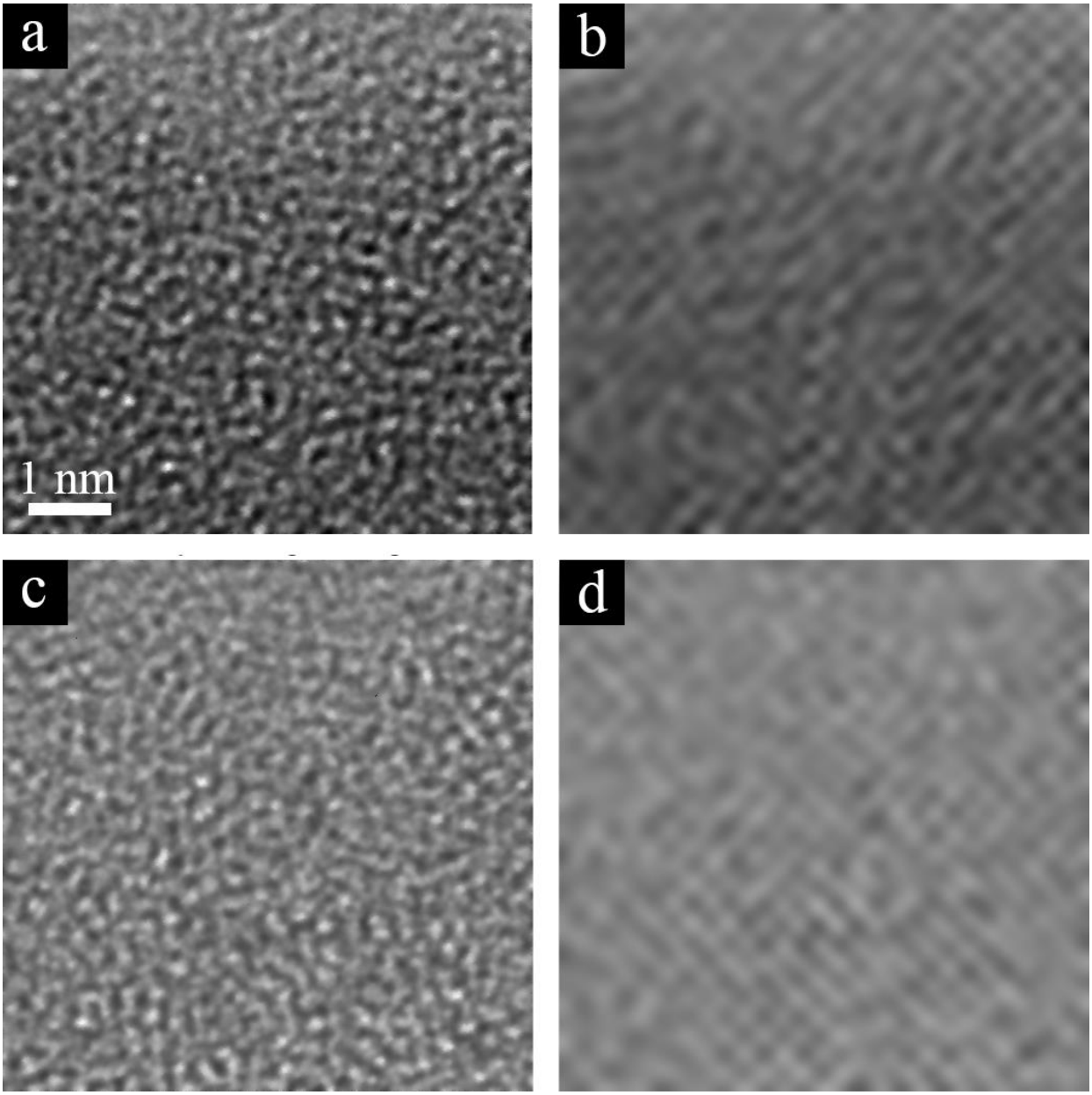


Figure S- 18: HRTEM and IDCT images from amorphous sample edges chosen because the entropy value of their 32X32 low-frequency coefficients were the lowest (a) and the highest (c), 4.40 and 8.86, respectively. (b,d) the associated IDCT images taken from the low-frequency 32X32 pixels to emphasis that long-range order exists in the images.

If the visual difference is absent the next step would be to analyse the individual DCT coefficients of the two images. Figure S- 19 shows two heatmaps of the DCT coefficients of the low-frequency 32X32 pixel blocks, the low entropy on the left (a) and high entropy on the right

(b). It can be seen that in the case of the low entropy data, there are 2-3 dominant high DCT coefficients at very low frequencies, i.e. wavelengths that are of the order of the full-size image. On the other hand, the high entropy case shows no dominant coefficients. Do these three high coefficients play a part in decreasing the entropy of the coefficients matrix? To address this, the three highest coefficients in the low entropy block (a) were manually changed to a value of 2, which is close to the maximum value in (b). As a result, the normalised power coefficients distribution changed to a more even spread as can be seen in Figure S- 19c by the before (blue bars) and after changing the three coefficients (red bars). The associated entropy was increased from 4.40 to 8.46, very close to the entropy of (b), 8.85. This example emphasises that the low-frequency DCT coefficients (i.e. close to DC) are prone to a somewhat stochastic nature, and these frequencies do not represent the crystal structure as they are lower than the minimum frequency of the REBCO crystal structure itself (i.e. the largest d_{hkl} in the real space).

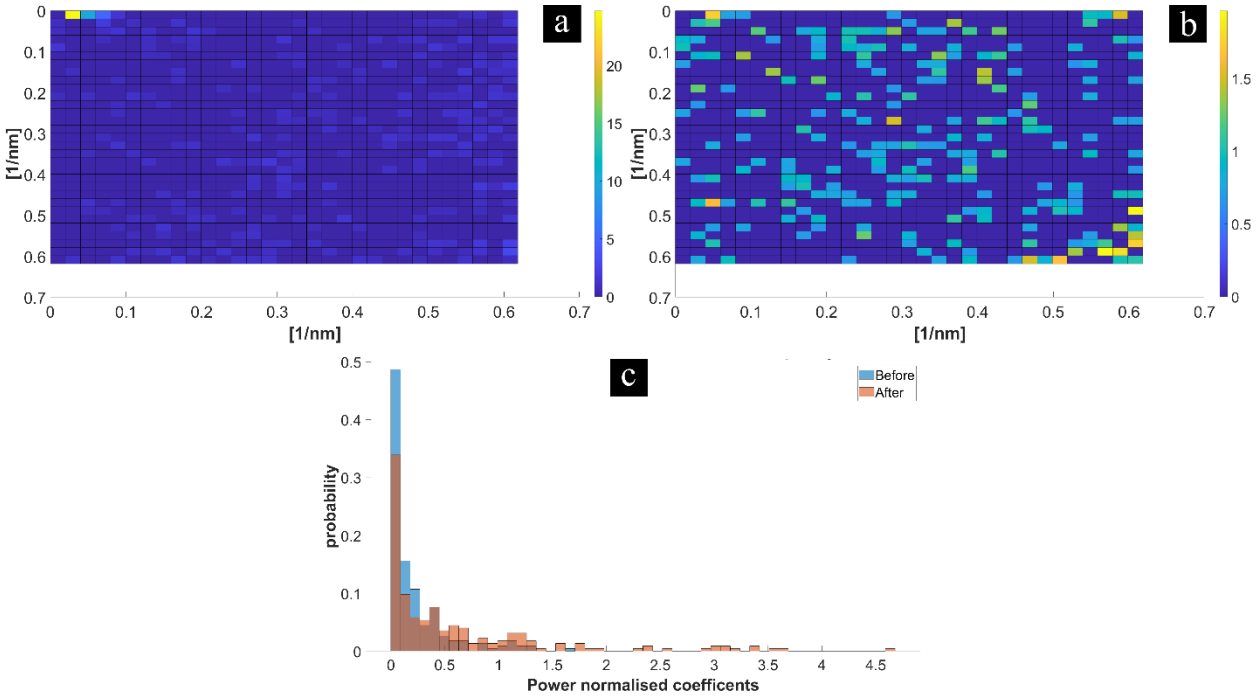


Figure S- 19: Heatmaps and distribution of the low-frequency (32X32 pixel block) DCT coefficients of two HRTEM images of the amorphous edge. (a-b) heatmaps corresponding to the lowest (a) and highest (b) entropy values among the amorphous edge HRTEM images, the values stand for the absolute value of individual coefficients. (c) Normalised power coefficients histograms of the un-changed low entropy block in blue bars and after deliberately changing the values of the three highest coefficients (bright region at the upper left) to a value of 2 in red bars, respectively.

DCT 'outliers' can be seen in Figure 6.5 (for example) it can be seen that the entropy values calculated from pristine and amorphous samples are well separated in the FFT domain but in the DCT domain some of the pristine samples have entropy values equivalent to those from the amorphous samples. In other words, in the FFT domain the separation is clear whereas in the DCT domain there is significant overlap. The following paragraphs carry on the theme of understanding the root-cause for the behaviour of the DCT entropy values.

Figure S- 20 shows the coefficient of variation of the DCT entropy values calculated from 410 pristine HRTEM images. It can be seen that the highest variability of the entropy is situated in

the low frequency components of the DCT coefficients matrix. This observation aligns with the low frequency components of the DCT coefficients shown in Figure S- 17 in the case of amorphous samples. However, despite the fact that this phenomenon is observed both in pristine and amorphous samples, the coefficient of variation at the lowest frequency is twice as large in the pristine images (Figure S- 20) compared to amorphous (Figure S- 17).

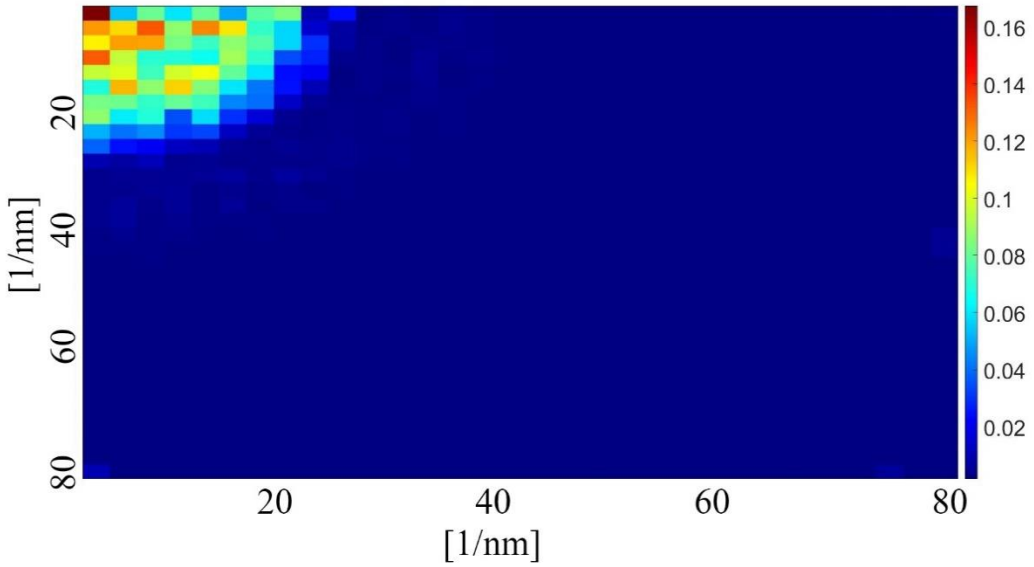


Figure S- 20: Heatmap of the coefficient of variation (CV) calculated from 410 HRTEM pristine images. First DCT was performed on each 1024X1024 pixel image, then the DCT coefficient matrix was broken into 32X32 pixel blocks and the entropy value was calculated from every block, lastly, statistical parameters were computed from every block across all images.

As a case in point, I took pristine HRTEM images with the lowest (Figure S- 21a) and highest (Figure S- 21b) DCT entropy values, 8.92 and 12.05, respectively. The low-entropy HRTEM image (a) has a very clear periodic structure whereas the high-entropy image (b) has a more poorly defined periodic structure. Thus, one indeed should expect a lower entropy where the periodic structure is more distinct. Mid-frequency FFT entropy values also support this observation, with values of 8.49 and 10.18 for (a) and (b), respectively. Figure S- 21c presents

the entropy evolution calculated from the DCT coefficients matrices for low- and high- entropy pristine samples and an HRTEM of an amorphous sample that has the lowest DCT entropy, as a comparison. The calculation was performed on increasing block sizes from 32X32 low-frequency components up to 1024X1024 pixels. It can be seen that the amorphous sample has a low entropy value at low frequencies but this quickly rises as the block size increases, whereas the two pristine images also underwent the same trend but from different starting points.

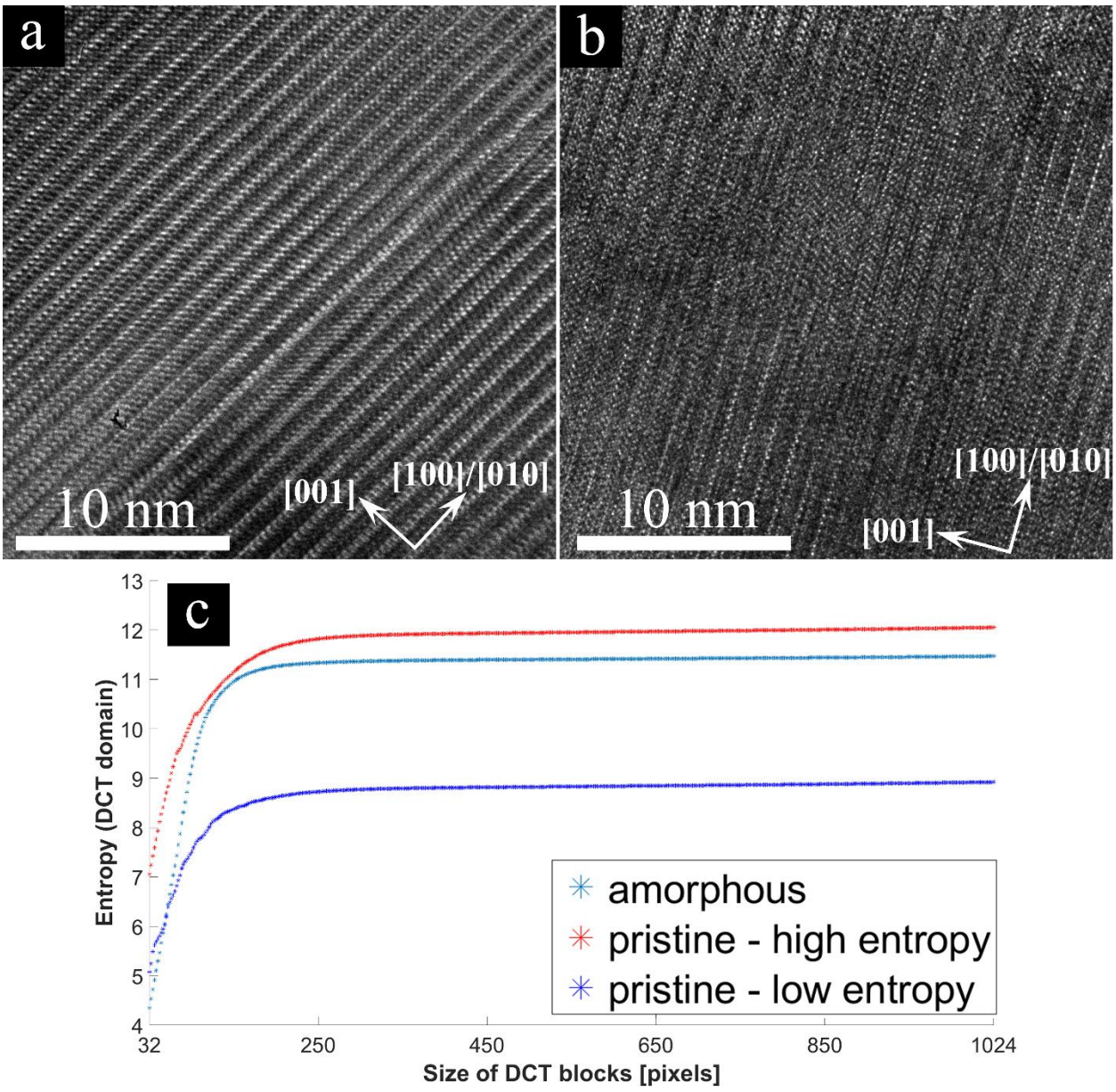


Figure S- 21: HRTEM images of pristine samples taken along [100]/[010] ZA (a-b) and (c) their DCT entropy values calculated from different block sizes. (a-b) HRTEM images with the lowest (a) and highest (b) DCT entropy values, 8.92 and 12.05, respectively. (c) DCT entropy values calculated directly from the DCT coefficient matrix starting from 32X32 pixels low-frequency block up to 1024X1024 pixels. As a comparison, entropy values of the lowest entropy amorphous images were also added to the graph. The images shown are 2048X2048 pixels size and were broken to 1024X1024 blocks for the calculation procedure, as was done throughout section 6.

This specific example of the lower entropy value measured in an amorphous sample in the low-frequency DCT coefficients than in pristine samples is not unique. Figure S- 22 shows the entropy percentage change from pristine to amorphous states calculated on different sizes of DCT coefficients blocks, namely, pristine value was subtracted from amorphous value and divided by the pristine value. The change in entropy was calculated as an average from 44 HRTEM images of both pristine and amorphous material. It can be seen that in the low-frequency coefficients, the amorphous state has a lower entropy up to about 50X50 pixels, and only when the block size is increased does it present a higher entropy. The plateau at high-frequency DCT coefficients implies that the degree of disorder between amorphous and pristine sample does not change once a particular frequency has been exceeded.

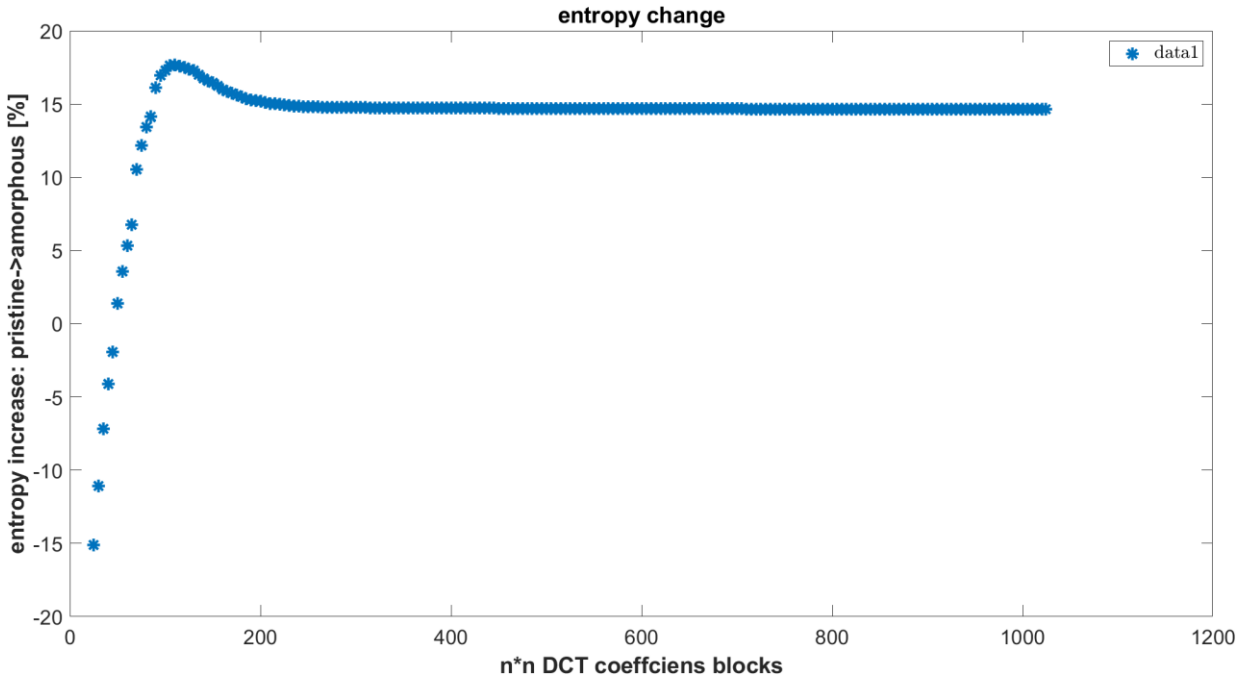


Figure S- 22: Entropy increase in percentage terms from pristine to amorphous material (i.e. pristine values were subtracted from amorphous values) as a function of the number of DCT low-frequency blocks from which the entropy was calculated. The data was extracted from 44 images at each state (pristine and amorphous).

To understand the stochastic nature of the low-frequency DCT coefficients it is necessary to take note of the spectral entropy they represent. Along either horizontal or vertical directions, (1,32) or (32,1) coefficients have a spectral frequency of 0.618 1/nm that is equivalent to 1.617 nm in the spatial domain. One may recall that the largest lattice parameter of the orthorhombic REBCO structure is 1.168 nm [129], which is lower than the reciprocal values represented by 32X32 low-frequency components. In other words, the 32X32 pixel DCT coefficients cannot capture the REBCO crystal structure, which explains the large variability of the coefficients at these frequencies. Further, as determined from Figure S- 22, the point at which the entropy of the amorphous samples exceeds that of the pristine samples is from about a frequency of 0.965 1/nm that represents 1.036 nm in the spatial domain, which is about the point that the real structural periodicity in the images can start to dominate the frequency analysis and not other random features of the images.

All in all, the DCT components can be broadly broken down into low frequencies that do not represent the lattice periodicity and higher frequency components that match REBCO periodicity and thus directly represent the structure. The low-frequency components tend to have large variations between images from the same type (see Figure S- 17 for amorphous and Figure S- 20 for pristine images) that have impact on the entropy of the whole DCT domain.